NTNU

Norwegian University of
Science and Technology

TIME DOMAIN SIMULATION PARAMETERS FOR FATIGUE ASSESSMENT OF AN OFFSHORE GRAVITY BASED WIND TURBINE

Alvaro Ortega Nadal

Maritime Engineering
Submission date: June 2018
Supervisor: Erin Bachynski, IMT

Norwegian University of Science and Technology
Department of Marine Technology

NTNU
Norwegian University of Science and Technology

NORDIC MASTER IN MARITIME ENGINEERING

Master Thesis

Time Domain Simulation Parameters for Fatigue Assessment of an Offshore Gravity Based Wind Turbine

Department of Marine Technology
Trondheim 2018

Author: Álvaro Ortega Nadal
Supervisor: Erin Bachynski
Co-Supervisor: Wengang Mao

CHALMERS UNIVERSITY OF TECHNOLOGY

PLOCAN consorcio PLATAFORMA OCEÁNICA DE CANARIAS

Time Domain Simulation Parameters for Fatigue Assessment of an Offshore Gravity Based Wind Turbine

Master Thesis

Degree of Master of Science in Maritime Engineering at the Norwegian University of Science and Technology & Master of Science in Naval Architecture and Ocean Engineering at Chalmers University of Technology

Álvaro Ortega Nadal
June 2018

Nordic Master in Maritime Engineering - Ocean Structures Track

Supervisor: Erin Bachynski
Co-Supervisor: Wengang Mao
PLOCAN External Advisor: Octavio Llinás

Norwegian University of Science and Technology
Faculty of Engineering Science and Technology
Department of Marine Technology

Chalmers University of Science and Technology
Department of Mechanics and Maritime Science
Division of Marine Technology

NORDIC
MASTER
IN **MARITIME**
ENGINEERING

NTNU
Norwegian University of
Science and Technology

CHALMERS
UNIVERSITY OF TECHNOLOGY

NTNU Trondheim
Norwegian University of Science and Technology
Department of Marine Technology – Group of Marine Structures

PROJECT THESIS IN MARINE TECHNOLOGY

SPRING 2018

FOR

STUD.TECHN. Alvaro Ortega Nadal

Time domain simulation parameters for fatigue assessment of an offshore gravity based wind turbine

Simuleringsparametre for utmattingsanalyse av en offshore vindturbin med betongunderstell

Background:
Offshore wind turbines are a promising technology for harnessing renewable energy. The industry is still young, and many design analysis practices are taken as a combination of experience from the oil and gas industry and the onshore industry. New locations are of interest – such as the coast of Gran Canaria – and present opportunities for innovation in design. Gravity based structures (GBS) for wind turbines have historically been applied in shallow water for small turbines, but may be cost competitive in other situations with improved installation procedures.

The present project develops a baseline GBS design to support a 5 MW wind turbine and examines the sensitivity of fatigue damage estimation to simulation parameters, such as the duration and number of realizations, and to the hydrodynamic load model which is applied.

Assignment:
The following tasks should be addressed in the project work:

1. Literature review regarding offshore wind turbine concepts, global (aero-hydro-servo-elastic) modelling, and fatigue damage estimation, especially for concrete structures.

2. Carry out a preliminary analysis and discretization of the metocean data for the Canary Islands. Select a range or representative conditions for the sensitivity studies.

3. Develop a GBS design to support the NREL 5 MW wind turbine for the selected water depth. Rational design estimates should be obtained based on first principles.

4. Carry out identification tests (decay and/or eigenvalue analysis, wave-only tests, constant wind tests) of an existing SIMA model of the concept. Compare the results against reference data.

5. Select several locations of interest (tower base, tower top, shaft base, etc). Compare fatigue damage predictions for the model using different simulation parameters, such as the hydrodynamic load model which is applied.

6. Report and conclude on the investigation.

The work scope could be larger than anticipated. Subject to approval from the supervisor, topics may be deleted from the list above or reduced in extent.

In the project, the candidate shall present his personal contribution to the resolution of problem within the scope of the project work.

Theories and conclusions should be based on mathematical derivations and/or logic reasoning identifying the various steps in the deduction.

The candidate should utilize the existing possibilities for obtaining relevant literature.

The project report should be organized in a rational manner to give a clear exposition of results, assessments, and conclusions. The text should be brief and to the point, with a clear language. Telegraphic language should be avoided.

The project report shall contain the following elements: A text defining the scope, preface, list of contents, main body of the project report, conclusions with recommendations for further work, list of symbols and acronyms, reference and (optional) appendices. All figures, tables and equations shall be numerated.

The supervisor may require that the candidate, in an early stage of the work, present a written plan for the completion of the work. The plan should include a budget for the use of computer and laboratory resources that will be charged to the department. Overruns shall be reported to the supervisor.

The original contribution of the candidate and material taken from other sources shall be clearly defined. Work from other sources shall be properly referenced using an acknowledged referencing system.
The project report shall be submitted in two copies:

- Signed by the candidate
- The text defining the scope included
- In bound volume(s)
- Drawings and/or computer prints which cannot be bound should be organized in a separate folder.

Erin Bachynski
Supervisor

Deadline: 10.06.2018

Summary

Renewable sources of energy are becoming more and more important as the years go by due to both technological development and a greener human attitude. Offshore wind turbines are presented as a productive source of energy since stronger and more constant winds are considered offshore and because less visual and noise impact is generated to the surrounded population. Specifically for this thesis, a concrete gravity based OWT has been studied whose design has been developed for 35 [m] of water depth where two large submerged diameters have been considered, 31 for the caisson and 7 [m] for the shaft of the gravity based structure. The OWT installed is a 5 MW design developed by NREL and positioned on top of the concrete shaft as reflected in figure 3.13a. So, the GBS will be installed by gravity on the seabed where no penetration on it will be necessary since, due a heavy mass design, the structure will remain on site avoiding capsizing or movements of it. However, a detailed and conscious foundation bed is necessary to prepare the seabed for withstanding the large vertical force pointing downwards from the structure to the seabed. Additionally, since large diameters are considered, important hydrodynamic loads will be present for an intermediate water depth where a finite water assumption has been applied.

In this thesis, an integrated dynamic analysis of an offshore gravity based wind turbine has been developed. Specifically, the SESAM package, property of DNVGL, developed in cooperation with SINTEF, has been widely employed. The finite element model was created through GeniE, the hydrodynamic loads computed with HydroD and WAMIT and the simulation of the OWT obtained through SIMA. Additionally, by the help of MATLAB, the TD results as well as other computational issues were processed to give answers to all the tasks performed during the thesis.

The first part of the graduation project covered the theory needed to properly understand the dynamic behaviour of the OWT and why the stresses and forces were induced leading to fatigue issues. A general overview of the different OWT concepts was introduced where the ocean waves as well as wind effects were notably described. Once the loads were mentioned, an aero-hydro-servo-elastic modelling concept was defined giving shape and physical answers to the effects of wind and waves on the OWT structure. This included three different hydrodynamic models description (Morison, potential flow and MacCamy&Fuchs), BEM development, as well as a structural modelling explanation where also some theory of control systems was covered. Finally, a general but detailed fatigue theory was introduced covering the whole spectrum of what it is happening in a fatigue estimation process. This included from crack growth rate during the three different stages to a stress counting method procedure as well as SN curves description and applicability to both steel and RC materials.

Secondly, the gravity based design concept was fully covered. It started from different GBS prototypes descriptions to a complete GBS preliminary design where an intermedi-

ate water depth was determined. Due to this, finite water equations were used to drive the static analysis, where the total vertical and horizontal forces as well as the total overturning moment were computed as shown in tables 3.3 and 3.4. This meant that the bearing capacity check had to be performed since the foundation bed needed to have the sufficient strength to withstand the heavy loads acting from the OWT to the seabed. This checking resulting in positive arguments since the bearing force was always larger than the vertical one for every rotational studied point, as shown in table 3.7.

Thirdly, an extensive metOcean analysis was performed covering marginal distributions of H_s and U_w and joint distributions of H_s and T_p. While the two Weibull parameter distribution determined good fitting for the wind speed values and underestimation of extreme data for the significant wave height, the log-normal plots were built for joint distributions in two different H_s ranges as shown in figures 4.8 and 4.9. Additionally, wind and wave roses were determined. It was clearly stated the prominent north-east wave and wind effect where alignment between the loads was considered for just one load direction. This, therefore, resulted in concentrated fatigue damage at that same location of the GBS. Finally, the generation of the binned environmental conditions for a 29 years spectrum was developed. In table 4.3 is shown how the 90.53% of the whole scatter was considered, ending up in a total operational status of 93.79% and 6.21% of idle consideration for the OWT.

Fourthly, a series of identifications tests were covered. The decay and eigenvalue analysis were employed to obtain and check the 10 different natural frequencies of the OWT as shown in table 5.3. Additionally, both the linear and quadratic damping values were computed for the 2 first bending modes, see table 5.1. In a last step, a constant wind test resulted in the mean rotor speed, thrust, torque, power and blade pitch angle whose values built the so-called wind turbine performance curves resulted in figures 5.5 and 5.6. Finally, a general spectrum analysis combined all the results projected here with an environmental condition simulation as reflected in figure 5.8. There, it was determined how the external excitations were distributed along the frequency spectrum and how important they were on the Y-Z bending moment response.

Fifthly, a complete hydrodynamic analysis was performed with three different models: Morison, MacCamy&Fuchs and potential flow. Here an extensive potential flow computation was performed through HydroD and WAMIT to obtain the different sectional forces as well as hydrodynamic loads where first-order wave excitation forces, damping and added mass values were computed. After having checked how the change in diameter size between the caisson and the concrete shaft had a notable influence on the results, a prior fatigue assessment was developed. It determined how potential flow giving fairly similar results as MacCamy&Fuchs was rejected for the full fatigue study since it requires much more work to actually obtain similar outputs.

Finally, in the full fatigue assessment it was determined how some doubts where around what model was the most accurate to estimate fatigue damage for the GBS design. It resulted that the hybrid one, a mixture between Morison and MacCamy&Fuchs, introduced some uncertainties when estimating the wave diffraction limit. However, it resulted to be

more conservative. In contrast, MacCamy&Fuchs was understood to give more accuracy since it better computes wave loads for small and large λ/D ratios when wave diffraction occurs. Therefore, none of the above methods, according to the obtained results, could actually determine what the best option was. Additionally, it must be highlighted the surprising low durability of the structure in the weakest points for both steel and concrete, 4 and 2 years and 8 months respectively. While for steel is not surprising, it was considered that concrete would lead to a much better fatigue life estimation since it is a more durable material than steel for the conditions presented. However, keeping in mind the high uncertainties introduced when estimating the SN concrete curve, the doubts were solved. This means that according to [64], the C_1 parameter, the one defining the stress-blocks location, have a super high influence on the number of cycles leading to fatigue failure. The lower it is, the more damage it creates. So, the lowest was chosen with a value of 8 to also be on the conservative side. Additionally, the low structural durability is understood since clear dynamic amplifications in both the Y and Z bending coordinate spectrums are always presented.

Preface

This master thesis is the final stage of the Master of Science in Naval Architecture and Ocean Engineering. This master program belongs to the Nordic Five Tech alliance in which the Nordic Master in Maritime Engineering with Study Track: Ocean Structures has been chosen. Specifically, this thesis has been conducted at the Norwegian University of Science and technology (NTNU) and at Chalmers University of Technology.

On the one hand, I would like to immensely thank Associate Professor Erin Bachynski for her extraordinary and constant support during this project. Since her first lecture in Dynamic Analysis of Offshore Wind Turbines I was amazed and inspired by all her knowledge. She was able to transmit me all her wisdom from where I have learned a totally brand-new and complex field like Floating and Fixed Offshore Wind Turbines. I will always be in debt. Likewise, I would like to thank Associate Professor Wengang Mao as my second supervisor from Chalmers University of Technology. He radically made me change the perspective I had for statistical analysis making it highly useful for the marine industry. Additionally, I will also like to thank Associate Professors Manuel Jose Chica Gonzalez and Tanausu Almeida Medina from the University of Las Palmas de Gran Canaria for their extraordinary support and constant interest of my progression during this two years Master's Degree program.

On the other hand, this master of science achievement would not have been possible without the financial support of the Fundacion Universitaria de Las Palmas (FULP). I have no words to express how grateful I am for having trusted me two years ago.

Lastly, I would like to thank my family and all the friends I have met during these two years. They did not only contribute to my academic progression but also to my growth as a better person. Additionally, I express my gratitude to PLOCAN for having trusted me to collaborate with them in this master thesis. Hopefully, one day, Gran Canaria will become a reference point in the Offshore Wind Industry.

Alvaro Ortega Nadal

Trondheim Norway - June 2018

Table of Contents

List of Tables

List of Figures

Abbreviations

ALS	Accidental Limit State
AEMET	Agencia Estatal de Metereologia
BEM	Bade Element Momentum Theory
C	Damping Matrix
DOF	Degree of Freedom
ECMWF	European Center for Medium-Range Weather Forecasts
EWEA	European Wind Energy Association
F	Floated
FD	Frequency Domain
FEA	Finite Element Analysis
FFT	Fast Fourier Transformation
FLS	Fatigue Limit State
FO	Foundation Only
GBS	Gravity Based Structure
H	Wave Height
HAWTs	Horizontal Axis Wind Turbine
IFFT	Inverse Fast Fourier Transformation
IT	Integrated Transportation
K	Stiffness Matrix
KDE	Kernel Density Estimator
L	Lifted Concept
LC	Load Center
LEFM	Linear Elastic Fracture Mechanics
LTH	Load Time History
M	Mass Matrix
OWF	Offshore Wind Farm
OWT	Offshore Wind Turbine
PDF	Probability Density Function
RC	Reinforced Concrete
RNA	Rotor Nacelle Assembly
SDOF	Single Degree of Freedom
SIMA	Simulation Workbench for Marine Applications
SLS	Serviceability Limit State
STD	Standard Deviation
TD	Time Domain
TLP	Tension Leg Platform
ULS	Ultimate Limit State
WTG	Wind Turbine Generator
WT	Wind Turbine

Chapter 1

Introduction

1.1 Background

World's population is increasing year by year and fossil fuel consumption seems to have a similar trend. With the natural resources set to a limit, renewable energy appears as a clean and never ending source of energy. Therefore, the turning point from non-renewable to unlimited sources of energy is becoming real and offshore wind turbines have appeared on scene.

It has been widely known for centuries how useful the utilization of wind energy has been to society. Starting with stone windmills in Egypt for food production and moving to electricity generation in early 1900 in Denmark. Since then, onshore wind turbines has been mostly developed until a new concept was introduced; offshore wind energy.

Some reasons for considering such a topic comes due to the fact of having large areas available at a low price where noise and visual impacts are reduced if compared to onshore installations. Furthermore, higher wind velocities with less percentage of turbulence is obtained. However, the wet and highly corrosive sea environment seriously affects the OWT's structural durability where also high capital and operational expenses are set as main drawbacks.

Nevertheless, due to expected benefits in the long run, offshore wind power has the potential to be popular. This is because, even though there is a low profit margin affecting this industry, a large number of OWTs are normally installed reducing marginal installation expenses. Additionally, and still considering the high cost of OWTs, new ways of reducing expenses are being considered as the new low-cost craneless installation prototype that has been developed (Elisa & Elican Project) and is about to be installed close to the coast of Gran Canaria (Canary Islands, Spain). This model represents a pilot project to study if GBSs have the potential to become a cost effective solution in the OWT industry. Therefore, high future expectations have been placed in the offshore sector which will become

more and more important in the years to come.

1.2 Objectives

The present thesis examines the sensitivity of fatigue damage estimation to simulation parameters, such as the duration and number of realizations. Therefore, detailed time domain simulations will be carried out where fatigue assessment will become the main outcome of a 5 MW offshore gravity based wind turbine.

1.3 Structure of the thesis

The structure of the master thesis is given in the following outline:

- **Chapter 2:** Literature review of offshore wind turbine concepts, aero-hydro-servo-elastic modelling and fatigue damage theory.
- **Chapter 3:** A general design of a GBS is considered where the soil structure interaction as well as the bearing capacity is also included. Additionally, a first dynamic response is studied including both 1P and 3P blade passing frequencies.

  Chapter 4: A full metocean analysis is covered where marginal and joint distributions have been built as well as wind&wave roses to finally determine the binned environmental conditions.
- **Chapter 5:** Includes the identification tests needed to determine how the OWT is reacting. Decay, eigenvalue and constant wind tests have been developed to finally obtain a general spectrum analysis.
- **Chapter 6:** Oversees the three hydrodynamic models implemented: Morison, MacCamy&Fuchs and potential flow to determine a prior fatigue assessment study.
- **Chapter 7:** Covers the full fatigue prediction where two hydrodynamic models will be compared establishing the main fatigue damage parameters.
- **Chapter 8:** Conclusions and future work will be included to summarize the most important details as well as mention future work perspective.

1.4 Scope and Limitations

The present thesis examines the sensitivity of fatigue damage estimation to simulation parameters, such as the duration and number of realizations. Therefore, detailed time domain simulations will be carried out where fatigue assessment will become the main outcome of a 5 MW offshore gravity based wind turbine. By means of time and frequency domain simulations, decay as well as wind turbine performance tests have been developed to estimate the cumulative fatigue for several points along the structure.

While working through the project, a series of limitations were found and some simplifications were applied. In order to give a better understanding of the process, the following have been considered:

- Wind measurements present some level of uncertainties since their values come from models created by ERA-Interim, that is the latest global atmospheric re-analysis product developed by ECMWF. The studied point P1 in figure 4.4 is the closest grid point to the zone of interest, PLOCAN, whose values have been gathered from a point located in figure 4.3. This of course introduces high uncertainties since ERA-Interim point is located far from Gran Canaria whose values have been obtained from simulations,not from physical wind measurements.

- Waves as well as wind have resulted to come from the same north-east Atlantic direction considering alignment a fact between them. Additionally, both sources present a strong direction dependence leading the design to a conservative assumption. As shown in the wind and wave roses from figure 4.10 to 4.13 other angles are also showing some wind and wave activity, but will be disregarded since small percentages have been computed. This obviously introduces some small inaccuracies that seem to work well during the analysis.

- During the metocean conditions, described in section 4, the generation of boxes representing 1 condition has its own limitation. When selecting a bin, some uncertainties are introduced as the whole scatter is not considered. This is something that should be taken into account when finally computing and correctly assessing the results. However, it must be mentioned that only the 9.47% of the whole scatter was not considered leading to a position where most of the events where taken into account in the binned conditions.

- If applying the Palmgren-Miner rule, the SN curves are introduced to estimate the fatigue damage at any point of the structure. Therefore, as mentioned in [25], this rule does not consider the effect of stress interaction where the final summation can definitely lead to a high level of uncertainties. Additionally, if focusing on RC, the SN curve used to estimate concrete damage seems to not work accurately for this material but the industry is still using it for now. Furthermore, the concrete damage actually refers to the whole RC material since stresses in the reinforcement have not been considered. However, one of the inputs in concrete introducing high levels of uncertainties is the C_1 parameter. Depending on this value, the number of cycles causing fatigue failure clearly changes, inducing a radical impact on the fatigue damage estimation.

- When dealing with simulations, a total 1-hour fatigue damage has been computed from 4000 [s] where the first 400 have been erased since non-steady solutions are considered. Therefore, this 1-hour fatigue has been employed to estimate the 20 years fatigue damage where some limitations are introduced. Since lots of conditions had to be run and the needed time in a TD simulation is relatively high, the 1 hour estimation had to be done to actually predict the 20 years structural behaviour.

Additionally, random wave seeds were employed whose random behaviour automatically generates uncertainties in the simulated model.

- When it comes to soil design parameters, it must be mentioned that idealized soil deposits were considered since real values could not be obtained. This means that the soil hydrostatic stiffness as well as the ultimate bearing capacity have been considered from an idealized location for a class B soil type as reflected in table 3.5.

- Even though the wave diffraction limit was established at a $T_p = 9[s]$ some uncertainties were introduced since 2 diameters are being considered $D_{shaft} = 7[m]$ and $D_{caisson} = 31[m]$. So, there are no reasons to state that wave diffraction will occur at just one of the two cylinders; a combination of both resulted in the final wave diffraction limit. This leads the design to an uncertain situation were the wave diffraction can actually occur before or after such T_p chosen value.

Chapter 2

Literature Review

2.1 Offshore Wind Turbine Concepts

Even though offshore wind generation is a relatively new idea, from the first offshore wind farm installed in Denmark, Vindeby, in 1991, different concepts has already been introduced and developed as much as their limitations have allowed them. Within this range, bottom-fixed structures and floating solutions have been considered. Depending on the water depth as well as the environmental loads' aggressiveness, a specific type of OWT will be studied.

Currently, regarding bottom-fixed designs, monopile and jackets arise as the most used solutions due to a market shift from shallow to deeper waters. The first concept will cover relatively shallow waters, up to 35 m, while jackets are more prone to be installed within a range of 20 to 55 [m]. However, gravity based structures, a concept that has not been yet fully covered in large depths, is now being seriously weighted for depths up to 50 [s]. This is basically due to the fact that GBSs have the potential to become a cost effective alternative foundation in the offshore wind industry by the use of concrete. However, fabrication timelines is set as one of the big drawbacks for this concept. In section 3.1 a more detailed explanation of the different GBSs concepts will be given as well as ideas about the trends that the market and industry are facing nowadays. Finally, in figure 2.1 a comparison between the different offshore wind foundations is given, pointing out to the 4 types of GBSs that can be developed and that will be described in 3.1.

In relation to floating wind turbines, the following designs are considered: TLP (tension-leg platform), Semi-Submersible and Spar designs. All of them covering a range from 5 to 10 MW of power and being considered for depths larger than 50 m, as reflected in figure 2.3. Additionally, floating solutions offer different ways of achieving static stability. While the spar keeps the up-right condition thanks to a large ballast and draught, the semi-submersible offers a buoyancy solution and the TLP is attached to mooring lines to the seabed. Nevertheless, every floating concept will present different motions that will affect

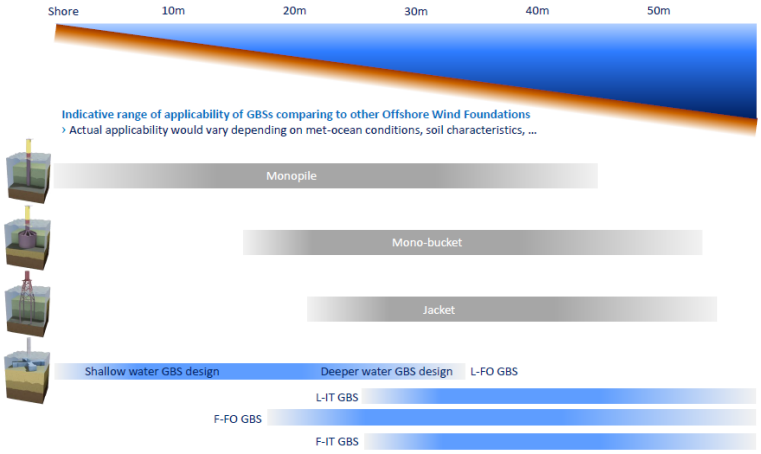

Figure 2.1: Offshore wind foundations - Range of applicability [8]

their performance as well as their structural reliability. TLPs offer good responses when heave, pitch and roll motion are considered but its mooring system to the seabed is quite expensive. On the other hand, Spars are not well suited when pitch and roll are considered due to a large draft as well as small water plane area [67]. Therefore, semi-submersibles arise as the best performance option even though large wave forces are presented because of big water plane areas in the floaters.

Concerning market trends in the offshore wind foundations, two of them will be highlighted:

- The main reason for moving from monopiles to jackets is due to the high arm presented between the rotor and the foundation when increasing the water depth. Large moments are then created, affecting gravely the tower structure. However, it seems that industry has fought back leading supersize monopiles ideas instead of jackets, where such diameter increment has obtained satisfactory experiences making it a potentially more cost effective solution.

  Jackets are expensive to manufacture where manual welding as well as casting of joints accumulates a big share of the budget. Furthermore, due to their big size, jackets take up large areas in the yard reducing noticeably its potential space.

- There has been a noticeable decrease on the installation of GBSs as the market has shifted from shallow to deeper waters. As mentioned, GBSs have proved to work successfully in shallow water wind farm projects, but the industry has failed to adapt GBSs designs to become a real solution for large-scale commercial projects. This is reflected in the cumulative market share pie charts given by EWEA-WindEurope during 2014 and 2016 where it can be seen how the GBS share has decreased almost a 3% with only 10 new installations during those 3 years.

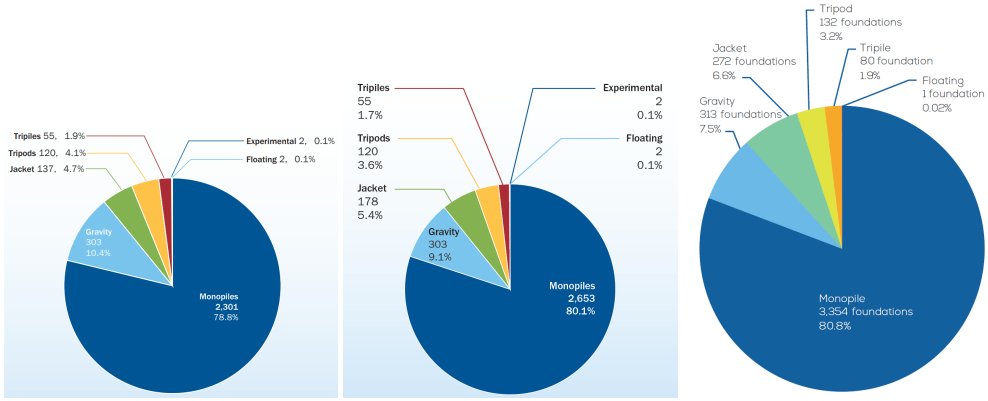

(a) Cumulative market share 2014 [36] **(b)** Cumulative market share 2015 [42] **(c)** Cumulative market share 2016 [37]

Figure 2.2: Cumulative market share: Substructures between 2014-2016

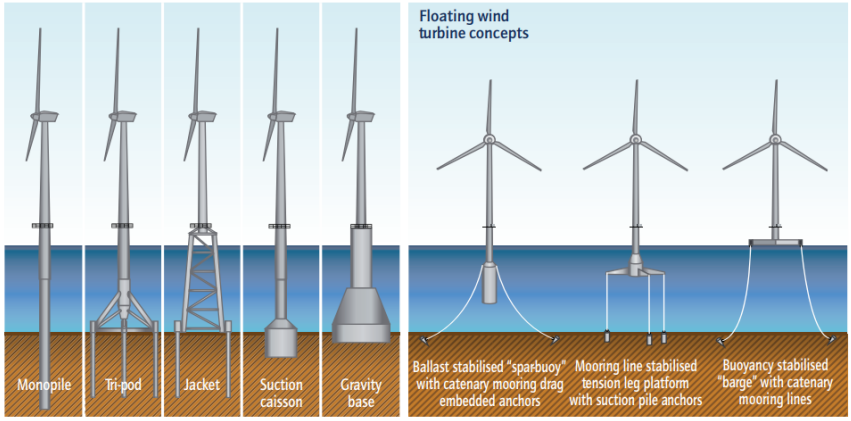

Figure 2.3: Different models of wind turbines - floating and fixed [6]

As offshore wind turbines are complex structures exposed to hydrodynamic and aerodynamic loads, the dynamic behaviour will have a deep impact in the fatigue analysis. Furthermore, the damping coefficients must be conscientiously taken care of since their effect in the magnitude of the structure's response is definitely related. This is because damping ratios are crucial for lifetime predictions as the amplitude of vibrations at resonance are inversely proportional to these ratios [33]. Therefore, in order to obtain precise fatigue values, this damping parameter should be corrected modelled. Finally, it should be mentioned that the aerodynamic damping is another critical factor in the fatigue assessment of offshore wind turbine structures. This is because the thrust force on the rotor suffers constant changes when the relative wind speed on the turbine changes. Therefore, this will result in a force that is opposing the excitation force [27].

Finally, other issues affecting fatigue life are the blade passing frequency in the tower and the misaligned wind and waves forces. However, the place of the platform structure experiencing the highest fatigue damage, will depend on the wave direction [46].

2.2 Sources of Loading

Different types of dynamic loads are present in marine structures whose intensity varies in space and time. Those that will be addressed here will be mainly from wind and wave. Due to this time varying behaviour, it is crucial to avoid dynamic amplification to prevent structures from collapse. From dynamics we can observe how the synchronization of the natural frequency of structures and wave/wind induced frequency can cause real damage.

From [48] time varying loads can be separated into:

1. Macro-Scale variations: not affecting structural response (Significant wave-height, currents, wind speed).
2. Micro-Scale variations: affecting structural response.

Due to the time varying aspect of loads, they are evaluated as non-stacionary in the long run. Nevertheless, when engineering modelling, a simplification is introduced for the long run where it can be understood as a combination of 3 hour stationary packages.

2.2.1 Ocean Waves

When describing the sea environment, some basic assumptions should be assumed when accounting for free surface fluid flow problems. Based on [38], the main points will be described as follows:

- Sea water is incompressible and inviscid.
- Fluid motion is irrotational.
- The velocity potential ϕ will describe the velocity vector of sea water:

$$V(x,y,z) = \nabla\phi \equiv i\Big(\frac{\partial\phi}{\partial x}\Big) + j\Big(\frac{\partial\phi}{\partial y}\Big) + k\Big(\frac{\partial\phi}{\partial z}\Big)$$

  This velocity potential has been introduced to make easier the irrotational fluid motion analysis, where the vorticity vector is described as:

$$\omega = \nabla x V$$

  Finally, as water is incompressible ($\nabla \cdot V = 0$) Laplace equation is satisfied by the velocity potential, where:

$$\frac{\partial^2\phi}{\partial x^2} + \frac{\partial^2\phi}{\partial y^2} + \frac{\partial^2\phi}{\partial z^2} = 0 \tag{2.1}$$

Pressure follows Bernoullis equation where the z axis is described vertical and positive upwards. Therefore following equation 2.2, this one is valid for irrotational, inviscid and unsteady fluid motion.

$$p + \rho g z + \rho\frac{\partial\phi}{\partial t} + \frac{\rho}{2}V \cdot V = C \tag{2.2}$$

Where:

- C: Arbitrary function of time.
- z: Equals 0 at the free-surface level.

Other general aspects affecting free surface fluid flow problems come when describing the boundary conditions. Here two points should be mentioned:

- **Kinematic boundary conditions**

  The general idea states that once a particle is in the free surface, it remains in the free surface. This means that equation 2.3 is always satisfied and $\frac{DF}{Dt} = 0$.

  Defining the z-position of a particle, where its normal velocity follows the normal velocity of the surface itself:

  $$z = \zeta(x, y, t)$$

  Where ζ is the wave elevation

  A new function is defined as:

  $$F(x, y, z, t) = z - \zeta(x, y, t) = 0 \tag{2.3}$$

  Finally, the kinematic boundary condition equations is applied as:

  $$\frac{\partial}{\partial t}(z - \zeta(x, y, t)) + \nabla\phi \cdot \nabla(z - \zeta(x, y, t)) = 0 \tag{2.4}$$

- **Dynamic free surface condition**

  For this case the pressure on the free-surface remains invariant; constant pressure across the free surface interface. Therefore $p = p_{atm}$ for $z = \eta$ and the following equation is obtained:

  $$p = -\rho\Big(\frac{\partial\phi}{\partial t} - \frac{1}{2}V^2 - gz\Big) + c(t) = p_{atm} \tag{2.5}$$

  Then, setting $c(t) = p_{atm}$ as an integration constant, the boundary condition on $z = \eta$ becomes:

$$\rho\Big(\frac{\partial\phi}{\partial t} + \frac{1}{2}V^2 + g\eta\Big) = 0 \tag{2.6}$$

However, it should be noted that linearity simplifies problems and thus, is applied to the non linear free-surface conditions described above. Due to this, any marine structure is assumed to have zero forward speed and zero current moving through them. Linear wave theory is then applied, where the velocity potential is proportional to the wave amplitude being only valid if the wave amplitude is much smaller than the wave length. So, applying linearity to the free surface equations and transferring conditions from $z = \eta(x, y, t)$ to $z = 0$ the following free surface equations are found:

$$\frac{\partial\eta}{\partial t} = \frac{\partial\phi}{\partial z}\ (Kinematic\ condition) \tag{2.7}$$

$$g\eta\frac{\partial\phi}{\partial t} = 0\ (Dynamic\ condition) \tag{2.8}$$

Finally combining both we end up having:

$$\frac{\partial\phi}{\partial z} + \frac{1}{g}\frac{\partial^2\phi}{\partial t^2} = 0 \tag{2.9}$$

$$\phi = \frac{g\hat{\zeta}}{w}e^{kz}sin(kx - wt) \tag{2.10}$$

Additionally, another important aspect to define is the dispersion relationship, where according to its definition, relates the wavelength of a wave to its frequency. Therefore, making use of equation 2.9 in combination with the wave potential definition, equation 2.10, the dispersion relationship can be obtained as shown in 2.11.

$$w^2 = gktanh(kH) \tag{2.11}$$

Where:

- H: Water depth [m]
- $k = \frac{2\pi}{\lambda}$ What it is the wave number and λ the wave length in [m].

So, according to the water depth, two considerations are kept in mind and reflected in figure 2.4.

- **Shallow Waters:** If kH $\ll$ 1 then: $tanh(kH)$ = kH

$$w = \pm k\sqrt{gH} \tag{2.12}$$

- **Deep Waters:** If kH tends to infinite then: $tanh(kH)$ = 1

$$w = \pm\sqrt{gk} \tag{2.13}$$

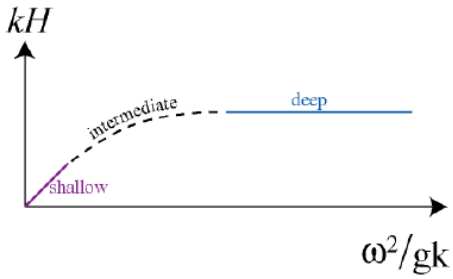

Figure 2.4: Dispersion Relationship

Therefore, the rule of thumb according to a given wave length is established as:

- Deep water: $h > \frac{\lambda}{2}$
- Shallow water: $h < \frac{\lambda}{20}$

Additionally, the phase velocity of a regular wave, rate at which the phase of the wave propagates in space, is defined as:

$$c_p = \frac{\omega}{k} \tag{2.14}$$

Where applying the dispersion relationship to equation 2.14, the following is updated for the phase velocity:

$$c_p = \frac{g}{\omega} tanh(kH) \tag{2.15}$$

If we distinguish between shallow and deep water the following is obtained:

- Deep water: $c_p = \frac{\omega}{k} \approx \frac{k\sqrt{gH}}{k} = \sqrt{gH}$

  Here, the speed is dependent of H.

- Shallow water: $c_p = \frac{\omega}{k} \approx \frac{\omega}{\frac{\omega^2}{g}} = \frac{g}{w} = \frac{\sqrt{gk}}{k} = \sqrt{\frac{g}{k}}$

  Here, the velocity increases when both wave length and wave period increase.

Finally, the following picture will summarize the relationship between the phase velocity of regular waves for the different water depths.

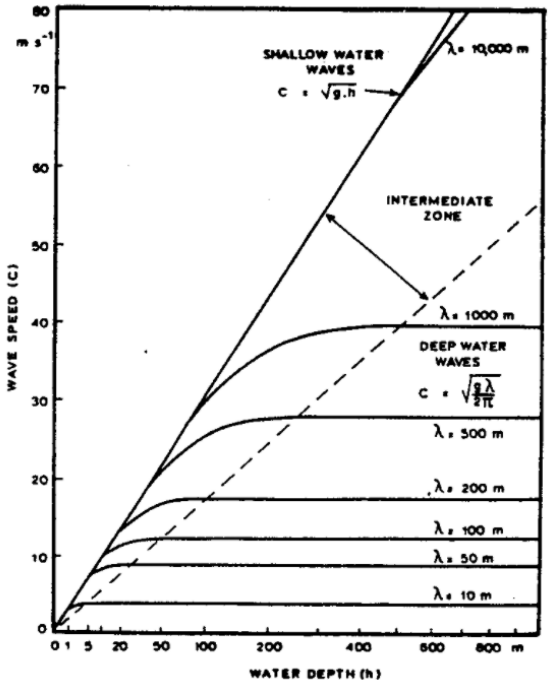

Figure 2.5: Phase velocity of regular waves [26]

Statistical Description of Waves

As commented, the random behaviour of such loads should be studied under statistical models that cover the stationary period described above. For waves description, a Gaussian statistical approximation seems to have close results to reality. Therefore, wave elevation will be described as Gaussian distributed with zero mean and variance. However, it should be remarked that this is only an approximation where in some cases, related to structural dynamic response, this is not applied. For this analysis, linear wave theory will be applied again in order to simulate an irregular sea state. Therefore, to start with, the water elevation of an irregular sea state can be described as the sum of numerous regular wave components having:

$$\zeta = \sum_{i=1}^{N} \zeta_i(t) = A_i sin(w_i t + \phi_i) \tag{2.16}$$

Where:

- A_i: Wave amplitude
- w_i: Circular frequency
- ϕ: Phase angle

Short-Term Wave Statistics

Firstly, a so called short-term statistics will be described, where the description of sea states and the statistical properties of the water surface elevation will be in focus. Taking 2.16 as a starting point, one can set the mean and variance as seen in equations 2.17 and 2.18 respectively. Furthermore, it must be added that each component is a random variable with μ_i and ${\sigma_i}^2$ where if the central limit theorem is applied, equation 2.16 gets closer to a Gaussian process.

$$\mu = \frac{1}{T}\int_0^T \zeta_i(t)dt = \sum_{i=1} \mu_i = 0 \tag{2.17}$$

$$\sigma^2 = \frac{1}{T}\int_0^T [\zeta_i(t)]^2 dt = \sum_{i=1} \frac{1}{2}{A_i}^2 = m_0 \tag{2.18}$$

It should be mentioned that m_0 represents the area under the wave spectrum.

Therefore, the sea surface elevation in an irregular sea state is Gaussian distributed with the probability density function (PDF) described as:

$$p(\zeta) = \frac{1}{\sigma\sqrt{2\pi}} e^{-\frac{\zeta^2}{2\sigma^2}} = \frac{1}{\sqrt{2\pi m_0}} e^{-\frac{\zeta^2}{2m_0}} \tag{2.19}$$

On the other hand, extremes in a sea state can also be described. For this case, where narrow-banded Gaussian sea states are mostly described, it can be mentioned that the wave local maxima, ζ_{max}, follows a Rayleigh distribution with the following PDF:

$$p(\zeta_{max}) = \frac{\zeta_{max}}{m_0} e^{-\frac{{\zeta_{max}}^2}{2m_0}} \tag{2.20}$$

Concurrently, wave heights, H, will also follow a Rayleigh distribution whose PDF is described as:

$$p(H) = \frac{H}{4m_0} e^{-\frac{H^2}{8m_0}} \tag{2.21}$$

In practice, the probabilities for an H value lower or higher than a marked threshold, H_q, need to be established . Therefore, the PDF equation for a lower threshold, see 2.22, and the PDF equation for a higher one, see 2.23, will be described as:

$$P(H < H_q) = \int_0^{H_q} \frac{H}{4m_0} e^{-\frac{H^2}{8m_0}} dH = 1 - e^{-\frac{{H_q}^2}{8m_0}} \tag{2.22}$$

$$Q(H > H_q) = 1 - P(H < H_q) = e^{-\frac{{H_q}^2}{8m_0}} \tag{2.23}$$

Where Q is defined as the number of response cycles and represented as:

$$Q = \frac{n_q}{N} \tag{2.24}$$

Where, according to a given H_q, is the wave height that is exceeded n_q times of N waves.

Finally, the H_q wave that is exceeded with the probability Q is:

$$H_q = \sqrt{8m_0 ln\Big(\frac{1}{Q}\Big)} \tag{2.25}$$

Long-Term Wave Statistics

Before, it has been explained how both the wave height and period are assumed to be constant during time for short-term statistics. However, a long-term sea state will now be considered where the parameters described above will vary in time. Therefore, in order to create a long-term prediction, the joint probability between the wave height and the mean wave period need to be known. This is what chapter 4 talks about. Therefore, according to what has been described in the short-term state, the maximum value for the wave elevation when a significant wave height has been given follows a Rayleigh distribution. So the long-term probability when a wave height does not overcome H is:

$$P(H) = 1 - \sum_{j=1}^{M} e^{-\frac{2H^2}{(H_{\frac{1}{3}}{}^j)^2}} p_j \tag{2.26}$$

2.2.2 Wind

When describing wind effect in marine structures, one should have in mind that wind speed is the most important parameter to look at. Variation of temperature will modify such parameter that will end up defining the different seasons throughout the year. According to [53]: *Wind velocity may be idealized as a superposition of a stochastic high frequency high velocity and a slowly varying mean wind, which carries the bulk of the energy* Furthermore, wind fluctuations can be split in two different categories:

1. **Macro-meteorological**: Governing mean wind speed (Global motions of the weather system)

   Mean wind speed: Flows parallel to the sea free-surface. However, the velocity field varies with the height.

2. **Micro-meteorological**: Governing gusts introduced by mechanical and/or thermal effects.

Therefore, in order to obtain a complete sketch of how wind will affect our offshore structure, the following information will be required:

- Vertical wind variation above sea surface.
- Direction of blowing wind.
- Joint probability between waves and wind.

Wind Problems

On the one hand, shear winds will be described as a condition caused by the surrounding environment. A portion of the incoming wind will separate from the main flow and will follow a vertical path parallel and in front of the wind turbine. Due to this, the blades are not linearly loaded sending variable loads to the drivetrain. On the other hand, turbulent winds can occur when a non-linear distribution of them occurs. The drivetrain then, receives non-constant loads leading to a worse performance of it.

Finally, taking fluctuating wind forces as a general idea, it should be mentioned that they can excite resonant oscillations of offshore structures as stated in [38].

2.2.3 Stochastic Analysis

Random loads from wind and waves will induce random responses on the OWT that will vary on time. Therefore, two possibilities are then presented when working with such data.

On the one hand, TD analysis, variation of signal amplitude with time, will result in accurate solutions since large load data is analyzed. This means that complex problems can be studied but large amount of time is needed meaning that sometimes is not the best option. On the other hand, FD analysis can be considered. This is just an analysis of the time each event occurs during an observation. It is a comfortable method to work with load spectrum, response analysis, damage computation... However, FD analysis requires linearization of the non-linear term ending up in an inaccurate solution. However, there is also a hybrid option in which both TD and FD analysis can be both considered. In this case FFTs should be applied moving from one domain to the other one retaining reliability. In figure 2.6 an example of the 2 domains are presented for the mudline bending stress variation in a monopile.

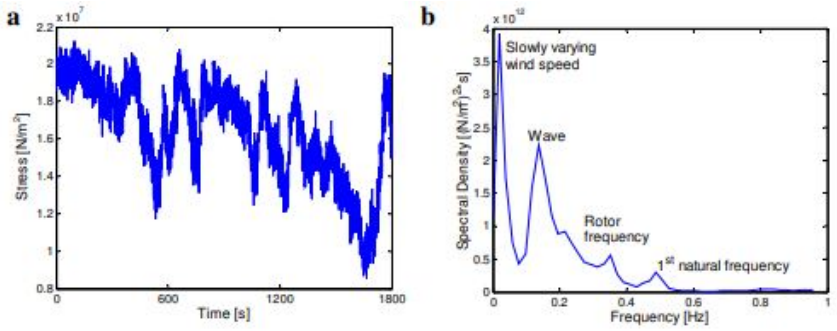

Figure 2.6: a: TD of measured mudline bending stresses - b: FD spectrum of same sample [62]

As mentioned, the algorithm implemented in the FFT is the most common computational tool to move from TD to FD analysis. If a reverse path want to be taken, the IFFT allows to

move from FD to TD analysis as shown in figure 2.7. Additionally, it should be mentioned that according to [62] the most common output is the power spectral density per frequency, defined in equation 2.27. If this power spectral density is displayed against the frequency, a power density spectrum is found.

$$S_{xx}(f) = \frac{1}{2}\left(\frac{A_{wave}^2}{\Delta f}\right) \tag{2.27}$$

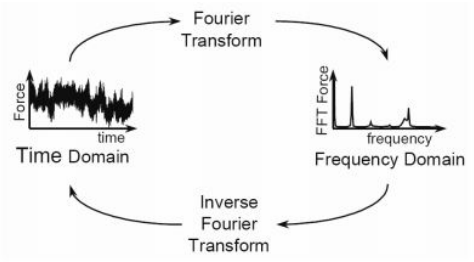

Figure 2.7: Conversion from TD to FD and vice versa [62]

2.3 Aero-hydro-servo-elastic modelling

2.3.1 Hydrodynamic Load Model

During the thesis, three different hydrodynamic models will be considered in order to properly analyzed the hydrodynamic characteristics correctly. The GBS is a quite singular structure where different scenarios can be built. Due to its design condition with large diameters, both MacCamy&Fuchs theory as well as potential flow should be revised together with the common Morison equation. Additionally, considering the short waves affecting the GBS (average wavelength equals to 37 m), obtained from metocean analysis 4, one should definitely consider wave diffraction theory as well as accounting for correct flow around the caisson. Therefore, the following is taking into account:

- Morison equation: It is the most common theory applied on slender marine structures with circular cylindrical shapes with a fixed design condition and where viscous forces are relevant. However, as it will be seen later, this equation probably overestimates fatigue since wave diffraction is not properly accounted for.
- MacCamy&Fuchs: It is a more correct theory when considering wave diffraction effects but assumes a single uniform cylinder, which is not exactly the case of the GBS. The presented design of the gravity based considers two cylindrical structures, one on top of each other, as shown in figure 3.7. However, does this large case at the bottom actually affect the flow around the shaft so much that we should not be even using MacCamy&Fuchs theory? One answer to this question can be applying potential flow to the entire GBS.

- Potential flow: Here, only first order waves are needed because it is fatigue assessment the target of the thesis, not big waves or other considerations. Potential flow would account for the fact that the flow goes around the caisson of the GBS more correctly.

Potential Flow

Potential flow represents an ideal flow solution that simplifies complex flow problems, providing a good approximation to reality. However, potential flow solutions does no exist when accounting for real flows.

Potential flow is commonly described outside the boundary layer as an incompressible, inviscid, irrotational and steady flow. Here, surface pressure distribution can be described by Bernoulli equation and such flow is normally described by two scalar parameters: Stream and potential functions.

On the one hand, stream lines, see figure 2.8, are tangential lines to velocity vectors where no flow pass through them. According to [61]: *The difference of stream functions Ψ between two stream lines gives the volume of fluid per unit depth flowing between them from left to right*. Within this, cartesian and polar coordinates are described in equations 2.28 and 2.29 respectively.

$$u = \frac{\partial \Psi}{\partial y} \quad v = -\frac{\partial \Psi}{\partial x} \tag{2.28}$$

$$v_r = \frac{\partial \Psi}{\partial \theta}\frac{1}{r} \quad v_\theta = -\frac{\partial \Psi}{\partial r} \tag{2.29}$$

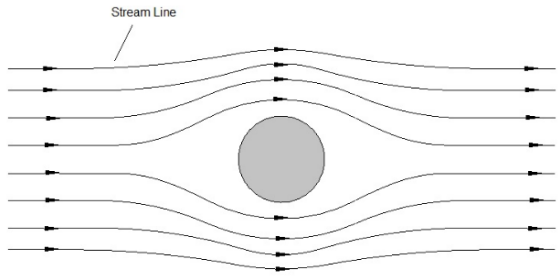

Figure 2.8: Streamlines representation [13]

On the other hand, a potential function, ϕ, is commonly defined such that, in any direction, its derivative gives the velocity in that direction [61]. It satisfies conservation of mass and momentum assuming the idea of the second paragraph Within this, cartesian and polar coordinates are described in equations 2.31 and 2.32 respectively.

$$\phi = \int_B^A v_m ds = \int_B^A v_p ds \tag{2.30}$$

$$u = \frac{\partial \phi}{\partial x} \quad v = \frac{\partial \phi}{\partial y} \tag{2.31}$$

$$v_r = \frac{\partial \phi}{\partial r} \quad v_\theta = \frac{\partial \phi}{\partial \theta}\frac{1}{r} \tag{2.32}$$

In addition to what have been added before, Laplace equation can be achieved by substituting the relationship between velocity and potential, obtaining equation 2.35.

$$\frac{\partial u}{\partial x} + \frac{\partial v}{\partial y} = 0 \quad \frac{\partial u}{\partial x} + \frac{\partial v}{\partial y} + \frac{\partial w}{\partial z} = 0 \tag{2.33}$$

$$\frac{\partial^2 \phi}{\partial x^2} + \frac{\partial^2 \phi}{\partial y^2} + \frac{\partial^2 \phi}{\partial z^2} = 0 \tag{2.34}$$

$$\bigtriangledown^2 \phi = 0 \tag{2.35}$$

Regarding Bernoulli, its equation assumes frictionless flow with no work or heat transfer. However flow can or can not be irrotational [61]. In our description, irrotationality is considered and the potential function is placed on the velocity vector resulting in equation 2.36.

$$\rho\Big(\frac{\partial}{\partial t} \bigtriangledown \phi + \frac{1}{2}(\bigtriangledown \phi)^2\Big) + \bigtriangledown p + \rho g \bigtriangledown z = 0 \tag{2.36}$$

Finally, the panel method is here introduced as a tool to apply the potential flow theory on practical examples. The idea is to discretize portions of the surface into panels solving the algebraic equations applied on them. As known, the more panels are used, the more accurate the result will be, but more time will be consumed. However, even though nowadays there are more exact methods of solving, the flexibility and relative low computation time of the panel technique makes it quite useful to still be used. Figure 2.9, obtained from the Ship Resistance and Computational Hydrodynamics course in Chalmers University of Technology, gives a representation of the panel method applied on a solid body. There, the sources are placed on flat panels on the surface of the body where it exists constant source strength and zero normal velocity at the center of each panel established by equation 2.37.

$$\overrightarrow{v} \cdot \overrightarrow{n} = \frac{\partial \phi}{\partial n} = 0 \tag{2.37}$$

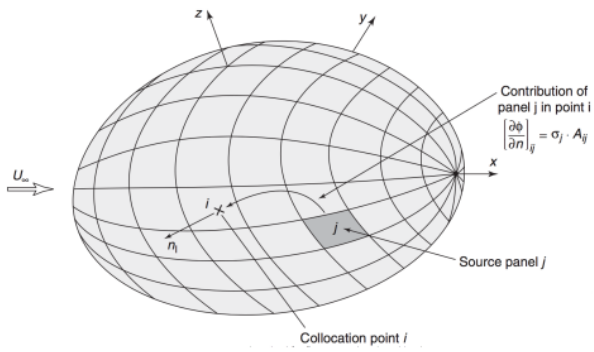

Figure 2.9: Panel Method

Morison's Equation

Morison's equation explained bellow, will be able to simplify the problem and capture the most relevant forces and moments coming from waves that are affecting the GBS. His equation presented here, considers both the inertia and drag forces for a cylinder that remains still in the water.

$$dF = \rho \frac{\pi D^2}{4} dz C_M a_1(z,t) + \frac{\rho}{2} C_D D dz \mid u(z,t) \mid u(z,t) \tag{2.38}$$

Where:

- Positive force direction is taken in from the wave propagation direction.
- ρ: Water mass density.
- D: Cylinder diameter.
- u: Horizontal undisturbed fluid velocity at mid point of the differential element.
- a_1: Horizontal undisturbed fluid acceleration at mid point of the differential element.
- C_M: Mass coefficient (Empirically determined).
- C_D: Drag coefficient (Empirically determined).

  These two last coefficients, C_M and C_D, depend on parameters that affect the flow and are taken into the viscous flow phenomena. According to [38] these parameters are:

  - Reynolds Number

$$R_e = \frac{U_{max} D}{\nu} \tag{2.39}$$

– Roughness Number

$$\epsilon = \frac{k}{D} \tag{2.40}$$

– Keulegan-Carpenter Number

$$K_C = \frac{U_{max}T}{D} \tag{2.41}$$

– Frequency Parameter - Oscillatory viscous flow

$$\beta = \frac{R_e}{K_C} = \frac{D^2}{\nu T} \tag{2.42}$$

Where:

* U_{max}: Maximum orbital particle velocity.
* T: Wave period [s]
* ν: Fluid kinematic viscosity [$\frac{m^2}{s}$]
* D: Monopile diameter [m]
* k: Characteristic cross-sectional dimension of the roughness on the body surface

So, this equation represents the resulting force on a body in an unsteady viscous flow which is a combination of an inertial term, first component of the sum, and a drag term, second component. However, one should take an step back to see that before viscosity were introduced, a purely inviscid steady flow was considered. Here the sum of all the forces was considered to be zero (D'Allabert's paradox) and the added mass effects were not taken into account. Nevertheless, in the real world, this is not happening and viscosity plays a large role and of course need to be assumed. Therefore, the added mass forces are introduced as well as the viscous drag effect resulted from separation and boundary layer friction.

Finally, to capture the moments and forces created by the wave loads, one should refer to figure 2.10. There, a cylinder is subjected to an inflow current with a horizontal wave speed changing in time and vertical position. A small section of the cylinder will be analyzed for a specified depth and then the total force will be obtained by integrating it all over the length.

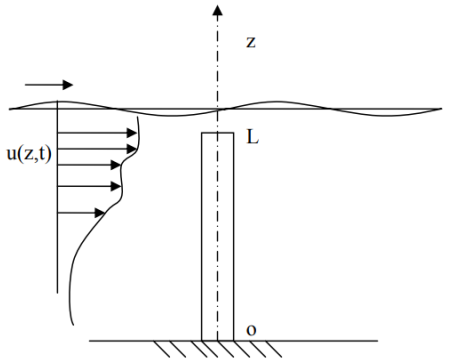

Figure 2.10: Cylinder in non-uniform inflow [60]

$$F(t) = \int_{z=0}^{z=L} dF(z,t) \tag{2.43}$$

However, if the total moment would like to be computed around the origin, the following integral must be carried out by integrating the height z times the dF.

$$M(t) = \int_{0}^{L} zdF(z,t) \tag{2.44}$$

Finally, it should be mentioned that a variation of Morison's equation can be presented when showing a moving body in a fluid. However, as it is not the case we are analyzing, no further comments will be made and if more information want to be found one should refer to [38].

MacCamy&Fuchs Theory

Stating that Morison's equation is applicable when $\frac{\lambda}{D}$ is larger than 5 [38], where λ is the wave length and D is the structure's diameter, the slenderness of the GBS relative to the wave length is of crucial importance. In case the structure has influence over the incoming waves, diffraction occurs and the inertia coefficient, C_M, must be corrected.

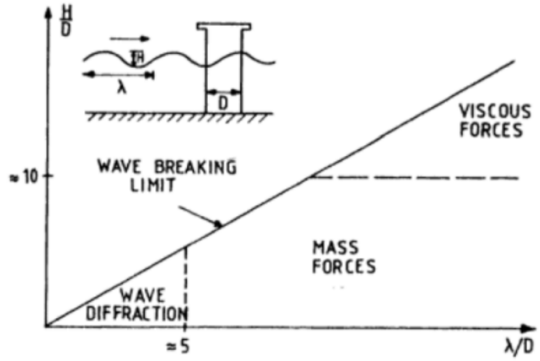

Figure 2.11: Classification of wave forces [38]

Therefore, in order to give a further explanation, Morison's equation for a fixed cylinder is again introduced in equation 2.45. The first term from the left accounts for the inertia force, reflected by the non-dimensional C_M coefficient, while the second establishes the drag term of the structure.

$$f(t) = \rho(1 + C_A)Aa + \frac{1}{2}\rho C_D D v \mid v \mid \tag{2.45}$$

Where:

- v: Water particle velocity $\frac{m}{s}$
- a: Water particle acceleration $\frac{m}{s^2}$
- D: Diameter of the element in study m
- A: Cross-sectional area of the element m^2
- C_D: Non dimensional drag coefficient
- C_A: Non dimensional added mass coefficient
- $C_M = 1 + C_A$

So, considering being inside the wave diffraction problem, where the waves are affected by the structure, the overestimation of the applied loads comes from the inertia term. While Morison's equation establish a C_M value much larger than the one happening in reality, see figure 2.12, Mac-Camy&Fuchs makes a much better estimation resulting in a much lower force range. This is clearly reflected in figure 2.13 where potential theory is applied for the wave diffraction problem.

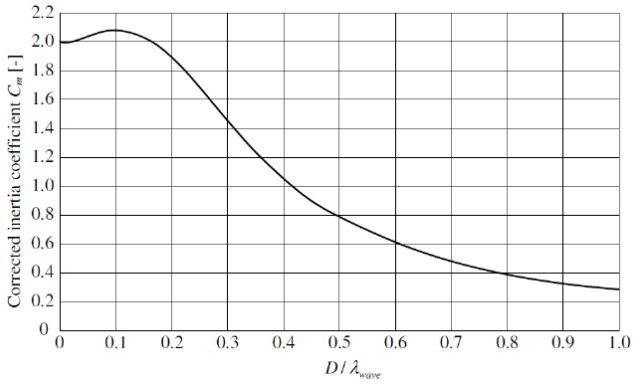

Figure 2.12: MacCamy&Fuchs C_M correction [62]

So, as the force per unit length is different from Morison's equation, the effects of linear incoming waves are described as [23]:

$$dF(z) = \sum_{i=1}^{N} \frac{4\rho g \zeta_a coshk(z+h)}{kcoshkh} Gcos(\omega t - \varepsilon - \alpha) \tag{2.46}$$

Where:

$$tan(\alpha) = \frac{J_1'(K\alpha)}{J_2'(K\alpha)} \tag{2.47}$$

$$G = \frac{1}{\sqrt{(J_1'(K\alpha))^2 + (Y_1'(K\alpha))^2}} \tag{2.48}$$

J and Y are Bessel functions

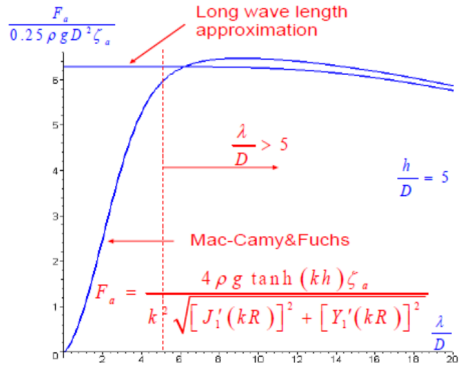

Figure 2.13: Morison - MacCamy&Fuchs limit estimation [38]

Finally, considering this adjustment in the hydrodynamic model, a good assessment of the diffraction problem can be achieved by means of MacCamy&Fuchs theory. This will result in more accurate values when computing wave loads in the fatigue assessment.

2.3.2 Blade Element Momentum Theory (BEM)

Firstly, it needs to be said that BEM is a theory that combines the momentum theory with the theory applied to the blade elements. This second point is introduced in order to describe the different local events happening in the different wind turbine blades.

In this theory, some assumptions and simplifications are introduced:

- Even though wind gusts are present in reality and wind is not steady at all, an steady state assumption is introduced over the whole range of the cross section area.
- If a blade is divided into different elements, it will be assumed that nothing will happen in between them. Each blade element has different velocity and direction.
- 2D flow is assumed to be uniform.
- No deflections are assumed to happen in the blades where they are considered perfectly stiff elements.
- 2D airflow blade theory is applied.

According to the momentum theory, both the thrust and torque equations 2.49, 2.50 respectively, can be written for an annular ring:

$$dT = 4a(1-a)\frac{1}{2}\rho {v_0}^2 2\pi r dr \tag{2.49}$$

$$dQ = 4a'(1-a)\frac{1}{2}\rho v_0 \Omega r^2 2\pi r dr \tag{2.50}$$

Considering [40], a perpendicular force to the rotor plane P_N as well as a tangential to it P_T is represented in the following airfoil section, figure 2.14. Besides, both the lift L, normal to the relative velocity V_{rel}, and drag D, parallel to V_{rel}, are also present. On the other hand, the ϕ angle refers to both the angle of attack as well as the blade pitch angle.

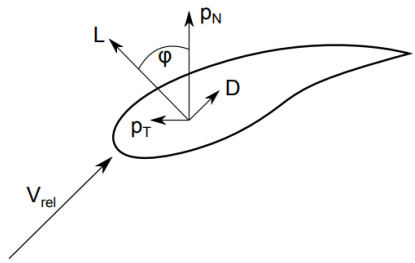

Figure 2.14: Airfoil Section [40]

So, taken into account [21], the following is derived for both, the torque and thrust:

$$p_n = Lcos(\phi) + Dsin(\phi) \tag{2.51}$$

$$p_t = Lsin(\phi) - Dcos(\phi) \tag{2.52}$$

$$dT = Bp_N dr = B(Lcos(\phi) + Dsin(\phi))dr \tag{2.53}$$

$$dQ = Brp_T dr = B(Lsin(\phi) - Dcos(\phi))dr \tag{2.54}$$

$$C_n = C_l cos(\phi) + C_d sin(\phi) \tag{2.55}$$

$$C_t = C_l sin(\phi) - C_d cos(\phi) \tag{2.56}$$

Where B is the blade number and C_n as well as σ are normal coefficient and solidity ratio respectively.

Therefore, combining equations 2.49 and 2.53, and applying the same for torque, the following axial induction factors are obtained:

$$a = \frac{1}{\frac{4sin^2(\phi)}{\sigma C_n} + 1} \tag{2.57}$$

$$a' = \frac{1}{\frac{4sin(\phi)cos(\phi)}{\sigma C_t} + 1} \tag{2.58}$$

However, these axial induction factors are unknown and an iterative process should be established as follows:

1. Giving starting values to a and a'.
2. Calculation of ϕ, α, C_l and C_d.
3. Updating a and a'.
4. Convergence should be checked for solution satisfaction.

Finally, the BEM briefly described above requires some corrections in order to obtain reasonable results. These corrections are:

1. **Prandtl's tip loss factor**: Serves as a correction for the assumption of infinite number of blades in BEM.

$$F = \frac{2}{\pi} cos^{-1}\Big[exp\Big(-\frac{B(1-R/r)}{2rsin(\phi)/R}\Big)\Big] \tag{2.59}$$

2. **Glauert correction for high values of a**: Applied when the axial induction factor becomes larger than 0.5. In this case, BEM theory is no longer valid and this correction is applied for a.

$$a = \frac{(C_T/F - C_{T1})}{C_{T2} - C_{T_1}(a_2 - a_1) + a_1} \tag{2.60}$$

Where:

- a_2 = 1
- C_{T2} = 1.82
- a_1 = 1-0.5$\sqrt{C_{T2}}$
- C_{T1} = 4a_1(1-a_1)

Finally, the next figure, represents for F = 1 the thrust curved used in the calculations when comparing to the momentum theory.

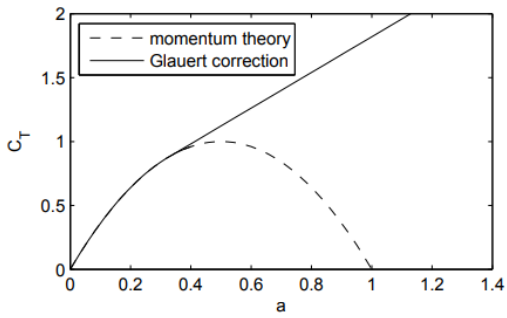

Figure 2.15: Glauert Correction [40]

2.3.3 Structural Modelling

In the structural modelling of an OWT, different elements and assumptions will be considered when defining the GBS. According to figure 2.19, taken from the Specialization Course of Integrated Dynamic Analysis of Wind Turbines taught in NTNU, the OWT can be splitted in different parts. However, the model exemplified here refers to a TLP OWT where the tendons as well as the anchor system must be erased from the GBS design.

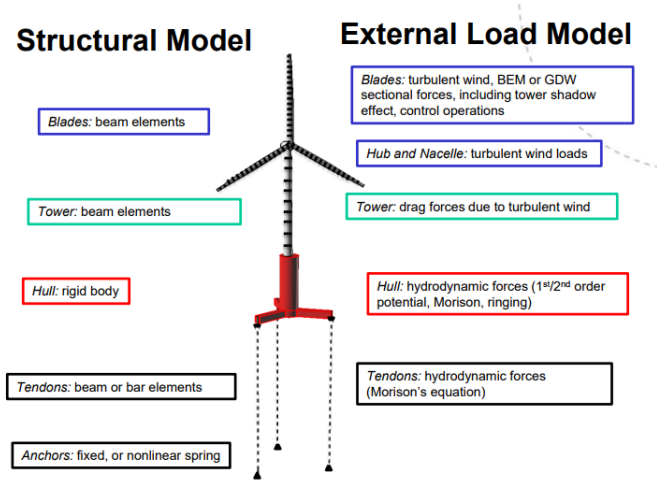

Figure 2.16: Different pats of the TLP OWT model

A non linear FEA will be considered where small and simple models are used as well as reliable and well-understood finite elements. The non-linearity models are applied to the blades, material and force boundary conditions. Specifically, and describing the two more general elements used, the following is considered:

- **2D - Bar Elements**: Bar with axial force applied to the mooring systems. Not relevant in the GBS design.
- **2D - Beam Elements**: Beam with axial force, bending and torsional moment applied to the TLP tendons (not applicable to GBS) and tower and blades.

Going deeper in the non linear beam element theory, one will assume the following:

- A plain section normal to the longitudinal axis remains plane and normal to such axis after bending.
- Lateral contractions due to axial elongation are considered negligible.
- Small strains.
- Lateral loading does not account for shear deformation.

Within this, the nonlinear beam element theory is characterized by beam elements containing different levels of cross-sectional symmetry and where co-rotated ghost element formulation is applied for large rotational deformations.

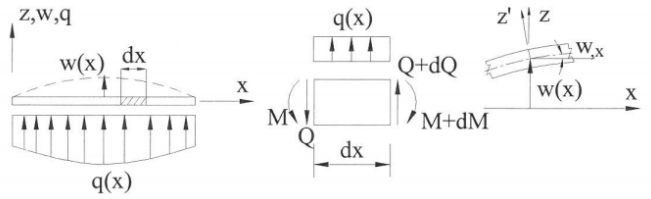

Figure 2.17: Beam displacements and forces [51]

On the one hand, according to the beam equilibrium in figure 2.19, one will end up formulating the differential equation for a beam bending element. After some equilibrium procedure where Navier's hypothesis is later applied as well as Hook's law, the bending moment is established as:

$$M = -EI\frac{\partial^2 \omega}{\partial x^2} \tag{2.61}$$

Within this, the differential equation for the beam is presented as:

$$\frac{\partial^4 w}{\partial x^4} = \frac{q}{EI} \tag{2.62}$$

Furthermore, the weak formulation (virtual work) for a beam element states:

$$\int_0^l \tilde{K}(EI)K dx = (\tilde{v'})^T S' + \int_0^l q\tilde{w} dx \tag{2.63}$$

Where the next items are according to figure [2.18]:

- The left hand side of equation 2.63 represents the internal virtual work and the right side the external one.
- V_i are nodal displacements where $(v')^T = [v_2, v_3, v_5, v_5]$
- S_i are the stress resultants where $(S)'^T = [S_2, S_3, S_5, S_5]$
- k is the curvature expressed as: $k = \frac{\partial^2 w}{\partial x^2}$
- q is the given load.

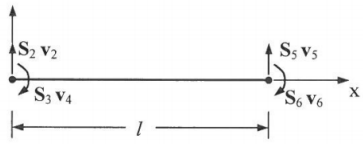

Figure 2.18: Nodal displacements and forces for a beam element [51]

So now, in order to give a finite element formulation and according to [51], the stiffness relation may be obtained by:

- Assuming a displacement pattern within the element.
- Applying the principle of virtual displacements.

Once all the different steps are considered, the following stiffness matrix is obtained for slender beams:

$$k = EI \begin{bmatrix} \frac{12}{l^3} & -\frac{6}{l^2} & -\frac{12}{l^3} & -\frac{6}{l^2} \\ -\frac{6}{l^2} & \frac{4}{l} & \frac{6}{l^2} & -\frac{2}{l} \\ -\frac{12}{l^3} & \frac{6}{l^2} & \frac{12}{l^3} & \frac{6}{l^2} \\ \frac{6}{l^2} & \frac{2}{l} & \frac{6}{l^2} & \frac{4}{l} \end{bmatrix}$$

On the other hand, a dynamic FEM model is analyzed where, normally, loads varying in time will result in time-dependent responses. As a result, this dynamic responses can be larger or smaller than the actual static responses. Within this, both inertia and damping forces are accounted for if structure motions' are large enough. While the inertia term comes from structure-water acceleration, the damping is induced by internal friction as well as viscosity and wave generation. So, the total load vector affecting our offshore structure can be described as:

$$R_{ext} = R_{internal} + M\ddot{D} + B\dot{D} \tag{2.64}$$

Where:

- M: Mass matrix.
- B: Stiffness matrix.
- D: Nodal displacements.
- R_{ext}: Including aerodynamic and hydrodynamic loads as well as the torque from the controller.

Finally, the last step to consider is the TD integration of the FEM. Here, applying a TD procedure, where the assumption of the acceleration value as well as certain variation of the motion is taken into account, we can end up obtaining the displacements and velocities for future time steps. Therefore, the following is described:

$$\dot{D} = \dot{D}(\tau = 0) + \int_{tn}^{tn+1} \ddot{D}dt = \dot{Dn} + \frac{\Delta t}{2}(\ddot{D_{n+1}} + \ddot{Dn}) \tag{2.65}$$

$$D = D(\tau = 0) + \int_{tn}^{tn+1} \dot{D}dt = Dn + \Delta t\dot{D_n} + \frac{\Delta t^2}{4}(\ddot{D_{n+1}} + \ddot{Dn}) \tag{2.66}$$

Where:

- $D_0 = D(t_0)$ is the displacement and t is the time
- $\dot{D_0} = \dot{D}(t_0)$
- $\frac{1}{2}(\ddot{D_n}\ddot{D_{n+1}}) = \ddot{D}(t)$

Now, applying Newmark-beta: Family of Implicit Methods

$$\dot{D_{n+1}} = \dot{D_n} + \Delta t[\gamma \ddot{D_{n+1}} + (1-\gamma)\ddot{D}n] \tag{2.67}$$

$$D_{n+1} = D_n + \Delta t\dot{D_n} + \frac{1}{2}(\Delta t)^2[2\beta \ddot{D_{n+1}} + (1-2\beta)\ddot{D}n] \tag{2.68}$$

Now the following steps are:

1. Solving equation 3.6b for $\ddot{D_{n1}}$

$$\ddot{D_{n+1}} = \frac{D_{n+1} - D_n - \Delta t\dot{D_n} - \frac{1}{2}(\Delta t)^2(1-2\beta)\ddot{D_N}}{\frac{1}{2}(\Delta t)^2 2\beta} \tag{2.69}$$

2. Combining now with eq.[3.6a] we end up having:

$$\dot{D_{N+1}} = \dot{D_N} + \Delta t\Big[\gamma\Big(\frac{D_{N+1} - D_N - \Delta t\ddot{D_N} - \frac{1}{2}(\Delta t)^2(1-2\beta)\ddot{D_N}}{(\Delta t)^2\beta}\Big) + (1-\gamma)\ddot{D}n\Big] \tag{2.70}$$

Therefore, all the equations described above are plugging into 2.71 and the time domain procedure is finally established.

$$M\ddot{D_{N+1}} + B\dot{D_{N+1}} + KD_{N+1} = R^{ext}_{N+1} \tag{2.71}$$

2.3.4 Control Systems

Blade Pitch Controller

Pitch control basically rotates the turbine blades around the blade center line whenever speed changes. However, why the blade should rotate around the blade center line when the speed of the wind changes?.

The lift is of big importance and it is one the aerodynamic principles of wind turbine blades. Any time the air flows around an airfoil shape, the lift is generated due to Bernoulli law and makes possible the rotation of the blades. However, when building a wind turbine blade this one needs to have some twist along its length in order to always have the relative flow velocity tangent to the airfoil in a given cross section. If this not happens, blades can catastrophically fail disintegrating themselves completely.

Therefore, the pitch control will allow the design point, assumed to be at the middle of the blade, to operate at optima speed at any given wind speed. So, when the wind speed

is low, the blades show the maximum area to the wind, however, when the wind speed approaches to the upper limit of the operational blade, the area is reduced to the minimum. Furthermore, if the wind speed continues increasing, blades should be built in the way of being able to reduce the lift effect by increasing even more the angle of attack (active stall) and the brake should also be activated.

Another important factor to keep in mind is that active pitch control offers a smoother start-up of the wind turbine and that means a smoother power output. Even though an electronic system is present to filter and adjust power output to grid frequency, it is always better to provide such equipment with minimum possible work. This electronic devices are quite sensitive and easy to be out of order. However, the time for repairing them is not that high. Additionally, different ways of making blades to rotate can be described by a simple hydraulic piston acting in all blades or by installing an individual electrical motor in every blade. Additionally, according to [40] a control diagram for a pitch regulated OWT will be shown in the next figure. Here, the controller does not respond to the wind speed but reacts to the power as:

$$\frac{d\Theta_p}{dt} = \frac{KI(P - P_{ref})}{1 + \frac{\Theta_p(t)}{KK}} \tag{2.72}$$

Where:

- KI: Integration constant.
- KK: Gain reduction - Reducing pitch rate at high values of the pitch angle.

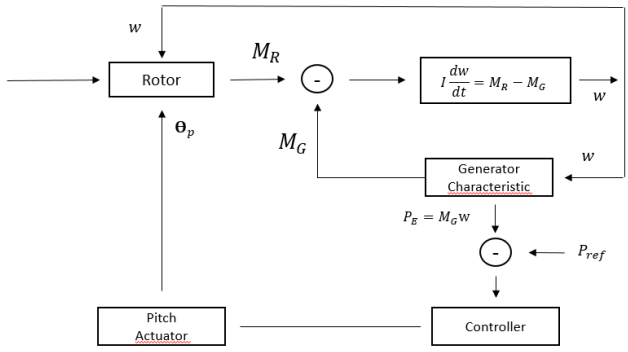

Figure 2.19: Control diagram for a pitch regulated OWT controlling power [40]

Where:

- M_R: Rotor torque.
- M_G: Generator torque.

- PE: Electrical power.
- w: Rotational speed of the rotor.
- I: Moment of inertia of the rotor about the rotational axis.
- $\alpha = \phi - \Theta$

  Where:

  - α: Angle of attack.
  - ϕ: Flow angle.
  - Θ: Pitch of the aerofoil.

Finally, an expression for the acceleration of the rotor is given when the M_R from the rotor blades also increases.

$$I\frac{dw}{dt} = M_R - M_G \tag{2.73}$$

This equation accounts for a situation where M_R overcomes $M_{nominal}$ and therefore the rotor starts to accelerate. If this happens, the control system will detect it and blade pitching occurs. This is good in the sense that the blade pitching time is less than the one the rotor needs to accelerate itself, existing enough time to correct such behaviour producing then a smoother power output than a fixed blade turbine could have.

Active Stall Control

As a self regulated blade pitch turbine is considered, a further explanation will be given to the active stall control. If the blades were fixed to the hub, such blades will be designed in a way where if the wind speed exceeds a maximum value (increasing angle of attack) the blades stall (passive stall) making the drag coefficient to increase and the lift to decrease.

Therefore, active stall can be described as the combination of stall and blade pitch control. Same regulation properties as for blade pitching are considered but now including stall characteristics. The most noticeable information here is that blades can be entirely turned 90 degrees and no blade tip brakes are needed as for passive stall. According to the electrical system, the power output obtained is compared with the reference value given from the incoming wind setting the blade angle to minimize the error.

Therefore, one of the big advantages of this combination method is that power output can be more accurately controlled than passive fixed blade turbines. Furthermore, the machine can be run almost exactly at rated power at all high wind velocities.

2.4 Fatigue Damage Estimation

2.4.1 General

Fatigue damage happens when cyclic loading occurs over time and where the affecting loads are normally bellow the yield stress of the studied material. As it is a cycle by cycle process, the damage that occurs per cycle may be insignificant, however, if the whole time spectrum is considered, for example 10^8 number of cycles, it may seriously affect the structural integrity of the offshore structure. During this time period, a growing crack can be documented where 3 clear periods are present:

1. N_i : Initiation time.
2. N_g : Crack Growth.
3. Final Failure.

   Where the total fatigue life is: $N_T = N_i + Ng$

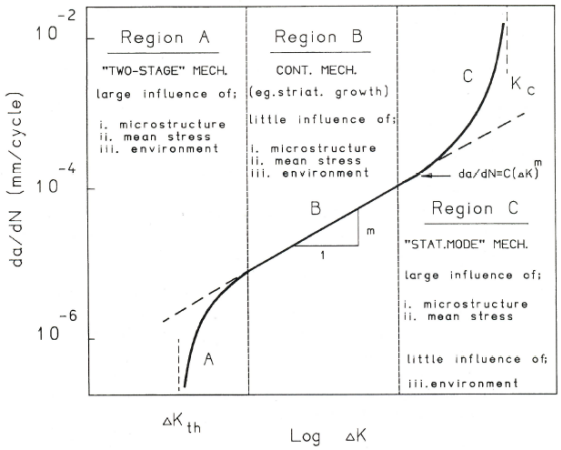

Figure 2.20: Crack growth rate (a-N Curve) during the 3 different stages [25]

Before describing SN curve theory, crack growth rate should be mentioned for a cyclic loading condition. Under these circumstances, the crack growth rate is influenced by the local stress/strain field where the values are far below the yield stress of the material and thus linear elastic fracture mechanics can be applied (LEFM), this situation is well described under region 2 of figure 2.20. Crack growth relationship with the given cyclic stress is represented as:

$$\Delta K = \Delta S \sqrt{\pi a} F(\alpha) \tag{2.74}$$

Where:

- Δ S: Nominal Stress Range.

- a: Initial Crack Length.
- F(α): Form function of the stress Intensity Factor. Depends on: External Geometry, Crack Length, Crack Geometry and Loading Configuration.

So, focusing in the finite life region, region B of figure 2.20 will be considered when computing fatigue assessment. Such region may be approximated by a straight line given the Paris-Erdogan crak growth relation, well known as Pari's Law:

$$\frac{da}{dn} = C(\Delta K)^m \tag{2.75}$$

Where C, dimensional dependent of m, are both material parameters.

If more information wants to be obtained regarding the three different types of regions as well as crack growth relationship with the giving cyclic loading, one should refer to [25].

In order to compare the alternating stresses against the number of cycles for a certain measurement, one can make use of the well known S-N curve to plot such relationship. The parameters used are empirically obtained defining the fatigue resistance of a certain structure. Therefore, for the finite life region, the data can be represented in the following form:

$$N(\Delta S)^m = A \tag{2.76}$$

Where A is a constant and the the SN diagram is given on a logarithmic scale for both the stresses and cycles. Therefore, equation 2.76, turns into equation 2.77 where the SN curve's slope is $-\frac{1}{m}$

$$log\Delta S = -\frac{1}{m} logN + \frac{1}{m} logA \tag{2.77}$$

However, according to [25], for environmentally loaded structures some stress ranges will be above the fatigue limit, and some will be below. The cycles that are above the fatigue limit will cause crack growth (active cycles). As the crack grows, the fatigue limit will be gradually lowered and more cycles in the spectrum will become active.

In cumulative damage calculations, if we assume a fatigue limit as found in constant amplitude testing, the resulting fatigue design will be non-conservative. If, however, we ignore the fatigue limit all together, the design may become over-conservative. That is why Halibach used a fracture mechanics model to demonstrate that with a fictitious extrapolation of the SN curve with a slope $(2m-1)^{-1}$ the effect of a growing crack on the fatigue threshold will be taken into account in cumulative damage calculations. The model is valid for stationary load histories, which is a good approximation for wave loaded structures. This therefore leads to a two slope SN curve with the following form:

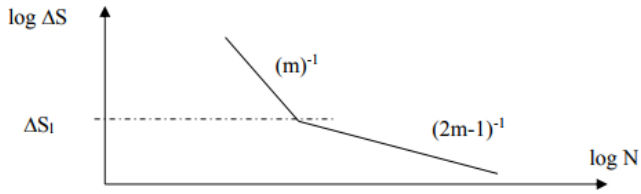

Figure 2.21: SN design curve with extrapolation beyond the fatigue limit to take into account the small cycles in the spectrum [25]

Additionally, it must be introduced that irregular stress histories on fatigue capacity must also be studied where the variable amplitude loading on steel structural components is a crucial factor. Here, the following figure will exemplify this stochastic loading whose different terms will be briefly described:

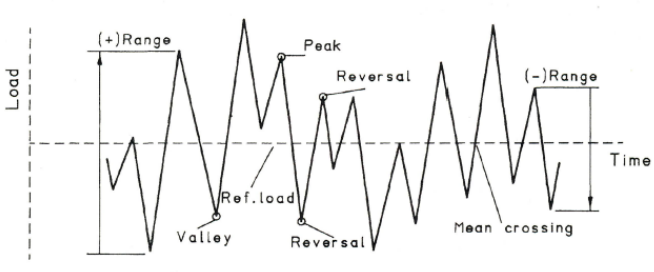

Figure 2.22: Irregular load history [25]

- **Peak:** Where the first derivative of the load time history (LTH) changes from positive to negative.
- **Reversal:** Where the first derivative of the LTH changes sign.
- **Valley:** Where the first derivative of the LTH changes from negative to positive.
- **Range:** Algebraic difference between successive valley and peak loads.
- **Mean Crossings:** Number of times that LTH crosses the mean load level.
- **Irregularity Factor:** Irregularity measurement defining the ratio between mean crossings with positive slope and the number of peaks or valleys.

This irregular loading, also known as spectrum loading, can be summed and cyclic counted where the cumulative damage analysis becomes highly important. Among different ways of counting like level crossing counting, peak counting and simple range counting, rainflow counting becomes the most popular in use.

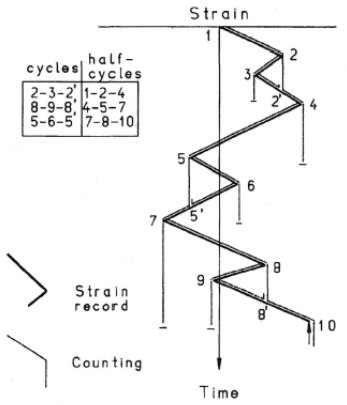

Figure 2.23: Rainflow analysis for a given LTH [25]

One of the largest advantages of such rainflow counting method is that it takes into account all peaks as well as the small amplitude ones. However, it should be checked that the cyclic stress-strains loops generated by the loading procedure are considered during the counting method. This close stress-strain loops are well known as hysteresis loops representing the dissipated energy due to material movement dislocation. Therefore, as stated in [25]: *The fatigue damage caused by a closed loop in a variable amplitude loading history is therefore equivalent to the damage caused by a cycle in a constant amplitude fatigue test with the same stress range*. In the following figure the hysteresis loops will be exemplified.

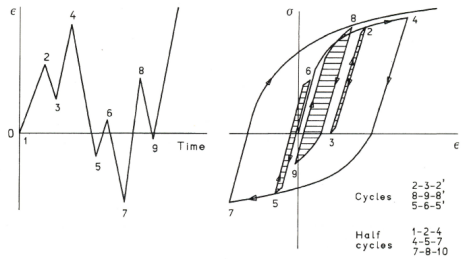

Figure 2.24: Hysteresis representation of a given LTH [25]

Finally, the cumulative damage mentioned above is always representing a giving value to a stochastic load history. Multiple ways for computing cumulative damage from SN records can be developed, but here the Palmgren-Miner (linear) summation will be used. In this method, the general idea is that the damage caused by one cycle is constant for a given stress range.

$$D = \frac{1}{N} \tag{2.78}$$

Where N is the number of times this same cycle equals to failure.

So, according to the failure criterion, in a constant amplitude test, the following is assumed:

$$D_{failure} \geq 1 \tag{2.79}$$

Additionally, if multiple stress ranges are considered, ΔS_i, in which every cycle has its own number of cycles, n_i, the following linear damage rule proposed by Palmgren and later again by Miner turns into the cumulative damage ratio as:

$$D_{total} = \sum_i \frac{n_i}{N_i} \tag{2.80}$$

Finally, the following figure gives a simple representation of this linear damage summation.

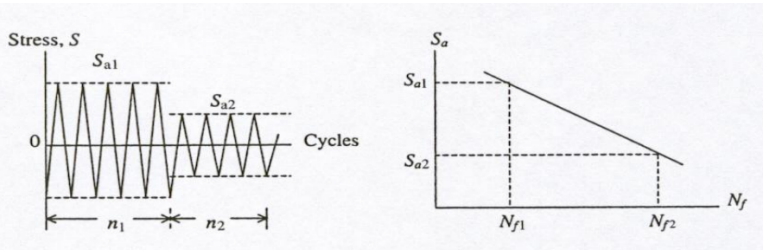

Figure 2.25: Left: Constant amplitude stress blocks. Right: SN Curve stress blocks representation [25]

2.4.2 Material Characteristics: Concrete, Reinforced Steel Bars

Concrete

Concrete is an heterogeneous material that during hardening micro cracks and multiple pores are created. Additionally, due to shrinkage and temperature differences macro cracks can be created before applying any load. Therefore, summing up heterogeneity and cracks formation, concrete can be considered as a strain-softening material, see figure 2.26. This indicates a reduction in the stress level beyond the ultimate strength with an increase in the deformation. In contrast, metal materials like the reinforcing steel bars behave in the opposite way exhibiting strain hardening. This means, increment of the stress level after the proportional limit with an increase in the deformation.

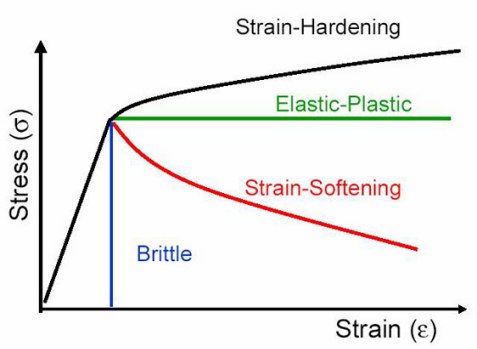

Figure 2.26: Stress-Strain relationship [12]

Furthermore, if concrete is under cyclic load influence, crack initiation will not be a clear process as the cracks already exist. Due to this, crack growth will increase until failure occurs and no topography surface will be easily found as for steel. This means that the concrete fatigue failure characteristics will be difficult to determine.

Concrete material's properties are thoroughly described by the Eurocode 2 [28] and linked to the European Standard EN 206-1:2000 [35] when describing the compressive strength of the concrete. Additionally, the characteristics strengths for f_{ck}, concrete compressive strength, and the corresponding mechanical characteristics are given in table 2.1. Within this, the compressive strength of the concrete decays with the age depending on the type of cement used, temperature and curing conditions. Specifically, for a mean temperature of 20 Celsius degrees and curing in accordance with EN 12390 [57], the compressive strength of concrete at various ages, $f_{cm}(t)$ may be estimated from equation 2.81.

$$f_{cm}(t) = \beta_{cc}(t) f_{cm} \tag{2.81}$$

Where:

- $f_{cm}(t)$: Mean concrete compressive strength at an age of t days.
- f_{cm} : Mean compressive strength at 28 days according to table 2.1.
- $\beta_{cc}(t)$: Coefficient which depends on the age of the concrete t.
- t: Age of the concrete in days.
- s: Coefficient that depends of the cement type
  - Class R: 0.20
  - Class N: 0.25
  - Class S: 0.38

$$\beta_{cc}(t) = exp\Big[s\Big[1 - \Big(\frac{28}{t}\Big)^{\frac{1}{2}}\Big]\Big] \tag{2.82}$$

Other important parameter to keep in mind is the elastic deformation of the concrete. Here it is of vital importance to establish the modulus of elasticity of the concrete which is determined by the modulus of elasticity of its components, to be more precise, the modulus of elasticity, E_{cm}, is established in table 2.1 for concretes with quartzite aggregates. For limestone and sandstone aggregates the values should be reduced by 10% and 30% respectively. Finally, if employing basalt aggregates, the value should be increased by 20%. Additionally, a variation of the such modulus can be determined by:

$$E_{cm}(t) = (f_{cm}(t)/f_{cm})^{0.3} E_{cm} \tag{2.83}$$

Where $E_{cm}(t)$ and $f_{cm}(t)$ are the values at an age of t days and E_{cm} and f_{cm} are the values determined at an age of 28 days.

Regarding elastic deformation parameters, 0.2 can be considered as a Poisson's ratio for uncracked concrete and 0 for cracked sections. Within this, if no information is provided, the linear coefficient of thermal expansion may be considered as $10 \cdot 10^{-6} K^{-1}$.

Strength classes for concrete															Analytical relation / Explanation
f_{ck} (MPa)	12	16	20	25	30	35	40	45	50	55	60	70	80	90	
$f_{ck,cube}$ (MPa)	15	20	25	30	37	45	50	55	60	67	75	85	95	105	2.8
f_{cm} (MPa)	20	24	28	33	38	43	48	53	58	63	68	78	88	98	$f_{cm} = f_{ck}+8$(MPa)
f_{ctm} (MPa)	1,6	1,9	2,2	2,6	2,9	3,2	3,5	3,8	4,1	4,2	4,4	4,6	4,8	5,0	f_{ctm}=0,30×$f_{ck}^{[23]}$ ≤C50/60 f_{ctm}=2,12·ln(1+(f_{cm}/10)) > C50/60
$f_{ctk,\ 0.05}$ (MPa)	1,1	1,3	1,5	1,8	2,0	2,2	2,5	2,7	2,9	3,0	3,1	3,2	3,4	3,5	$f_{ctk;0,05}$ = 0,7×f_{ctm} 5% fractile
$f_{ctk,0.95}$ (MPa)	2,0	2,5	2,9	3,3	3,8	4,2	4,6	4,9	5,3	5,5	5,7	6,0	6,3	6,6	$f_{ctk;0,95}$ = 1,3×f_{ctm} 95% fractile
E_{cm} (GPa)	27	29	30	31	33	34	35	36	37	38	39	41	42	44	E_{cm} = 22[(f_{cm})/10]$^{0.3}$ (f_{cm} in MPa)
ε_{c1} (‰)	1,8	1,9	2,0	2,1	2,2	2,25	2,3	2,4	2,45	2,5	2,6	2,7	2,8	2,8	see Figure 3.2 $\varepsilon_{c1}(^0/_{00})$ = 0,7 $f_{cm}^{0,31}$ ≤ 2,8 [MC]
ε_{cu1} (‰)	3,5									3,2	3,0	2,8	2,8	2,8	see Figure 3.2 for f_{ck} ≥ 50 Mpa $\varepsilon_{cu1}(^0/_{00})$=2,8+27[(98-$f_{cm}$)/100]^4
ε_{c2} (‰)	2,0									2,2	2,3	2,4	2, 5	2,6	see Figure 3.3 for f_{ck} ≥ 50 Mpa $\varepsilon_{c2}(^0/_{00})$=2,0+0,085($f_{ck}$-50)^{0,53}
ε_{cu2} (‰)	3,5									3,1	2,9	2,7	2,6	2,6	see Figure 3.3 for f_{ck} ≥ 50 Mpa $\varepsilon_{cu2}(^0/_{00})$=2,6+35[(90-$f_{ck}$)/100]^4
n	2,0									1,75	1,6	1,45	1,4	1,4	for f_{ck}≥ 50 Mpa n=1,4+23,4[(90- f_{ck})/100]^4
ε_{c3} (‰)	1,75									1,8	1,9	2,0	2,2	2,3	see Figure 3.4 for f_{ck}≥ 50 Mpa $\varepsilon_{c3}(^0/_{00})$=1,75+0,55[($f_{ck}$-50)/40]
ε_{cu3} (‰)	3,5									3,1	2,9	2,7	2,6	2,6	see Figure 3.4 for f_{ck} ≥ 50 Mpa $\varepsilon_{cu3}(^0/_{00})$=2,6+35[(90-$f_{ck}$)/100]^4

Table 2.1: Strength and deformation characteristics for concrete [28]

Finally, creep and shrinkage are two physical properties of the concrete that must be considered. Concrete is originated from calcium silicate hydrates (C-S-H) in the cement paste. It occurs in all stress levels and depends linearly on the stress if the pore water content is constant. This results in aging caused by chemical hardening due to the hydration of the structure. Additionally, changes in pore water content due to drying or wetting processes cause significant volume changes of concrete in load-free specimens, what leads to shrinkage of the structure [2].

Within this, and according to [28], creep and shrinkage of the concrete depend on the ambient humidity, the dimensions of the element and the composition of the concrete. Creep is also influenced by the maturity of the concrete when the load is firstly applied and depends on the duration and magnitude of the loading. However, as it is not part of this master thesis content, their effects on concrete will not be studied.

Reinforcing Steel Bars

Firstly, it should be mentioned that there are two different types of existing reinforced steel bars. Passive action where such steel is not working until loads are applied and active mode where a pre-stressed condition has been induced. This means that before applying any load a compressive condition prevails, helping the reinforced concrete structure when tensile loads are considered.

Reinforcing bars inside concrete are those normally made of steel and have a corrugated shape to enhance bonding between concrete and the bars. Furthermore, a minimum bendability must be ensured when employing minimum mandrel diameters specified in table 8.1 of [28].

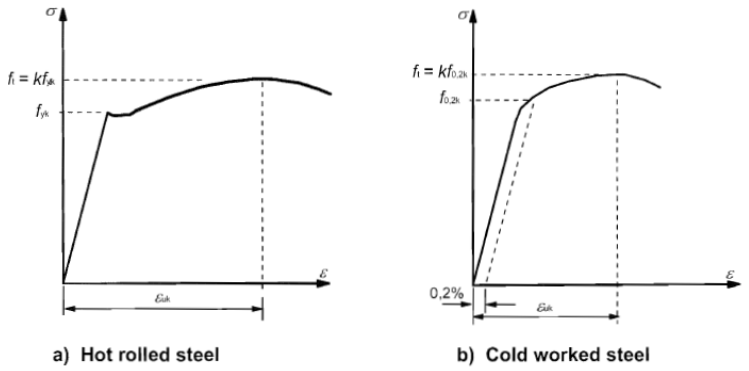

Figure 2.27: Stress-Strain diagrams for reinforced steel [28]

Regarding strength capacity, both the yield and tensile strength are defined respect to the yield and maximum load in the direct axial tension. However, rules applied in [28] are

valid for a yield strength rate between 400 to 600 MPa.

As displayed in 2.26, steel behaves as a strain hardening material reflected in figure 2.27 where both hot rolled and cold worked steel curves are shown. Where f_t applies to tensile strength, f_{yk} or $f_{0.2k}$ to yield strength and ϵ_{uk} to ultimate strain.

Finally, design assumptions, based on the nominal cross-section area of the reinforcement, are based on figure 2.28.

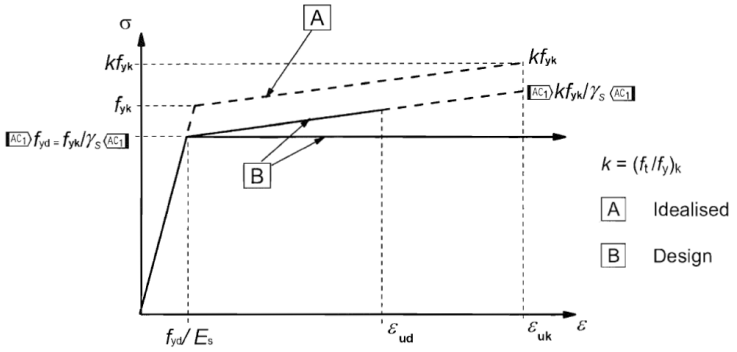

Figure 2.28: Idealized and design Stress-Strain diagrams for reinforced steel [28]

Where:

- A: Inclined top branch with strain limit ϵ_{ud} and maximum stress of (kf_{yk}/γ_s) at ϵ_{uk}, where $(k = f_t/f_y)_k$.
- B: A horizontal top branch without the need to check the strain limit.

  ϵ_{ud} recommended value is $0.9\epsilon_{uk}$ and $(k = f_t/f_y)_k$ is given in annex C of [28].
- Mean density value is assumed as 7850 kg/m^3

2.4.3 Reinforced Concrete under Fatigue

When employing this composite material, the low tensile strength and ductility of the concrete is improved by the inclusion of the reinforcement. Therefore, steel reinforcing bars (rebars) are widely used to increase both ductility and tensile strength.

As for steel, cyclic loads in the concrete can make cracks to appear on it where the tensile stresses will be redistributed until reaching its reinforcement. This means that fatigue failure can happen in the concrete, reinforcement or where both elements meet. Within this, different fatigue failure modes determined by bending appear, characterized by the different loads applied. To exemplify this, a simple beam with and without transverse reinforcement has been considered and presented in figures 2.29 and 2.30.

Firstly, the reinforcement can fail if tensile forces are introduced. If this occur, no obvious strain seems to happen making it difficult to predict. However, if over-reinforced, compression failure mode applies in the compression zone. Secondly, shear failure mode is determined by the installation of a shear reinforcement. If not applied, structures like beams can fail under shear crack conditions right after few cycles. This shear crack appears since the concrete's tensile strength has been reached. Nevertheless, when including shear reinforcement, fatigue behaviour depends on the reinforcement's properties. Therefore, according to [39], the above described and the following figures 2.29 and 2.30 are introduced. The images represent the different failure modes associated to beams with shear and without shear protection respectively.

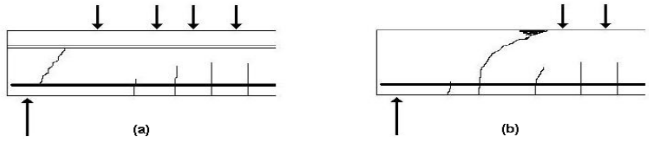

Figure 2.29: Shear cracks with no shear reinforcement [39]

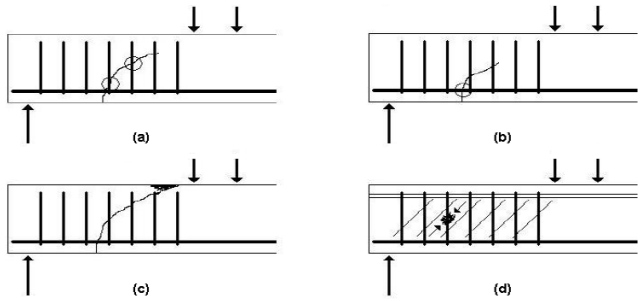

Figure 2.30: Shear cracks with shear reinforcement [39]

Finally, bond failure appears when the structure has failed between the concrete and the reinforcement. Three failure modes are described in [39]: *Splitting of the surrounding concrete, concrete failing in shear along the perimeter of the reinforcement bar and break down of the shear strength of chemical bonds between the reinforcement bar and the concrete.*

Firstly, bond failure happens as the external radial pressure expelled from the reinforcing bar cracks the adjacent concrete. Due to this, the cyclic load applied makes the stress pattern to change due to a stress redistribution. This ends up meaning that the ultimate failure happens earlier, since longitudinal cracks are opened due to the cyclic load behaviour.

Second mode applies to bond failure due to shear concrete failure. This is because the

concrete accumulates splitting force that results in fatigue bond effects. Finally, last mode will not be explained since chemical bonds are rarely used.

Spanish & Eurocode Regulations

After having introduced how a reinforced beam reacts and behaves under cyclic loads, specific rules and guidelines will be given here according to [52]. The information provided by this source differentiates between concrete and the reinforcing bars when estimating the fatigue design. Additionally, and following the requirements of [32] safety under fatigue conditions is again achieved by analyzing separately concrete and the steel bars. Both texts refer to a well known reinforced concrete Spanish book and to a Spanish reinforced concrete booklet given by the Spanish Ministry of construction.

Therefore, conventional reinforced concrete structures like buildings are not subjected to fatigue studies as the applied loads do not compromise the fatigue limit. However, structures like bridges for trains or in this case wind turbine's supports are strongly influenced by high - super/high cycle loads. So as mentioned, the fatigue limit state must be computed separately for concrete and reinforcing bars.

The load hypothesis established in the fatigue limit is determined by:

- **Reinforcing bars:** Only the variable loads subjected to be cyclical.
- **Concrete:** Both the constant as well as the variable loads.

  When computing stresses in both the steel and the concrete, a linear behaviour will be assumed without considering tensile contribution in the concrete.

Concrete Checking

When checking concrete's fatigue resistance, maximum compressing values from constant and variable loads must be limited. Additionally, compressing loads are introduced by normal and tangential tensions.

Reinforcing Steel Bars Checking

Stresses induced in the reinforcing bars by the cyclic loads can not exceed a maximum value. This data is provided by [32] as 150 N/mm^2. Additionally, joint welds must be avoided where if impossible, such stresses can not exceed half of the above value.

In case bending bars are implemented, fatigue limit must be reduced by a β value as:

$$\beta = 1 - 3\frac{d}{D} \tag{2.84}$$

Where d is the bar's diameter and D is the bending's diameter.

The Eurocode [30] suggests maximum variable stresses values depending on the number of cycles. Such limitation is introduced in table 2.2 and projected in figure 2.31.

Table 2.2: SN Curve reinforced steel bars curve

Type of Reinforcing Bar	N [cycles]	k_1	k_2	$\Delta\sigma_{max}[MPa]$
Straight and Bending bars	10^6	5	9	162.5
Weld bars	10^7	3	5	58.5

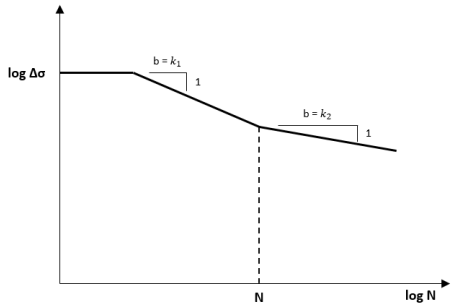

Figure 2.31: SN Curve reinforced steel bar [52]

DNV - Offshore Concrete Structures

Following [64], a Palmgren-Miner rule is employed which does not really work accurately for concrete. However it is what the industry is still using for now and seems to predict reasonably good results. Again, concrete and the reinforcing bars must be separately studied.

Therefore, based on cumulative linear damage theory, the applied stresses are organized in stress-blocks with constant amplitude corresponding to n_i stress cycles as given in equation 2.25. However now the cumulative damage ratio depends on the access for inspection and repair or if located above or below the splash zone, as given in table 2.3.

No access for inspection and repair	*Below or in the splash zone*[1)]	*Above splash zone* [2)]
0.33	0.5	1.0

1) In typical harsh environment (e. g. the North Sea or equivalent) structural details exposed to seawater in the splash zone are normally to be considered to have no access for inspection and repair, i.e. the cumulative damage ratios is to be reduced to 0.33.
2) For reinforcement, which cannot normally be inspected and repaired; the cumulative damage ratio for reinforcement above splash zone is reduced to 0.5.

Table 2.3: Cumulative damage ratios [64]

Concrete Checking

So, the design life of the concrete subjected to cyclic stresses can be computed from the SN proposed in equation 2.85.

$$logN = C_1 \frac{1 - \frac{\sigma_{max}}{f_{rd}}}{1 - \frac{\sigma_{min}}{f_{rd}}} \tag{2.85}$$

Where:

- f_{rd} : Compressive strength for the type of failure in question.
- σ_{max} : Numerically largest compressive stress computed as the average value within each stress-block.
- σ_{min} : Numerically least compressive stress computed as the average value within each stress-block. If σ_{min} is in tension, a zero value must be chosen.
- C_1**:** Taken as:
  - 12: Structures in air.
  - 10: Structures in water for those stress-blocks having stress variation in the compression-compression range.
  - 8: Structures in water for those stress-blocks having stress variation in the compression-tension range.

Additionally, if the calculated design life log N is larger than the value of x given by the equation 2.86, the design life may be increased further by multiplying the value of log N by the factor C_2 given in equation 2.87.

$$X = \frac{C_1}{1 - \frac{\sigma_{min}}{f_{rd}} + 0.1C_1} \tag{2.86}$$

$$C_2 = 1 + 0.2(logN - X) > 1 \tag{2.87}$$

Reinforcing Steel Bars Checking

As done for concrete, the design life for the reinforcement is subjected to cyclic stresses based on a SN curve provided by equation 2.88.

$$logN = C_3 - C_4 log\Delta\sigma \tag{2.88}$$

Where:

- $\Delta\sigma$: Stress variation in the reinforcement [MPa]
- C_3 and C_4 : Factors dependent on the reinforcement type, bending radius and corrosive environment.

- σ_{max} on the reinforcement must be less than $\frac{f_{sk}}{\gamma_s}$. Where γ_s is taken from table 2.4

- For straight reinforced bars exposed to moderate (NA) and mildly (LA) aggressive environment, $C_3 = 19.6$ and $C_4 = 6.0$. However, if exposed to specially (SA) or severely (MA) aggressive environment, corrosion influence on the fatigue properties shall be assessed separately. Values of C_3 and C_4 for straight bars are suggested in table 2.5.

Limit State		*Ultimate limit state*	*Accidental and Fatigue limit state*	*Serviceability limit state*
Reinforced concrete	Concrete, γ_c	1.25[1] (1.40)[2]	1.10[1] (1.20)[2]	1.0
	Reinforcement. γ_s	1.15[1] (1.25)[2]	1.00[1] (1.10)[2]	1.0
Plain Concrete	γ_c	1.50[1] (1.75)[2]	1.25[1] (1.50)[2]	1.0

1) When the design is to be based on dimensional data that include specified tolerances at their most unfavourable limits, structural imperfections, placement tolerances as to positioning of reinforcement, then these material coefficients can be used. When these coefficients are used then any geometric deviations from the "approved for construction" drawings must be evaluated and considered in relation to the tolerances used in the design calculations.

2) Design with these coefficients allows for tolerances in accordance with C400 or alternatively on cross sectional dimensions and placing of reinforcements that do not reduce calculated resistance by more than 10 percent. If specified tolerances are in excess of those given in C400 or the specified tolerances lead to greater reductions in calculated resistance, the excess tolerances or the reduction in excess of 10 percent is to be accounted for in resistance calculations. Alternatively, material coefficients may be taken according to those given under [1].

Table 2.4: Material coefficients for concrete and reinforcement [64]

	Level of Stress Variations (MPa)		
	$400 > \Delta\sigma > 235$	$235 > \Delta\sigma > 65$	$65 > \Delta\sigma > 40$
C_3	15.7	13.35	16.97
C_4	4.5	3.5	5.5

Table 2.5: Stress variations levels [64]

Finally, it must be established the environment's aggressiveness to correctly choose C_3 and C_4 parameters affecting the SN curves. Therefore, table 2.6 will determine the environment criteria once the pH, Cl, $S0_4$ and Resistivity parameters are found.

Table 1.1a Criteria for Substructure Environmental Classifications

Classification	Environmental Condition	Units	Steel		Concrete	
			Water	Soil	Water	Soil
Extremely Aggressive (If any of these conditions exist)	pH		< 6.0		< 5.0	
	Cl	ppm	> 2000		> 2000	
	SO_4	ppm	N.A.		> 1500	> 2000
	Resistivity	Ohm-cm	< 1000		< 500	
Slightly Aggressive (If all of these conditions exist)	pH		> 7.0		> 6.0	
	Cl	ppm	< 500		< 500	
	SO_4	ppm	N.A.		< 150	< 1000
	Resistivity	Ohm-cm	> 5000		> 3000	
Moderately Aggressive	This classification must be used at all sites not meeting requirements for either slightly aggressive or extremely aggressive environments.					

pH = acidity ($-\log_{10}H^+$; potential of Hydrogen), Cl = chloride content, SO_4 = Sulfate content.

Table 2.6: Environment's Aggressiveness [4]

DNV - Guidelines for Design of Wind Turbines

Finally, one last document must be checked regarding fatigue design [66]. Here it is again stated that fatigue analysis must be performed separately for reinforcing steel and concrete, giving priority to the base load components: Tower tilt moment and normal shear force.

Concrete Checking

Under compression the following must be satisfied:

$$\frac{\sigma_{c,max}}{f_{cd,fat}} \leq 0.5 + 0.45\frac{\sigma_{c,min}}{f_{cd,fat}} \leq 0.9, \quad for \quad f_{ck} \leq 50MPa \tag{2.89}$$

$$\frac{\sigma_{c,max}}{f_{cd,fat}} \leq 0.5 + 0.45\frac{\sigma_{c,min}}{f_{cd,fat}} \leq 0.8, \quad for \quad f_{ck} \geq 50MPa \tag{2.90}$$

Where:

- $\sigma_{c,max}$: Maximum compressive stress at a fibre under the frequent combination of actions.
- $\sigma_{c,min}$: Minimum compressive stress at the same fibre where $\sigma_{c,max}$ occurs.
- σ_{cd}: Design compression strength of the concrete. Table 2.7 provides the strength characteristics of concrete and the reinforcement.

$$f_{cd,fat} = f_{cd}\left(1 - \frac{f_{ck}}{250}\right) \tag{2.91}$$

Compression strength of concrete[1]	(M)	f_{ck}	>25 MPa
	(A)		>35 MPa
	(E)		>40 MPa
Yield strength of rein-forcement[2]	Ks410S	f_{yk}	410 MPa
	Ks550S		550 MPa
	Tentor		550 MPa
Modulus of elasticity		E	$\frac{51000}{1+13/f_{ck}}$
Poisson's ratio		ν	0.1 – 0.25
Shear modulus		G	$E/2(1+\nu)$
Unit mass		ρ	2500 kg/m^3

1. Environmental classes acc. to DS 411, moderate (M), aggressive (A) and extra aggressive (E).
2. Selected steel qualities most often used.

Table 2.7: Mechanical properties of RC [66]

Reinforcing Steel Bars Checking

For the reinforcement to have enough fatigue capacity, the following criteria shall be met:

$$\Delta\sigma_s = \Delta\sigma_{s,max} - \Delta\sigma_{s,min} \leq \Delta\sigma_{Rsk} = 70MPa \tag{2.92}$$

Where:

- $\Delta\sigma_s$: It is the stress range in the reinforcement subjected to cyclic loading.
- $\Delta\sigma_{Rsk}$: Maximum allowed stress range in the reinforcement subjected to cyclic loading.

However, it must be stated that equation 2.92 is simply an assumption placed on the safe side. If the stress range were larger than 70MPa, the already mentioned Wohler curve in 2.4.3 must be employed with the stress components specified in table 2.31.

Summary

Three different but similar rules to cover fatigue in RC concrete have been previously presented. Here, it has been finally decided that DNGL - Offshore Concrete Structures will be the one to implement. The reason is because it is the only one offering a SN curve for concrete whose results will be later compared with the steel ones. Additionally, it is also offering, as the Spanish rule, a SN curve for the reinforcement inside the concrete. However, this will not be covered since the computed stresses with TD simulations will only be considered for the concrete part.

Finally, it is of vital importance to keep in mind that properties of the composite along different directions can be computed by simply using the mixture law provided by [18]. However, RC can seldom be considered homogeneous and isotropic, therefore computing the mean value of elastic parameters does not really make sense. Concrete's Young modulus is usually employed, with the steel properties homogenized to the concrete ones.

Chapter 3

Gravity Based Structure Description

3.1 General GBS knowledge

A gravity based structure has been originally used in common applications in the offshore oil sector, see figure 3.1b. It is a support that it is normally towed and afterwards sank with water and held in place by gravity. They are structures built with reinforced concrete where the building framework is made of steel reinforced bars (rebars) offering both tensile strength as well as ductility. What's more, concrete is used in order to reduce the amount of steel needed, offering good behaviour in compression resistance, see figure 3.1a.

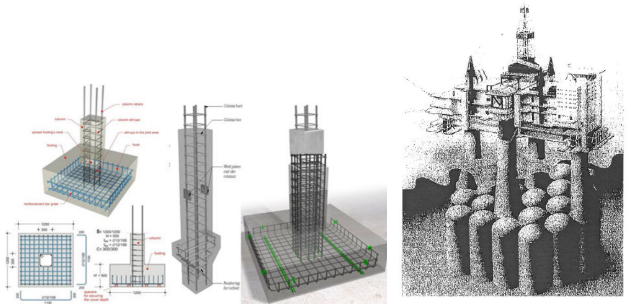

(a) Meaning of reinforced concrete [11] **(b)** GBS for an oil rig [51]

Figure 3.1: Reinforced concrete and GBS in the offshore oil industry [11] [51]

When it comes to cost effective solutions, large amounts of concrete are used with the minimum amount of steel needed to ensure the sufficient resistance of the structure. Therefore,

the GBS is then designed to endure against tensile, compression and bending loads.

However, in this thesis, the approach given to the GBS has been the wind industry. Here, the study will deal with the fatigue assessment of a GBS supporting a 5 MW wind turbine located in the east coast of Gran Canaria. Therefore, in the following paragraphs a detailed explanation of the different GBS typologies will be given.

GBS can be arrange in 4 main blocks with 2 clear classifications. They are distributed in:

- **Mode of transportation to the installation site:**
  - Float-out-and-sink concept - ”Floated” (**F**)

    Self-buoyant structures with large geometric volumes where tugboats are used in the transportation to the OWF and no heavy-lift vessel is needed. In the sinking operation the different cells are firstly filled with water until the GBS reaches the seabed. Once it has touched the ground permanent ballast is added by means of sand or aggregate.

    The reason of building different compartments or cells is to have a better control of the buoyancy once the structure is taken down to the sea bead. This is shown in figure 3.2

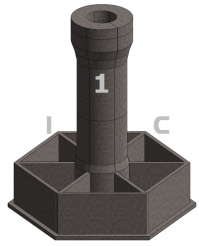

Figure 3.2: GBS Cells Example [5]

  - Lifted concept (**L**)

    Smaller designs than the floated ones with less concrete used but higher expenses in transportation due to the need of heavy lift cranes, auxiliary and transportation vessels.

- **Mode of installation of the foundation and WTG to the OWF**
  - Foundation Only (**FO**)

    Only the foundation is taken to the OWF.

– Integrated Transportation (**IT**)

All WT components (foundation, tower and RNA) are assembled onshore and towed to the OWF.

Therefore, with the above described, the 4 blocks are then formed as:

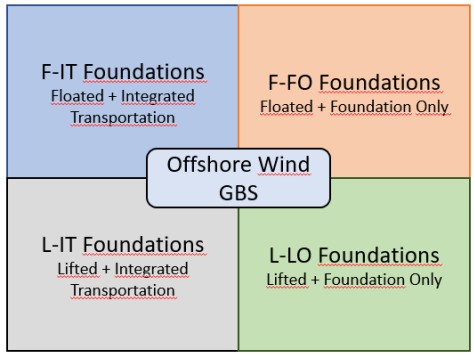

Figure 3.3: Offshore Wind GBS [8]

Within this approach, the concept that will be studied in this thesis will be the F-IT solution. Therefore, only a detailed description of the foundation typology particularities of this design will be addressed. So, according to [8] the following is mentioned.

1. **Design**
   - **Common Trends:** Floated designs normally have a caisson height between 7 to 10 [m] and concrete weight around 5000 tonnes. Additionally, the sand ballast is used on final position to secure and give extra weight to the structure.
   - **F-IT:** Largest caisson diameter of all GBS typologies. Notably, more concrete used than lifted designs (more than 20%)
2. **On-Site**
   - **Common Trends:** GBSs are used in multiple soil conditions except in unconsolidated sediments which can be dredged to make them a useful deposit. However, those soils presenting higher shear strength are desired due to the high mass of the foundation. Additionally, GBSs are becoming more competitive structures in deeper waters due to concrete implementation and larger turbine's diameter installation. Finally, a gravel bed is in need in most of the cases between the soil and the structure.
   - **F-IT:** GBSs' dimensions determined by floating requirements as well as soil bearing capacity. Furthermore, if rocky soils are implemented a 15% reduction in the structure's weight can be achieved.
3. **Yard & Load-out operation**

- **Common Trends:** A suitable and easy access to the yard from land and sea is preferable with the fabrication place close to the quayside. Here, it is of extreme importance a sufficient quay bearing capacity as well as good systems to transport heavy weights like skidding.
- **F-IT:** Large caisson diameter limits beam capacity of the yard as well as large draft dimensions affecting the quayside and towing route. Finally, special cranes are in need to assemble high hub heights, more than 130 [m].

4. **Operation & Maintenance**

   - **Common Trends:** Here it is one the largest advantages of GBSs due to very little maintenance needed compared to steel structures, where concrete's marine lifetime clearly overtakes the steel one. Because of this, regularly inspections are set to no more than an annual visual check.
   - **F-IT:** Same as above.

5. **Transport and Installation**

   - **Common Trends:** Big importance of weather windows where the planning and operations are subjected to them. Additionally, a smooth water ballast procedure must be ensured avoiding capsizing of the GBS and guarantying a suitable touch down.
   - **F-IT:** Crucial check of dynamic behaviour of the GBS when being towed to avoid capsizing and sinking

So, according to what has been mentioned before, the following advantages and drawbacks are found for the GBSs and also applied to the typology of study, F-IT.

Advantages

- Cost effective structure in deeper waters (over 30 [m]) with larger WTGs.
- High concrete's marine lifetime where maintenance and fatigue are noticeably reduced.
- Higher soil flexibility as well as potential installation in unfavourable environments for piled or bucket foundations.
- Stability of concrete price avoiding cost escalation. Besides, much cheaper option over steel. Furthermore, fabrication tolerances are not as strict as in steel, enabling a faster fabrication procedure.
- No transition pieces are needed as in monopiles, where hydraulic hammers are used to take the structure down into the seabed adding extra forces. Additionally, this implies a more environmental friendly procedure due to the exclusion of noise during installation.
- Easily removed if decommissioning applies.

Disadvantages

- High investment during first project phase mainly applied to yard manufacturing. This is exemplified in enough quayside space required if serial production is sought. This end up leading to a costly procedure.
- Not unified criteria in design principles between experts, introducing uncertainties.
- Lack of large scale projects and floating concepts still to be further developed where industry is leading to.
- Clients not convinced enough due to variability of seabed preparation methods. This turns into lack of market clarity to enable GBSs implementation. This is definitely a large barrier to knock down.
- High transportation and installation difficulties when facing harsh environments to ensure buoyancy integrity.

3.1.1 GBS general installation procedure

In this sub-section the GBS installation procedure will be addressed where only a general scope is sought. Therefore, according to [55] the following process is executed.

1. **Dredging of foundation pits**

   In order to correctly place the GBS on the seabed, a preparation of a bed for this structure must be performed. Depending on the typology of the GBS, pit's dimensions will change. For instance, a depth of 7 [m] measuring 50 x 80 [m] can be found in the most well known GBS OWF, Thornton Bank [55]. Therefore, once the bulk dredging stage is performed, part of the dredged materials are kept in disposal areas for later re-utilization. This disposal has double purpose, they are used as backfill material, once the installation of the GBS is performed, and as ballast infill within the GBS to make it heavier and more stable.

2. **Foundation beds installation**

   This stage arises to be as one of the most important in the project where the foundation bed aims to maintain the stress induced levels in the base plate of the GBS within reasonable limits. Additionally, it provides crucial initial verticality of the GBS as well as correct weight transfer from the structure to the subsoil. As mentioned above, gravel is implemented to form the foundation bed between the soil and the structure and it is normally shaped in two stages. Firstly, a filter layer from the dredged level is placed with crushed gravel of minor dimensions (mm) and consequently a gravel layer with a thicker gravel nature is used. Finally, a horizontal surface must be achieved on the foundation bed allowing minimum tolerances for tilt position.

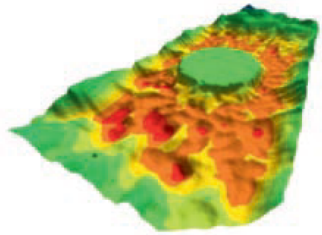

Figure 3.4: Foundation bed description [55]

3. **GBS transport and installation**

   As already mentioned, the F-IT GBS design will be towed to the installation site bearing in mind the dynamic behaviour of the structure. Thus, avoiding capsizing and/or sinking is the target where no heavy lift operations will be considered. Finally, water ballast will be used to take the GBS down to the seabed securing stability requirements.

4. **Backfill of foundation pits**

   This technique employs the dredged material from the first stage (sand, gravel or rocky material) to fill the foundation pit once the GBS has touched the ground. This is performed to fulfilled the geotechnical stability of the structure as well as to provide the sufficient uplift resistance.

5. **Ballast infill**

   In this stage, the hollow shaft of the GBS is normally filled with the dredged material from 1. fulfilling the geotechnical requirement. Furthermore, the infill needed amount is linked with the backfill design and therefore linked with the erosion protection design that covers the backfill. Additionally, both hydraulic and dry infill types of backfill can be employed within the same GBS. Once the hydraulic infill is finished and the materials are settled, dry infill can be executed.

6. **Scour protection**

   In the surroundings of the GBS a scour protection is considered for the backfill materials to not be moved away because of currents and waves. Two layers can be considered (filter and armour) whose designs depend on the geotechnical characteristics applied.

Finally, figure 3.5 clearly shows the different layers that apply in a GBS installation procedure. As this figure belongs to the Thornton Bank OWF the values and method used are simply illustrative.

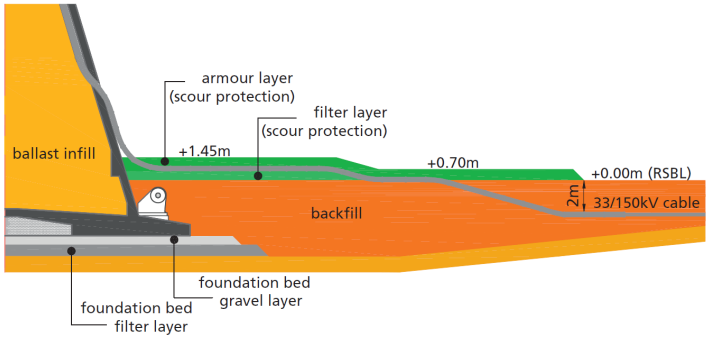

Figure 3.5: Scour protection lay-out [55]

3.2 GBS Design

3.2.1 Design Procedure

When it comes to define the GBS structure a general overview of previous GBS examples must be considered. Specifically, those models from the Thorntonbank wind farm, 24 [m] of water depth, as well as the Gravitas, 35, and the Elisa/Elican project, 30 [m], have been chosen, where the design factor has been the water depth. Those models have been presented in figure 3.6.

The water depth of study is 35 [m], so it should be checked if the wave description should be considered for shallow or infinite waters. According to the dispersion relationship already mentioned in 2.11, both the wave number as well as wave lengths can be established. The process to obtain such parameters is described as follows:

1. Wave period values, taken from metocean analysis, 4, need to be transformed into frequency. The period range covers 1 to 26 [s].

$$\omega_i = \frac{2\pi}{T_i} \tag{3.1}$$

2. Playing around with 2.11, the following is considered for the wave number.

$$k_i = \frac{{\omega_i}^2}{g \cdot tanh(hk_i)} = \frac{{\omega_i}^2}{9,8 \cdot tanh(35 \cdot k_i)} \tag{3.2}$$

   According to each value of ω, a different wave number as well as different wave lengths will be computed. In order to obtain the wave number value k an iteration process is needed.

3. Once every wave number value has been obtained, the wave length can be computed as:

$$\lambda_i = \frac{2\pi}{k_i} \tag{3.3}$$

Therefore, the following rule of thumb must be applied from [20] and as it has already been mentioned in section 2.2.1:

- Deep water: $h > \frac{\lambda}{2}$
- Shallow water: $h < \frac{\lambda}{20}$

Where h is the water depth and λ the wave length.

(a) ThorntonBank Model **(b)** Gravitas Model **(c)** Elisa/Elican Model

Figure 3.6: GBS designs

Therefore, table 3.1 will summarize the conditions applied to every wave period differentiating between deep and shallow waters.

Table 3.1: Deep and Shallow check for every wave period

Period [s]	Deep	Shallow	**Period [s]**	Deep	Shallow
1	✓	x	14	x	x
2	✓	x	15	x	x
3	✓	x	16	x	x
4	✓	x	17	x	x
5	✓	x	18	x	x
6	✓	x	19	x	x
7	x	x	20	x	x
8	x	x	21	x	x
9	x	x	22	x	✓
10	x	x	23	x	✓
11	x	x	24	x	✓
12	x	x	25	x	✓
13	x	x	26	x	✓

So, according to the results obtained in table 3.1, one must treat the wave description as intermediate water depth since neither the shallow not the infinite water theory is fully applied. Within this, the finite water equations must be considered from [38] in the GBS structure described in figure 3.7.

Therefore, considering a first approach in the design procedure, one can establish that the most relevant forces that apply to a GBS structure are the vertical and horizontal forces and the overturning moment. Such moment is the result of the horizontal, aero and hydrodynamic loads, times the arm between the point load and the seabed. Therefore, there is a quite simple design procedure that applies a GBS. The structure and foundation must be designed in a way that the vertical forces are correctly transferred to the seabed and that there is enough restoring moment to prevent the GBS from capsizing. Within this, the ultimate limit state is analyzed and reflected in the environmental conditions applied. Additionally, the bearing capacity of the soil must be studied according to [65] to check that it has the enough strength to withstand the vertical forces.

So, making a force description the following is considered:

- Vertical Forces:
  - GBS weight
  - Turbine weight
  - Ballast weight
  - Dynamic Pressure: This pressure is afterwards converted into force if multiplied by the area of the circle of the GBS' caisson. The pressure for finite waters is characterized by equation 3.4.

$$P_{dyn} = \rho g \xi_a \frac{coshk(z+h)}{coshkh} \tag{3.4}$$

Where:

* ρ : Sea water density [kg/m^3]
* g : Gravity acceleration [m/s^2]
* ξ_a : Wave amplitude [m] - ULS design
* k : Wave number - Finite waters, see equation 3.2
* ω : $2\pi/T$
* T : Wave period [s] - ULS design
* z : Mean water level = 0
* h : Water depth [m]

– Buoyancy force: It is the result of a body when it is being submerged in a fluid with equation 3.5.

$$Buoyancy_{Force} = \rho * Volume * g \tag{3.5}$$

- Horizontal Forces:

  – Aerodynamic thrust: Taken from wind turbine's performance curves. It is the largest value of the thrust from figure 5.5.

  – Wave loads: Morison's equation is applied in the shaft and caisson according to the drag and inertia terms considered in 2.3.1. For a cylinder C_M and C_D equal 1 are normally assumed. Keeping in mind that Morison for large diameters and short waves will probably overestimate the forces. So a conservative assumption is being considered.

- Overturning Moment respect to seabed:

  – Aerodynamic thrust moment: It is the result of multiplying the thrust force times hub height + water depth.

  – Wave loads moment: Every Morison's load will be computed for a discretized element of the cylinder and afterwards multiplied by their respective distance to the seabed.

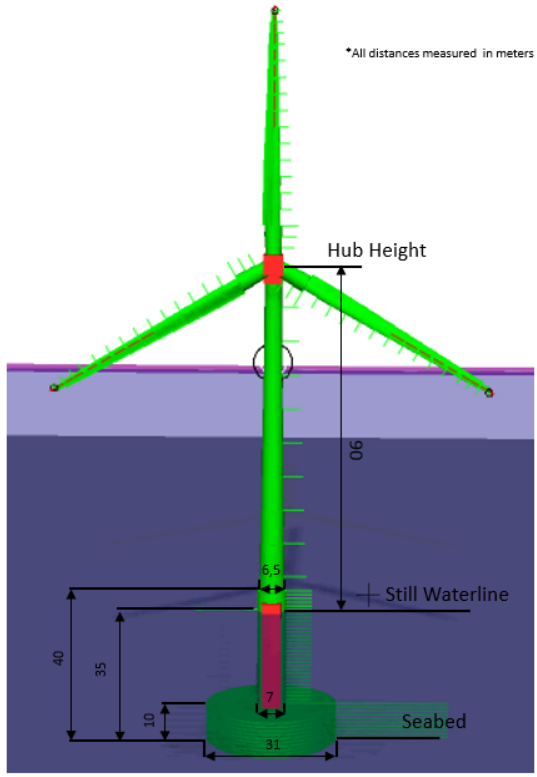

Figure 3.7: GBS Layout

Therefore, the values used as well as their computed results are stored in tables 3.2, 3.3 and 3.4.

Table 3.2: Design OWT Parameters

Design Parameters			OWT Parameters		
Parameter	Value	Unit	Parameter	Value	Unit
ρ	1025	kg/m^3	Hub Height	90	m
g	9.81	m/s^2	Turbine Weight	640680	kg
Wave Amplitude [ULS]	3	m	Caisson Height	10	m
Wave Period [ULS]	26	s	Shaft Height	30	m
Water Depth	-35	m	Caisson Diameter	31	m
Aero-Thrust	800	kN	Shaft Diameter	7	m
C_D	1	-	Caisson Thickness	1	m
C_A	1	-	Shaft Thickness	0.5	m
			GBS Volumen	7312	m^3
			GBS Weight	$3{\cdot}10^3$	$Tons$

Table 3.3: Static Analysis GBS design 1

Vertical Force	Value [MN]	**Horizontal Force**	Value [MN]
GBS Weight Force	29.4	Thrust Force	0.8
Turbine Weight	6.3	Morison Forces	
Buoyancy Force	73.5	Total Drag	0.4
Dynamic Force	20.5	Total Inertia	3.7
Ballast Force	58.8	**TOTAL**	4.9
TOTAL	188.5		

Table 3.4: Static Analysis GBS design 2

Overturning Moment	Value [MNm]
Thrust Induced Moment	100
Morison Induced Moment	35.3
TOTAL	135.3

3.2.2 Soil-Structure Interaction Modelling

The ground type chosen according to [29] has been class B. It is described as deposits of very dense sand, gravel, or very stiff clay. The design soil parameters have been selected according to [56] where a GBS integrated approach has been considered. As it is not part of the thesis project, the most characteristic soil data will be provided by such source assuming an idealized condition.

The most reasonable thing to do would have been to apply soil conditions described in location 4. However, data could not be obtained from the company and idealized conditions had to be assumed with the characteristics described in table 3.5.

Table 3.5: Soil parameters for idealized condition

Soil	Hydrostatic Stiffness	Ultimate Bearing Stress
Class B	$K_{\theta\theta} = 1299456.1 MNm/rad$	$q_{max} = 2.3 MPa$
	$K_{zz} = 14715.87 MN/m$	
	$K_{hh} = 23676.74 MN/m$	

Therefore, in table 3.5, the hydrostatic stiffness parameters are given. They build the so-called hydrostatic stiffness matrix, given in reference 3.6, which describes how the sum of the weight and buoyancy of the GBS varies with changes in position. Additionally, the ultimate bearing soil stress will determine if the soil is able to bear the foundation with the given GBS diameter. So, in the bearing capacity subsection 3.2.3, the soil capacity will be computed.

$$K = \begin{bmatrix} K_{hh} & 0 & 0 & 0 & 0 & 0 \\ 0 & K_{hh} & 0 & 0 & 0 & 0 \\ 0 & 0 & K_{zz} & 0 & 0 & 0 \\ 0 & 0 & 0 & K_{\theta\theta} & 0 & 0 \\ 0 & 0 & 0 & 0 & K_{\theta\theta} & 0 \\ 0 & 0 & 0 & 0 & 0 & 0 \end{bmatrix} \tag{3.6}$$

The last point on this section is to compute the right linear damping matrix. This means that making use of a single DOF system, equation 3.7, the damping coefficients can be found making use of the critical damping value and the natural frequencies obtained in section 5.1. The critical ratio is provided by [63] [0.4-1.5%] based on [19]. Therefore, applying the damping ratio definition in equation 3.8, the linear soil damping matrix is found as stated in equation 3.9.

$$M\ddot{x}(t) + C\dot{x}(t) + Kx(t) = 0 \tag{3.7}$$

$$\beta = \frac{ActualDamping}{CriticalDamping} = \frac{C}{2\sqrt{KM}} = \frac{C}{2Mw_{natural}} = \frac{Cw_{natural}}{2K} \tag{3.8}$$

$$C = \frac{2K\beta}{w_{natural}} \tag{3.9}$$

Where:

- M: Mass matrix
- C: Damping matrix
- K: Stiffness matrix, from 3.6
- β : Damping ratio [0.4-1.5%]. 1% chosen
- $w_{natural}$: Natural frequency, from 5.1

Therefore, the obtained soil damping matrix is described in 3.10.

$$C = \begin{bmatrix} 2.59 \cdot 10^8 & 0 & 0 & 0 & 0 & 0 \\ 0 & 2.59 \cdot 10^8 & 0 & 0 & 0 & 0 \\ 0 & 0 & 1.61 \cdot 10^8 & 0 & 0 & 0 \\ 0 & 0 & 0 & 1.42 \cdot 10^{10} & 0 & 0 \\ 0 & 0 & 0 & 0 & 1.42 \cdot 10^{10} & 0 \\ 0 & 0 & 0 & 0 & 0 & 0 \end{bmatrix} \tag{3.10}$$

Where C_{11}, C_{22} and C_{33} have units of $[Ns/m]$ and C_{44} and C_{55} of $[Nsm]$.

3.2.3 Bearing Capacity

As the GBS is directly supported by the foundation, all the forces acting on the design will be transferred to the subsoil. This means that it is of big importance to establish subsoil's properties since static and dynamic loads will influence the geotechnical characteristics.

Bearing capacity has been studied according to [65], whose equations seem to predict conservative results. This is because they do not include the increasing stress levels in the subsoil when loading is happening. Additionally, only static loads are considered, leading to a reduced bearing capacity when dynamic loads are introduced [45]. Finally, it should also be mentioned that a simple geotechnical study will be covered since discussing various soil parameters is not the aim of the thesis work.

Therefore, the bearing capacity is computed to establish foundation stability under extreme loads. Within this, the combination of the vertical force and overturning moment will induce an eccentricity that will reduce the effective bearing area and therefore, the bearing capacity. This is exemplified in figure 3.8 where the LC is denoted as the load center where the vertical force meets the horizontal one.

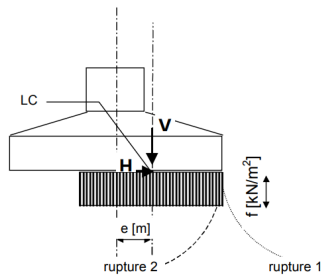

Figure 3.8: Eccentricity of load center [65]

So, firstly the forces and overturning moment must be computed to determine the eccentricity distance. Afterwards, the effective foundation area will be computed making use of the real foundation's dimensions and therefore, the bearing capacity will be calculated.

A. Eccentricity Computation

As already mentioned, the combination of the vertical force and overturning moment will result in an eccentricity value. This is simply the distance between the load center and the symmetry line of the GBS. Therefore, the following is obtained:

$$e = \frac{M_d}{V_d} \tag{3.11}$$

Where M_d is the overturning moment and V_d the resulting vertical force.

B. Effective Foundation Area

Here the effective area, A_{eff}, is built such that its geometrical center coincides with the load center, following as closely as possible the true area contour of the foundation caisson [64]. Therefore, for a circular foundation area with radius R, an elliptical effective foundation area is defined as:

$$A_{eff} = 2\Big[R^2 arccos\Big(\frac{e}{R}\Big) - e\sqrt{R^2 - e^2}\Big] \tag{3.12}$$

Within this, the effective foundation area, A_{eff}, can be represented by a rectangle with dimensions 3.13, represented in figure 3.9.

$$l_{eff} = \sqrt{A_{eff}\frac{l_e}{b_e}} \tag{3.13}$$

Where:

$$b_e = 2(R - e) \tag{3.14}$$

$$l_e = 2R\sqrt{1 - \Big(1 - \frac{b_e}{2R}\Big)} \tag{3.15}$$

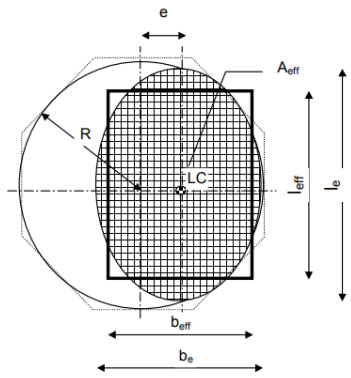

Figure 3.9: Circular and octangular footings with effective foundation area [65]

C. Bearing Capacity Checking

In this step, the effective foundation area is multiplied by the maximum bearing capacity stated in table 3.5. Therefore, if this value is larger than the vertical forces transmitted to

the subsoil, the foundation will be able to bear such loads.

$$Bearing_{Capacity} = q_{max} \cdot A_{eff} \tag{3.16}$$

Therefore, the following values presented in tables 3.6 and 3.7 are those referring to the GBS under design conditions.

Table 3.6: Overturning Check

Overturning Check			
Eccentricity			Restoring Moment [MNm]
Most Favorable	Rotation Point 1	15 m	623
Less Favorable	Rotation Point 2	12 m	500
CRITICAL	Rotation Point 3	3.26 m	135

Table 3.6 shows the self restoring moment capacity of the GBS due to the vertical load action. As the LC will be displaced according to 3.11, the minimum self GBS restoring capacity is then computed. This means that if the soil makes the GBS turn around a point with a shorter distance than the eccentricity, the GBS will capsize since the minimum restoring moment capacity is not fulfilled. Additionally, it should be reminded that the values computed throughout this procedure refer to ULS conditions where the worst scenarios have been built.

As it can be observed, the critical restoring moment is equal to the overturning moment computed in table 3.4. Within this, 2 more rotation points have been analyzed where the restoring moment capacity is noticeably increased since the arm between the center line and point of rotation increases.

Table 3.7: Bearing Capacity Check

Bearing Capacity Check			
Rotation Point	Effective Area [m^2]	Bearing Capacity [GN]	Vertical Force [MN]
Most Favorable	5.22	12	714
Less Favorable	93.86	216	
CRITICAL	554.39	1280	

In this last step, the bearing capacity is checked in order to see if the soil is able to withstand the vertical forces acting on it. As it can be seen in table 3.7, the soil will not be compromised since the bearing capacity is much larger than the total vertical force value.

3.2.4 Dynamic Response

If the frequencies of external loads get closer to the natural frequencies of the GBS, amplification of loads will happen, possibly leading to a resonance system. This is nowadays

enhanced by deeper waters which induce large dynamic loading to the tower and substructure. Therefore, loads amplification in the frequency domain are started to be considered as useful fatigue loads.

Before computing the GBS's natural frequencies, it can already be mentioned that such frequencies will need to fall between 1P and 3P ranges. This is because structures like monopiles or GBS are designed within the soft-stiff region. This results in a soft and flexible structure with the needed thickness and resistance capacity to face the 20 years design environmental conditions. Reasons for not considering a soft-soft design results in possible buckling modes due to a combination of high mass of blades and nacelle and thickness reduction in the tower. Additionally, more waves will be present at lower frequencies structurally compromising the OWT's structure. On the opposite side, the stiff-stiff region will result in a quite expensive design since the thickness will need to increase making the model more difficult to build, transport and install. Figure 3.10 exemplify these three regions.

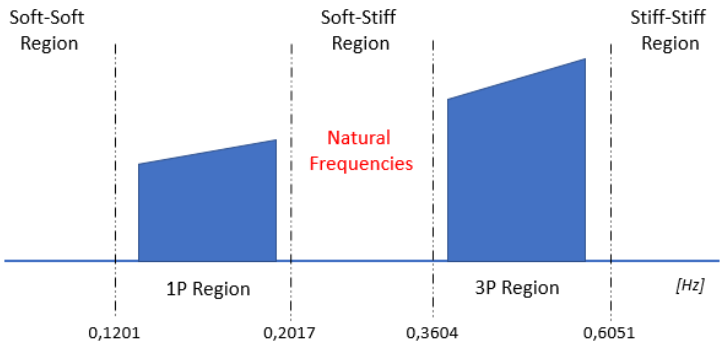

Figure 3.10: Design regions GBS

Specifically for the NREL wind turbine, the 2 regions delimited in figure 3.10 by the blade passing frequency are: 1P from 0.1201 to 0.2017 [Hz] and 3P from 0.3604 to 0.6051 [Hz]. This 2 ranges have been computed according to the constant wind test developed in section 5.3. Therefore, the computed and designed natural frequencies of the GBS must fall within 0.2017-0.3604 [Hz] in order to avoid resonance and dynamic amplification problems.

3.2.5 Design Checking

After all the design procedure explained above, two final steps will need to be considered to check the correct functioning of the modelling. Here, both the natural frequencies as well as the pitching of the caisson of the GBS will be revised.

Soil stiffness has been reduced half of the values, as shown in table 3.5. This means that, as it was expected, the natural period for both motions, side to side and fore aft, have

increased. Additionally, the average pitching value of the caisson is practically negligible, determining no risky behaviour of it. There are no rules regarding maximum pitching output for a GBS, but to be on the safe side, it was considered that an angle less than 0.1 degree was safe enough. Tables 3.8 and 3.9 show the different results obtained.

Table 3.8: Decay values with modified soil stiffness

	Motion	**Natural Frequency [Hz]**	**Natural Period [s]**
Original Soil Stiffness	Fore-Aft	0.2918	3.427
	Side-Side	0.2899	3.449
Modified Soil Stiffness	Fore-Aft	0.28909	3.459
	Side-Side	0,2872501	3.4812

Table 3.9: Mean and maximum value of GBS pitching

Mean Pitching Value [degrees]	**Maximum Pitching Value [degrees]**
0.0029	0.06

3.2.6 GBS Design Softwares

Most of the design softwares used and implemented in the thesis belong to the SESAM package provided and developed by DNV-GL. SESAM is a suite specialized in structural and hydrodynamic analysis of ships and offshore structures which employs the displacement formulation of the finite element method. Additionally, WAMIT (The state of the art in wave interaction analysis) has also been employed being developed at MIT in 1987. This software allows the user to completely analyze the interaction between waves and ships or offshore structures.

Making use student licenses, an integrated dynamic analysis of the GBS could be performed thanks to SIMA (Simulation of Marine Operations). Additionally, GeniE was employed to create a FEM model to be later hydrodynamically analyzed by HydroD. However, since WAMIT license can not be run outside NTNU's facilities my supervisor had to run a potential flow simulation to obtain the first order wave transfer function, added mass and linear damping values for every section of the GBS described in 6.3.

GeniE

GeniE is a FEM software able to model, analyze and code check beams, plates and shells in offshore structures and ships. Introducing the marine environment, static and dynamic analysis can be performed with a powerful and friendly graphical interface.

Specifically in this thesis, GeniE has only been used to model and mesh the GBS. This will create two FEM files that will represent the FEM and mass models. Once this is done, the FEM file will be imported into a hydrodynamic software for the potential flow to be computed thanks to HydroD.

Therefore, once the model was built, different mesh types were analyzed as shown in figure 3.11. From left to right, it can be described that the first mesh model, the one finally chosen, is described by normal square elements, the second by advance square elements and the last one by triangular ones. The reason why mesh 1 was chosen is because square elements offer a simpler mesh and because the number of cells were enough for the forces to be computed. As known, the higher the elements the higher the accuracy but much more time is needed. That is why mesh 3 was finally rejected.

Therefore, table 3.10 shows the results for the three simulations. Finally, in every model, 500 mm of element size has been considered.

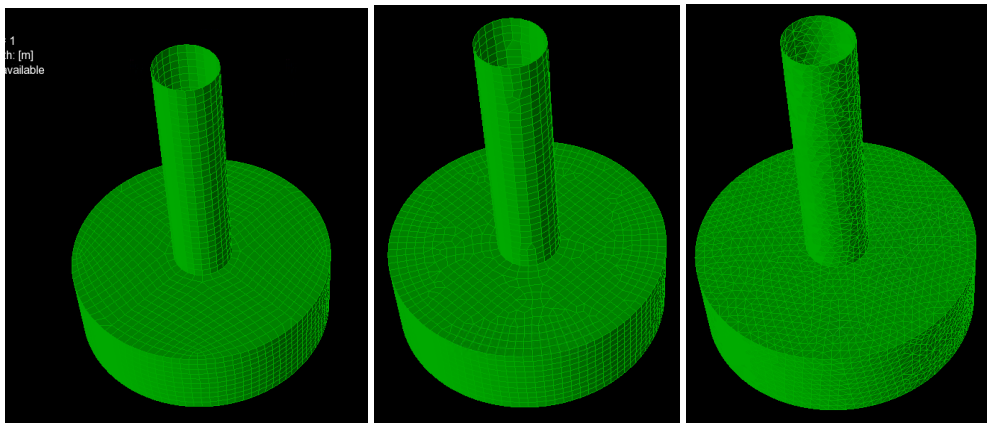

(a) Mesh 1 **(b)** Mesh 2 **(c)** Mesh 3

Figure 3.11: GBS GeniE meshing models

Table 3.10: Mesh properties characteristics

Mesh	Nodes Number	Elements Number
1	2540	2480
2	2487	2456
3	2795	5466

HydroD

HydroD is an advance stability and hydrodynamic analysis tool applied on offshore structures and ships. It is able to perform multi-body analysis in the frequency domain including

full hydrodynamic interaction between them. Within this, post-processing is characterized by global responses data like RAOs and unique information for specific selected panels.

In this thesis, the FEM file created by GeniE has been imported into HydroD where potential flow theory has been run. Before results were obtained, a set-up had to be made defining frequency set, location, loading condition and mass model among other inputs. So, figure 3.12 shows the HydroD interface where the intersection between the symmetry line of the GBS with the seabed has been considered the center of origin. Additionally, the water surface is represented by the horizontal pink square mesh located at 35 m over the seabed. Finally, WADAM offbody mesh points are introduced by the filled pink squared to perform gap calculations or free surface wave elevation animations. However, this option has not been finally implemented in the results section.

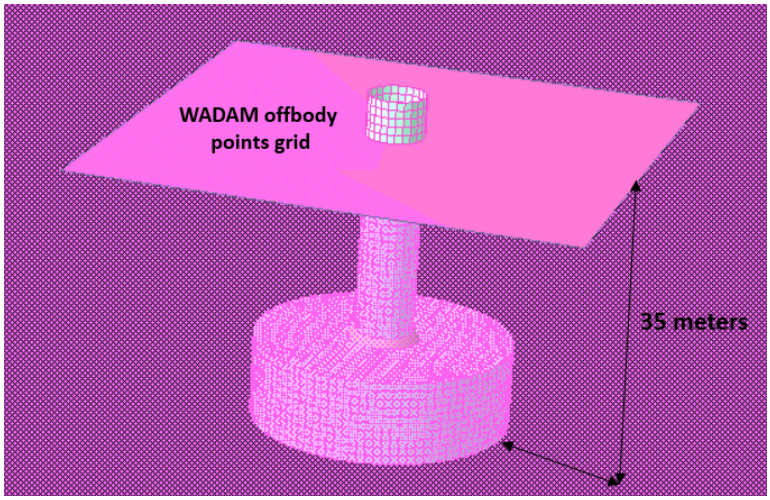

Figure 3.12: HydroD setup of the GBS

The results of the potential flow calculation as well as the comparison between the three hydrodynamic models will be developed in chapter 6.

SIMA

SIMA is a tool able to perform simulations of marine operations with a main focus on dynamic analysis. It has an intuitive interface able to model, simulate and perform analysis in a powerful workbench offering 3D and 2D graphics. Within this, SIMA offers the possibility of employing two different numerical softwares: SIMO and RIFLEX.

On the one hand, SIMO performs time domain simulation of multi-body hydrodynamic systems with a focus on marine operations and stationkeeping analysis. On the other hand, RIFLEX offers a non-linear time domain FEM analysis of slender marine structures. However, there is also a possibility of joining both together resulting in coupled SIMO-RIFLEX. Specifically, this coupled option has been the core tool applied in my thesis in

order to perform hydrodynamic analysis on the GBS. The different tasks that have been developed were:

- Environments definition (Wave and wind inputs).
- Bodies description (Nacelle, hub and soil springs).
- Slender system Definition.
- Eigenvalue analysis.
- Dynamic calculations:
  - Decay tests.
  - Constant wind tests.
  - Morison theory.
  - Diffraction theory.
  - Fatigue estimation.

The general coupled SIMO-RIFLEX model simulated in SIMA is shown in figure 3.13a. Here, the slender system defines large part of the GBS with 3 bodies attached (Nacelle, hub and soil springs representation). Additionally, this slender system is partly described by 4 essential system components described in table 3.11.

Table 3.11: Slender system elements

	Supernodes	**Lines**	**Line Types**	**Cross Sections**
Number of elements	15	10	6	32

In order to properly understand how the slender system of the GBS has been built, the following idea must be carefully understood: Supernodes are the start and ending points of lines. Lines are made up of segments characterized by line-types. These segments are made up of elements where the number of nodes in 1 segment are the number of elements in that segment plus 1.

With the previous information in mind, one can already draw the GBS slender system outline, see figure 3.13b, to properly identify how the system has been built. Furthermore, tables 3.13 and 3.12 will describe the 4 different slender system components.

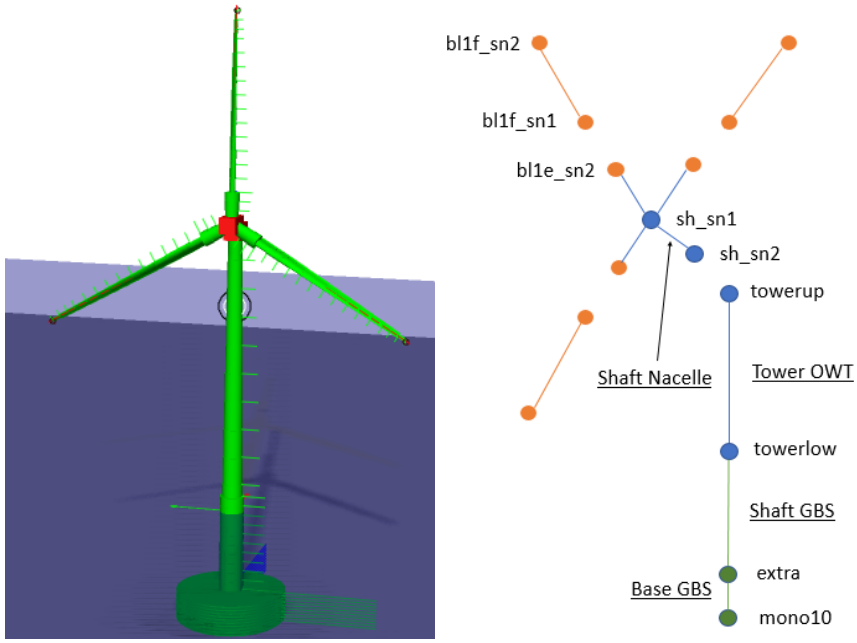

(a) SIMO-REFLEX Coupled model **(b)** REFLEX model

Figure 3.13: GBS model descriptions

Finally, the SIMO bodies that will be implemented when computing potential flow in SIMA are presented in red color in the GBS shaft and caisson in figure 3.14. These bodies will be used to introduced the total hydrodynamic loads (first order wave excitation forces, added mass and radiation damping) computed from WAMIT and employing potential flow trough the panel method. This process is fully described in 6.2.1.

Table 3.12: Line, line types and supernodes description

Line	Line Type	End1	End2
shaft	shaft_{lt}	sh_{sn1}	sh_{sn2}
bl1ecc	bl_{ecc}	sh_{sn1}	bl1e_{sn2}
bl1foil	bl_{foil}	bl1f_{sn1}	bl1f_{sn2}
bl2ecc	bl_{ecc}	sh_{sn1}	bl2e_{sn2}
bl2foil	bl_{foil}	bl2f_{sn1}	bl2f_{sn2}
bl3ecc	bl_{ecc}	sh_{sn1}	bl3e_{sn2}
bl3foil	bl_{foil}	bl3f_{sn1}	bl3f_{sn2}
tower	tower_{lt}	towerlow	towerup
BaseBGS	BaseGBSlineType	mono10	extra
ShaftGBS	ShaftGBSlineType	extra	towerlow

Table 3.13: Supernodes slender system description

Supernode	**Height** [m]
mono10	-35
extra	-25
towerlow	5
torwerup	87.6
sh_{sn1}	90
sh_{sn2}	89.913
$bl1e_{sn2}$	91.5
$bl1f_{sn1}$	91.5
$bl1f_{sn2}$	152.94
$bl2e_{sn2}$	89.26
$bl2f_{sn1}$	89.26
$bl2f_{sn2}$	58.89
$bl3e_{sn2}$	89.259
$bl3f_{sn1}$	89.259
$bl3f_{sn2}$	58.89

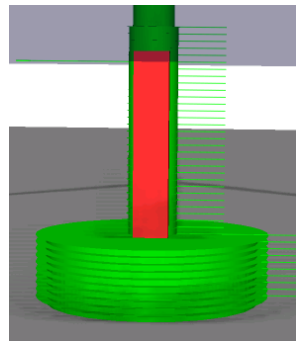

Figure 3.14: Bodies used in SIMA to implement the potential flow hydrodynamic loads

WAMIT

According to product description [14]: *WAMIT is a computer program based on the linear and second-order potential theory for analyzing floating or submerged bodies, in the presence of ocean waves*. The panel method is employed to obtain the velocities and pressure distributions in the different elements of the submerged body. Additionally, second-order nonlinear quantities can also be satisfied, but they are not relevant in our study case.

Therefore, in order to run the model in WAMIT, one must firstly create the FEM and mass files employing the GeniE software and later import them in HydroD running the panel method theory. Once this set-up is concluded, HydroD files are imported in WAMIT to obtain specific data according to the sectional description in table 6.1. The reason to

evaluate the GBS with this software is to obtain the several outputs that will be imported in SIMA to model the potential flow scenario. The items listed bellow were computed from potential flow and later imported in SIMA. Such results are presented in section 6.2. Additionally, the 3D WAMIT output is shown in figure 3.15 to check that the modelled structure has been the right one.

- First order wave forces excitation [Sections & Complete Structure]
- Added mass [Sections & Complete Structure]
- Radiation damping [Sections & Complete Structure]

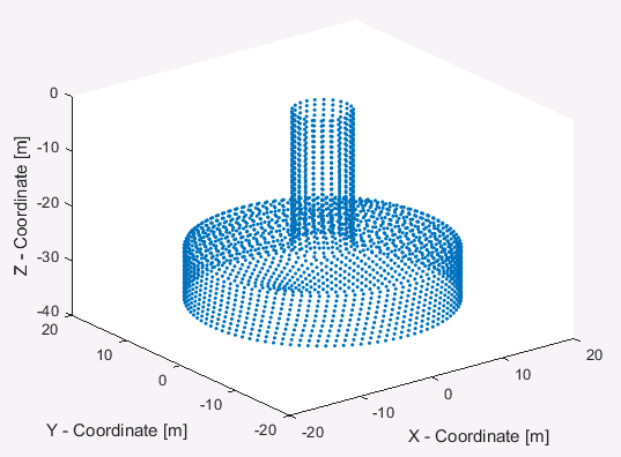

Figure 3.15: WAMIT 3D GBS output

Summary of the Modelling Procedure

As many steps in the design have been considered, a brief summary of the modelling procedure is here described.

Firstly, GeniE was used to create both the FEM file as well as the mass model that were later implemented in HydroD. In this hydrodynamic software, potential flow theory was used and computed thanks to the panel method that resulted into the integrated force computation. In a second step, WAMIT was employed to resolve both the diffraction and radiation problems for the whole structure. This means that WAMIT results were later used to compute the total hydrodynamic loads (first order wave excitations, added mass and radiation damping) for every described section along the GBS. Finally, the results for every section were later implemented in SIMA where a SIMO-RIFLEX coupled model was considered. Specifically for the potential flow model, some bodies were introduced in SIMA at the same coordinates as in WAMIT with their respective total hydrodynamic loads for every section-body alliance. So, to have a final better understanding of the procedure, figure 3.16 is shown.

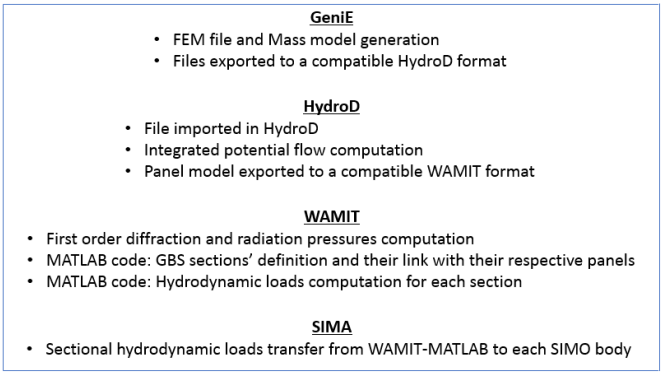

Figure 3.16: Modelling procedure description

3.2.7 Offshore Wind Turbine Parameters

The selected offshore wind turbine for this project is the 5 MW Reference Wind Turbine for Offshore System Development [44]. It is a three bladed upwind variable speed and variable blade pitch whose control system properties, aerodynamic and structural parameters are thoroughly described in the cited document. However, a general and brief description of such wind turbine is given in table 3.2.7.

The GBS is a simple structure where a cylindrical shaft on top of a caisson is supported on the seabed. As already explained in 3.1, the F-IT GBS will be designed for depths between 30 and 55 [m], forcing today's industry to upgrade itself and coming up with new challenges to assess offshore structures within such water depth limits. Therefore, large diameters will be employed for the shaft and caisson to hold up the 5 MW Reference Wind Turbine in 35 [m] of water depth. However, these diameters must be able to provide the enough stiffness for such design, where fabrication and installation procedures become more complex.

Specifically for the GBS, the critical loads and bending moments will typically occur in the connection between the shaft and the caisson. This is exactly where there is a change in the cross-section areas where one of its biggest limitations comes when overall deflection and vibrations must be taken into account. Additionally, cyclic loads, determining axial stresses as a result of axial forces and large bending moments combination are also present. This obviously will affect and determine the limits and design requirements of the modelled structure. Therefore, two of the four limit states described bellow will be studied. While ULS will determine GBS design's parameters, FLS will define the durability of the model.

- **Serviceability limit states (SLS):** Daily functionality (deformations, accelerations,etc...) during operational conditions.
- **Ultimate limit states (ULS):** Extreme load situation, ultimate strength, structural stability, maximum load carrying-capacity.

- **Fatigue limit states (FLS):** Long-term usage during all operation conditions, fatigue and fracture analysis and design.
- **Accidental limit states (ALS):** Less common situations such as collision or grounding, ice-load interaction, fire and explosions.

Additionally, regarding natural frequencies, one must be aware that avoiding resonant behaviour in a structure's dynamic response is one of the major design drivers. Natural frequencies of the GBS must be considered in order not to coincide with those coming from the excitation fields. Therefore, preventing the GBS from such event will significantly reduce the stresses and fatigue damage contribution.

To conclude, according to [22], it must be stated that nonlinear wave loads can be present and therefore induce resonant ringing-type response. Ringing refers to transient, resonant response which is triggered by steep, irregular waves and can happen for flexible structures in storm conditions. However, even though the GBS presents a relatively stiff design, these very steep waves can cause significant higher-order wave loads acting at higher frequencies than the normal carrying wave, 3-4 ω, causing a severe damage.

Table 3.14: 5 MW Wind Turbine Parameters

5 MW Wind Turbine Key Parameters	
Rotor Orientation	Clockwise rotation - Upwind
Control	Variable Speed - Collective Pitch
Cut-in Wind Speed	3 m/s
Cut-out Wind Speed	25 m/s
Rated Wind Speed	11.4 m/s
Rated Power	5 MW
Number of Blades	3
Rotor Diameter	126 m
Hub Diameter	3 m
Hub Height	90 m
Drivetrain	High Speed, Multiple-Stage Gearbox
Rated Rotor Speed	12.1 rpm
Rated Generator Speed	1173.7 rpm
Gearbox Ratio	97:1
Maximum Tip Speed	80 m/s
Rotor Mass	110,000 kg
Nacelle Mass	240,000 kg
Tower Mass	347,460 kg
Blade Mass	17,740 kg
Total Mass	640,680 kg

Chapter 4

MetOcean Data Analysis

The structural design is strongly influenced by metocean site conditions and site investigations. Metocean conditions are determined by detailed hydrodynamic analysis based on long-term hindcast model data and calibrated against short-term site wave measurements. Therefore, an analysis and discretization of the metocean data will be carried out, where joint distributions will be used to compute wind power as well as fatigue lifetime. A selection of representative conditions including their probabilities of occurrence will be performed and simulations will be run and later extrapolated to the long-term.

As mentioned, the study zone of interest is delimited by PLOCAN requirements located at the east coast of Gran Canaria, comprehending 23 km^2, see figures 4.2 and 4.1. Specifically, the platform is situated at 1.5 km from Telde municipality and established at 30.5 [m] of depth.

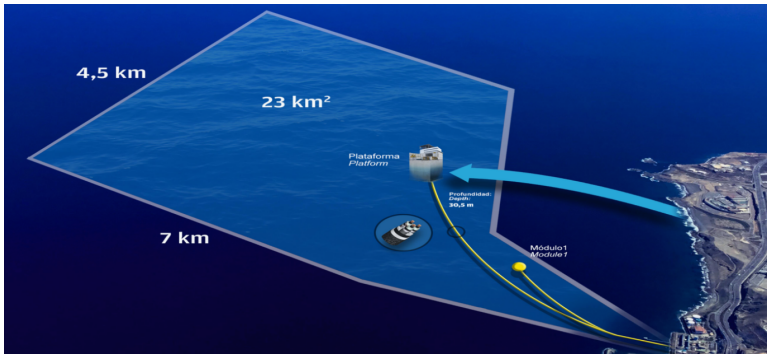

Figure 4.1: PLOCAN test area 1 [9]

Regarding climate description, Gran Canaria is influenced by subtropical traits determined by its north-west African location. Additionally, a singular atmospheric description is

shaped by the Azores Anticyclone and the never ending humid Trade Winds. The relative position of such anticyclone regarding the Canary archipelago, makes the Trade Winds to become more intense in summer, when it is far from the Canary Islands, and less powerful in winter when it is closer. This effect is clearly seen in the wind roses description for the different seasons presented.

Finally, the water temperature is colder than it should be for the latitude of study. This is because the warm ocean Gulf current moves up to the north in the Atlantic Ocean and descends cooler parallel to Portugal affected by the Trade Winds that helps introducing the upwelling effect.

Additionally, Canary waters, inside Atlantic Ocean conditions, have a T_p average value larger than the one presented in the North Sea. This is due to vast open sea areas presented where swell is more prone to happen in comparison with North sea areas where wind-generated waves prevail.

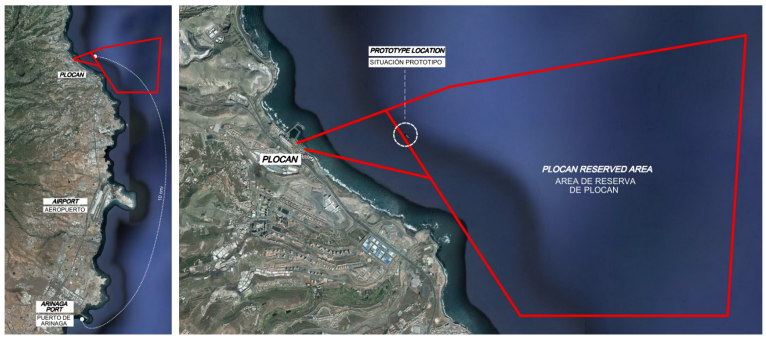

Figure 4.2: PLOCAN test area 2 [3]

As commented, the selected GBS will be operating under Atlantic Ocean conditions, with a depth of 35 [m] and a hub height of 90 [m]. Wave and wind data has been provided by an external company (AWS Truepower, S.L.U.) where new and high-resolution techniques have been applied to generate data from numerical modelling. However, it must be mentioned that data from measurements was firstly considered but later rejected due to unclear results.

On the one hand, the buoy used by this company to gather the existing data comes from the so-called "Boya de Las Palmas Este" located at 2 km from shore, with coordinates $[28.0456^oN - 15.39^oO]$. This buoy is found at 30 [m] of depth measuring scalar wave spectrum with hourly cadence. Finally, it employs a directional sensor and belongs to the REDCOS (Network of Coastal Buoys of the Spanish State Ports Authority).

On the other hand, wind measurements have been gathered from ERA-Interim, that is the latest global atmospheric re-analysis product developed by ECMWF. Based on spectral

representation, a hybrid representation of vertical co-ordinates and sigma-pressure and a semi-explicit, semi-Lagrangian time scheme has been done. Keeping this in mind, the wind time series have been provided for 100 [m] of height at point P1 in figure 4.4, based on the closest grid point to the zone of interest, PLOCAN. The grid point presented in figure 4.3 is found relatively far from Gran Canaria, where uncertainties are introduced in wind results. Lastly, the wind modelling presents a 6-hourly cadence with 3/4 degrees of atmospheric spatial resolution and with coordinates $[28.40^oN - 15.00^oO]$.

As mentioned, wind measurements have been gathered for a height of 100 [m], however, the study point must be at the hub height where power estimation is required making use of the mean wind speed. Normally, when employing wind speed at higher levels, results seem to be more precise if the wind profile presents a non stable development. Therefore, the vertical wind profile is normally adjusted to a potential-type curve due to the shear layer in the atmosphere. The following expression is then used:

$$U_{w_1} = U_{w_2}\left(\frac{h_1}{h_2}\right)^{\alpha} \tag{4.1}$$

Where:

- U_{w_1}: Mean wind speed at the desired height.
- U_{w_2}: Mean wind speed given data.
- h_1: Desired height. In our study, 90 [m]. Differences will not be quite noticeable.
- h_2: Height for the given data. In our study, 100 [m].
- α: Wind Shear - It is the result of adjusting the potential function using minimum squares. According to [17] the wind shear value for the P1 location is 0.0591.

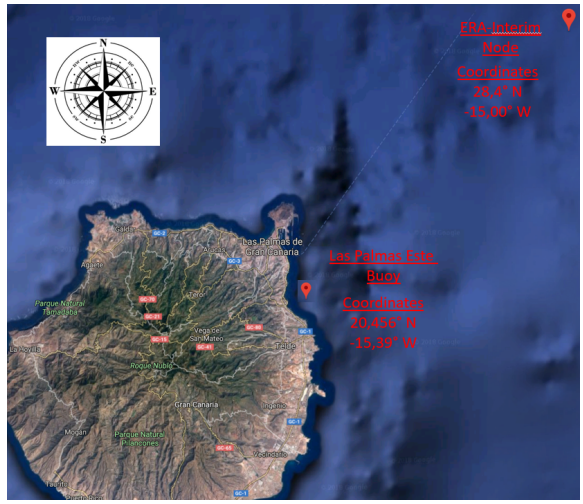

Figure 4.3: Buoy and ERA-Interim grid point locations [10]

Figure 4.4: Buoy and P1 point locations

Additionally, the average wind power density can be estimated making use of the mean power density value at each hour between the years of study, 1980 to 2009. Therefore, the following expression is considered:

$$P_{wind} = \frac{\rho_{air}}{2} U_{Hub}^3 \tag{4.2}$$

- ρ_{air}: Air density.
- U_{Hub}: Wind Speed at the design hub height, 90 [m].

As a starting point, the hindcast data has been gathered every six hours for wind and waves during 1980 and 2009. In order to predict long-term environmental conditions the following parameters are of major importance:

- U_w: Wind speed [m/s] at 100 [m] and adapted to hub height according to equation 4.1.
- H_s: Significant wave height [m].
- T_p: Wave spectral peak period [s].

Finally, the turbulent wind has been introduced in the dynamic analysis since it will represent real life wind effects. In order to create such wind behaviour, TurbSim software has been employed to randomly create 3D wind speed vectors in a 2D rectangular grid. Therefore, both temporal and spatial wind fields are created taken into account boundary layer flow instabilities. Figure 4.5 represents this situation with the inflow seen by the rotor.

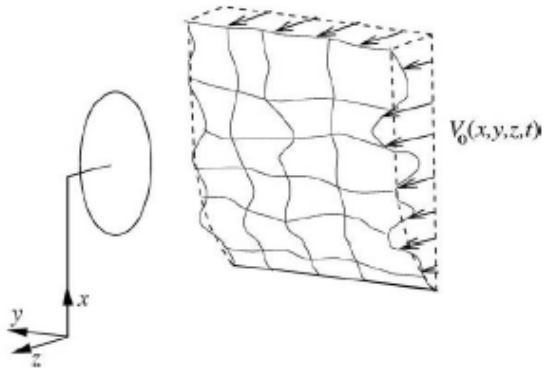

Figure 4.5: Turbulent inflow seen by the rotor [40]

4.0.1 Marginal and Joint Distributions

Based on [49], marginal and joint distributions of wind and wave can be achieved by fitting analytical distributions to raw data. On the one hand, and working separately, marginal distribution of U_w is considered for wind power estimation if the wind turbine power curve is provided. On the other hand, wave power estimation can be achieved by the joint distribution of H_s and T_p. Finally, linearity between waves and wind must be considered for structural reasons. If misalignment between both loads is an issue, lack of damping appears being the aerodynamic one of major importance. However, if alignment prevails, some points of the structure will always get the loads enhancing fatigue damage at that location. This, of course, is a disadvantage to keep in mind as the loads are concentrated and not spread around the circular diameter of the GBS.

Marginal Distribution of Mean Wind Speed U_w

The two parameter Weibull distribution will be applied to both, H_s and U_w with PDF given in equation 4.3. Therefore, figures 4.6 and 4.7 show the fitting curve of marginal distributions at PLOCAN area on the Weibull probability papers.

$$f(x;\lambda,k) = \frac{k}{\lambda}\left(\frac{x}{\lambda}\right)^{k-1} e^{-(\frac{x}{\lambda})^k} \quad x \geq 0 \tag{4.3}$$

Where k and λ denote the shape and scale parameters respectively.

As it is confirmed by [49], U_w offers a good agreement between raw data and the Weibull fitting in figure 4.6. However, H_s seems to diverge in both tails, figure 4.7, being the upper one of major importance due to the logarithmic scale. Because of this upper tail misalignment, H_s offers some underestimation of extreme values that will be assumed to be good enough in this met-ocean data analysis. Therefore, if a better fitting is sought, a Lonowe

model must be applied being a combination of Weibull and lognormal distributions.

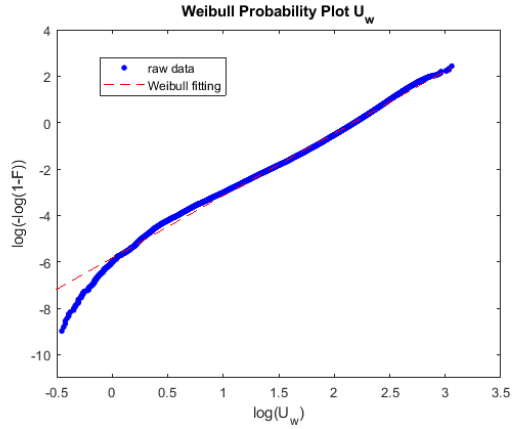

Figure 4.6: Weibull plot of marginal distribution of U_w

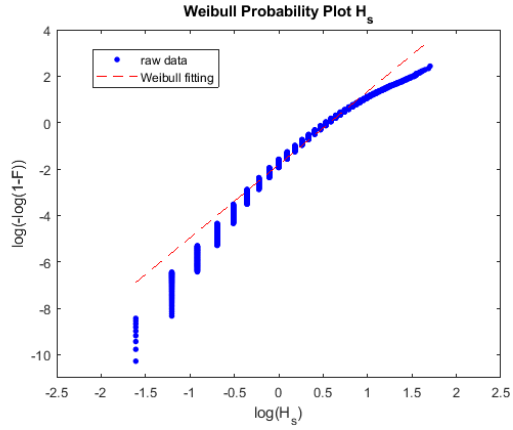

Figure 4.7: Weibull plot of marginal distribution of H_s

Joint Distribution of H_s and T_p

Only evaluating wave data, the joint PDF of T_p and H_s can be built considering a marginal distribution of H_s and a conditional distribution of T_p for given H_s. This is reflected in equation 4.4 where the marginal distribution of H_s has been already introduced in figure 4.7.

$$f_{H_s,T_p}(h,t) = f_{Hs}(h) \cdot f_{T_p|H_s}(t \mid h) \tag{4.4}$$

As suggested by [43] a conditional distribution of T_p for given H_s appear to look like a lognormal distribution with PDF given in equation 4.5. When estimating the plotting, two different H_s ranges have been considered with 2 [m] of bin size as reflected in figures 4.8 and 4.9.

$$f_{T_p|H_s}(t \mid h) = \frac{1}{t} \cdot \frac{1}{\sigma\sqrt{2\pi}} exp\Big(- \frac{(ln(t) - \mu)^2}{2\sigma^2} \Big) \tag{4.5}$$

Where μ and σ are the mean and standard deviation of the variable's natural logarithm respectively.

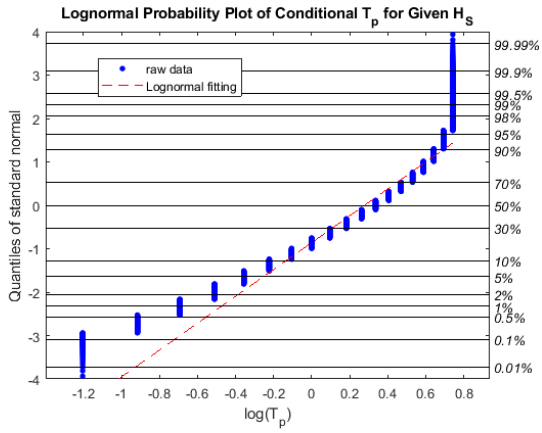

Figure 4.8: Lognormal plot of conditional distribution of T_p for given H_s (0.2 [m] $\leq$ H$_s\leq$ 2.2 [m])

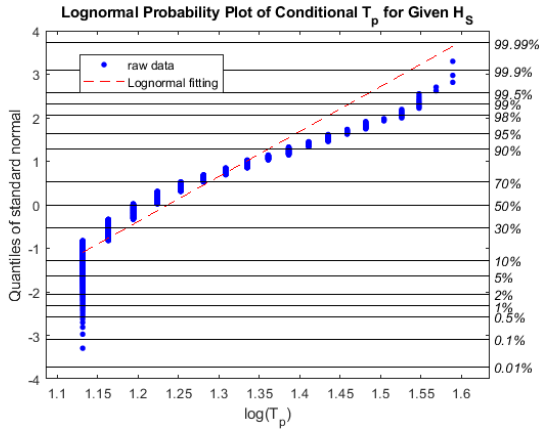

Figure 4.9: Lognormal plot of conditional distribution of T_p for given H_s (3 [m] $\leq$ H$_s\leq$ 5 [m])

4.0.2 Wind and Wave Roses

When referring to wind conditions, the wind rose is of a big help. It basically tells us how wind speed and direction are normally distributed for our particular north sea location. A polar coordinate system is used where the frequency of winds over a time period is plotted and where different speed ranges are represented by their respective color band. Therefore, the following wind roses will be showing the different seasons covering the whole year spectrum analyzed; from 1980 to 2009. As commented, these varying low density aerodynamic loads make the structure suffer structurally giving rise to high fatigue issues.

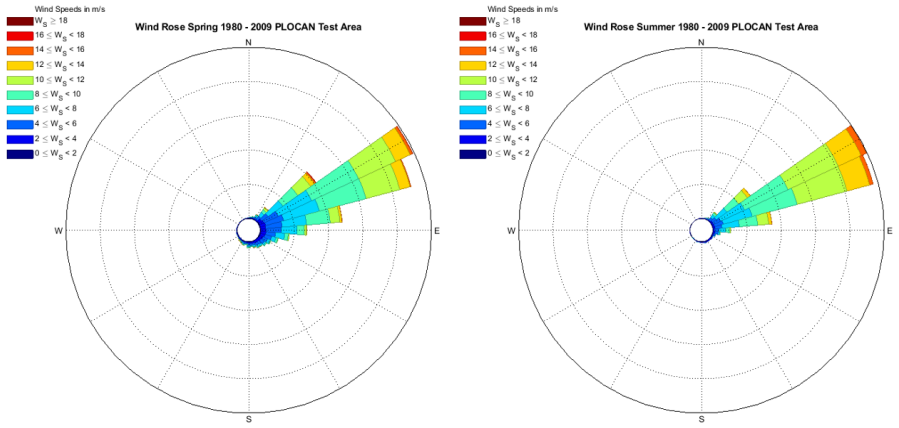

Figure 4.10: Wind Roses PLOCAN test area Spring and Summer 1980-2009

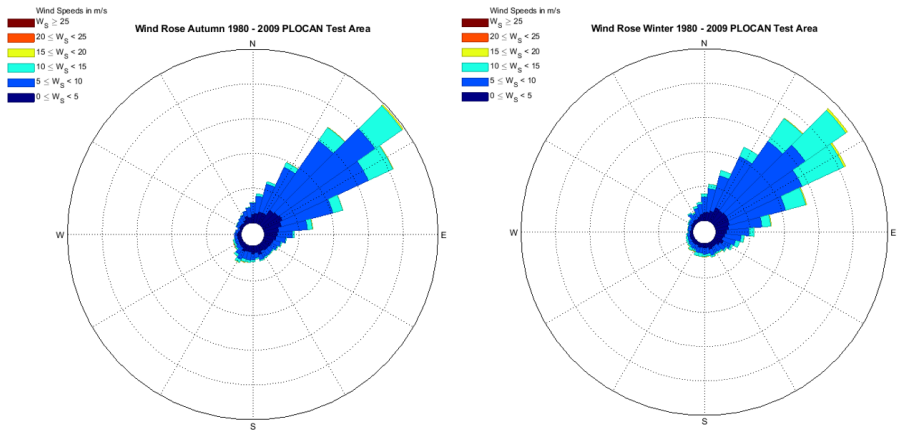

Figure 4.11: Wind Roses PLOCAN test area Autumn and Winter 1980-2009

The wind roses presented in figures 4.10 and 4.11 clearly state the north east direction

of the Trade Winds being affected by the west rotation of the earth around its own axis. As mentioned before, summer intensity reflects stronger winds due to the further distance of the Azores Anticyclone regarding the Canary Islands. The opposite happens in winter where less powerful winds appears on scene.

Additionally, one can discuss how results would have differed if instead of a middle Atlantic Ocean location, the measured point had been in the North Sea. Obviously, different wind roses would have been obtained due to the different obstacles the wind needs to face, as well as the external atmospheric events affecting such wind.

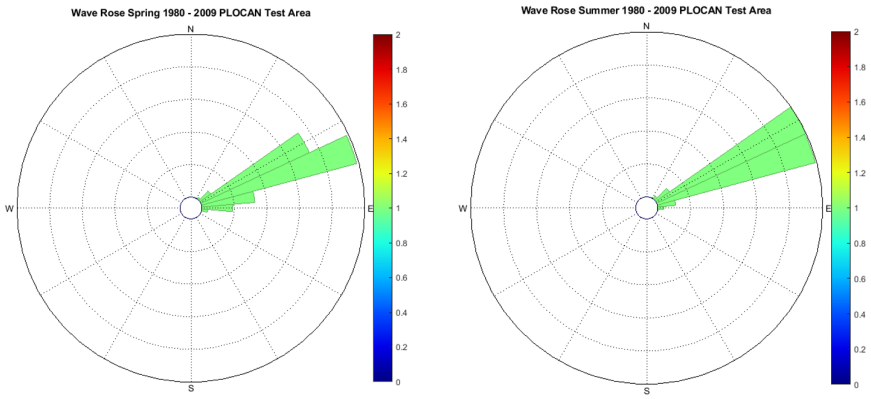

Figure 4.12: Wave Roses PLOCAN test area Spring and Summer 1980-2009

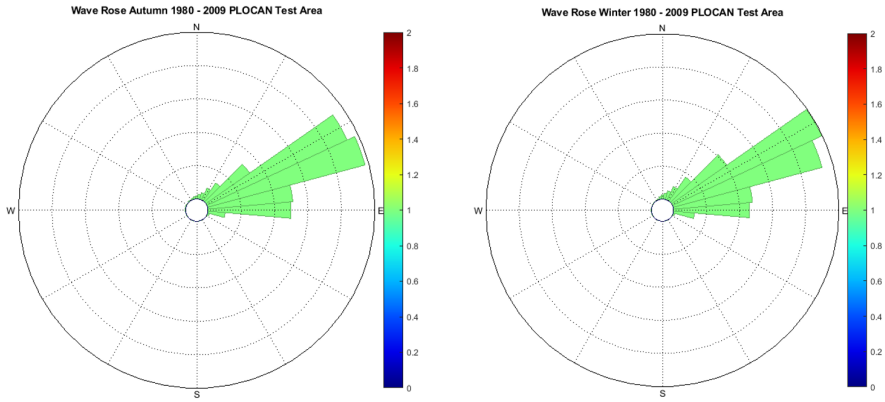

Figure 4.13: Wave Roses PLOCAN test area Autumn and Winter 1980-2009

Finally, as mentioned above, wind and wave loads misalignment must be checked for structural considerations. Once the wind roses were plotted, wave direction has also been

studied and projected in figures 4.12 and 4.13. From the results one can seen how a strong wind and wave alignment dependency is obtained. This means that mostly the same points of the GBS will be affected by the wind and wave loads causing concentrated fatigue damage at the same location. Obviously, the more spread the loads the better as the GBS will not be overloaded at the same points. However, this alignment event, widely used in the offshore industry, leads the design to a conservative assumption placing our analysis in the safe side. However, there are still some minor uncertainties that will be dealt with when the results come up.

From the wave roses, only wave direction was sought and therefore wave intensity has been set to a unitary value, as reflected in the bar coloured legend. As mentioned, the north east dependency is clearly shown for both wind and waves and alignment between both loads will be studied in the following scatter diagrams for different wind speed ranges.

4.0.3 Scatter Diagrams and Binned Environmental Conditions

Scatter diagrams are charts normally used to estimate wave forces according to the joint probability combination of H_s and T_p. In order to predict the fatigue life of the GBS, those bins accounting for the higher occurrence will result in the highest fatigue damage. Additionally, low T_p combined with high H_s can also lead to high fatigue due to the effect of large waves on the structure.

So, in figure 4.1, the wave scatter diagram for the whole spectrum is provided. The obtained % refers to a joint probability between the different values of H_s and T_p without considering wind speed. Obviously, this scatter does not provide a descriptive wind speed consideration but it contributes on giving a general idea about how H_s and T_p are related to each other in the whole spectrum. Furthermore, and as it has already been mentioned, the Atlantic Ocean presents larger T_p values. That is reflected in 4.1 where 25 [s] of peak wave period values are found, against the maximum 17-18 [s] normally obtained in North Sea locations.

However, in order to make a better analysis, each H_s and T_p combination for each wind speed range must be analyzed to get the fully correct environmental relationship of a defined condition. Thus, all the wave scatter diagrams have been placed in the appendix section referring to those bins that will account for the most damage. When selecting a bin, some uncertainties are introduced as the whole scatter is not considered. This is something that should be taken into account when finally computing and correctly assessing the results.

Additionally, as an example, the scatter in figure 4.2 shows how the bins are built according to the H_s and T_p distribution for a wind speed range of 0 to 1 m/s.

In figure 4.2 two bins have been created giving a representation of the events that have the highest percentage of occurrence. Several values with low percentages are also spread over the scatter and have not been considered as their impact on the design conditions do

not affect much. So, the process ends up summing the bins content saying that they represent the events of the whole scatter. Again, this is just an approach of how to deal with this information where uncertainties are introduced. However, it is considered to be low enough having minimum impact on the results. With this, the reason why bins are created is due to the fact that computing all cases from a scatter would require a high computation demand and additionally, similar H_s and T_p combinations will end up having close stresses and moments on the GBS.

Percentage of ocurrence (%) - Peak Wave Period vs Significant Wave Height of all Data																									
Significant Wave Height [m]	5-6	0,000	0,000	0,000	0,000	0,000	0,000	0,000	0,000	0,000	0,002	0,007	0,000	0,000	0,002	0,000	0,000	0,0023	0	0	0	0	0	0	0
	4-5	0,000	0,000	0,000	0,000	0,000	0,000	0,000	0,009	0,043	0,039	0,043	0,014	0,000	0,025	0,064	0,002	0,0502	0,005	0	0	0	0	0	0	0
	3-4	0,000	0,000	0,000	0,000	0,000	0,007	0,025	0,395	0,294	0,242	0,260	0,392	0,021	0,468	0,333	0,005	0,1666	0,046	0	0	0	0	0	0	0
	2-3	0,000	0,000	0,000	0,000	0,018	0,737	1,476	5,670	1,492	2,165	2,400	3,931	0,128	2,482	1,113	0,005	0,3719	0,103	0,002	0,0023	0	0	0	0	0
	1-2	0,000	0,000	0,005	0,402	1,894	5,738	6,243	10,822	5,736	8,615	7,187	8,497	0,265	4,130	1,451	0,034	0,4518	0,062	0,007	0,0183	0	0	0	0	0
	0-1	0,002	0,018	0,274	0,673	0,169	0,516	0,566	2,608	1,832	2,654	1,458	1,647	0,027	0,675	0,180	0,005	0,0548	0,021	0	0	0	0	0	0	0,0046
		1-2	2-3	3-4	4-5	5-6	6-7	7-8	8-9	9-10	10-11	11-12	12-13	13-14	14-15	15-16	16-17	17-18	18-19	19-20	20-21	21-22	22-23	23-24	24-25	25-26
		Peak Wave Period [s]																								

Table 4.1: Wave Scatter Diagram for the whole spectrum 1980-2009

Percentage of ocurrence (%) - Peak Wave Period vs Significant Wave Height vs 0-1 [m/s]																										
Significant Wave Height [m]	5-6	0,000	0,000	0,000	0,000	0,000	0,000	0,000	0,000	0,000	0,000	0,000	0,000	0,000	0,000	0,000	0,000	0	0	0	0	0	0	0	0	0
	4-5	0,000	0,000	0,000	0,000	0,000	0,000	0,000	0,000	0,000	0,000	0,000	0,000	0,000	0,000	0,000	0,000	0	0	0	0	0	0	0	0	0
	3-4	0,000	0,000	0,000	0,000	0,000	0,000	0,000	0,000	0,000	0,000	0,000	0,000	0,000	0,000	0,000	0,000	0	0	0	0	0	0	0	0	0
	2-3	0,000	0,000	0,000	0,000	0,000	0,000	0,000	0,000	0,000	0,000	0,000	0,002	0,000	0,000	0,005	0,000	0	0,002	0	0	0	0	0	0	0
	1-2	0,000	0,000	0,000	0,000	0,000	0,000	0,000	0,025	0,030	0,023	0,018	0,018	0,000	0,005	0,000	0,000	0	0,002	0	0	0	0	0	0	0
	0-1	0,000	0,000	0,000	0,000	0,000	0,002	0,002	0,023	0,011	0,041	0,011	0,016	0,000	0,005	0,000	0,000	0	0	0	0	0	0	0	0	0
		1-2	2-3	3-4	4-5	5-6	6-7	7-8	8-9	9-10	10-11	11-12	12-13	13-14	14-15	15-16	16-17	17-18	18-19	19-20	20-21	21-22	22-23	23-24	24-25	25-26
		Peak Wave Period [s]																								

Table 4.2: Wave Scatter Diagram for a wind speed range of 0-1 m/s

			Bin 1		Bin 2		Bin 3		Bin 4		Bin 5		Bin 6					
Turbine Condition	Wind Speed Range (m/s)		Hs 1 (m)	Tp 1 (s)	Hs 2 (m)	Tp 2 (s)	Hs 3 (m)	Tp 3 (s)	Hs 4 (m)	Tp 4 (s)	Hs 5 (m)	Tp 5 (s)	Hs 6 (m)	Tp 6 (s)	Binned Percentage of Ocurrence (%)	Extrapolated Percentage of Ocurrence (%)	Total Percentage of Non-Operating Ocurrence (%)	Total Percentage of Operating Ocurrence (%)
Parked	0	1	0,5	10,5	1,5	9	-	-	-	-	-	-	-	-	0,22	0,239		
	1	2	1,5	17,5	1	14	1	11	0,5	8,5	-	-	-	-	2,04	2,248	6,21	93,79
	2	3	1	10,5	1	14,5	1,5	12	1	9	1,5	17	0,5	5,5	3,37	3,727		
Operating	3	4	1	14	0,5	10,5	0,5	9	1,5	17,5	0,5	7	-	-	5,27	5,819		
	4	5	2	17,5	1,5	14,5	1,5	12	1,5	9,5	0,5	6,5	-	-	6,23	6,885		
	5	6	1,5	7	2	14,5	1,5	12	1,5	9	-	-	-	-	9,04	9,988		
	6	7	1,5	17,5	1,5	7	2	14,5	1,5	12	0,5	9	-	-	10,81	11,943		
	7	8	1,5	17,5	1,5	7	2	14	1,5	11	1,5	9	-	-	9,74	10,756		
	8	9	3	17	1,5	7	2	15	1,5	11,5	1,5	8,5	-	-	11,69	12,914		
	9	10	3	17,5	1,5	6,5	2,5	14,5	2	11	1	8	-	-	10,96	12,102		
	10	11	3	17	1,5	7	2,5	14	2	11,5	2,5	8	-	-	8,35	9,224		
	11	12	3,5	17	1,5	6	2,5	14,5	2,5	12	2	8	-	-	5,88	6,495		
	12	13	3,5	17,5	3	14	2	7	3	12	2,5	8,5	-	-	3,69	4,078		
	13	14	4,5	17,5	3,5	14,5	3	7,5	3	11	2	8	-	-	1,86	2,051		
	14	15	3	11	3,5	14,5	2,5	7	3,5	8,5	2,5	8,5	-	-	0,87	0,965		
	15	16	3,5	17,5	4	15	3	8,5	3	12	-	-	-	-	0,319	0,353		
	16	17	1,5	12,5	4	15	3	8,5	3	12	1,5	8,5	-	-	0,110	0,121		
	17	18	5	11,5	4,5	9,5	1,5	9	-	-	-	-	-	-	0,039	0,043		
	18	19	5	10,5	2,5	11,5	1,5	10	-	-	-	-	-	-	0,021	0,023		
	19	20	5,5	11,5	4	9,5	4	9,5	1,5	6	-	-	-	-	0,011	0,013		
	20	21	2,5	14,5	1,5	7	-	-	-	-	-	-	-	-	0,009	0,010		
	21	22	2	12	-	-	-	-	-	-	-	-	-	-	0,002	0,003		
													Total		90,53	100,00		

Table 4.3: Whole range spectrum to be modelled

Therefore, knowing that n number of bins do not include all the probabilities that occur for

a given speed range, the following figure 4.3 is introduced. It has two percentage of occurrence columns where the binned one represents raw percentages from the scatters and the extrapolated column values are those that have been scaled-up from the binned one. This scale had to be made since, if all the raw bins from the scatters are summed, the result is not 100%. Therefore, a scale is then created where operating and non-operating wind turbine conditions are considered. From the whole spectrum, 90.54% represents 100% in the extrapolated column where in a 93.79% the turbine remains in the operating condition. Thus, a 6.21% represents a parked wind turbine condition.

So, in order to finish this section, figure 4.3 will be remodelled into 4.4 and 4.5 where some new columns had been added specifying the number of wave seeds as well as the final environmental wind speed.

Additionally, the following items describe some important criteria that has determined the selection of the 93 different environmental conditions affecting the GBS.

- **Several combinations with the highest percentage of occurrence for H_s and T_p**

  Largest probability of occurrence will lead to more repetitive loads and therefore more axial stresses presented in the location of study of the GBS.

- **Large values of H_s in combination with low T_p**

  Larger H_s values mean bigger waves, larger wind speeds, affecting the GBS and therefore, more damage.

- **Bins creation for low probabilities**

  In this situation, the combination of large H_s and T_p values with low probabilities of occurrence will also be considered. The response of the structure will be of considerably importance since the biggest waves will be affecting the GBS.

Turbine State	Condition Number	Hs [m]	Tp [s]	Wind Speed [m/s]	Probablity [%]	Numbers of Wave Seed	Extra Wave Seeds
Operational	1	1	14	3	1,16	4	2
	2	0,5	10,5	3,5	1,16	4	
	3	0,5	9	3	1,16	4	
	4	1,5	17,5	3,5	1,16	4	
	5	0,5	7	3	1,16	4	
	6	2	17,5	4	1,38	4	
	7	1,5	14,5	4,5	1,38	4	
	8	1,5	12	4	1,38	4	
	9	1,5	9,5	4,5	1,38	4	
	10	0,5	6,5	4	1,38	4	
	11	1,5	7	5	2,50	4	
	12	2	14,5	5,5	2,50	4	
	13	1,5	12	5	2,50	4	
	14	1,5	9	5,5	2,50	4	
	15	1,5	17,5	6	2,39	4	
	16	1,5	7	6,5	2,39	4	
	17	2	14,5	6	2,39	4	
	18	1,5	12	6,5	2,39	4	
	19	0,5	9	6	2,39	4	
	20	1,5	17,5	7	2,15	4	
	21	1,5	7	7,5	2,15	4	
	22	2	14	7	2,15	4	
	23	1,5	11	7,5	2,15	4	
	24	1,5	9	7	2,15	4	
	25	3	17	8	2,58	4	
	26	1,5	7	8,5	2,58	4	
	27	2	15	8	2,58	4	
	28	1,5	11,5	8,5	2,58	4	
	29	1,5	8,5	8	2,58	4	
	30	3	17,5	9	2,42	4	
	31	1,5	6,5	9,5	2,42	4	
	32	2,5	14,5	9	2,42	4	
	33	2	11	9,5	2,42	4	
	34	1	8	9	2,42	4	
	35	3	17	10	1,84	4	
	36	1,5	7	10,5	1,84	4	
	37	2,5	14	10	1,84	4	
	38	2	11,5	10,5	1,84	4	
	39	2,5	8	10	1,84	4	
	40	3,5	17	11	1,30	4	
	41	1,5	6	11,5	1,30	4	
	42	2,5	14,5	11	1,30	4	
	43	2,5	12	11,5	1,30	4	
	44	2	8	11	1,30	4	
	45	3,5	17,5	12	0,816	4	
	46	3	14	12,5	0,816	4	
	47	2	7	12	0,816	4	

Table 4.4: Binned environmental operational conditions for North-East Gran Canaria location

Turbine State	Condition Number	Hs [m]	Tp [s]	Wind Speed [m/s]	Probablity [%]	Numbers of Wave Seed
Operational	48	3	12	12,5	0,816	4
	49	2,5	8,5	12	0,816	4
	50	4,5	17,5	13	0,41	4
	51	3,5	14,5	13,5	0,41	4
	52	3	7,5	13	0,41	4
	53	3	11	13,5	0,41	4
	54	2	8	13	0,41	4
	55	3	11	14	0,193	4
	56	3,5	14,5	14,5	0,193	4
	57	2,5	7	14	0,193	4
	58	3,5	8,5	14,5	0,193	4
	59	2,5	8,5	14	0,193	4
	60	3,5	17,5	15	0,0882	4
	61	4	15	15,5	0,0882	4
	62	3	8,5	15	0,0882	4
	63	3	12	15,5	0,0882	4
	64	1,5	12,5	16	0,0242	4
	65	4	15	16,5	0,0242	4
	66	3	8,5	16	0,0242	4
	67	3	12	16,5	0,0242	4
	68	1,5	8,5	16	0,0242	4
	69	5	11,5	17	0,012	4
	70	4,5	9,5	17	0,012	4
	71	1,5	9	17,5	0,012	4
	72	5	10,5	18	0,0076	4
	73	2,5	11,5	18,5	0,0076	4
	74	1,5	10	18	0,0076	4
	75	5,5	11,5	19	0,0032	4
	76	4	9,5	19,5	0,0032	4
	77	4	9,5	19	0,0032	4
	78	1,5	6	19,5	0,0032	4
	79	2,5	14,5	20	0,005	4
	80	1,5	7	20,5	0,005	4
	81	2	12	21	0,0025	4
Non Operational	1	0,5	10,5	0,5	0,12	4
	2	1,5	9	0,5	0,12	4
	3	1,5	17,5	1,5	0,56	4
	4	1	14	1	0,56	4
	5	1	11	1,5	0,56	4
	6	0,5	8,5	1	0,56	4
	7	1	10,5	2	0,62	4
	8	1	14,5	2,5	0,62	4
	9	1,5	12	2	0,62	4
	10	1	9	2,5	0,62	4
	11	1,5	17	2	0,62	4
	12	0,5	5,5	2,5	0,62	4

Table 4.5: Binned environmental operational and non operational conditions for North-East Gran Canaria location

Chapter 5

Identification Tests

5.1 Decay Test

Decay tests are done in order to obtain important parameters for the damping estimation of a certain structure. Natural frequencies, added mass and damping ratios can then be analyzed and computed.

From SIMA software, one can obtain the decay results and process them with the help of MATLAB. The figures obtained here, 5.2 and 5.1 are the time domain representation of such decay tests. From these results, one can directly obtained the natural frequencies and the linear and quadratic damping from a cubic fit. However, SIMA also allows the possibility of using a post-processor where there is no need of implementing any external MATLAB code to compute the natural excitations.

In order to give value to the results obtained for the decay tests it should be focused on both the natural responses of the wind turbine structure (frequencies-periods) and the damping coefficients obtained in table 5.1.

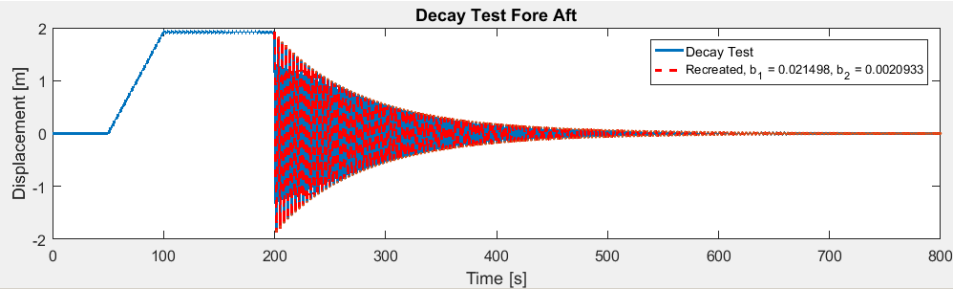

Figure 5.1: Decay Test Fore-Aft

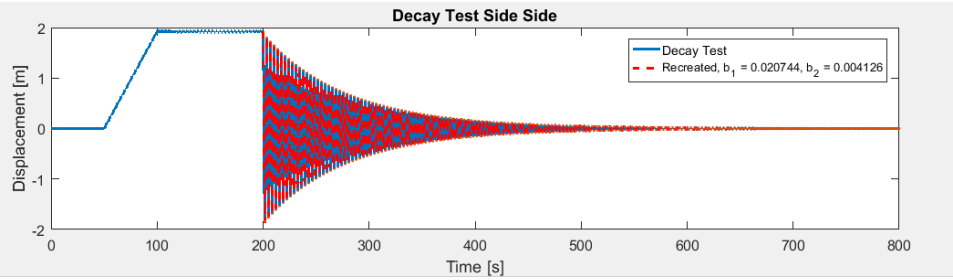

Figure 5.2: Decay Test Side-Side

Table 5.1: Decay Results for both motions

Motion	Fore-Aft	Side-Side
Natural Frequency [Hz]	0.2919	0.29
Natural Period [s]	3.426	3.448
Linear Damping [kg/s]	0.02149	0.02074
Quadratic Damping [kg/m]	0.00209	0.00413

Regarding the damping values one can separate between linear and quadratic damping. The following conclusions have been considered:

- Linear damping: These values, computed from potential theory, reflects the structural damping and therefore the waves radiated away from the structure. As seen in table 5.1, small values have been obtained reflecting the little affection of the GBS in the surrounding water due to its fixed design condition.
- Quadratic damping: The nonlinear, drag type, quadratic viscous damping obtained from Morison's equation, is not of high relevance for the GBS offshore wind turbine. Actually, the value obtained for the side to side motion reflects the aerodynamic damping effect on the quadratic term. From a physical perspective it can be explained why the fore-aft aerodynamic quadratic term is smaller than the side to side value. Considering that blades are feathered when performing the decay test, it is reasonable to think how, when moving from side to side, blades offer more resistance to the air than the fore-aft motions does. Therefore, this leads to more damping for the side to side motion.

5.2 Eigenvalue Analysis

As a support to the decay tests, a full eigenvalue analysis has been performed where both the eigenfrequencies as well as the eigenmodes have been computed according to the most relevant 10 values. As it can be observed, it exists a small difference between the two first eigenfrequencies regarding the decay tests results. This gap presented is not of high importance but it needs to be taken into account that the new computed 1st bending modes

are now closer to the low range of the 3P blade passing frequency. This, as already commented, can enhance the dynamic amplification.

Table 5.2: Full eigenvalue analysis result

Number	Mode	Natural Frequency [Hz]
1	1 st Side-Side Bending	0.3109
2	1 st Fore-Aft Bending	0.3135
3	1 st Fix-Free	0.6514
4	1 st Asymetric flap with yaw	0.6602
5	1st Asymetric flap with tilt	0.6685
6	1st Colective flap mode	0.9675
7	1st Assymetric edge 1	1.0368
8	1 st Assymetric edge 2	1.0561
9	2 nd Assymetric flap with yaw	1.8080
10	2ns Assymetric flap with tilt	1.8132

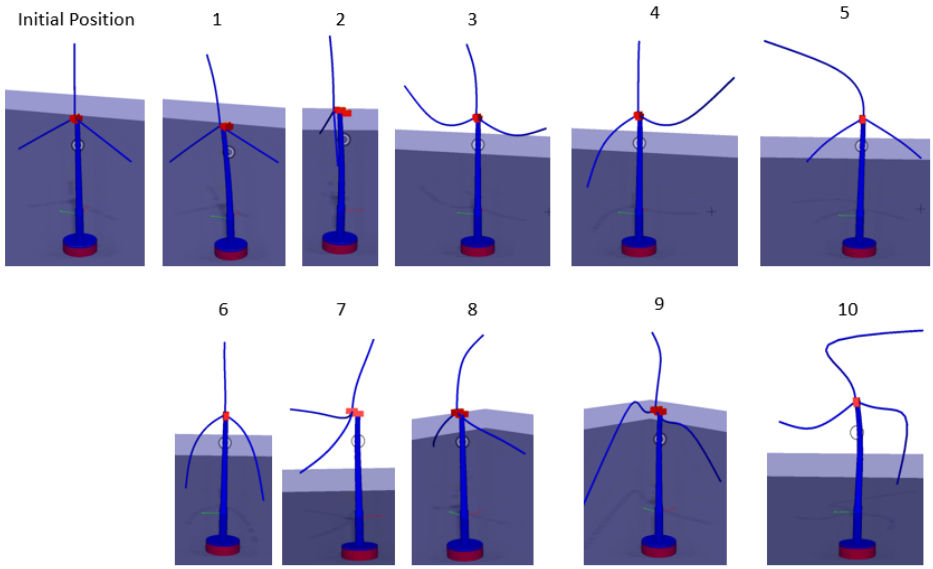

Figure 5.3: Mode shapes for every natural frequency of the OWT

5.3 Constant Wind test

The uniform constant wind test is characterized by minimal or practically zero change in the wind speed across the whole diameter of the wind turbine disc. Furthermore, neither vertical nor lateral speed variation is assumed and a constant wind speed is considered

throughout the entire running time. Therefore, the idea is to achieve a constant flow with small variations in mean wind speed in order to build the so-called wind turbine performance curve.

The idea of building up such curve is to gradually quantify the average values of important wind turbine inputs like mean rotor speed, mean thrust, mean torque, mean power and mean blade pitch. In the following figures, 5.5 and 5.6, the performance curves of the NREL 5 MW OWT are presented. Finally, while the wave environmental condition remains the same from the decay test (Hs = 0,001 [m] and Tp = 20 [s]), the wind speed here is varying from 4 to 24 [m/s] keeping constant its value for each run. Furthermore, the turbine condition changed from parked in the decay test to operational condition. Additionally, it also needs to be mentioned that, as it has been considered for the decay analysis, transients have been taken into account. Therefore, in order not to include non-steady values in the wind performance data, each output (Rotor Speed, Thrust, Torque, Power and Blade Pitch) has its own start time for data to be considered.

Finally, both the external, wind and waves spectrum, and the natural excitations of the GBS, must never be close enough or overlapping each other in order to avoid dynamic amplification or resonant behaviour. If any of the above situations happen, the computed stresses will significantly contribute to a much higher and faster fatigue damage. The effect of this event is then shown in figure 5.4, where if $\omega_{Excitation}/\omega_{Natural} = 1$, resonance happens.

This concept has been introduced here because the 1P as well as the 3P blade passing frequencies have been computed in this section and therefore, will be commented in the results.

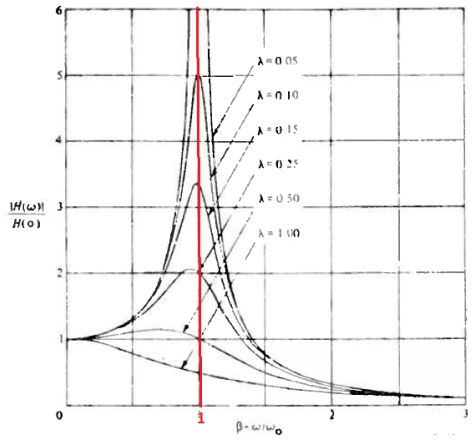

Figure 5.4: Dynamic load factor as a function of the frequency ratio [47]

Next table gives values of the different parameters needed to build the turbine performance curves shown in figures 5.5 and 5.6.

	Mean Values				
Wind Speeds [m/s]	Rotor Speed [Hz]	Thrust [kN]	Torque [kNm]	Power [kW]	Blade Pitch [deg]
4	0,120	122,13	273	195	0
6	0,133	237,96	984	777	0
8	0,155	394,11	2029	1871	0
10	0,194	611,25	3166	3646	0
11,4	0,202	658,97	4180	5000,1	1,69
12	0,202	580,99	4180	5000,3	3,86
14	0,202	458,73	4180	5000	8,21
16	0,202	394,57	4180	5000	11,38
18	0,202	353,48	4180	5000	14,07
20	0,202	324,83	4180	5000	16,50
22	0,202	303,82	4180	5000	18,74
24	0,202	288,00	4180	5000	20,84

Table 5.3: Wind Turbine Performance Results

From the results in table 5.3 and pictures 5.5 - 5.7 the following is observed:

- To verify if the constant wind test was performed correctly, the power generation output was compared to the given power generation for the wind turbine in figure 5.5. As it is defined for the thesis, a 5 MW OWT is considered and therefore, the obtained power value from the simulations indicates correct calculations when the speed is increasing from 4 to 24 [m/s].

- Due to an active pitch control, the turbine blades rotate around the blade center line when the wind speed increases. This is clearly identified in figure 5.6 where as soon as the wind speed is larger that 10 [m/s], the active pitch control starts acting.

  Therefore, the pitch control will allow the design point, assumed to be at the middle of the blade, to operate at optimal speed at any given wind speed. When the wind speed is low, the blades show the maximum area to the wind. However, when the wind speed approaches to the upper limit of the operational blade, the area is reduced to the minimum.

  Active control pitch offers a smoother start-up of the wind turbine, which means a smoother power output. Even though an electronic system is always acting to filter and adjust power output to grid frequency, it is always better to provide such equipment with minimum possible work.

- The design rated speed for the NREL 5 MW wind turbine is settled for 11.4 [m/s]. This is clearly seen in figures 5.5 and 5.6 where a turning point is present for such wind speed. Additionally, to give a representation in the time spectrum, one should check the appendix section in A.2.5 to see how the rotor speed, blade pitch angle, thrust, torque and power output vary on time. Therefore, the wind speed is divided into two groups where for higher speeds than the rated one the wind turbine will be fully loaded, and will be partially loaded when facing lower winds than 11.4 [m/s]. On the one hand, it can be mentioned how the generator power, mean rotor speed, and mean generator torque are increasing until the rated speed is achieved. Once

there, all the values can be considered as constant. On the other hand, it can also be seen how the mean thrust start to decrease once the rated speed is achieved while the power output is kept constant.

- In figure 5.7, both the excitation from the wind (1P and 3P), reflected in the angular rotor speed, and the natural frequencies from the 1st fore-aft and side-side bending moment are presented. It can be seen how resonance will not happen due to a proper distribution of both the natural frequencies and excitation loads along the frequency spectrum. Differently from monopiles, the GBS's natural frequencies are further from both blade passing ranges meaning that dynamic amplification will not be an important issue at least from now. Later, frequency spectrums will determine whether or not dynamic amplification will need to be taken cared of.

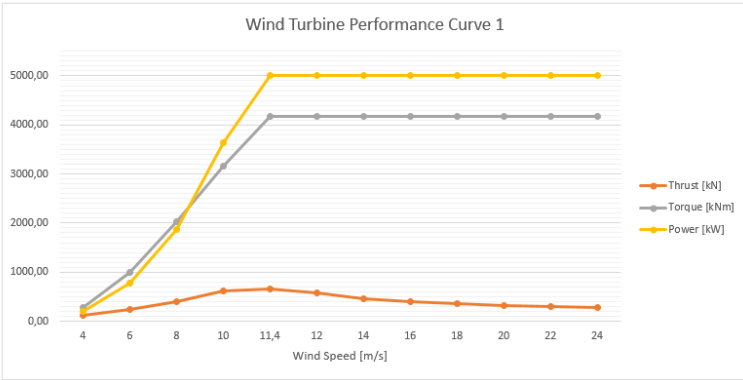

Figure 5.5: Wind Turbine Performance Curve 1

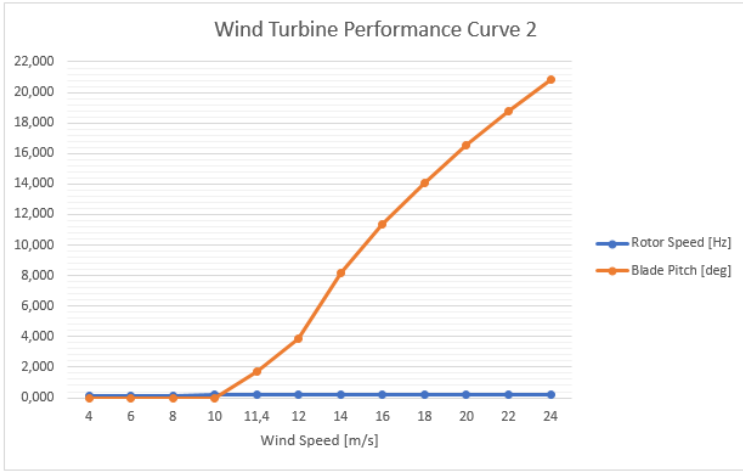

Figure 5.6: Wind Turbine Performance Curve 2

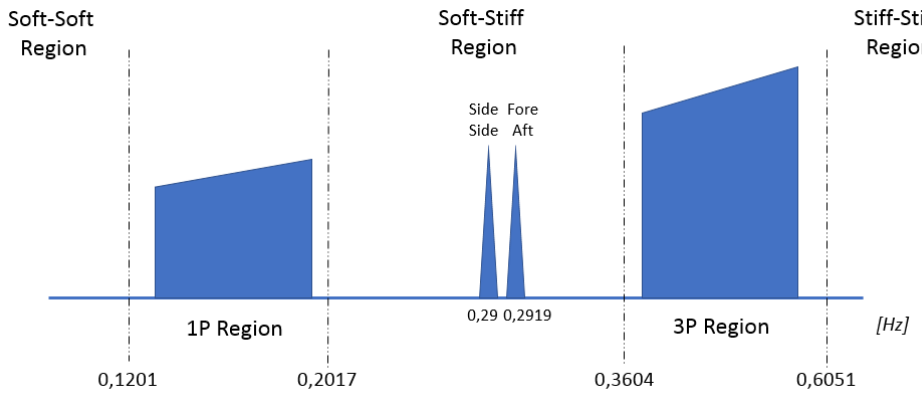

Figure 5.7: Natural and Blade Passing Frequencies (1P-3P)

5.4 General Spectrum Analysis

The spectral analysis is performed to analyze the different excitation frequencies that affect the structure in study. As already mentioned, excitation and natural frequencies must never be together or even close in order to avoid resonance effect or dynamic amplification. The excitation frequencies to be described here are the 1P and 3P, from the 1 blade passing and from the 3 blades passing frequency respectively and those coming from the wind and waves.

Therefore, the following analysis will be done to place and identify all these external excitations in a bending moment spectrum. As part of my project, I am in need and it is of big interest to know what effects or combination of them make my structure to bend. The computed axial stresses obtained, during a time domain simulation at different points of the GBS, are the result of the combination of bending moments and axial forces as stated in equation 6.26.

- **1P and 3P excitation frequency:** As already introduced in 5.3, 1P and 3P excitations are from the 1 blade full rotation frequency and from 3 passing blade frequency respectively. So having a 1P range of 0,1201-0.2017 [Hz] and a 3P range of 0,3604-0,6051 [Hz], see figure 5.7, it has already been verified how the natural frequencies (side-side and fore-aft) placed in the middle of both blade passing ranges, do not produce any overlapping situation.

- **Wave Excitation:** Depending on what condition it is analyzed, the wave spectrum varies for a different Tp value. Due to wave characteristics, a spread and wide spectrum is considered without noticeable peaks in the spectrum shape. In our spectral analysis, condition 58 from 4.5 will be analyzed with a T_p = 8.5 [s] and a H_s = 3.5 [m]. Therefore, in figure 5.8 we will expect to see same waves effect around 0,117 [Hz].

- **Wind Excitation:** Wind excitation offers the lowest frequency values in the spectrum. As it will be seen in figure 5.8, such values are found in a frequency range from 0 to 0.05 [Hz] approximately, being quite far from the first fore-aft and side-side natural frequencies. Again no overlapping issue is considered. It is obvious that the higher effect is shown in the Y bending moment since the wind is always coming in the fore-aft direction.

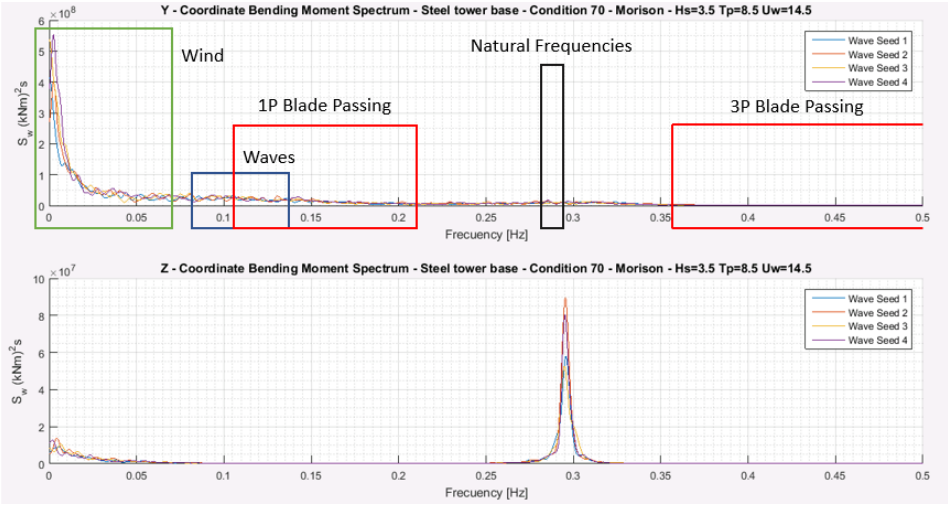

Figure 5.8: Bending Moment's Spectrums for condition 58 in 4.4

Therefore, from figure 5.8 the analysis of the spectrum results can be divided in:

- **Bending Moment Spectrum Y Coordinate:** As expected, wind effect is quite noticeable for this bending moment. Y axis rotation reflects the bending of the structure in the fore and aft direction where the wind is able to have more influence. Additionally, waves effect can also be appreciated around 0.12 [Hz] with a more spread spectrum than the wind one. Finally, some dynamic amplification can be found around 0.29 [Hz], where the natural frequency is located. However, the value is negligible since wind effects are notably much higher.

- **Bending Moment Spectrum Z Coordinate:** In this side-side mode, wind is much less important with a maximum peak around $10^7[kNm^2s]$ in contrast with $5.5 \cdot 10^8[kNm^2s]$ offered by the fore-aft spectrum. Obviously, this was expected since the wind is always flowing in a fore-aft direction. Additionally, waves are not relevant since no spectrum is appearing at a T_p = 8.5 [s] because both the study point is the tower base located at 5 [m] above the still water level and because waves are also coming from that fore-aft direction. However, the most relevant information is the clear dynamic amplification shown around 0.29 [Hz], where the natural frequencies have been computed. Here, it is not clear what external source is producing the

amplification effect since neither from the left not the right of 0.29 [Hz] a clear spectrum is shown. It can only be guessed that according to figures in the appendix, see A.2.4, the dynamic effect is produced from the waves as it happens in the idle status for Y bending moment spectrum. Nevertheless, since this mode does not offer much information about how the external sources are related to it, no clear conclusions can be drawn.

With this analysis it should be concluded that the natural frequency of the GBS gives relevant results in the spectrum analysis due to the high stiffness of the structure. Therefore, one could think on the idea of shifting the natural frequency, by design procedures, in order to move away the natural frequency from the low 3P range that is causing the amplification effect. Therefore, with this is mind, the following figure is introduced being a modification and extension of 5.7.

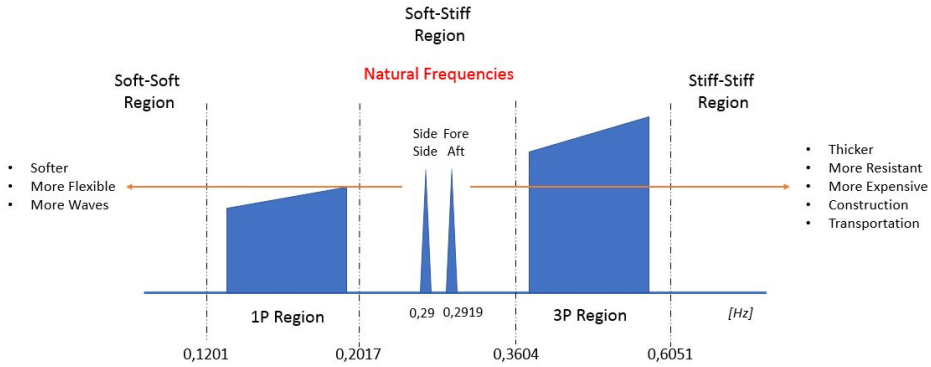

Figure 5.9: Natural frequency shifting procedure

So, according to figure 5.9, two ways are presented for the natural frequency to be shifted. The following is conclude:

On the one hand, if the design is shifted to the left a more flexible and softer structure is obtained. This means that both the diameters as well as the thicknesses will be notably reduced. Taking this into account we should keep in mind that even reducing the amount of steel of the wind turbine structure, and the concrete on the GBS there will still be present a high mass on the top of the OWT containing all the equipment of the nacelle as well as the blades' weight. This leads to a position where buckling can occur in the tower due to the fact of not having introduced the enough amount of steel. Furthermore, more waves are to be present at lower frequencies that, afterwards, will structurally compromise the OWT.

On the other hand, the design can be shifted to the right where a much thicker, heavier and more resistant model can be obtained. However, there is a big compromise with the economical aspect, where due to the high amount of steel and concrete, the design will end up to be quite expensive and not profitable at all considering the 20 years expected

operating life. Furthermore, installation as well as transportation requirements should be met, and having a really heavy structure does not make this process easy at all.

Therefore, one can end up concluding that none of the above shifting ideas can be of a great help when trying to modify the natural frequency value of the wind turbine. However, we could say, not being wrong, that the design problem can be reduced by only considering the diameters of the structures, thicknesses and lengths of both the GBS and the wind turbine's tower. With this in mind, the design principle becomes quite simple to establish but ends up in a complex problem to solve.

Chapter 6

Hydrodynamic Models

In this section, the hydrodynamic models presented in 2.3.1 will be tested and analyzed. One of the main ideas is to compare the results from the different theories to see how different or similar they are from each other. Normally, Morison's equation is applied on slender pipes in order to obtain the loads acting on the structure. However, as relatively big diameters are now present for the shaft and caisson, 7 and 31 [m] respectively, other hydrodynamic models should be kept in mind (MacCamy&Fuchs and potential flow) in order to properly estimate the hydrodynamic loads. As it has already been mentioned, Morison will overestimate the loads if wave diffraction happens and MacCamy&Fuchs will not correctly model the flow around the caisson. Therefore, this means that potential flow will need to be considered.

6.1 Integrated Force

In this section, the integrated force in the whole GBS will be computed and compared between the three hydrodynamic models already mentioned in 2.3.1. For each frequency, the amplitude of the force will be presented where linear and regular waves are applied. The whole wave period will cover 26 [s] with steps of 1 between them and a wave amplitude of 1 [m] will be considered for simplicity reasons. Finally, while Morison (Finite and infinite waters) and MacCamy&Fuchs will be analytically analyzed, potential flow results will be obtained through HydroD software.

As mentioned, the total Morison and MacCamy&Fuchs integrated force will be analytically computed. Both, the wave kinematics for regular waves, with periods described in previous paragraph, and the inertia forces, will be calculated with MATLAB. It must be stated that only the inertia term will be taken into account in Morison equation since the comparison will be done regarding potential flow and MacCamy&Fuchs theories.

Here, MacCamy&Fuchs will be displayed in terms of a frequency-dependent C_M value, slightly different as it was previously presented in 2.3.1. According to [31], and applying the general formula for the inertia force in equation 6.1, the following is developed:

$$dF_1 = C_M \rho V \frac{\partial u}{\partial t} \tag{6.1}$$

Where:

- ρ : Water density $[kg/m^3]$
- V : Volume applied
- $\frac{\partial u}{\partial t}$: Water particle acceleration $[m/s^2]$
- C_M : Mass coefficient (Frequency dependant value)

$$C_M = \frac{4G(\frac{D}{\lambda})}{\pi^3(\frac{D}{\lambda})^2} \tag{6.2}$$

  Where:

  - D : Cylinder diameter [m]
  - λ : Wave length [m]
  - $G(\frac{D}{\lambda})$: Function including Bessel functions of first and second kind (J and Y respectively) and their derivatives (J' and Y').

$$G\Big(\frac{D}{\lambda}\Big) = \frac{1}{\sqrt{J_1'(ka)^2 + Y_1'(ka)^2}} \tag{6.3}$$

Therefore, equation 6.1 turns into equation 6.4 after same manipulation. It must also be mentioned that as the amplitude is the only interested term at the moment, the $cos(\omega t - \alpha)$ term can be ignored.

$$dF = \frac{\rho \lambda^2 \omega^2 \zeta_a}{\pi^2} \frac{coshk(z+h)}{kcoshkh} G\Big(\frac{D}{\lambda}\Big) \tag{6.4}$$

6.1.1 Results

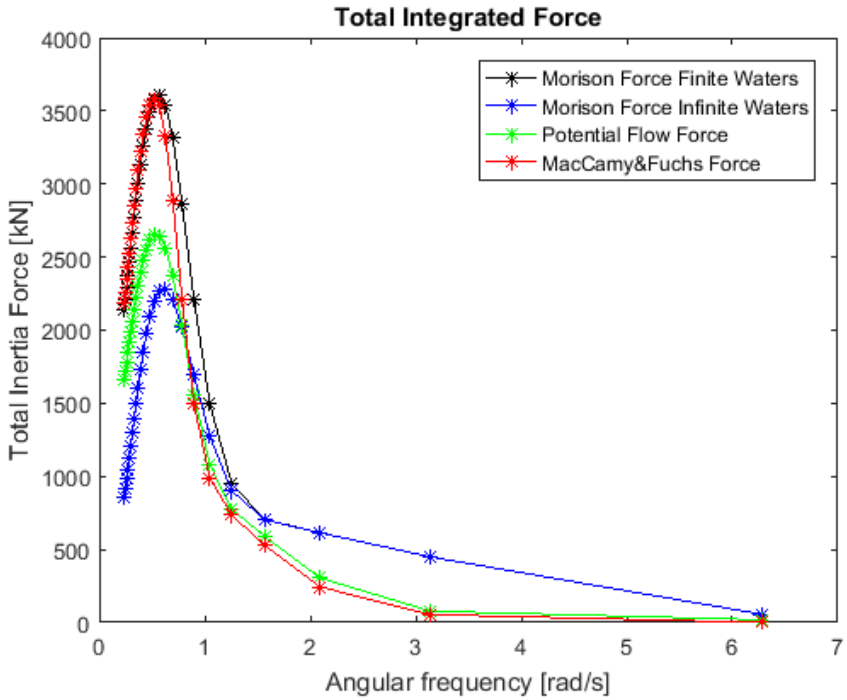

Figure 6.1: Total Integrated GBS force

Results from figure 6.1 can be divided into two groups. On the one hand, the 3 methods reveal similar force patterns for long waves, small frequencies, until 1.5 [rad/s]; such values were expected. On the other hand, when moving to shorter waves, larger frequencies, Morison results are located over the potential flow and MacCamy&Fuchs outputs. Additionally, it exists a clear jump between Morison and the two other theories from 1.5 [rad/s] onwards that looks quite reasonable. Therefore, as it was expected, all theories' work pretty well at very low frequencies, long waves, but have a much worse agreement at shorter periods.

Additionally, figure 6.2 must be introduced. As it can be observed, a similar pattern is obtained when comparing this with figure 6.1. This is due to a correction effect induced by the wave diffraction. As it has been developed in 2.3.1, Morison is computed for submerged members that do not affect the waves. However, when considering a shaft diameter of 7 [m] and a caisson of 31 [m], Morison must be corrected reducing the magnitude of the inertia component. As reflected in both figures, the C_M parameter is reduced when increasing the D/λ ratio.

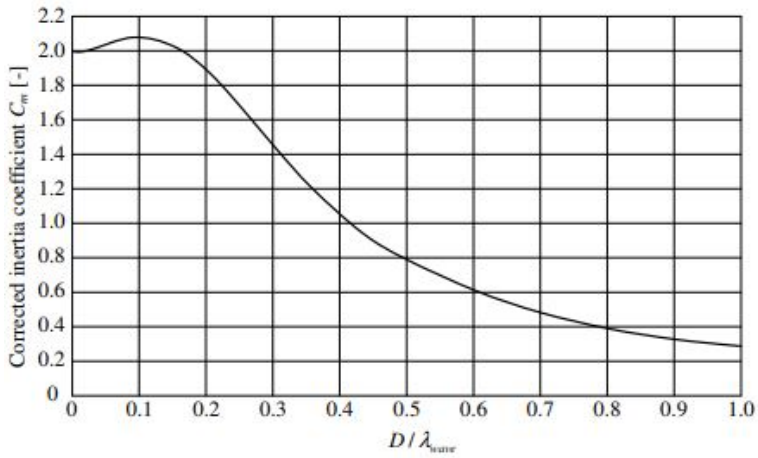

Figure 6.2: MacCamy&Fuchs diffraction correction of the inertia coefficient C_M in the Morison equation for cylinder over wave length [62]

6.2 Dynamic Sectional Loads - Potential Flow

In this subsection, the load distribution will be computed for certain nodes placed along the GBS as shown in figure 6.3. Additionally, table 6.1 shows how this nodes have been distributed along the GBS with their identification code provided by the HydroD software. The reference height is considered from the seabed, being the waterline established at + 35 [m].

The idea of performing this sectional computation is to obtain the first order wave transfer function, added mass and damping values for every node of the GBS. This will be done employing the HydroD and WAMIT softwares using potential flow theory. Afterwards, the obtained results will be used to create the potential flow model in SIMA, whose implementation will be fully presented in subsection 6.3. The aim is to perform a prior fatigue assessment, including the three hydrodynamic models, to establish if it exists a real gap between them and to determine how big the difference is. This is done to decide if it is worth doing the effort of performing a full fatigue assessment for every hydrodynamic model or just for the theory that suits better.

Table 6.1: Nodes description for sectional loads

Node Number	Node Height [m]	HydroD Node Identification
1	0	301
2	2	302
3	4	303
4	6	304
5	8	305
6	10	306
7	12	307
8	14	308
9	16	309
10	18	310
11	20	311
12	22	312
13	24	313
14	26	314
15	28	315
16	30	316
17	32	317
18	34	318
19	35	319

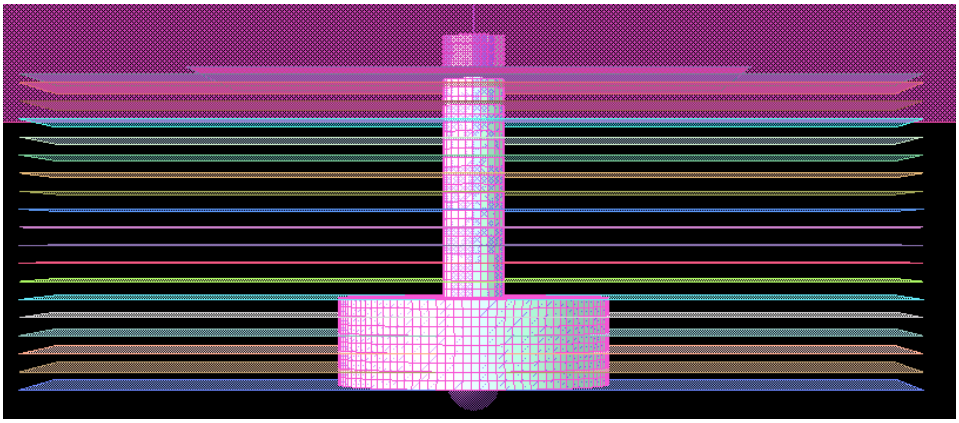

Figure 6.3: Load cross sections distribution

6.2.1 Results

HydroD Results

The results presented in figures 6.4 to 6.9 have been obtained from HydroD once the load cross sections has been established as shown in figure 6.3. So, the forces have been plotted in [kN] against the angular frequency in [rad/s] in the following plots.

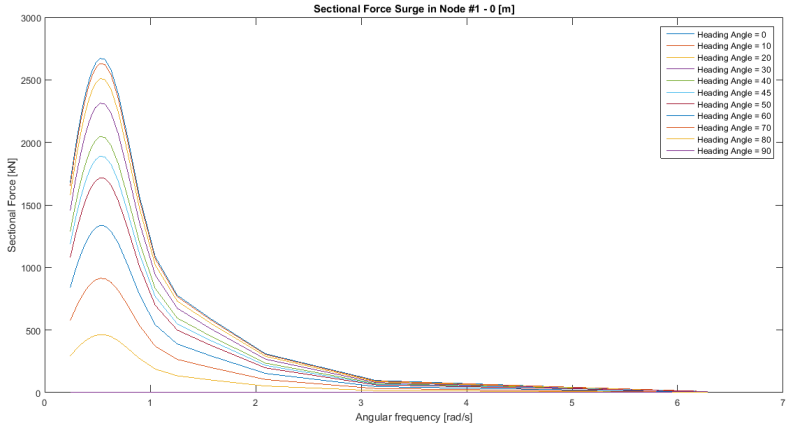

Figure 6.4: Node 1 - Sectional Force in Surge Distribution

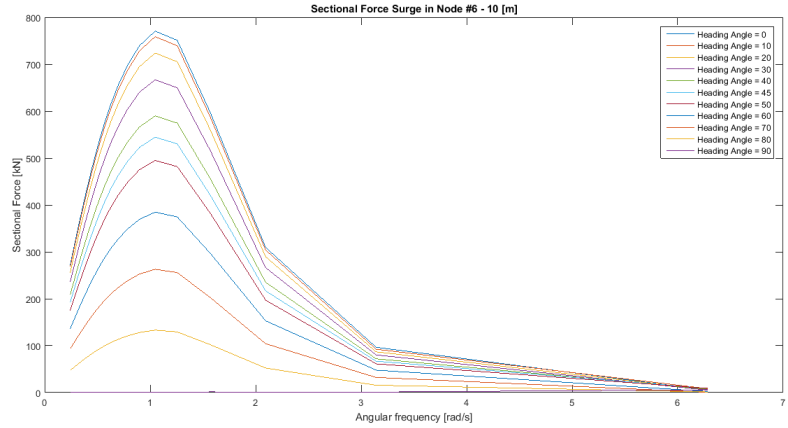

Figure 6.5: Node 6 - Sectional Force in Surge Distribution

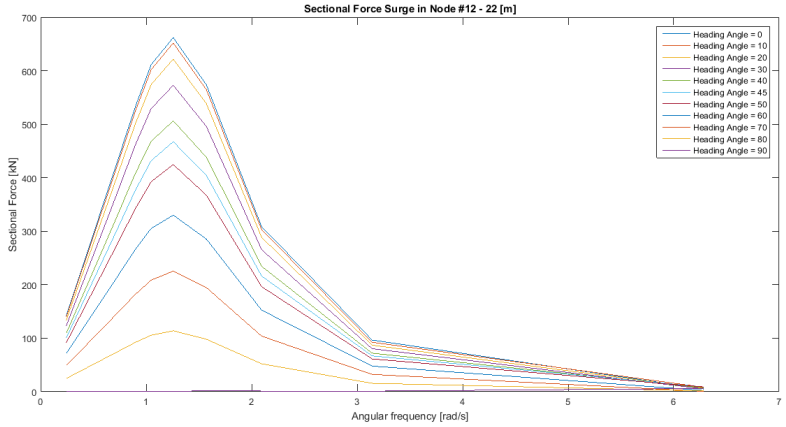

Figure 6.6: Node 12 - Sectional Force in Surge Distribution

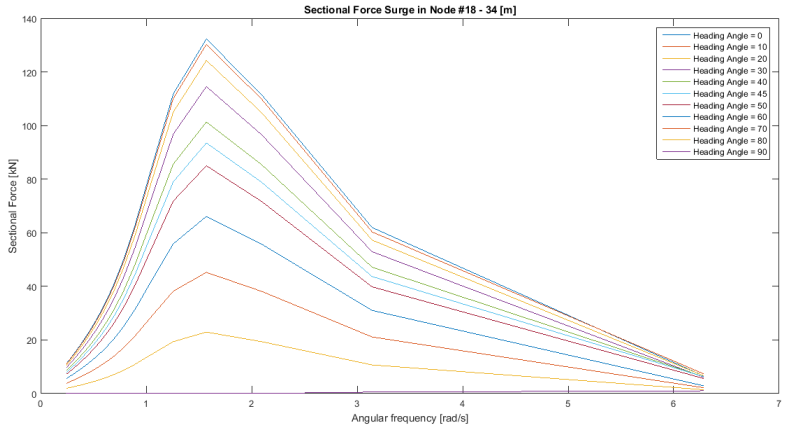

Figure 6.7: Node 18 - Sectional Force in Surge Distribution

From figure 6.4 to 6.9, the force distribution for the surge motion is shown for the nodes with number 1, 6, 12, 18 and 19 which means 0, 10, 22, 34 and 35 [m] above the seabed respectively, see table 6.1. The first two points refer to the bottom and top of the caisson, while the other 3 refer to half of the submerged shaft, 1 [m] below the waterline and exactly in the waterline respectively.

As it can be observed, the graphs show reasonable good results since the maximum values are always obtained for the 0 degrees and the minimum ones for the 90 degrees wave heading angle for the surge motion. However, to also check that the model is giving the right response, figure 6.8 shows the response for node 18 in sway motion. As it can be

checked, the results for sway are the same as for surge but now 90 degrees give the highest value while 0 accounts for the lowest. Additionally, as expected, the largest excitations are located at the bottom of the GBS while at the water surface such force distribution is reduced to 0 [kN].

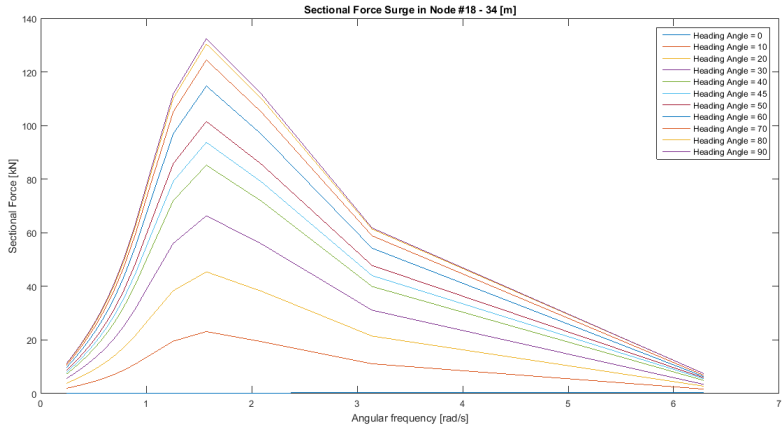

Figure 6.8: Node 18 - Sectional Force in Surge Distribution

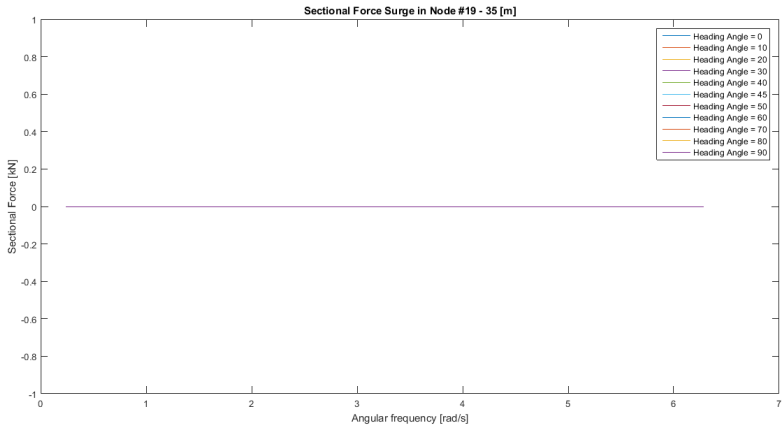

Figure 6.9: Node 19 - Sectional Force in Surge Distribution

Finally, if we summed up all the sectional forces contributions for the surge motion, the one we are mostly interested in, the integrated total force would be computed as it was previously done, analytically, in figure 6.1.

WAMIT Results

As mentioned, WAMIT results from potential flow theory have also been plotted. Applying the panel method procedure, figure 6.10 to 6.18 shows the first order wave excitation forces, radiation damping and added mass components for every panel for the most relevant motions of study (surge, heave and pitch). According to the results, it must be stated that surge and sway would give practically the same results if the first motion, X_1, had been computed for 0 wave heading angle and sway for 90 degrees wave heading angle. This is also applied to pitch and roll where the same phenomena is happening. Finally, while heave is interesting since it is crucial for the GBS to remain on a vertical position, yaw is not relevant in this study.

Whole Structure Results

In this part of the assessment the structure has been considered as a whole. This means that the total added mass, first order wave excitation forces and radiation damping results have been computed summing up all the panels that define the structure. As known from theory, the first order potential solution solves the diffraction pressure and linear radiation. So, the frequency dependant parameters, added mass and wave excitation can be obtained from the radiation and diffraction pressure respectively.

From figures 6.10 and 6.11 it must be firstly pointed out that two plots have been created for every studied motion. On the one hand, the blue dashed line refers to the GBS as a distributed solid where the sum of the bodies ends up building the whole structure. On the other hand, the continuous green one refers to the GBS as a whole structure.

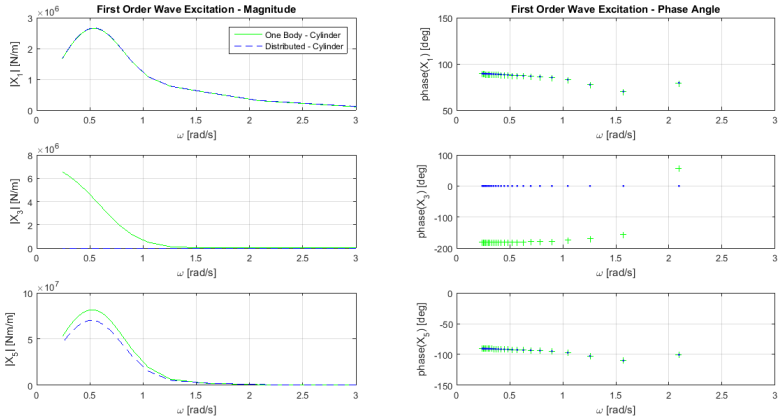

Figure 6.10: First order wave excitation forces - Magnitude and Phase angles for Surge X_1, Heave X_3 and Pitch X_5

So, figure 6.10 reveals good results since according to [54] the magnitude parameter goes

to zero for low and high frequencies except for the heave motion that stars at high values. Here, only 0 degrees of wave heading has been chosen since this has been the general approach during the GBS design. All waves have been considered in one direction. Additionally, it can be observed how the maximum value for the first order wave excitation is obtained around 0.5 [rad/s] for both surge and pitch. Maximum in heave is obtained at approximately 0.25 [rad/s].

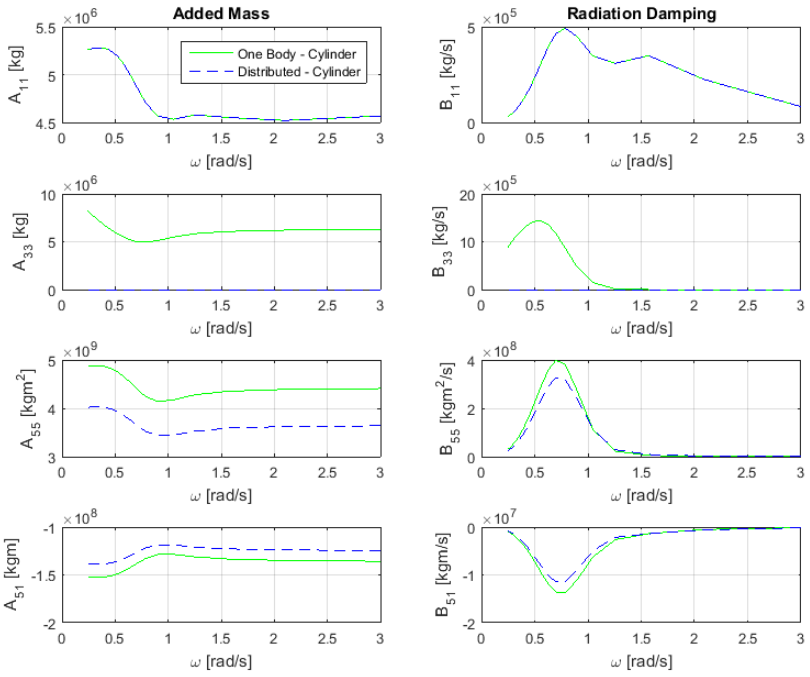

Figure 6.11: Added mass and Radiation Damping for Surge X_1, Heave X_3, Pitch X_5 and Combined X_{51}

The plotted results in figure 6.11 refers to the 6 by 6 added mass and linear radiation damping, A_{66} and B_{66} respectively. On the one hand, from added mass results it can be concluded that mostly surge and heave motion show a frequency dependence behaviour. However, pitch and A_{51} motion reveal a reasonably constant value in the whole frequency. On the other hand, the linear damping shows a much stronger frequency dependence with a maximum value around 0.75 [rad/s] for every studied motion. As stated in [59] and checked in [54], good results have been found since the radiation damping results approach to zero for both low and high frequencies. It is important to know that at very low or high frequencies the energy is not carried away since body oscillations do not create surface waves.

Finally, it should be mentioned that in both figures 6.10 and 6.11, the results for surge should be exactly the same but some small differences have been found at high frequencies. However, the results for pitch are not expected to be equal since all the possible elements that can compose the GBS have not been chosen when modelling. As already mentioned before, the more elements used, the higher the accuracy. So, employing the panel method theory, it must be mentioned that the values of pressure and velocities have been obtained at the middle of every element what in practice introduces some important errors since those elements belong to a whole big section.

Sectional Loads on the GBS

Differently as for the whole structure, now the hull has been sliced into different sections as already explained in 6.2. Therefore, the total hydrodynamic loads can be obtained for every section applying the panel method theory. This means that the sum of the loads in the panels where a section is defined, will give the total hydrodynamic force for that section.

Here, taking as reference [59], the description of how the implemented algorithm computes the hydrodynamic loads for every section will be done. As written before, the sum of the loads in the panels where a section is defined, will give the total hydrodynamic force for that section. This means that the added mass, linear damping and wave excitation forces will be computed for every section according to the affected panels, as shown in equations 6.5, 6.6 and 6.7.

$$A_{section} = \sum_{n=1}^{N} A_{panel} \tag{6.5}$$

$$B_{section} = \sum_{n=1}^{N} B_{panel} \tag{6.6}$$

$$X_{section} = \sum_{n=1}^{N} X_{panel} \tag{6.7}$$

Therefore, employing a MATLAB script, provided by the supervisor, the pressure components from a WAMIT output file (WAMIT OPTN.5P) can be used to compute the hydrodynamic coefficients. They will be obtained by integrating the pressure from the diffraction and radiation potentials. This means that the radiation pressure can be obtained as shown in equation 6.8.

$$p_i = \omega^2 \rho \xi_i \phi_i \tag{6.8}$$

Where:

- ω: Angular frequency

- ρ: Water density
- ξ_i: Unit motion
- ϕ_i: Velocity potential

So, firstly considering that the radiation damping, B_{ij}, and added mass, A_{ij}, can be obtained from the radiation potential integration over the wetted surface, equation 6.9 is considered. Within this, if equation 6.8 is substituted in 6.9, the radiation damping and added mass coefficients can be written in terms of the pressure from radiation potential as shown in equation 6.10. Within this, the excitation forces can be described in terms of pressure according to the diffraction potential as shown in 6.11.

$$A_{ij} - \frac{i}{\omega} B_{ij} = \rho \iint_{S} {}_{B}\phi_i n_i dS \tag{6.9}$$

$$A_{ij} - \frac{i}{\omega} B_{ij} = \rho \iint_{S} {}_{B}\phi_i n_i dS = \frac{1}{\omega^2} \iint_{S} {}_{B} n_i \frac{p_i}{\xi_i} dS \tag{6.10}$$

$$X_i = -i\omega\rho \iint_{S} {}_{B} n_i \phi_D dS = \iint_{S} {}_{B} n_i p_D dS \tag{6.11}$$

As mentioned, the WAMIT OPTN.5P file is used since it contains non-dimensionalized parameters like the diffraction, $\bar{p_D}$, and the radiation pressure, $\bar{p_i}$ each panel. So, if the non-dimensional pressure is employed, the non-dimensional excitation, added mass and damping will be computed. As reflected in [59] the following non-dimensional parameters from equation 6.12 to 6.16 are shown.

$$\bar{p_i} = \frac{p_i}{\rho g \xi_i L^n} \tag{6.12}$$

$$\bar{p_D} = \frac{p_D}{\rho g Area} \tag{6.13}$$

$$\bar{A_{ij}} = \frac{A_{ij}}{\rho L^k} \tag{6.14}$$

$$\bar{B_{ij}} = \frac{B_{ij}}{\rho L^k \omega} \tag{6.15}$$

$$\bar{X_i} = \frac{X_i}{\rho g Area L^m} \tag{6.16}$$

Where:

- $Area$: Area of the panel.
- L: Non-dimensional WAMIT length.

- m, n and k depends on the i and j indices, described as:

  On the one hand, k is influencing the damping and added mass coefficients varying with j and i as shown in figure 6.12.

		j					
		1	2	3	4	5	6
i	1 2 3	**k = 3**			**k = 4**		
	4 5 6	**k = 4**			**k = 5**		

Figure 6.12: Variation of k parameter according to i and j [59]

  On the other hand, m influences the excitation coefficients varying with i and n is related to the radiation pressure according to j. This is exemplified in figure 6.13.

i	1 2 3	**m = 2**
	4 5 6	**m = 3**

j					
1	2	3	4	5	6
n = 0			**n = 1**		

Figure 6.13: Variation of m and n parameters according to i and j respectively [59]

Before computing the hydrodynamic sectional loads, the hydrodynamic coefficients will be firstly obtained with the MATLAB code. This means that the low-order panel method will be employed where the potential is considered constant on each panel. Therefore, this results in the excitation, linear damping and added mass coefficients exemplified in equations 6.10 and 6.11:

$$A_{ij,panel} - \frac{i}{\omega} B_{ij,panel} = \frac{1}{\omega^2} Arean_i \frac{p_i}{\xi_i} \tag{6.17}$$

$$X_{i,panel} = Arean_i p_D \tag{6.18}$$

Finally, the total hydrodynamic loads are computed from equations 6.5 to 6.7 for all the panels affecting each section. As described before, the sectional loads will be introduced

in SIMA through SIMO bodies where the total hydrodynamic loads will be attached to them. Such SIMO bodies have been specifically distributed according to the same nodes height as described in 6.2 and have been attached to the RIFLEX elements discribed in 3.2.6.

So, talking about results, it should be mentioned that in order to have a clear idea of what it is being plotted in the following figures, the general plot with all the sectional components, see 6.3, has been divided into two groups. First group refers to 8 depths from -35 to -19 [m] and the second one alludes to depths from -17 to -1 [m], being the still water line the reference point. This is done to give a much cleaner and simpler way to read the sectional results.

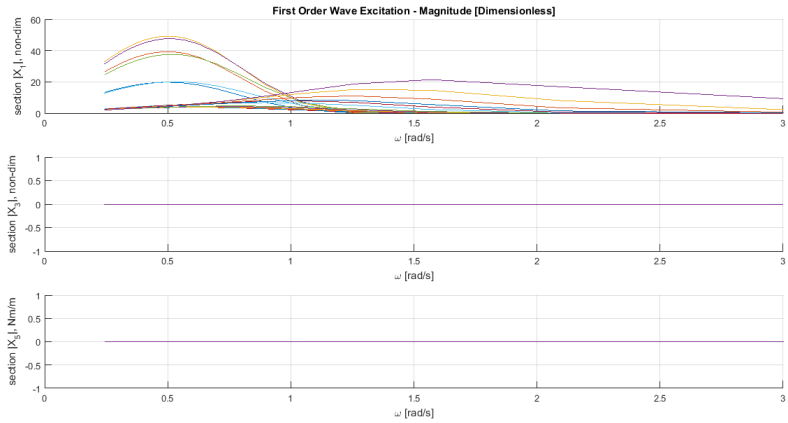

Figure 6.14: Non Dimensional First order wave excitation forces for Surge X_1, Heave X_3 and Pitch X_5

From 6.14 to 6.21, it can again be said that the sectional wave excitation forces and linear damping values tend to zero in the low and high frequency zones. Within this, it can also be observed how the maximum value for each section is given for a certain frequency according to the first order wave excitation forces, linear damping and added mass coefficients.

For the first order wave excitation, the maximum value for the first group, -35 to -19 [m], is given for around 0.5 [rad/s]. However, if the depth is decreased, the maximum value is shifted to approximately 1.5 [rad/s] in figure 6.16; meaning that the larger the depth the lower the frequency at which the maximum value is given. Additionally, the highest force is obtained at larger depths with a peak in figure 6.15 of approximately 50 [-]. However, such magnitude gets decreased at around 2.5 [-] and increase again when decreasing the depth until approximately 22 [-] in figure 6.16. This means that the influence of the change in diameter is quite noticeable since the magnitude of the wave excitation force gets modified when moving from the shaft to the caisson of the GBS and from deep to shallow

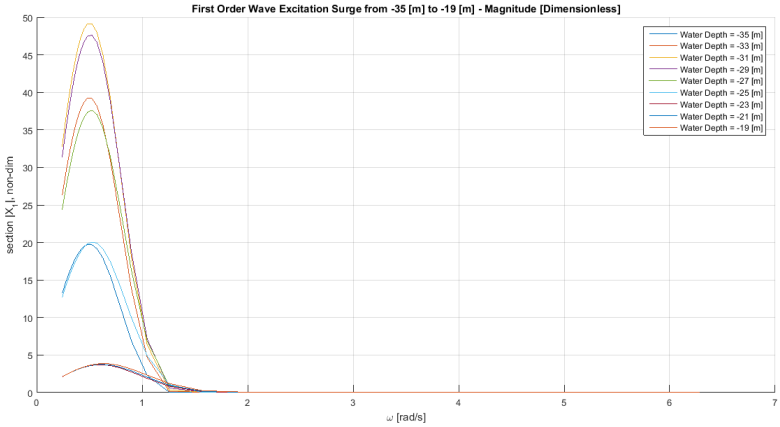

Figure 6.15: Non Dimensional First order wave excitation forces for Surge X_1 from -35 to -19 [m] of water depth

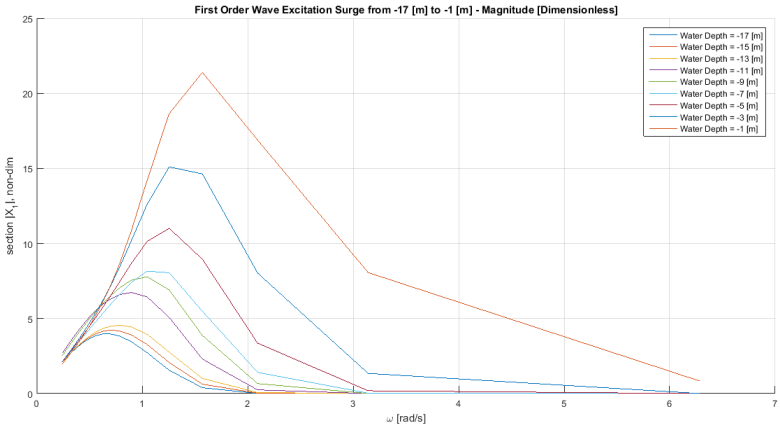

Figure 6.16: Non Dimensional First order wave excitation forces for Surge X_1 from -17 to -1 [m] of water depth

waters.

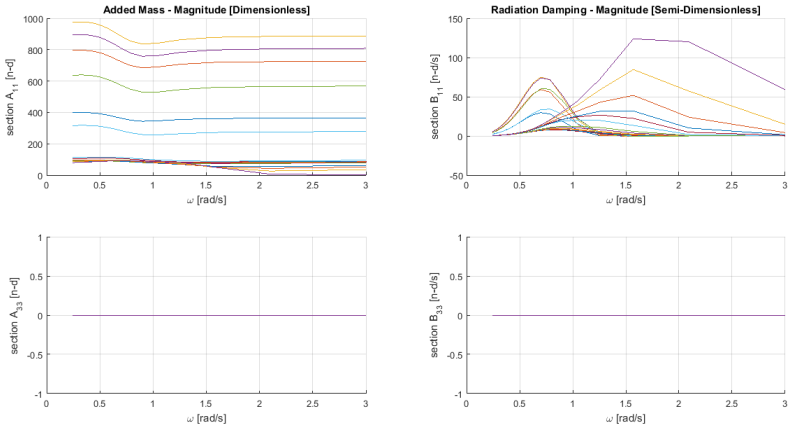

Figure 6.17: Non Dimensional Added Mass and Radiation Damping for Surge X_1 and Heave X_3

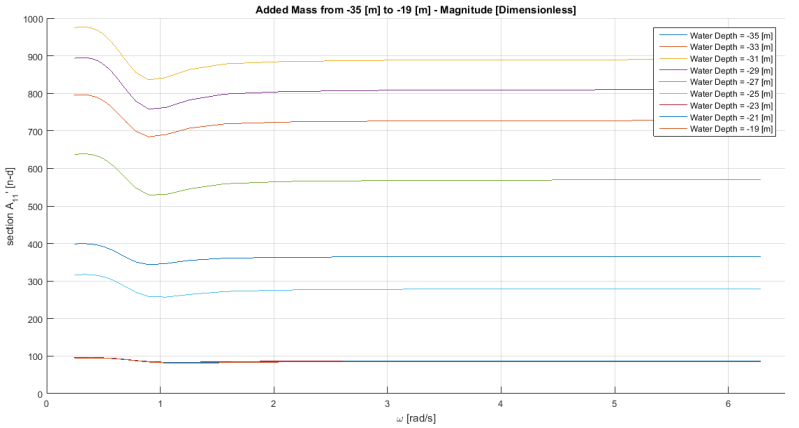

Figure 6.18: Non Dimensional Added Mass for Surge X_1 from -35 to -19 [m] of water depth

Regarding the added mass magnitude, this one is increased from shallow to deeper waters. On the contrary, such maximum value for every section gets shifted from 1 to 3 [rad/s]. Again, the frequency dependence for the surge motion is clearly stated in figures 6.19 and 6.18 since the value is not constant through all the frequency spectrum.

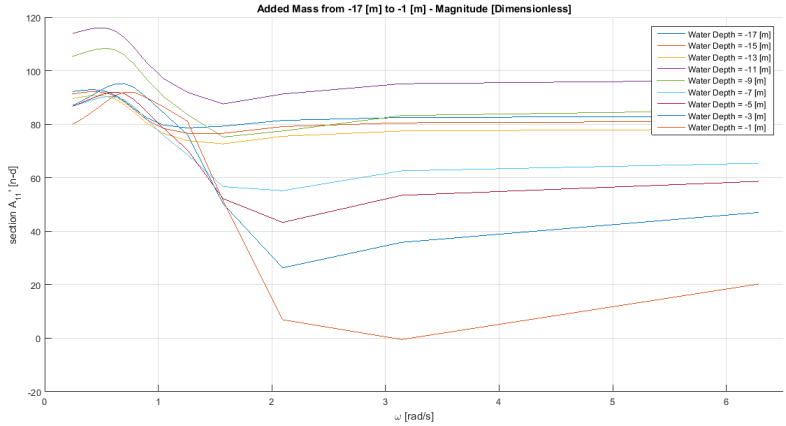

Figure 6.19: Non Dimensional Added Mass for Surge X_1 from -17 to -1 [m] of water depth

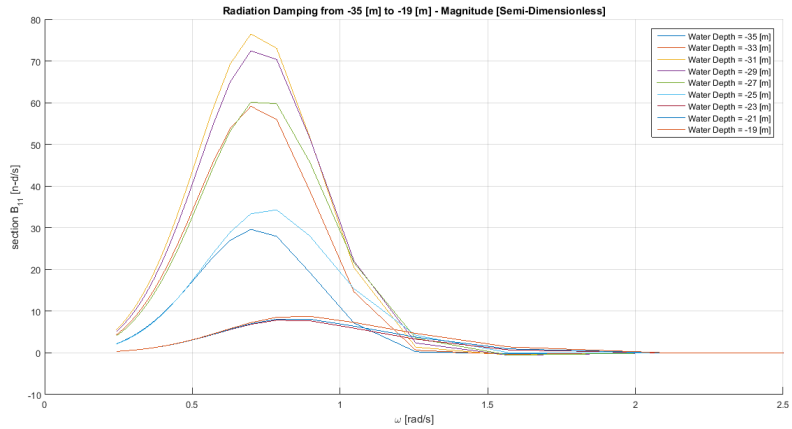

Figure 6.20: Non Dimensional Radiation Damping for Surge X_1 from -35 to -19 [m] of water depth

Concurrently, in figures 6.20 and 6.21 the radiation damping values are shown. The maximum value for every section is increased when moving from deep to shallow waters resulting the highest at around 120 [n-d/s] for 1.6 [rad/s]. Again, it can be observed how the change in diameter size is reflected in the magnitude since the lowest values in the two figures are obtained at the place where the shaft meets the GBS caisson.

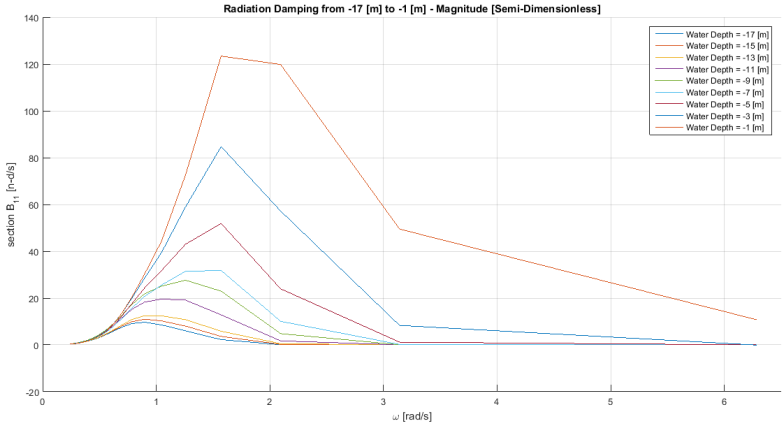

Figure 6.21: Non Dimensional Radiation Damping for Surge X_1 from -17 to -1 [m] of water depth

6.3 Prior Fatigue Assessment Study

As mentioned in the previous subsection, a prior fatigue assessment will be performed to see what hydrodynamic models offer the most accurate response to the GBS. In order to cover this part, SIMA will be used and the three hydro models will be implemented. Once all the parameters are settled, TD simulations will be run with irregular waves and wind and wave data will be introduced from the metocean analysis in section 4. More specifically, as all the conditions will not be covered in this assessment, only the most relevant combinations will be considered from tables 4.4 and 4.5. This means that from condition 1 to 81 only until the 44 will be studied now since the total probability will cover a 86% of the total occurrence for the operational range. This is practically the whole operational status occurrence.

During the analysis, wind effects will be included and will induce both damping and excitation that together with waves will directly give the total effect on the GBS. This means that differences among the hydrodynamic models will be easier to compare in terms of their total relevance. Additionally, turbulent wind files will be considered and only the first wave seed from column 7, in tables 4.4 and 4.5, will be taken into account. This is done because the target is to compare the three different hydrodynamic models and not to see how accurate each of them are. In section 7, a study will be performed to test the hypothesis of how many waves seeds are sufficient to get a reasonable estimation of the fatigue damage.

Additionally, when establishing the different hydrodynamic models in SIMA, both Morison and MacCamy&Fuchs are of simple implementation. Starting with Morison, the quadratic drag coefficient, viscous related, as well as the added mass have been considered with a unit dimensionless value. However, the linear drag type related to the radiated waves from the GBS, is still to be defined but not required during this simulation. Regard-

ing MacCamy&Fuchs, this method requires a bit more of work since SIMO bodies will need to be inserted in SIMA. These SIMO bodies will be placed along the GBS exactly in the same position as the nodes described in table 6.1 and they will represent the added mass value of a specific circular cross section of the GBS. The two cross-sections employed are the 31 and 7 [m] of diameter for the caisson and shaft respectively, and therefore, two different results will be obtained. The added mass for a cylinder is considered in equation 6.19 and developed from [61].

$$m_a = \rho \pi R^2 L \tag{6.19}$$

Where:

- ρ : 1025 $[kg/m^3]$
- R : Radius of the cylinder $[m]$
- L : Length of the cylinder $[m]$

In contrast, potential flow requires much work than the two other previous hydrodynamic models. Here, the calculated loads: wave excitation forces, added mass and linear damping coefficients, computed in subsection 6.2, will need to be implemented in SIMA representing the total hydrodynamic potential flow load. Therefore, the bodies placed along the GBS have frequency dependant coefficients. This means that first order wave transfer functions will be used in every body-node giving a more accurate description of the loading accounting also for the wave diffraction effect.

6.3.1 Set-up

The dynamic computation has been considered for a time length of 4000 [s] (short-term). This means 1 hour of simulation with 400 [s] of transient period for the results to achieve the steady solution. Within this, the points of study will be the tower base, where the steel meets the RC GBS, located at 5 [m] over the still water line, and where the shaft meets the concrete caisson, located at 10 [m] over the seabed; this is clearly identified in figure 6.22. Within this, the structural parameters considered are the OWT's tower base diameter, 5.9 [m], with 0.027 [m] of thickness and the GBS's shaft radius and thickness with 3.5 and 0.5 [m] respectively, as shown in table 6.4.

Therefore, in this subsection, the fatigue damage at both locations will be computed based on the axial stresses resulting from the combination of an axial force as well as the two bending moment components, see equation 6.26. In order to compute the damage, once the resultant axial stresses are calculated, the stress-time history generated must be broken down into individual cycles which are summed up to a distribution of stress ranges. For the summation, one of the most employed counting methods is the rainflow counting process as already explained in 2.4. So, once the stress range is computed, a short-term (1-hour) fatigue damage will be performed. Here, it must be stated that two approaches

will be considered: steel and reinforced concrete fatigue assessment. Even though similar procedures will be applied, the approach will differ when establishing the fatigue damage for both scenarios according to the SN curves applied.

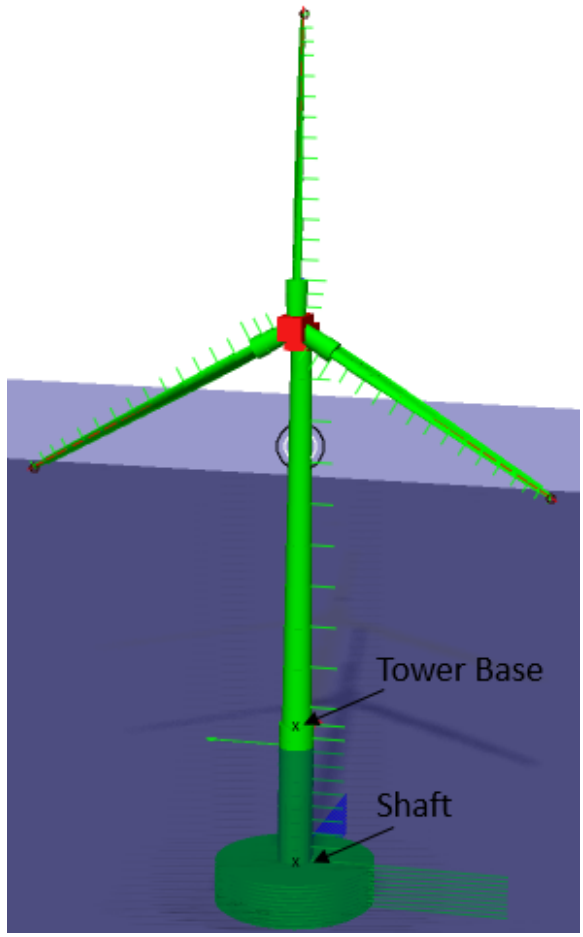

Figure 6.22: Points description of study during pre-fatigue analysis

On the one hand, the DNV SN curve D class for marine steel in air specified in [34] (table 2-1) will be applied for the OWT's tower. More in detail, this curve presented in figure 6.23 has in the lowest cycle region the maximum stress range given by the B1 curve. However, as stated in [34], the main contribution to fatigue damage in offshore structures, subjected to wave and wind loading, is located in the region where $N > 10^6$ cycles with a two slope curve as shown. Additionally, table 6.2 is provided to understand this bi-linear SN curve presented.

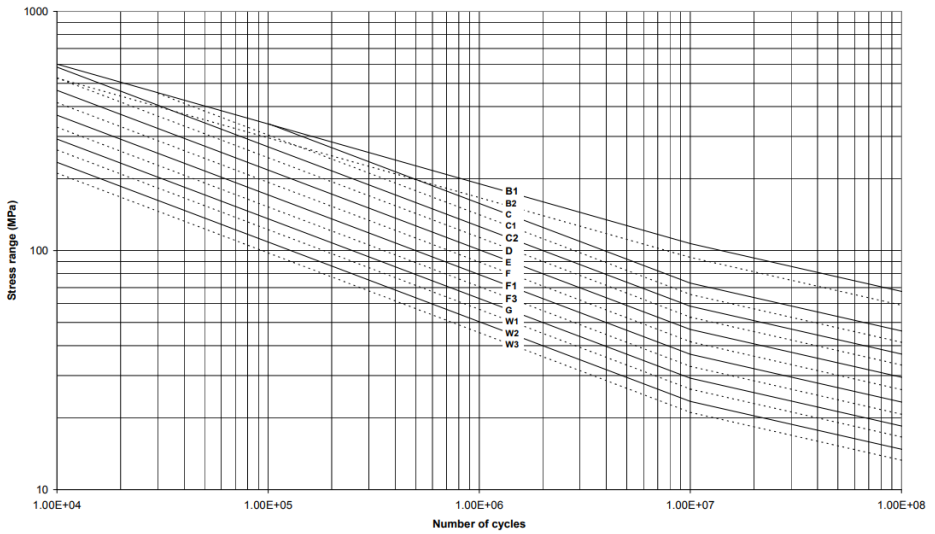

Figure 6.23: Bi-linear SN curves in air for offshore structures [34]

Table 2-1 S-N curves in air						
S-N curve	*$N \leq 10^7$ cycles*		*$N > 10^7$ cycles* $\log \bar{a}_2$ $m_2 = 5.0$	*Fatigue limit at 10^7 cycles *)*	*Thickness exponent k*	*Structural stress concentration embedded in the detail (S-N class), ref. also equation (2.3.2)*
	m_1	$\log \bar{a}_1$				
B1	4.0	15.117	17.146	106.97	0	
B2	4.0	14.885	16.856	93.59	0	
C	3.0	12.592	16.320	73.10	0.15	
C1	3.0	12.449	16.081	65.50	0.15	
C2	3.0	12.301	15.835	58.48	0.15	
D	3.0	12.164	15.606	52.63	0.20	1.00
E	3.0	12.010	15.350	46.78	0.20	1.13
F	3.0	11.855	15.091	41.52	0.25	1.27
F1	3.0	11.699	14.832	36.84	0.25	1.43
F3	3.0	11.546	14.576	32.75	0.25	1.61
G	3.0	11.398	14.330	29.24	0.25	1.80
W1	3.0	11.261	14.101	26.32	0.25	2.00
W2	3.0	11.107	13.845	23.39	0.25	2.25
W3	3.0	10.970	13.617	21.05	0.25	2.50
T	3.0	12.164	15.606	52.63	0.25 for SCF ≤ 10.0 0.30 for SCF >10.0	1.00
*) see also section 2.11						

Table 6.2: Bi-linear SN curves numerical values in air for offshore structures [34]

Due to structural considerations, a thickness correction must be applied since the design thickness is larger than the reference one given by DNVGL. Precisely, the design thickness is 27 [mm] and the reference one is 25 [mm]. So, the two slope SN curve applied is given in equation 6.20 with parameters shown in table 6.3.

$$logN = log\bar{a} - mlog\Big(\Delta S\Big(\frac{t_{design}}{t_{ref}}\Big)^k\Big) \tag{6.20}$$

Table 6.3: S-N Curve D class values

N$\leq 10^7 cycles$		N$\geq 10^7 cycles$		Fatigue Limit at $10^7 cycles$	k	t_{ref}
m	$log\bar{a}$	m	$log\bar{a}$			
3	12,164	5	15,606	52,63 MPa	0,20	25 mm

Table 6.4: OWT's and GBS's design parameters

	OWT's Tower	GBS
Outer Diameter [m]	5.9	7
Thickness [m]	0.027	0.5

On the other hand, when estimating fatigue damage in the GBS, the **DNV-GL Offshore Concrete Structures - DNV-0S-C502** rule will be considered as described in 2.4.3. More specifically, equation 2.85 must be filled in accordingly to the right stress variation range criteria to correctly assess the fatigue damage in the concrete. It must be mentioned that only the concrete's fatigue life will be of study and no reinforcing bar's evaluation will be considered. As commented in 2.4.3 this approach is still based on Palmgren-Miner rule which does not really work accurately for concrete. However, the industry still use this for now. Therefore, this will end up in the SN curve described in equation 6.21.

$$logN = C_1 \frac{1 - \frac{\sigma_{max}}{f_{rd}}}{1 - \frac{\sigma_{min}}{f_{rd}}} \tag{6.21}$$

Where:

- f_{rd} : Compressive strength for the type of failure in question, 30 [MPa].
- σ_{max} : Numerically largest compressive stress computed as the average value within each stress-block.
- σ_{min} : Numerically least compressive stress computed as the average value within each stress-block. However, if σ_{min} is in tension, a zero value must be chosen.
- C_1**:** 8 since it is implemented for structures in water for those stress-blocks having stress variation in the compression-tension range. Here, it should be stated that 281689 blocks are considered in this prior fatigue assessment. Out of this, 9029 blocks are inside a compression-tension rage, 3.2 % of the total. So, even though this percentage is not high enough to consider the structure being in the compression-tension range, a conservative assumption will be made, meaning that C_1 will have the value of 8. This is described in [64] where a value of 10 would need to be considered for those structures in water within the compression-compression range, as described in 2.4.3.

Additionally, it is of high importance to understand that unlike steel, fatigue in concrete also depends on the mean stress level. Standard rainflow count algorithms normally return

the mean of cycles together with the cycle amplitude and number of cycles. Therefore, σ_{min} and σ_{max} can be computed by subtracting and adding the amplitude to the mean, respectively, as shown in equations 6.22 and 6.23.

$$\sigma_{max_{i,j}} = \bar{\sigma_{i,j}} + \sigma_{ampi,j} \tag{6.22}$$

$$\sigma_{min_{i,j}} = \bar{\sigma_{i,j}} - \sigma_{ampi,j} \tag{6.23}$$

Where:

- j: Refers to the jth stress block of the rainflow count.
- i: Refers to the different simulated realizations.
- $\bar{\sigma_{i,j}}$: Mean stress level.
- $\sigma_{ampi,j}$: Cycle amplitude.

Once this is done, the calculated design life should be checked as stated in equation 2.86. In case $logN$ is larger than the value of X in equation 6.24, $logN$ must be multiplied by C_2 given in equation 6.25

$$X = \frac{C_1}{1 - \frac{\sigma_{min}}{f_{rd}} + 0.1C_1} \tag{6.24}$$

$$C_2 = (1 + 0.2(log_{10}N - X)) > 1.0 \tag{6.25}$$

Finally, a SN curve of concrete is plotted in figure 6.24 for a given stress block. Specifically, the parameters describing this randomly chosen stress-block are:

- Turning points: 3.5421 - 3.6117 [kPa]
- Mean stress: 3.7931 [kPa]
- Compressive Strength: 30 [MPa] (Always the same)

Additionally, figure 6.25 shows the local element axis that are applied to every cylindrical RIFLEX element of the OWT. This accounts for the GBS shaft and caisson as well as the OWT's tower. Additionally, directions for moments and forces as well as angle criterion is shown and applied in the computation procedure. From the own description of SIMA it is commented that axial and shear forces, as well as bending moments, are outputs from RIFLEX established in its local coordinate system.

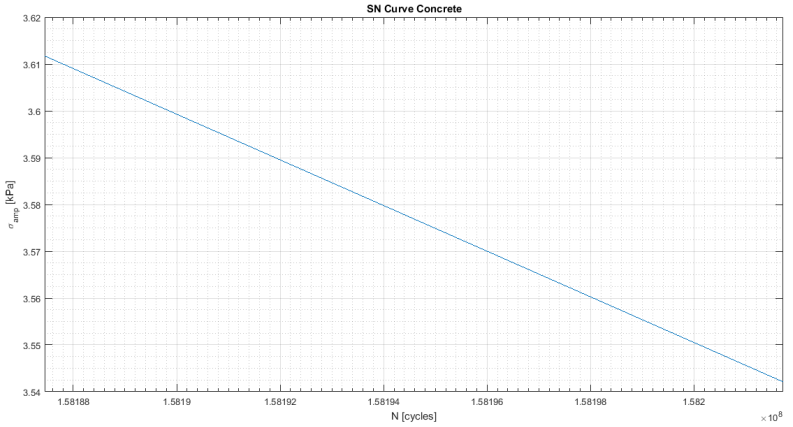

Figure 6.24: SN curve for concrete of a randomly chosen stress-block

- Nx: DOF1 Axial force from RIFLEX.
- MY: -1 · (DOF3 Moment about local y-axis, end 1 from RIFLEX.
- Mz: DOF5 Moment about local z-axis, end1 from RIFLEX.

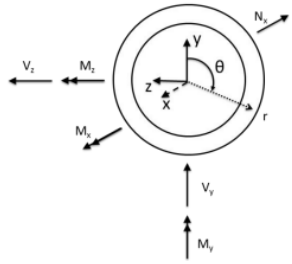

Figure 6.25: Coordinate systems for tower base fatigue damage calculation

The axial stress computation is calculated with equation 6.26 where the axial force as well as the bending moments in the other two directions are present.

$$\sigma = \frac{N_X}{A} + \frac{M_y}{I_y} r sin(\theta) + \frac{M_z}{I_z} r cos(\theta) \tag{6.26}$$

Where:

$$I_y = I_z = \frac{\pi}{4}(r^4_{external} - r^4_{internal}) \tag{6.27}$$

$$r_{internal} = r_{external} - t_{design} \tag{6.28}$$

However, it should be noted that normally all locations in the cross-section should be considered when computing fatigue damage. In our case, since wind and waves have been considered to be aligned, it is permissible to only consider a point on the outer radius, specified in table 6.4, where θ =270 degrees.

Finally, it should be noted that in order to compute the 20 years fatigue damage prediction at any point of the OWT, the 1-hour fatigue damage, computed from axial stresses, must be inserted into equation 6.29. Here, according to the number of conditions and probability value from 4.4 and 4.5, the total fatigue damage can be finally estimated.

$$Damage_{20Years} = \sum_{i=1}^{n} Damage_n \cdot t \cdot P_i \tag{6.29}$$

- n: Number of conditions
- $Damage_i$: 1-hour average damage from wave seeds for each condition
- t: Number of hours in 20 years
- P_i: Probability of occurrence for condition i, shown in tables 4.4 and 4.5

6.3.2 Results

In this results subsection, different plots are shown to establish the difference in fatigue output for the three hydrodynamic models analyzed. The results refer to figures 6.26, 6.27 and 6.30, 6.31 stating the estimated 1 hour fatigue damage and 20 years fatigue prediction respectively, for the 2 points of consideration. Again it should be reminded that the first 44 operational conditions have been the ones simulated in this study. They cover the 86% of occurrence and are described in tables 4.4 and 4.5.

Expected fatigue life

On the one hand, the figures in this subsection show results in accordance to the hydrodynamic loads computed in figure 6.1. This means that Morison output in every fatigue plot gives the highest damage. Again, this model does not account for the wave diffraction and therefore, a non real damage is being assumed for waves of small period affecting the relatively large diameters of the GBS. Additionally, while steel results offer a relatively obvious gap between the three hydro models, concrete's difference is mostly insignificant. Furthermore, there is a clear difference in the 1 hour fatigue response for the two points analyzed.

On the other hand, steel results vary with a relatively linear increment, see figure 6.26, and concrete is clearly driven by the wind speed as shown in figures 6.27 and 6.28. This means

that every plateau achieved in the concrete's response refers to the same wind speed. For instance, conditions 1 to 5, first plateau, refers to 3 and 3.5 [m/s] of wind speed as stated in 4.4.

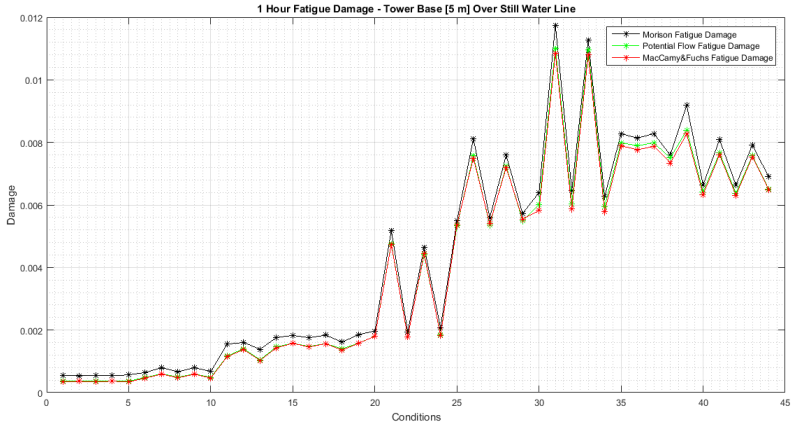

Figure 6.26: Estimated 1 hour fatigue in the tower base including the 3 Hydrodynamic models

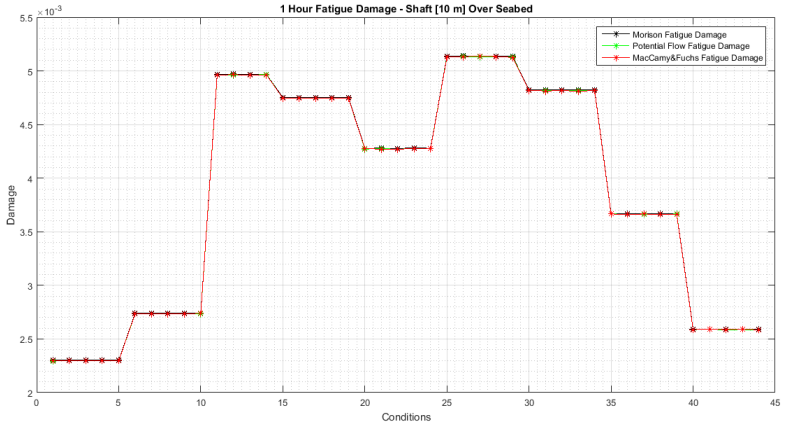

Figure 6.27: Estimated 1 hour fatigue in the concrete shaft including the 3 Hydrodynamic models (1)

Additionally, the estimated 1-hour fatigue in both steel and concrete, shown in figures 6.26 and 6.27, revealed how different the responses are. Even though both materials are clearly driven by the percentage of occurrence and wind speed, steel is slightly more affected by the latter. This is reflected in conditions 30-34 where even though being driven by a lower percentage of occurrence than the maximum one, 2.58%, they offer the highest damage.

In contrast, concrete is definitely more influenced by the percentage of occurrence, since conditions 25-29, offering the highest occurrence, 2.58%, offer the largest damage. This means that other conditions with higher wind speed and slightly minor occurrence offer less concrete damage. In addition to steel results, it can also be observed how damage is increasing when both the wind speed and H_s are rising according to figure 6.29. Finally, as it will be seen later in the spectrum plot, the lower the T_p, the higher the damage.

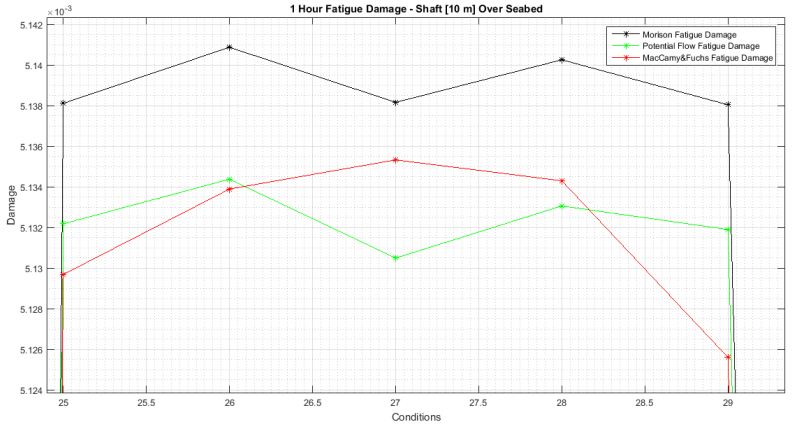

Figure 6.28: Estimated 1 hour fatigue in the concrete shaft including the 3 Hydrodynamic models (2). Highest damage at 8-8.5 [m/s] for conditions 37 to 41

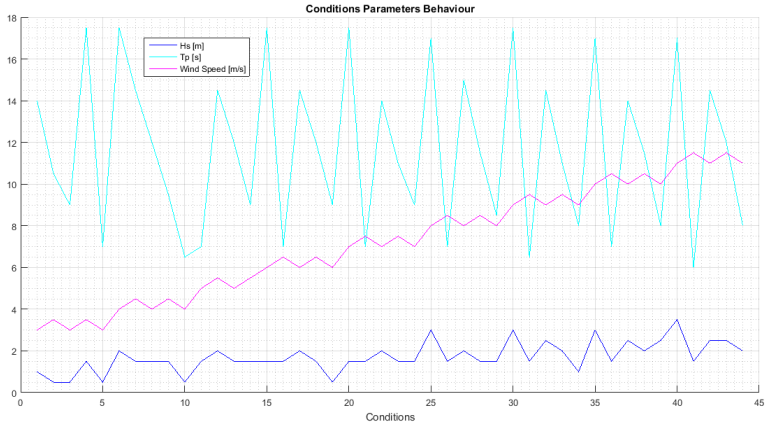

Figure 6.29: Parameters behaviour affecting conditions for the 3 Hydrodynamic models

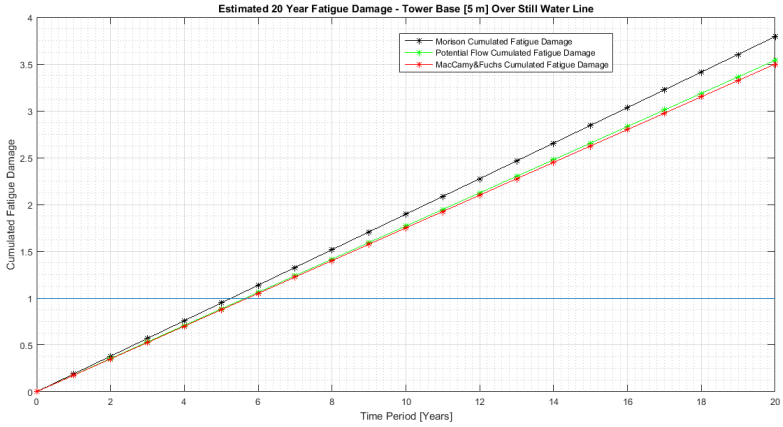

Figure 6.30: Estimated 20 years fatigue in the tower base including the 3 Hydrodynamic models

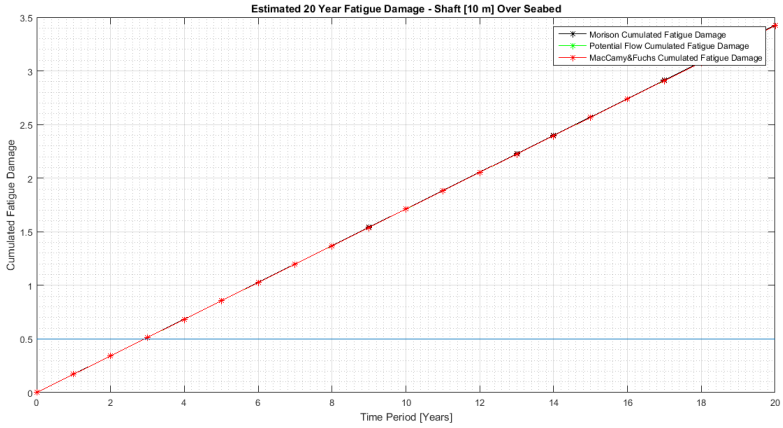

Figure 6.31: Estimated 20 years fatigue in the concrete shaft including the 3 Hydrodynamic models (1)

Furthermore, the expected fatigue life for both steel and concrete must also be commented. From figures 6.30 and 6.31 it can be observed how failure occurs at around 5.5 years for steel and 3 years for concrete. Additionally, as mentioned above, no reasonable gap is shown between the different models. This leads to a position where no matter what hydrodynamic model is computed that the expected life for the RC would be the same. In contrast, steel results reveal 7 months of difference between Morison and the wave diffraction models. This obviously is an insignificant value but where at least some difference is actually appearing in contrast to concrete. Furthermore, the reason why both materials have different cumulative damage ratio is due to table 2.3. This is because steel is consid-

ered above the splash zone while concrete is located below it. Within this, it is definitely surprising to obtain such survival years when 20 is the normal expected life for an offshore structure. Therefore, if the fatigue life for both, steel and concrete, wants to be increased the following parameters must be further studied.

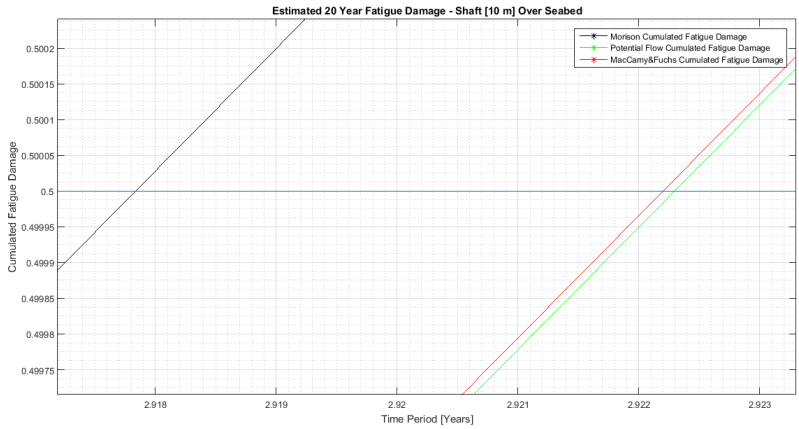

Figure 6.32: Estimated 20 years fatigue in the concrete shaft including the 3 Hydrodynamic models (2)

- **OWT's steel tower:**

  After some simulations it was considered that different stresses could be obtained if the thickness or diameter of the OWT's steel tower were modified according to equation 6.26. This means that if any of the above parameters had increased, the obtained stresses would have notably decreased. Specifically, if the OWT's diameter were increased by a 16.9% without modifying the thickness, 20 years of fatigue life would be achieved. Likewise, if 20 years want to also be obtained without modifying the OWT's diameter, the thickness must be increased up to a 50% from the original value.

  Therefore, it can be clearly observed how the outer base diameter is the parameter improving the fatigue life the most with a smaller increase than the thickness. However, it should also be kept in mind that even though the thickness will offer a higher increment to achieve the 20 years, maybe it could result in a cheaper option. So, an economical study must be performed to determine what parameter result more profitable if increased. Within this, it should also be kept in mind that increasing any of the two parameters will lead to a bigger OWT that will complicate the transportation and manufacturing process.

- **Concrete shaft:**

  In this case, concrete's fatigue life varies quite a lot from the steel one. Here, referring to equation 6.21, one can determine how modifying previous steel parameters the fatigue concrete life is not altered. Specifically, the C1 value is the parameter influencing the most. This means that if changed from 8 to 8.7 20 years are obtained and we are still inside the conservative assumption of having stress-blocks variation in the compression-tension range.

Additionally, it can be said that it is difficult to have an idea that just one parameter alone can affect all the conditions in the similar way. But in general, within the environmental conditions there is a close relationship between Hs, Tp and wind speed. As it can be observed, while increasing wind speed, Hs values are growing as well as the wave period. This is a common trend happening in real life since wind creates waves.

Therefore, in order to understand why this failure is appearing so soon, a FD study is performed in the following paragraphs. This is done to identify how the loads and the nature of them are affecting the GBS and the OWT's tower.

Time and frequency domain analysis

In order to be able to explain the difference in fatigue for the three hydrodynamic models, a combination of time series and spectra analysis is covered. More specifically, TD statistical parameters for conditions 1, 31 and 44 in both the OWT's tower and concrete shaft are shown in tables 6.5 and 6.6. These conditions have been chosen for being the one with the lowest damage for concrete and steel, the one with the highest damage for steel and for being the last studied condition in both materials respectively. Additionally, figures 6.33 and 6.34 represent the physical TD spectrum for the computed axial stresses only for condition 1. The other TD plots for conditions 31 and 44 have been placed in the appendix, see A.2.4.

The TD results show how the stresses are fluctuating for a certain condition in steel and concrete and for the three hydrodynamic models analyzed. In tables 6.5 and 6.6, it can be observed how the maximum and minimum values for Morison in steel are always higher than the two other hydrodynamic models as well as the mean output. This reflects again how Morison stresses lead to a higher damage as shown in previous fatigue plots, figure 6.26. However, this is not happening in concrete, what seems surprising, since Morison is always given the highest 1 hour damage in the shaft base as shown before in 6.28. For the concrete, both MacCamy&Fuchs and potential flow give exactly the same values that are slightly larger than the Morison ones. Additionally, the standard deviation shows how data are close or far to the average value revealing how spread the values are over the total range.

Another important point of study is to comment that how it is possible that condition 44 offers a higher mean for both concrete and steel than condition 31 if this condition is giving more fatigue in figure 6.26. Therefore, to answer this question, another one needs to

be asked: Is the probability of occurrence being included in figure 6.26? The answer is yes, so one should refer to new figures, see 6.35 and 6.36, where the probability of occurrence has not been included in any condition. Then, it will be observed how condition 44, with the highest mean value in table 6.6, is actually giving the highest damage where no probability of occurrence has been included.

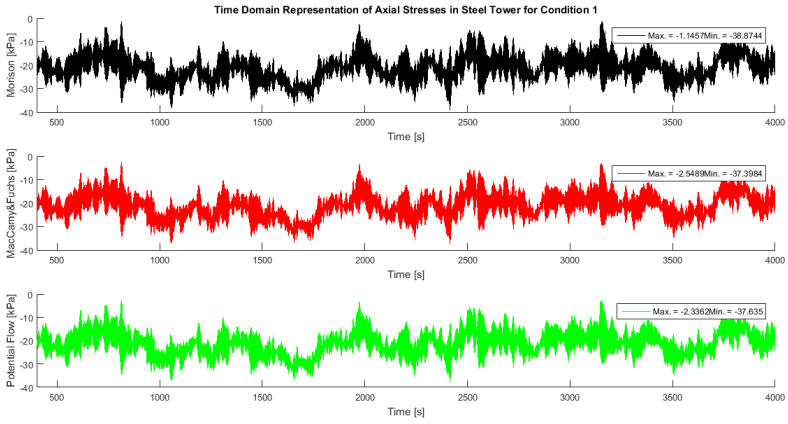

Figure 6.33: TD representation of condition 1 for the three hydrodynamic models in OWT's tower base

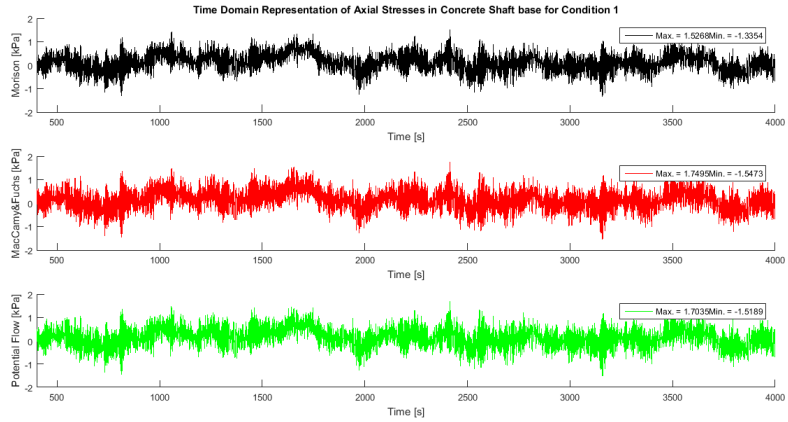

Figure 6.34: TD representation of condition 1 for the three hydrodynamic models in concrete shaft

Table 6.5: Mean, standard deviation, maximum and minimum values of axial stresses for both OWT's steel tower base and concrete shaft for conditions 1, and 31

		Condition 1		Condition 31	
Material Type		**Steel**	**Concrete**	**Steel**	**Concrete**
Mean [kPa]	Morison	-21.1867	0.1211	-77.4960	3.6466
	MacCamy&Fuchs	-21.1866	0.1336	-77.4963	3.6616
	Potential Flow	-21.1867	0.1336	-77.4963	3.6616
Standard Deviation [kPa]	Morison	5.4979	0.38	14.7771	0.9988
	MacCamy&Fuchs	5.2155	0.4274	14.7115	1.0286
	Potential Flow	5.2518	0.4179	14.7171	1.0227
Maximum Value [kPa]	Morison	-1.1457	1.5268	-23.6632	6.4527
	MacCamy&Fuchs	-2.5489	1.7495	-25.193	6.8847
	Potential Flow	-2.3362	1.7035	-25.105	6.6384
Minimum Value [kPa]	Morison	-38.8744	-1.3354	-110.2752	-0.1849
	MacCamy&Fuchs	-37.3984	-1.5473	-109.2943	-0.3098
	Potential Flow	-37.635	-1.5189	-109.5077	-0.5319

Table 6.6: Mean, standard deviation, maximum and minimum values of axial stresses for both OWT's steel tower base and concrete shaft for condition 44

		Condition 44	
Material Type		**Steel**	**Concrete**
Mean [kPa]	Morison	-82.9216	3.9820
	MacCamy&Fuchs	-82.9223	3.9974
	Potential Flow	-82.9222	3.9974
Standard Deviation [kPa]	Morison	11.7190	0.8507
	MacCamy&Fuchs	11.6480	0.9113
	Potential Flow	11.6556	0.8955
Maximum Value [kPa]	Morison	-44.6211	6.9036
	MacCamy&Fuchs	-46.8524	6.9341
	Potential Flow	-46.3106	7.0631
Minimum Value [kPa]	Morison	-115.7573	1.2713
	MacCamy&Fuchs	-115.9389	1.044
	Potential Flow	-115.8486	1.0835

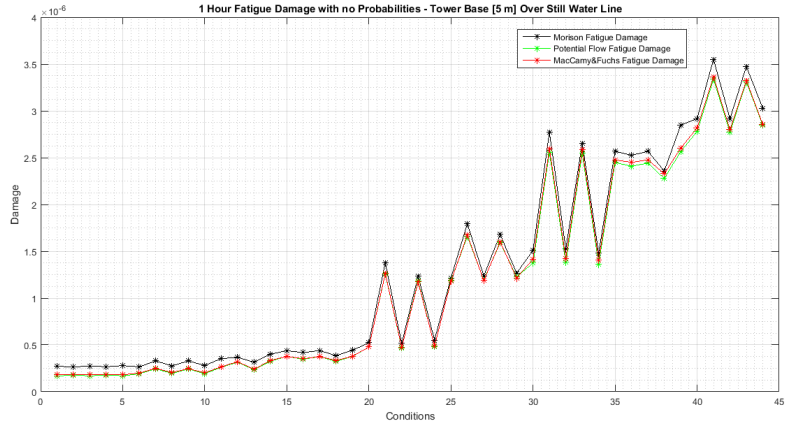

Figure 6.35: Estimated 1 hour fatigue in the tower base including the 3 Hydrodynamic models with no probability included

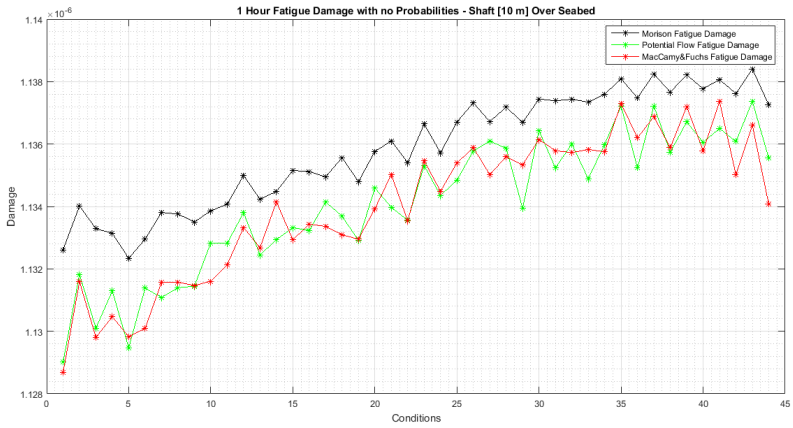

Figure 6.36: Estimated 1 hour fatigue in the concrete shaft including the 3 Hydrodynamic models with no probability included

As described in 2.2.3, fatigue analysis in the FD is also considered since the responses are easily analyzed. Here, it will be determined how the bending moments are leading to fatigue for the different hydrodynamic models presented. Therefore, from figure 6.37 to 6.42 the same conditions as above have been considered showing a comparison in the FD for both steel and concrete.

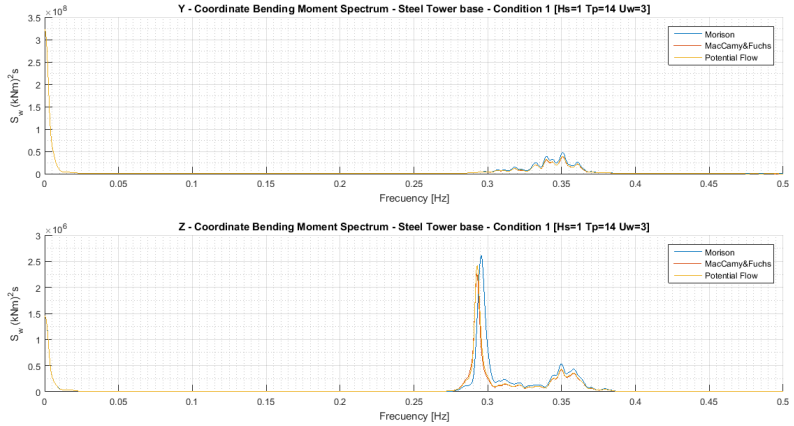

Figure 6.37: FD representation of condition 1 - Steel tower for the three hydrodynamic models

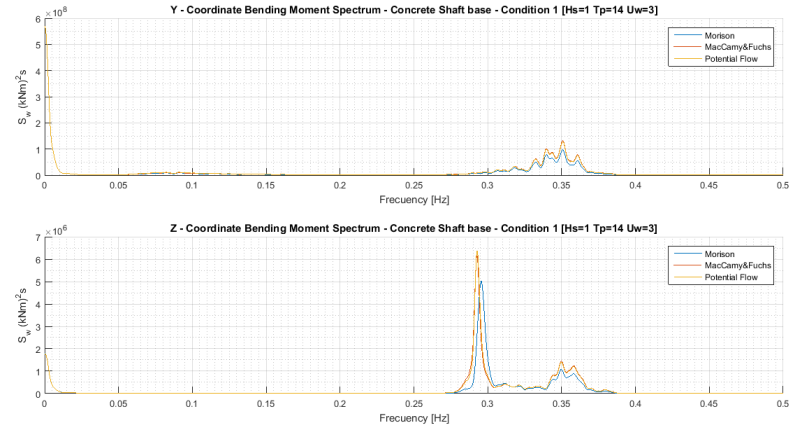

Figure 6.38: FD representation of condition 1 - Concrete shaft for the three hydrodynamic models

On the one hand, in figure 6.37 to 6.42 it can be firstly pointed out that it exist a clear difference between the OWT's steel tower base and concrete shaft base results. While in steel Morison is set as the highest hydrodynamic model, the concrete locates MacCamy&Fuchs and potential flow always over it. However, the disagreement between the models is so small to actually make a difference in both the steel and shaft base responses. This leads to a situation where no clear conclusions can be made of and where it is the amplitude the parameter influencing the most in the bending response. Additionally, it should be mentioned that the higher the H_s the higher the bending response due to waves in the Y coordinate spectrum. While in the tower base is not so noticeable, with a point located 5 [m] over the still water line, the concrete shaft base point reveals how for condition 44,

with an $H_s = 2[m]$, waves are acting at 0.125 [Hz], see figure 6.42. This concrete point is located 10 [m] over the seabed where wave effects are clearly contributing to the fore-aft bending of the structure as also the wind is always doing in every spectrum. Additionally, when addressing concrete's results, one could think that as it is too sensitive to the number of cycles, as seen in figure 6.24, then the frequency is the parameter influencing the most in the bending response.

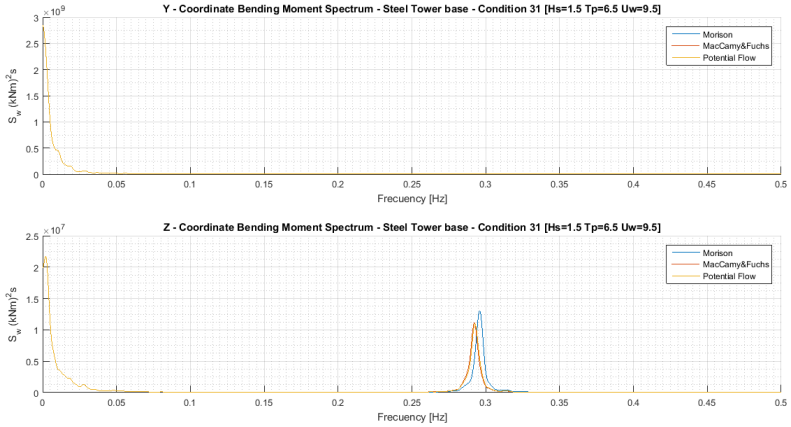

Figure 6.39: FD representation of condition 31 - Steel tower for the three hydrodynamic models

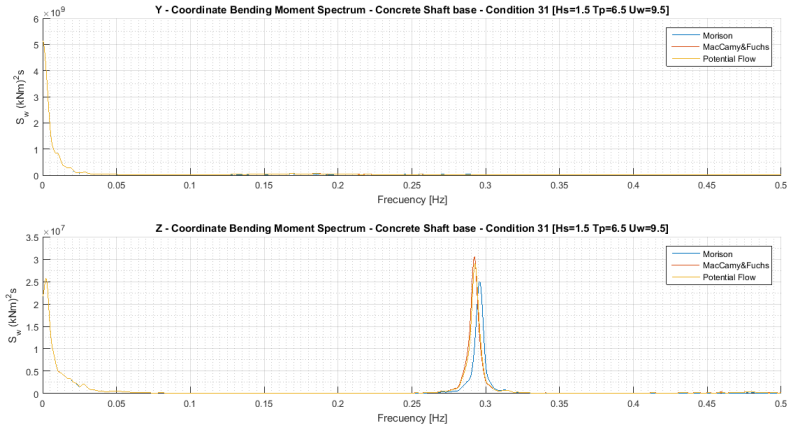

Figure 6.40: FD representation of condition 31 - Concrete shaft for the three hydrodynamic models

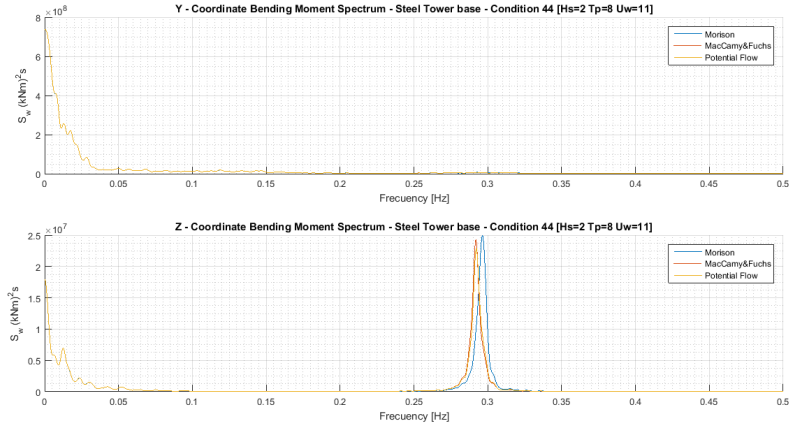

Figure 6.41: FD representation of condition 44 - Steel tower for the three hydrodynamic models

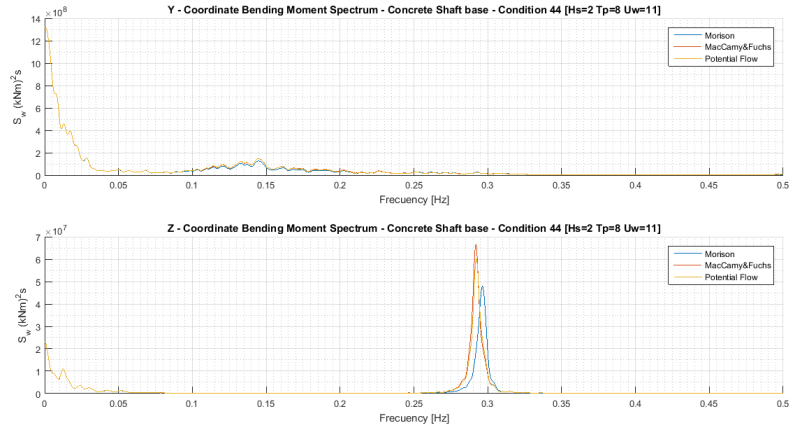

Figure 6.42: FD representation of condition 44 - Concrete shaft for the three hydrodynamic models

On the other hand, from the Z coordinate spectrum much information can not be drawn of since neither the waves nor the wind is coming from that side-side direction. However, it is clear to see how responses are much lower than the Y coordinate's ones where waves are not shown at all and wind effect is noticeably much smaller. Nevertheless, a clear dynamic amplification is shown always at the natural frequency of the OWT, 0.29 [Hz], as a result of the low range of the 3P blade passing frequency interaction located at 0.36 [Hz], as seen in 6.38. However, this dynamic effect due to the 3P frequency is only clearly shown in the previous mentioned figure. The other two conditions, 31 and 44 also offer that amplification effect with no clear reasons around to determine why. Therefore, as already mentioned, not much information is considered from this mode and no other comments

can be made. So, as shown in 5.4, a clear dynamic amplification is appearing resulting in a higher bending moment response that will definitely lead to fatigue issues in a future. This can start explaining the relatively low fatigue life found in previous subsection.

Another point to consider is that it can make sense that the concrete spectrum reveals higher Z bending moments responses than for steel in the same condition. It can result that the GBS is so stiff that the bending moment appearing on the concrete is not being really transferred to the OWT's tower. If we considered an external load, this one must be taken up by the stiffness, inertia or damping of the structure. This means that for example, having little displacement of the nodes of the GBS means that not much inertia will be induced. Keeping in mind that inertia is a way to transfer the loads from the GBS to the tower, with little displacement this will not happen. So, with only bending happening in the GBS, large stiffness forces will appear and therefore no loads will then be transferred to the OWT's tower.

Therefore, in the following figure, see 6.43, it is confirmed how practically zero displacement is occurring to the selected nodes of the OWT. According to table 7.1 it can be determined how the Z coordinate stays in the same vertical position while X and Y do not suffer any relevant lateral displacement. Additionally, this is also confirming that the whole structure is neither being sunk nor lift by any external load. More deeply, the analyzed nodes have been the ones used in the full fatigue assessment covering 9 points from the bottom of the GBS to the top of the OWT's tower, as shown in figure 7.1. So, with these results it can be finally mentioned that the GBS is so stiff that no bending moments are being transferred to the OWT's tower, meaning that inertia is not relevant at all.

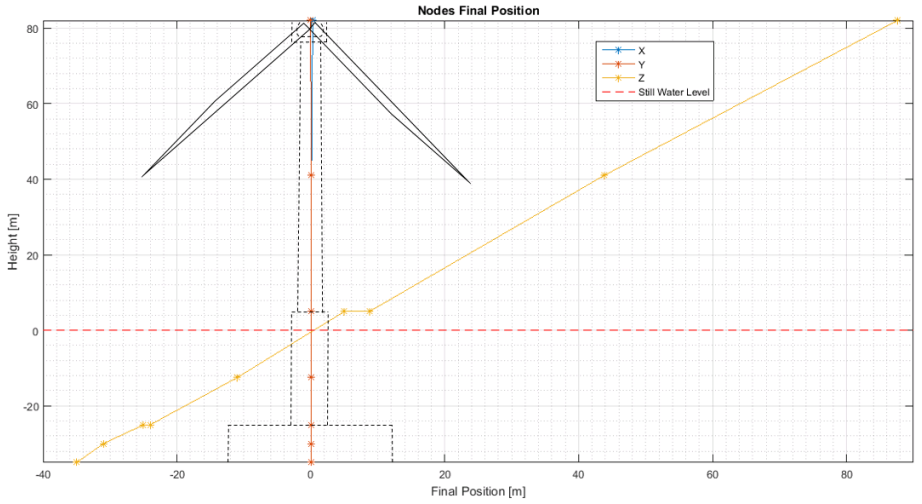

Figure 6.43: Final position of the nodes after dynamic simulation

To end this FD analysis section, pictures 6.44, 6.45 and 6.46 have been included to show

how different conditions result in different bending moment's responses. Specifically for this case, Morison theory has been applied where 3 combinations of H_s, T_p and U_w have been presented. Within this, it should be reminded that Y coordinate represents the fore-aft bending mode, while Z coordinate refers to the side-side bending motion.

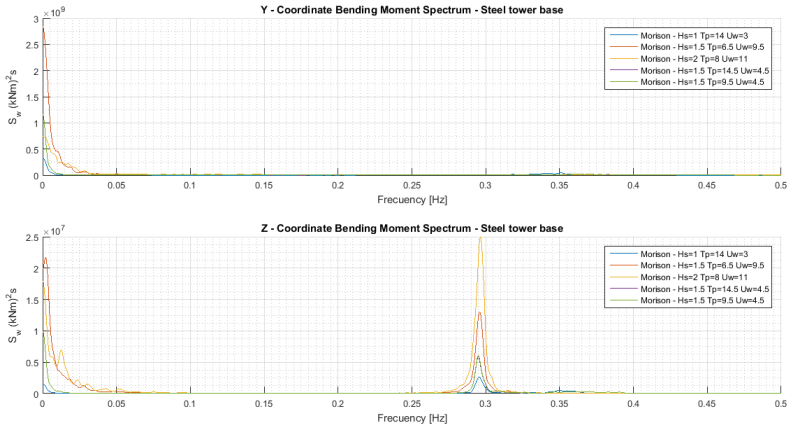

Figure 6.44: FD analysis for steel tower, for 3 different conditions: 1, 31 and 44 employing Morison theory

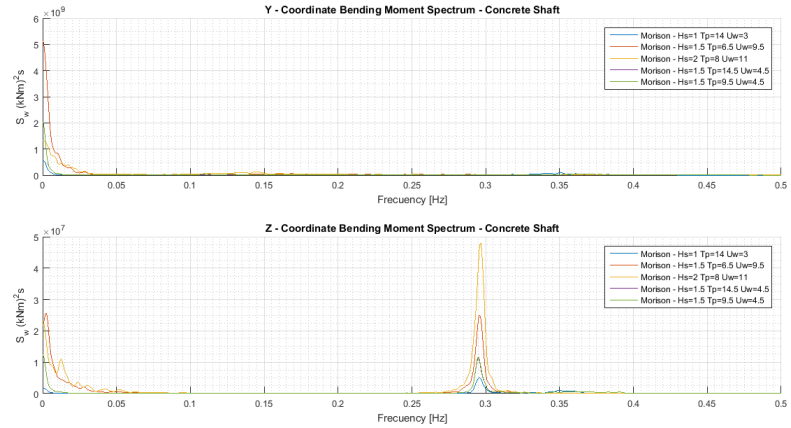

Figure 6.45: FD analysis for concrete shaft, for 3 different conditions: 1, 31 and 44 employing Morison theory (1)

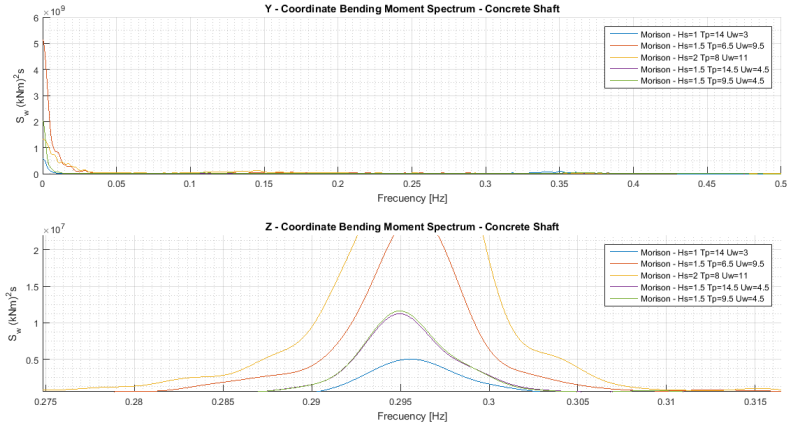

Figure 6.46: FD analysis for concrete shaft, for 3 different conditions: 1, 31 and 44 employing Morison theory (2)

As it can be observed in the second subplot for every figure 6.44 - 6.46, the highest bending response in the Z direction is associated to the largest H_s, as expected. This highest response will lead to a larger fatigue estimation. Furthermore, the last two conditions in the legend show how for the same H_s a lower T_p results in higher bending moments' responses, see for more detail 6.46. However, wind speed is the parameter influencing the most when accounting for bending spectrum and therefore for fatigue life estimation.

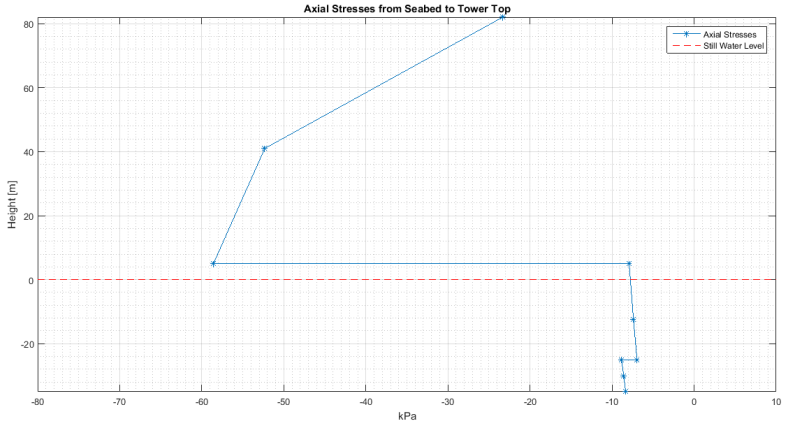

Figure 6.47: Axial stress distribution along the OWT for condition 30

Finally, figure 6.47 has been plotted to represent how the axial stresses, computed from 6.26, are distributed along the OWT. It can be observed how concrete's compression

stresses are relatively low in comparison to the large kPa, also in compression, obtained for the steel tower. The location of the tower/GBS, where the steel meets the concrete, is definitely a place to keep in mind. The large variation of stresses makes that point to be quite interesting since different magnitudes are assumed for each material at the same location. Additionally, the results can be taken as good since compression is always happening meaning that the structure will remain in the seabed while the bearing capacity will not be compromise.

MacCamy&Fuchs and Potential Flow overview

This last subsection has been developed to quantify the difference in 1 hour fatigue between the three hydrodynamic models for both steel and concrete. Since the full fatigue study requires several days for the TD results to be obtained, it is convenient to determine which of the three hydrodynamic models or a combination of them should be employed. It should be reminded that Morison theory, good for slender elements will not account for the wave diffraction effect as MacCamy&Fuchs and potential flow will do when large diameters and short waves are considered. Therefore, figures 6.48 - 6.51 will quantify the difference between the three models in % for the OWT's steel tower and the concrete shaft of the GBS.

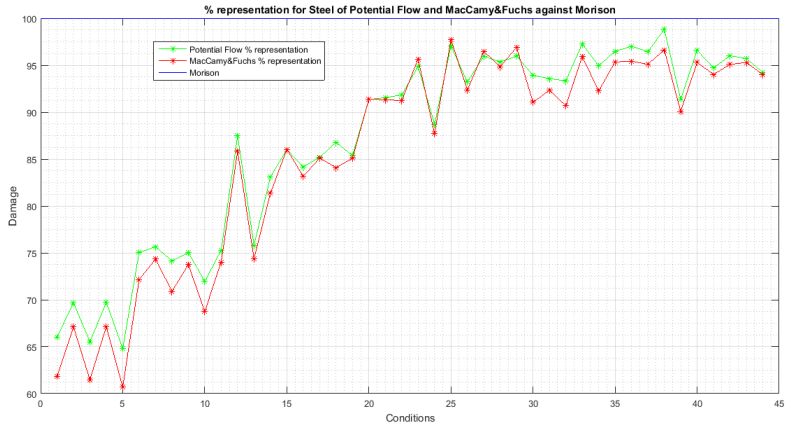

Figure 6.48: % representation for steel of Potential Flow and MacCamy&Fuchs against Morison

On the one hand, OWT's steel tower results, see figures 6.48 and 6.50, offer a clear gap between MacCamy&Fuchs and potential flow respect to Morison. The largest difference is set to almost 40% between MacCamy&Fuchs and Morison for condition 5. However, there is not much difference between MacCamy&Fuchs and potential flow as already seen in 6.50 where the largest gap between both is considered for condition 1 with almost 6.5%. On the other hand, concrete results, see 6.49 and 6.51, offer a similar trend since the damage is increasing when increasing the wind speed. Nevertheless, the differences respect to

Morison are practically zero where no clear reason is obtained to determine what hydrodynamic model should be employed.

Regarding the steel results on figure 6.48, it is of vital importance to understand why until condition 20 the difference respect to Morison is much larger than the following ones. Condition 5, with a T_p = 7 [s] and a H_s = 0.5 [m] refers to a situation where diffraction theory can explain such disagreement between the three models. Therefore, applying figure 2.11, one can locate a certain condition in its respective place keeping in mind the finite waters assumption described in 3.3.

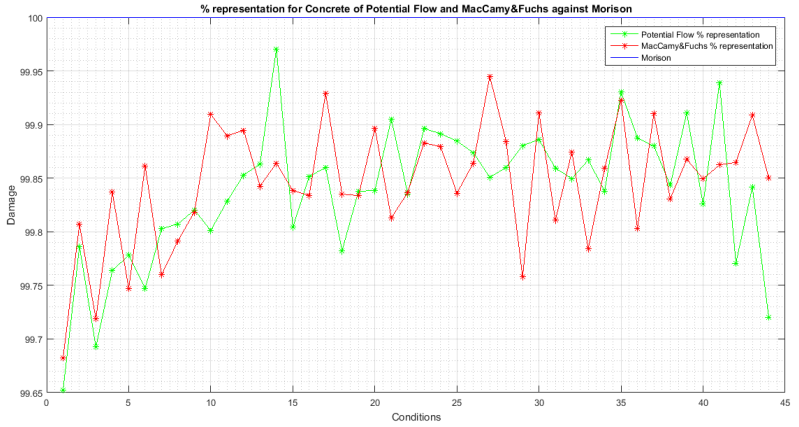

Figure 6.49: % representation for concrete of Potential Flow and MacCamy&Fuchs against Morison

So, two diameters must be considered D_{shaft} = 7 [m] and $D_{caisson}$ = 31 [m] that will result in equation 6.30 where the wave diffraction limits are established at 35 [m] for D_{shaft} and 155 [m] for $D_{caisson}$ of wave length. This results in 4 and 10 [s] of T_p for the shaft and caisson respectively. However, there are no reasons to state that wave diffraction will happen at just one of the two T_p presented since both the shaft and caisson are clearly affecting the wave progression in the finite waters assumption. However, there are no doubts that waves at the surface will be more affected than those at deeper depths. So, choosing one or another cylinder to actually determine the wave diffraction limit becomes a difficult task. Therefore, it will be concluded that wave diffraction will occur, also according to figure 6.49, for waves containing a T_p inside the range of 1 to 9 [s].

Therefore, having a look at 4.4 and 6.48, one can understand how low wave periods results in a larger difference since wave diffraction is considered. However, such difference gets shorter while increasing the wind speed whose hilly shape is clearly driven by the wind speed changing value. So, the lower the T_p the higher the gap but the larger the wind speed the lower the difference between the three models since wind effects become more important.

$$5 = \frac{\lambda_{D_i}}{D_i} \tag{6.30}$$

Table 6.7: Wave periods with respective wave lengths for finite waters (1)

Tp [s]	1	2	3	4	5	6	7	8	9
λ **[m]**	1.56	6.25	14.05	24.98	39.03	56.21	76.44	99.29	123.48

Table 6.8: Wave periods with respective wave lengths for finite waters (2)

Tp [s]	10	11	12	13	14	15	16	17
λ **[m]**	147.81	170.68	193.06	214.81	236.06	256.92	277.46	297.75

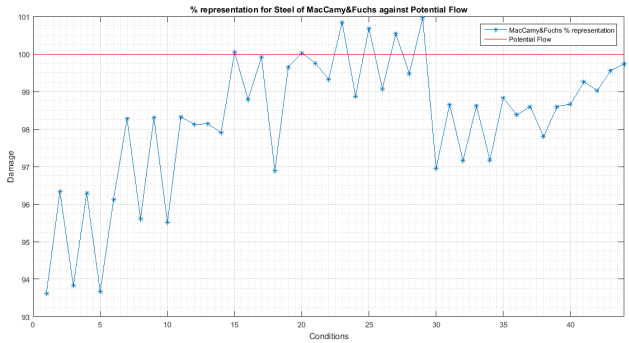

Figure 6.50: % representation for steel of MacCamy&Fuchs against Potential Flow

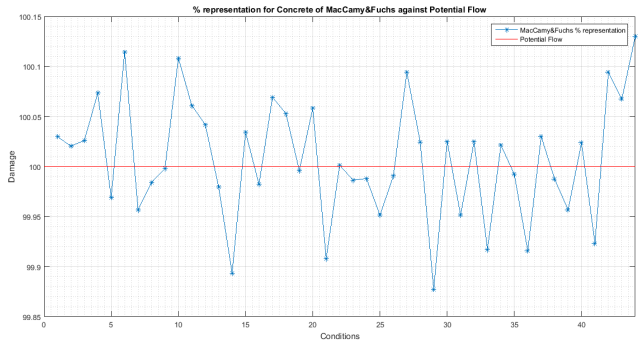

Figure 6.51: % representation for concrete of Potential Flow and MacCamy&Fuchs against Morison

Finally, pictures 6.50 and 6.51 reveal no practical difference between MacCamy&Fuchs and potential flow for concrete but the latter hydrodynamic model results in higher damage for steel. However, due to similar results, 1 of the two models will not be considered in the full fatigue analysis. Therefore, the following reasons are given to determine why MacCamy&Fuchs has been finally chosen to be compared with Morison in the last chapter of the thesis.

- MacCamy&Fuchs is much simpler to implement than potential flow since only the diameter is needed. In contrast, potential flow requires much more work since the total hydrodynamic loads: first-order wave transfer functions, added mass and linear damping coefficients have to be computed and implemented, as reflected in figure 3.16
- The big change in the diameter size between the caisson and shaft of the GBS does not contribute to a real difference in the prior fatigue assessment. This means that the frictionless and irrotational flow around the big caisson, potential flow, does not give unique values, as maybe were expected from a first perspective.
- Employing MacCamy&Fuchs means employing a similar theory to Morison where a correction of the C_M value will be performed. Therefore, a similar approach will be used in both hydrodynamic models where only the wave diffraction effect will be considered from MacCamy&Fuchs.

6.4 Conclusions

To summarize this section the following items are described:

- The total integrated force, shown in figure 6.1, reveals how low frequencies, long waves, offer higher force amplitudes. Additionally for this low frequency range the three models analyzed: Morion, MacCamy&Fuchs and potential flow seem to follow the same pattern. However for larger frequencies, shorter waves, divergence occur for Morison in comparison to potential flow and diffraction theory. For shorter periods, Morison is always giving the highest force amplitude that will lead afterwards to overestimation of fatigue damage when diffraction happens.
- HydroD sectional loads, first order wave transfer functions, have been firstly computed to check if the GBS design was performed correctly and to verify the total integrated force results. As shown in 6.2.1, the shape and values are according to figure 6.1. Longer waves are exhibiting larger amplitude forces and the values for each section are lower than the total integration provided in the first analysis.
- In addition to the potential flow results commented in previous paragraph, WAMIT software was also employed to compute the total hydrodynamic loads: First order wave transfer functions, linear damping and added mass coefficients. Employing the panel theory it could be observed how the added mass results for surge and heave showed a frequency dependence behaviour, while linear damping offered a

much stronger dependence for every motion, see figure 6.11. Additionally, the first-order wave excitation and linear damping offered good responses since both the low and high frequency values tend to zero. Finally, for the sectional load study, one could observe how the larger the depth, the lower the frequency at which the maximum value is given for the first order wave excitation. Concurrently, for the radiation damping is observed how the maximum values in every section increase when decreasing water depth. In both cases, the influence of the diameter size is clearly noticeable as seen in figures 6.14 and 6.17.

- According to frequency spectrums and structural displacement analysis of the whole structure, it resulted that the GBS was so stiff that the bending moments occurring due to large stiffness forces were not actually being transferred to the OWT's tower. This means that inertia is not considered at all when taking up the external loads affecting the GBS.

- The prior fatigue assessment has verified that the Morison hydrodynamic model accounts for the highest fatigue damage as shown in the 1 hour plot and the 20 years expected fatigue life for both steel and concrete, see figures 6.26 and 6.30. However, as mentioned, Morison is not accounting for the diffraction effect and that is why MacCamy&Fuchs theory is also studied in addition to potential flow. Therefore, according to the results, in the future full fatigue study 2 models will be analyzed: Morison and MacCamy&Fuchs. This is considered since potential flow, accounting for a more correct flow around the big caisson (31 [m] of diameter), give practically the same results as MacCamy&Fuchs does.

- Fatigue life expectation for the two points of study, reflected in figure 6.22, showed unpredictable results. Concrete's life has been set up to approximately 3 years and the steel one to approximately 5.5 years. The reason why those points of study were chosen was because they were considered the most critical locations where higher arms were presented, the OWT's tower base and where the concrete shaft meets the GBS caisson. To end up with, the time and frequency domain analysis showed results in accordance to the fatigue life expectations. On the one hand, mean and maximum values in tables 6.5 and 6.6 described the largest values for Morison in steel but not for concrete even though Morison is always giving the highest damage in the shaft, in the different figures presented. On the other hand, the frequency spectrums showed a clear dynamic amplification for every studied condition (1,31 and 44) due to the interaction of the natural frequencies of the GBS with a external excitation force. However, since not much information is considered from the Z coordinate, it is not clear what is the external source causing such dynamic amplification even though figure 6.37 shows the 3P - natural frequency interaction.

Chapter 7

Fatigue Damage Prediction

This is the last chapter of the thesis where a full fatigue analysis will be performed according to the conditions described in tables 4.4 and 4.5. Full study means that every condition with their four waves seeds included will be run for both the operational and idle OWT's status. Again, 20 years as well as 1 hour fatigue damage will be computed to determine the overall fatigue life of the GBS and the unit damage for every condition. This will determine what condition contributes to fatigue the most.

However, before starting any analysis, it must be checked if 4 wave seeds are enough to accurately predict fatigue estimation. This means that depending on the results every condition will be studied for a specific number of wave seeds. Additionally, more points in the OWT will be studied in contrast to the two covered in the prior fatigue assessment, as shown in figure 6.22. This new situation will lead to figure 7.1 where 9 nodes will be further investigated but where axial stresses, computed from equation 6.26, are expected to be lower than the two previous studied points. Therefore, according to what has been introduced in section 2.4, increment of stresses, if happened, can lead to crack initiation where if the yield stress is overcome, the problem will be placed into plastic conditions for the steel consideration. Due to this matter, non-linearities are introduced which have to be solved in the frequency domain.

From figure 7.1 points a, b and c refer to the caisson of the GBS, d, e, f to the concrete shaft and g, h and i to the OWT's steel tower. To make this easily interpreted, table 7.1 offers a summary of the study points that will be covered in the full fatigue assessment where the still water line has been set as reference for the nodes height. Additionally, the relative position column has been introduced to facilitate points name location in the three different positions for every element: GBS caisson, shaft and OWT's tower.

As already presented before, 105 different environmental conditions will be simulated in SIMA in order to obtain the different TD results for fatigue damage estimation. Within this, two hydrodynamic models will only be implemented since it was discovered that

MacCamy&Fuchs and potential flow will compute similar fatigue damage results. Therefore, Morison and wave diffraction theory from C_M correction will be compared during this full fatigue analysis.

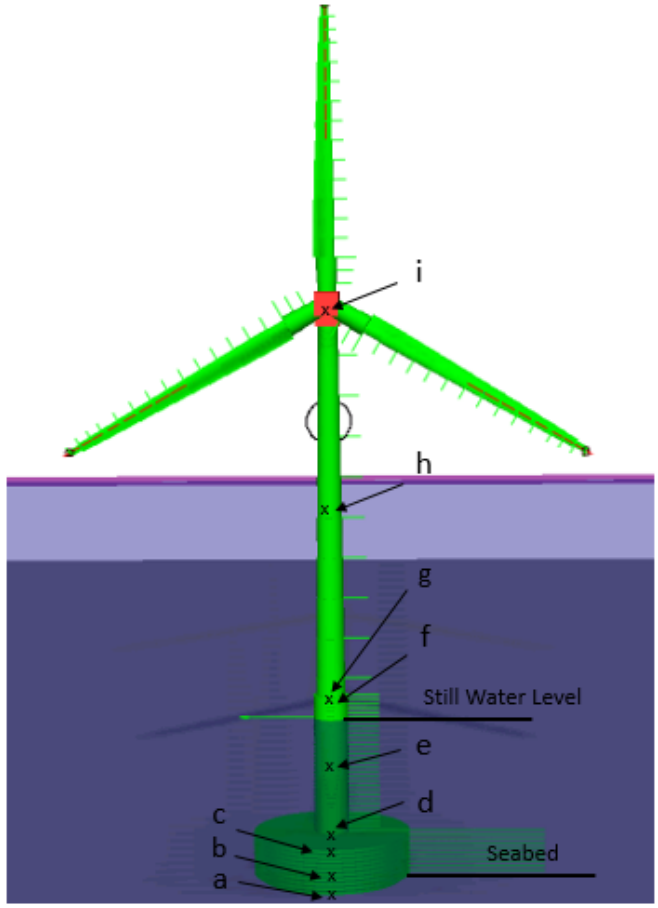

Figure 7.1: Points description of study during full fatigue analysis

Table 7.1: Points description for stresses computation

Relative Position	Concrete caisson [m]		Concrete Shaft [m]		Steel Tower [m]	
Base	**a**	-35	**d**	-25	**g**	5
Middle	**b**	-30	**e**	-12.5	**h**	41
Top	**c**	-25	**f**	5	**i**	82

Finally, as previously done during the pre-fatigue study, wind and waves will still be considered in the same direction, positive x, as it was investigated in 4. This consideration, widely used in the offshore industry, leads to a conservative assumption placing our analysis in the safe side. However, there are still some uncertainties regarding this topic and therefore different directions for wind and waves can still be further investigated during metocean conditions.

Therefore, the following inputs, obtained from figure 4.3, are associated to all the conditions during this full fatigue analysis:

- While 93.79% of the time the turbine is in operational condition, 6.21% of time no power production will be considered. However, fatigue analysis for such idle status will also be considered since wave and winds loads are also present in such circumstances.
- Each condition will be run for a simulation time of 4000 [s] for each wave seed. Assuming and erasing a transient time of 400 [s], results will be established according to 1 hour damage fatigue at every node analyzed from figure 7.1 and table 7.1.
- Wind input files have been created using TurbSim software, according to the wind velocities considered from 4.4 to 4.5.

7.1 Wave Seeds Estimation

In this section the idea is to determine how many wave seeds are needed to obtain a reasonable fatigue damage estimation. These wave seeds are randomly generated sets of numbers where the probability distribution of waves, assuming this random generation of values, generate the random wave statistics.

Therefore, before running the full fatigue estimation, one must be sure that 4 waves seeds, for every condition, will give the enough accuracy when computing fatigue damage. This means that condition 1 will be firstly run with 2 extra more wave seeds to have a wider spectrum to analyze. During the analysis, the mean as well as the standard deviation will be plotted to really understand how many wave seeds are needed to obtain that accurate result. That is why, figures 7.3 and 7.4 show a convergence study to check if both statistical parameters achieve a stable solution.

On the one hand, figure 7.2 represents the obtained one-hour fatigue damage for the 6 different wave seeds analyzed for condition 1 from 4.4. From this figure, one can extract that different damage estimations are obtained for the same condition. This mean, for instance, that it exists a 62% of difference between wave seed 6 and 3 being the minimum and maximum damages obtained respectively. All differences are presented in table 7.2.

On the other hand, figures 7.3 and 7.4 refer exactly to what have been sought. It can be observed how from wave seed 5 for the mean and wave seed 3 for the standard deviation a convergence behaviour starts appearing. Probably, if 8 or 9 waves seeds would have been

employed, the result would have been much more clear. However, the figures clearly state how the more wave seeds are used, the more accurate the damage will be.

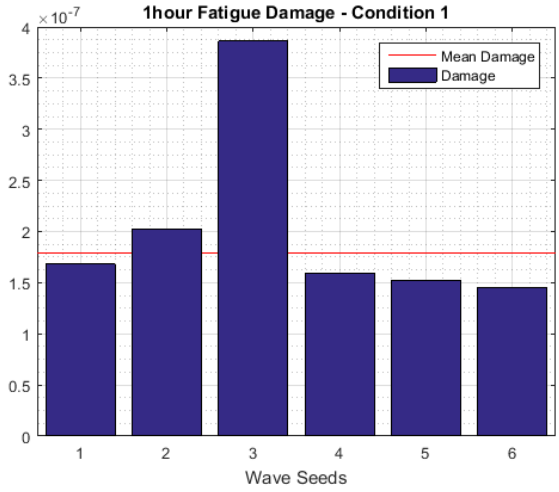

Figure 7.2: One hour fatigue damage at tower base for 6 wave seed - Condition 1

Table 7.2: Relative % of difference between wave seed 3 and the rest

Wave Seeds	1	2	3	4	5	6
% Difference	56.5	47.57	0	58.75	60.45	62.38

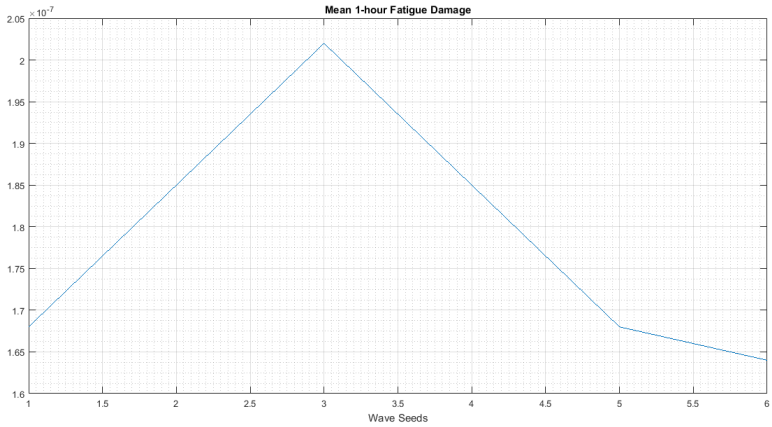

Figure 7.3: Mean value - One hour fatigue damage at the tower base for 6 wave seed - Condition 1

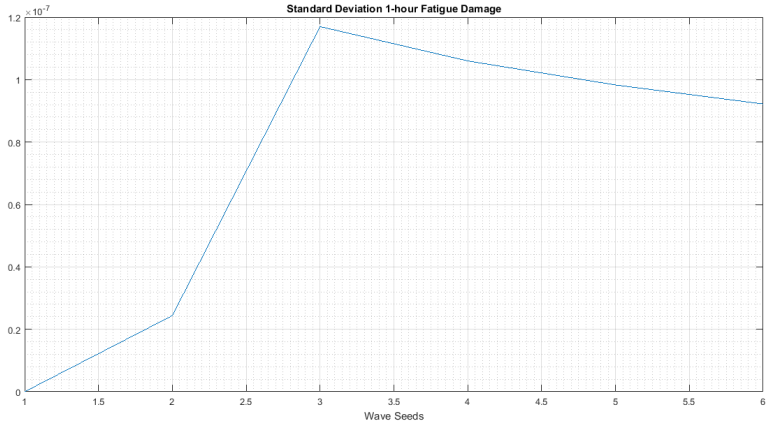

Figure 7.4: Standard Deviation - One hour fatigue damage at the tower base for 6 wave seed - Condition 1

So, it can be concluded that the more wave seeds are used the higher the accuracy in the results. This obviously would lead to a better estimation of the fatigue damage, but will also compromise the time employed for every analysis. As it has been described, TD procedures will result in accurate solutions since large load data is analyzed, however, they are highly time consuming. So, both the time and accuracy have been balanced meaning that it has been finally decided that 4 wave seeds are enough to have both and accurate and a relatively fast TD computation.

7.2 20 Years Fatigue Prediction

As previously studied in the prior fatigue assessment, a 20 years fatigue prediction will now be covered considering the full conditions range as well as the 4 waves seeds. Both, operational and idle status will be considered applying equation 6.29 once the time domain simulations have been carried out.

In this section, spectrum analysis and fatigue life expectation will again be shown to determine what effects lead to fatigue and how much the GBS will last during the 20 years. Additionally, normalized fatigue damage for every condition will also be shown determining what combination of H_s, T_p and U_w will lead to the most fatigue considering the probability of occurrence.

7.2.1 Operational Status

A comparison between Morison and MacCamy&Fuchs is here developed for the full fatigue analysis. Different and similar plots, as the ones in the prior-fatigue assessment, will

be shown to fully determined what is the real difference between both models. This will determine if it was worthwhile to have done all the previous work.

In the Morison and MacCamy&Fuchs comparison, frequency spectrum plots will be only showed for the base location according to the relative position in table 7.1 for the three elements in design: GBS shaft and caisson and OWT's tower. The rest of the spectrums for the other 6 points have been included in the appendix section, see A.2.2. Additionally, both normalized annual damage per condition and 20 years fatigue damage will be displayed for the GBS shaft and caisson and for the OWT's tower containing the three relative position points described in 7.1. These results will then create a general view where a real difference between the models can be captured.

In a second stage, the axial stresses will be shown to exemplify how they are distributed from the seabed to the OWT's tower top. For this study the 81 operational conditions have been considered with only 1 wave seed simulated. This was performed like this since it is just a visual representation of how the whole wind turbine is subjected to such stresses.

Finally, a hybrid model is presented where both Morison and MacCamy&Fuchs theories have been fused. Only the OWT's tower base and the middle point of the shaft has been studied since the first is the weakest point in the steel tower and the latter is an interested location of the submerged shaft.

Morison and MacCamy&Fuchs Comparison

From figure 7.5 to 7.6 is difficult to make a comparison between Morison and MacCamy&Fuchs since every condition with its respective 4 wave seeds has been plotted. This means that just by looking at the plots it is complicated to decide if Morison is given higher Y bending moments than MacCamy&Fuchs. Therefore, specifically looking at condition 28 from 4.4, unpredictable results were obtained. While Morison is slightly larger than MacCamy&Fuchs for steel, the latter is larger in the concrete. This is reflected in table 7.3 where also a % difference has been included relative to the Morison value. Therefore, looking at figures 7.11 - 7.13, it will be determined if MacCamy&Fuchs, with a larger spectrum density value, will lead to a shorter fatigue life. Additionally, it is clearly observable how big moments due to wave effects occur for the base of the GBS caisson in the Y coordinate. Since waves and wind come from the fore-aft direction it is obvious that the responses are notably presented in this bending coordinate. Furthermore, it is seen how large the Y component is compared to the Z one since the latter is basically responding to the dynamic amplification happening at the natural frequency of the OWT. Additionally, this Z component is not of big interest since it is not in the wave and wind direction.

Most of the facts mentioned here have been already commented in the prior fatigue assessment. One should not forget that in the full fatigue analysis all the conditions are now presented with their respective 4 wave seeds. Here, the analysis is now only focus on MacCamy&Fuchc and Morison where similar study procedures will be done as in 6.3.

Other important issues to remark is that the larger the depth the larger the bending moments in the Y coordinate and the larger the natural frequency response. This is exemplified in a maximum peak of almost $6 \cdot 10^8 [kNm^2 s]$ for the base of the GBS caisson and a maximum of $2.5 \cdot 10^8 [kNm^2 s]$ for the OWT's tower base in the Z coordinate for the Morison results. However, as mentioned, not much information is known for this mode and no clear conclusions can be drawn.

Table 7.3: Morison and MacCamy&Fuchs values and relative difference for spectrum density

$S_w\ [kNm^2 s]$	**GBS Caisson base**	**GBS Shaft base**	**OWT's Tower base**
Morison	9.16e^6	5.28e^6	2.63e^6
MacCamy&Fuchs	9.75e6	5.57e^6	2.61e^6
Difference %	106.4	105.5	99.2

Regarding the normalized annual damage it needs to be said that all the conditions have their probability of occurrence included. This means that even though other conditions could lead to a higher fatigue without the probability included, the occurrence is also a crucial factor since it is how nature is affecting the whole wind turbine. Therefore, focusing on the results, it exists a clear difference between concrete and steel values. On the one hand, concrete results in figure 7.8 and 7.9 show again a strong wind dependence, the higher the wind speed the higher the damage. Additionally, it is clearly seen how the conditions leading to the highest damage result in those having the largest probability of occurrence 2.58% for conditions 25 to 29. This also means that the higher the occurrence the higher the damage. Results are exactly the same for the caisson and shaft of the GBS.

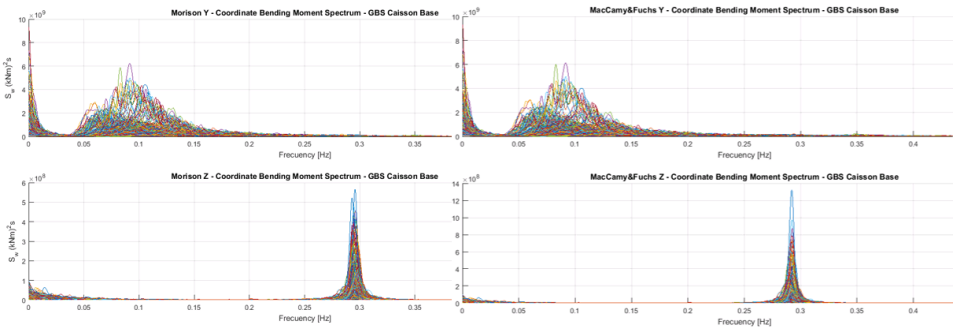

Figure 7.5: Full fatigue analysis spectrum in the GBS caisson base

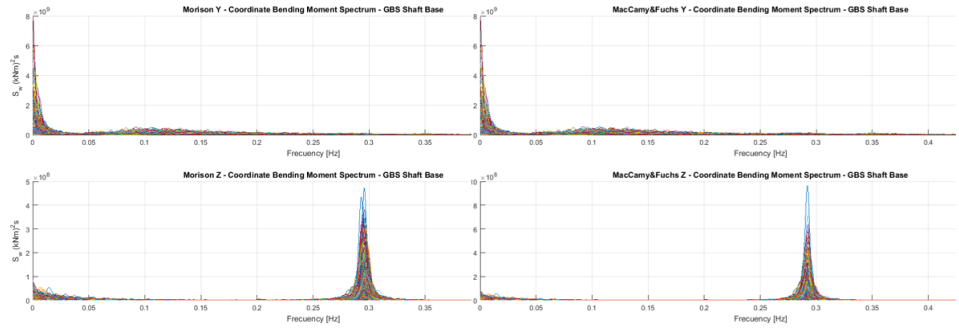

Figure 7.6: Full fatigue analysis spectrum in the GBS shaft base

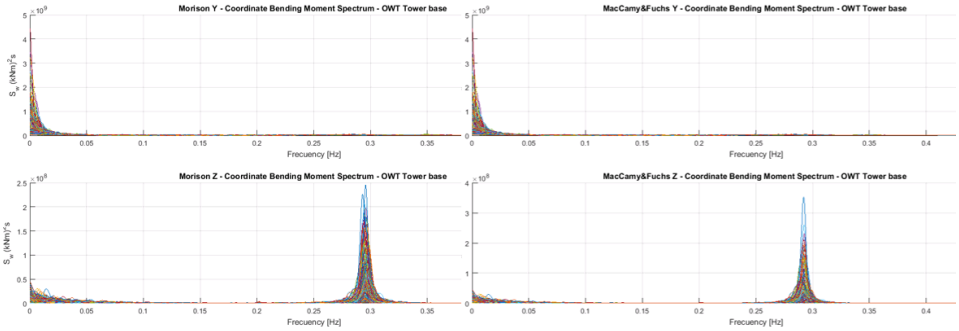

Figure 7.7: Full fatigue analysis spectrum in the OWT's tower base

On the other hand, steel results projected in figure 7.10 also show a strong wind dependence but a slightly lower influence from the probability of occurrence. This is reflected from condition 30 to 34 where even though they do not contain the highest occurrence they are resulting in the highest damage for the base and middle studied points of the OWT's tower. In contrast, the results from the top of the tower diverges from the two other ones. Here the highest damage is given from condition 40 to 44 where 11 and 11.5 m/s of wind speed are considered as well as 1.30% of occurrence. This obviously reflect how the larger the wind speed the larger the damage, with a reasonable high probability of occurrence value. It must be stated that the OWT's tower top values were not expected from a first consideration.

To conclude the normalized damage conditions, the difference between Morison and MacCamy&Fuchs must be commented. It is seen again how for concrete there is not an appreciable gap between both models while for steel the difference is more appreciable. Steel results show how both models swap their positions in leading the damage in every condition, see figure 7.10, but resulting in Morison more harmful as shown in the 20 years fatigue damage reflected in figures 7.11 - 7.13.

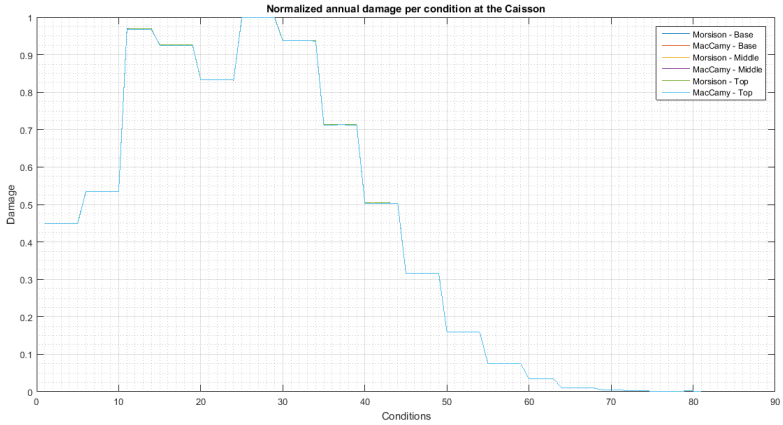

Figure 7.8: Normalized annual damage per condition at the GBS base

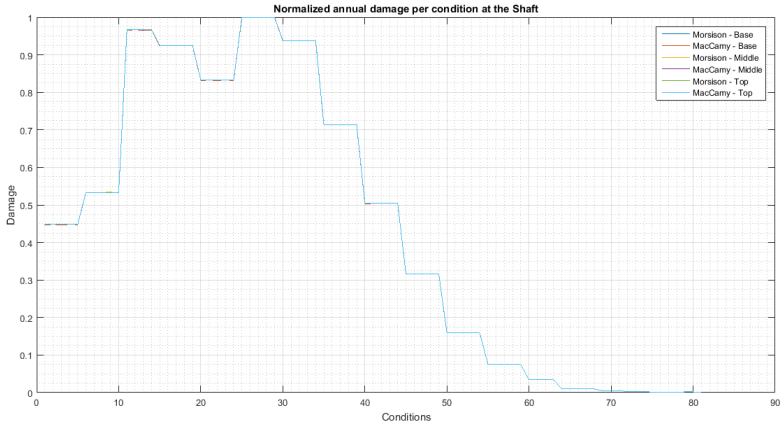

Figure 7.9: Normalized annual damage per condition at the GBS shaft

So, to finish this subsection the 20 years fatigue damage plots are here explained. Regarding concrete results it must again be mentioned that practically no difference is appreciated between the results as shown in figures 7.11 and 7.12. It seems that it does not matter what point is being studied that the whole concrete will fail altogether. Definitely there is still a big topic to study here where a future master thesis can actually go much deeper into concrete fatigue computation to estimate why all the results are so close to each other.

On the one hand, it can be said that the base of the shaft turns to be the weakest point considering Morison theory. However, the gap is so small that it could be said that the whole shaft will last for 2.68 years, independently the hydro model employed. It must be

reminded that according to the DNVGL rule, [64], the cumulative damage ratio equals the unit for locations above the splash zone and is equal to 0.5 for points located below or in the splash zone. This means that in figure 7.12 another red horizontal line must have also been added at 1 since the top of the shaft is located above the splash zone. However, after having checked that the base of the shaft is the one giving the highest damage and that the top of it can be perfectly considered to be on the splash zone, no additional red horizontal line has been included.

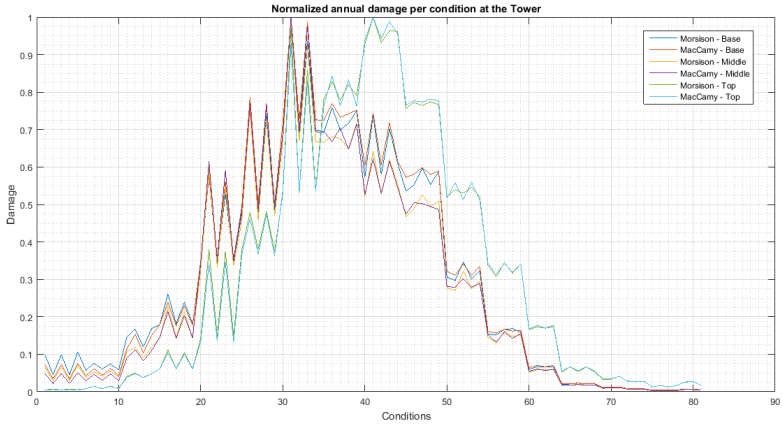

Figure 7.10: Normalized annual damage per condition at the OWT's tower

On the other hand, looking at the concrete GBS caisson results, figure 7.11, one can see how the first three lines from the left, the ones with the highest damage, refer to Morison where the damage is increasing from the top to the bottom of the structure. The other three lines refer to MacCamy&Fuchs where the damage order is also applied from the bottom to the top of the caisson. This is exactly what I was expecting from this study. Finally, the steel results presented in figure 7.13 were also expected. Morison is always over MacCamy&Fuchs and again the damage gets decreased from bottom to top of the OWT's tower. The survival of the tower is expected to be around 4 years whose weakest point is exactly the same it was assumed to be in the prior fatigue assessment, the OWT's tower base.

Therefore, while steel has always given predictable results since it is a material that has been deeply studied for years during the academic training, concrete is something that still requires a more profound study. It is necessary to explain how its extremely sensibility to cycles changing can actually lead to more or less damage since the axial stresses are notably modified.

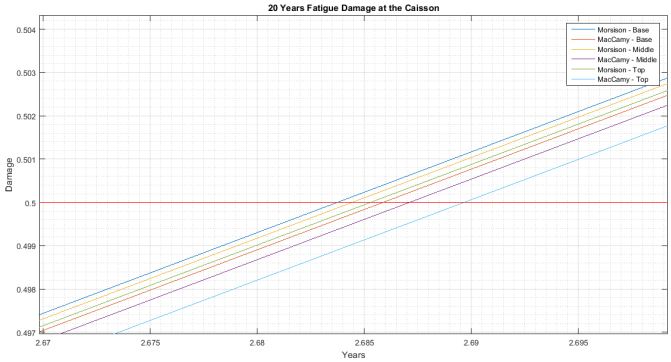

Figure 7.11: 20 years fatigue damage at the GBS caisson

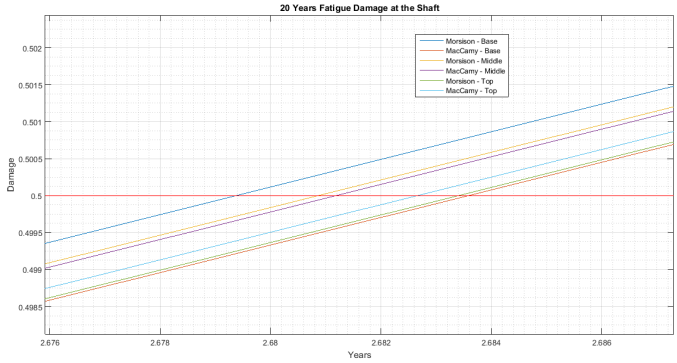

Figure 7.12: 20 years fatigue damage at the GBS shaft

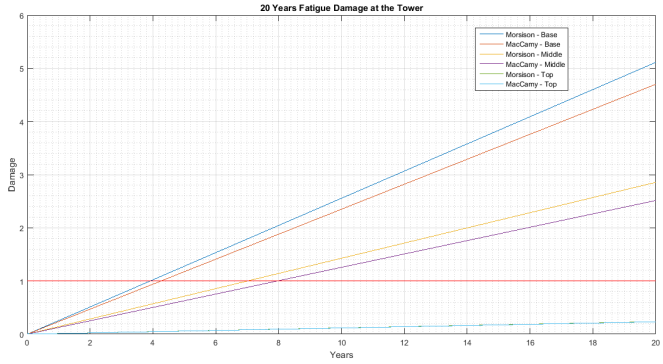

Figure 7.13: 20 years fatigue damage at the OWT's tower

Hybrid Model

Here, the combination of both hydrodynamic models has been developed to actually account more correctly for the wave diffraction effect. As stated in 6.3.2 those conditions with a T_p equals or lower than 9 [s] will need to account for the C_M correction at low wave periods. This means that for condition 3, 5, 10, 11, 14, 16, 19, 21, 24, 26, 29, 31, 34, 36, 39, 41, 44, 47, 49, 52, 54, 57, 58, 59, 62, 66, 68, 71, 78 and 80 from tables 4.4 and 4.5 MacCamy&Fuchs theory will be employed. This will then result in a more accurate fatigue damage prediction since no loads overestimation will be computed for the range where wave diffraction is happening, see figure 2.11.

Therefore, two of the weakest points from 7.1 have been considered; the OWT's tower base and the shaft middle point. However, since the whole concrete fails practically altogether choosing between the shaft or caisson, whichever the point is considered, do not influence at all in the results. So, starting from the 20 years fatigue damage it can be perfectly observed in figures 7.14 and 7.15 how the hybrid model is located at the middle between Morison and MacCamy&Fuchs. This was clearly expected since Morison theory would increase the damage output but MacCamy&Fuchs would lower it down. Again, the survival output is similar to the ones previously obtained where both models were studied separately: 4 years for the OWT's tower base and 2.68 years for the shaft middle point. Additionally, giving relative numbers to the difference in percentage according to Morison, it is obtained that the Hybrid model represents the 95.88% of the Morison damage while MacCamy&Fuchs is up to 91.93%.

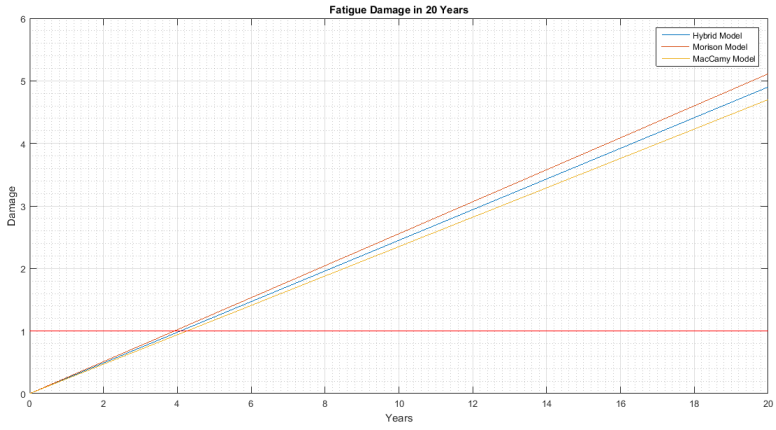

Figure 7.14: 20 years fatigue damage at the OWT's tower base with hybrid model

So, one of the ideas to perform both the prior and full fatigue assessment was to actually determine what hydrodynamic models should be employed and how big the difference is. The prior fatigue accounted for 86.1% of the total probability of occurrence while the full study covered the 93.75%. This 7.65% of difference is actually reflected on the survival

years where tables 7.4 and 7.5 compare, for the steel tower base and shaft middle points, the durability of the concrete and OWT's tower structure.

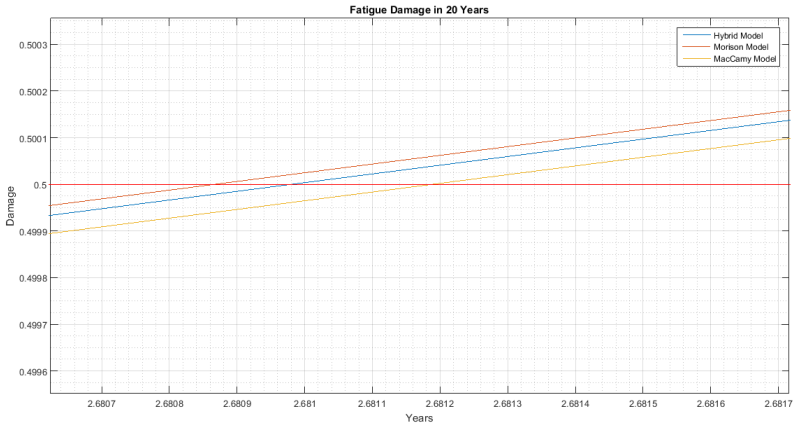

Figure 7.15: 20 years fatigue damage at the GBS shaft middle with hybrid model

Table 7.4: Fatigue life expectation of the OWT's steel tower base

OWT's tower base	% of Occurrence	Morison	Hybrid	MacCamy&Fuchs
Prior Fatigue	86.1	5 years + 2.4 months	-	5 years + 8.4 months
Full Fatigue	93.75	3 years + 10.8 months	4 years + 1.2 months	4 years + 3.6 months

Table 7.5: Fatigue life expectation of the concrete shaft base

Concrete shaft base	% of Occurrence	Morison	Hybrid	MacCamy&Fuchs
Prior Fatigue	86.1	2 years + 11.01 months	-	2 years + 11.06 months
Full Fatigue	93.75	2 years + 8.1702 months	2 years + 8.1717 months	2 years + 8.1742 months

On the one hand, regarding the OWT's tower life expectation in table 7.4, it can be seen how there is an actual difference between both studies, prior and full. It can be determined that it exists a gap of 1.5 years between both analysis leading the prior one to a major fatigue life since less conditions are assumed. On the other hand, fatigue life in concrete does not vary much considering the full or prior analysis. Only a difference of 3 months

is observed where, as already commented, it does not matter neither what hydrodynamic model is employed nor what point in the concrete is chosen that the GBS will fail altogether. Additionally in both tables, the hybrid model is located at the middle of Morison and MacCamy&Fuchs since, as mentioned, Morison does not account for the wave diffraction effect where overestimation of loads are considered.

So, a point of discussion must be made here according to the results obtained in tables 7.4 and 7.5. As seen, there is not a big difference between Morison and MacCamy&Fuchs fatigue life results, 5 months in steel and 0 in concrete, to actually choose between one or another. Additionally, if the GBS and OWT's tower did not fail so soon, the difference of fatigue life between the hydrodynamic models would be larger since the damage is increasing linearly for both. Therefore, it is hard, according to the results, to determine what hydrodynamic model should be employed to more accurately predict the durability of the concrete and steel structures.

Firstly, it needs to be mentioned that Morison must be definitely rejected since wave diffraction effects are not accounted for. So, the discussion is now reduced to the Hybrid and MacCamy&Fuchs model. Therefore, checking figure 2.13, one could think that applying only MacCamy&Fuchs would be the most accurately way of accounting for wave effects since it considers wave diffraction for short waves and estimate similar results to Morison when going for large λ/D ratios. Additionally, since two different diameters are considered, the hybrid model introduces some important uncertainties when choosing the wave diffraction limit, $T_p = 9[s]$. This leads to a situation where MacCamy&Fuchs is considered the best option. However, since the differences in steel for the 2 hydrodynamics models are quite small and the hybrid results have offered more conservative values, the discussion is still open.

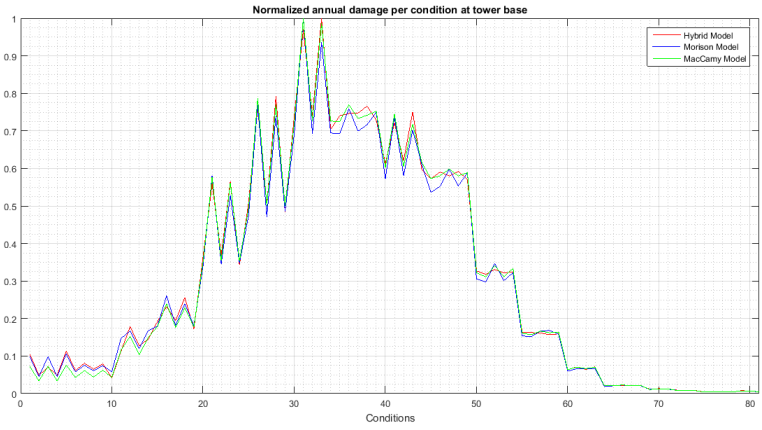

Figure 7.16: Normalized annual damage per condition at the OWT's tower base with hybrid model

Finally, the normalized annual damage per condition is again shown in figures 7.16 and

7.17 since it was thought that maybe it would change for the hybrid model. On the one hand, concrete's results are exactly the same as for the previous subsection 7.2.1 whose properties are strongly influenced by the wind speed and probability of occurrence. Again, it does not matter what hydrodynamic model is employed that results will not differ at all for concrete. On the other hand, results in steel reveal similar values with very little variance. For the whole spectrum, the different hydrodynamic models are being superposed with each other giving less or more damage depending on the H_s, T_p and U_w employed. However, according 7.14, Morison will lead to the highest damage since it is giving the soonest structural failure.

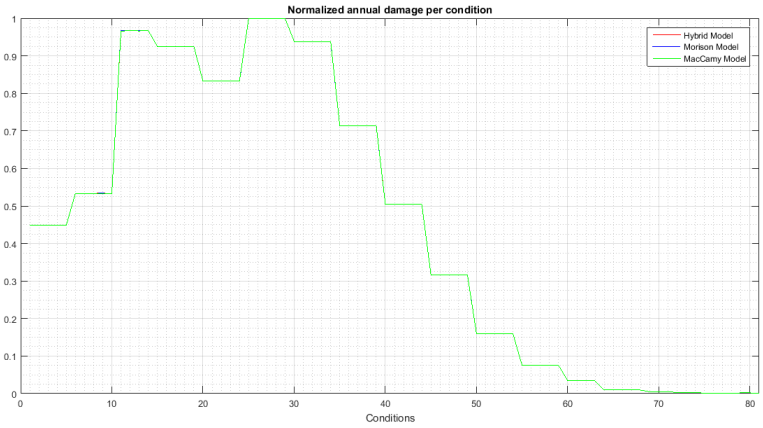

Figure 7.17: Normalized annual damage per condition at the GBS shaft middle with hybrid model

7.2.2 Non-Operational Status

With an exactly similar approach as for the operational conditions, here the idle turbine status has also been analyzed. Even though the OWT will not be producing any electric power, non-operational conditions must be considered since they also contribute to fatigue damage.

For the analysis, it must be mentioned that a hybrid model has been built. As previously seen, the difference between Morison, the hybrid and MacCamy&Fuchs model is practically negligible for both the concrete and steel material. Therefore, it was considered that employing a mixture between Morison and the wave diffraction theory was still the most useful consideration, keeping in mind the uncertainties introduced when choosing the wave diffraction limit. So, conditions 2, 6, 10 and 12 has been modelled according to a C_M correction factor for small periods of waves. Additionally, since the turbine will be in idle status, the blades will be stopped and in feathered position. This is later reflected in the frequency spectrum plots where wind effect in both coordinates has practically disappeared.

Therefore in figure 7.18 it can be observed how both the steel and concrete structure will not fail during the 20 years life expectation. While the steel shows practically no countable damage, the concrete structure reveals some fatigue accumulation that it does not result in failure thou. So, one of the most important reasons to determine why the damage is so low is due to practically zero wind effect due to the feathered blades position. This is reflected in every non-operational frequency spectrum plot, see figures 7.19 - 7.21, since no bending is appearing in low frequencies, where the wind is always acting. However, wave effects are still present as shown in the figures, where their importance is increasing while going for deeper depths, as known. Additionally, in contrast to any operational frequency spectrum plot, waves have now become the largest reason why the structure is bending in the Y coordinate as clearly reflected in figure 7.21. If we compared this last figure with exactly the same one but in the operational status, it will be seen how for the latter wind becomes the most important reason for the OWT to bend in the Y coordinate, as reflected in figure 7.6. Furthermore, some dynamic amplification is now appearing in the Y coordinate as the result of the wave interaction. This effect, with a maximum peak of $1.5 \cdot 10^8 (kNm)^2 s$ in figure 7.21, was probably hidden by the wind component in the operational status since its value was around $8 \cdot 10^9 (kNm)^2 s$, depending on the studied point. Lastly, it must be mentioned that the Z coordinate bending moment has now decreased for every plotted figure, 7.19 - 7.21, since wind is not practically contributing now to the bending of the OWT. The rest of the non-operational frequency spectrum plots have been added in the appendix section, see A.2.3.

Finally, the normalized annual damage has again been plotted in figure 7.22 showing what conditions are leading to the most fatigue damage. Once more, concrete and steel materials' failure are definitely driven by the wind speed and % of occurrence. Additionally, it must never be forgotten that the higher the H_s the higher the damage while the lower the T_p the higher the damage.

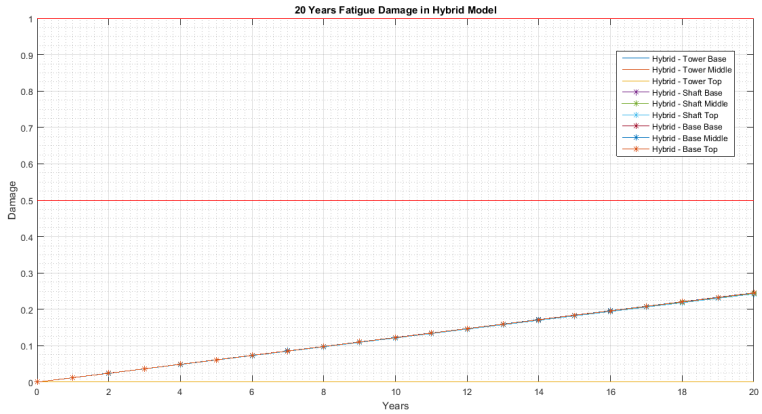

Figure 7.18: 20 years fatigue damage at the whole wind turbine for idle status

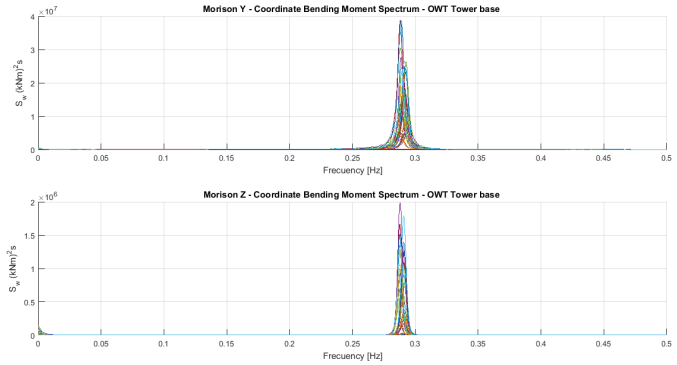

Figure 7.19: Non operational frequency spectrum at the Tower base

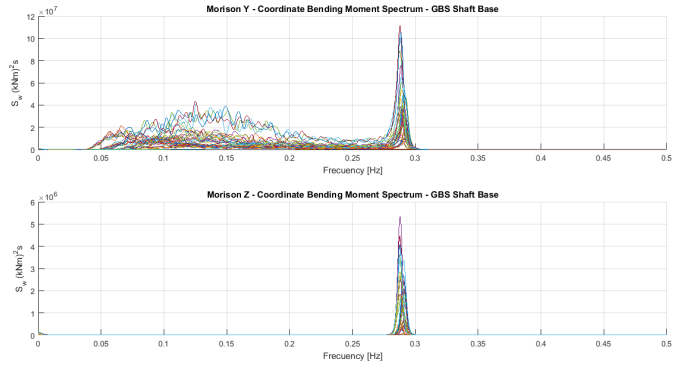

Figure 7.20: Non operational frequency spectrum at the GBS shaft base

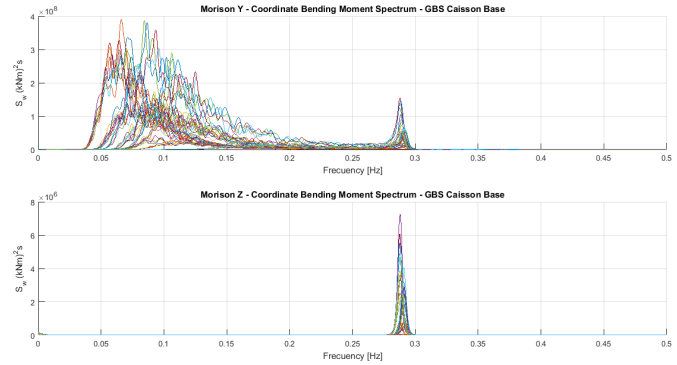

Figure 7.21: Non operational frequency spectrum at the GBS Caisson base

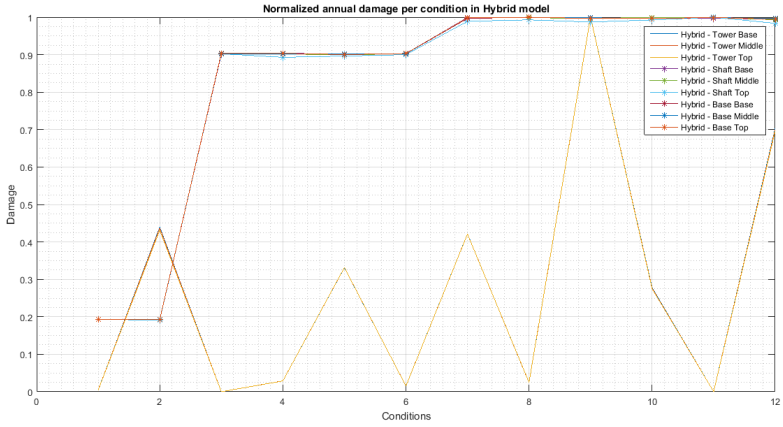

Figure 7.22: Normalized annual damage per condition at the whole wind turbine for idle status

7.3 Conclusions

To summarize this section the following items are described:

- Wave seed estimation study revealed that the more wave seeds are used the higher the accuracy when estimating the fatigue damage at any point of the OWT. According to the mean and standard deviation convergence studies, it was considered that 4 wave seeds give a reasonable good damage estimation keeping in mind accuracy and time need for the whole TD simulation to be run.

- From Morison and MacCamy&Fuchs comparison it can be checked in table 7.3 how the spectral density differences do not exceed more than a 6.5% in concrete and a 1% in steel for condition 28. This condition, with the highest % of occurrence, shows how MacCamy&Fuchs is over Morison for the caisson and shaft of the GBS while Morison is leading for the OWT's tower base. However, as seen in figures 7.11 - 7.13, Morison will always lead the shortest fatigue life with a clear gap over MacCamy&Fuchs for steel and practically no difference for concrete studies. Additionally, the normalized annual damage plots, see figures 7.8 - 7.10, reconfirm the strong wind and % of occurrence dependence for the concrete material as well as a strong wind effect for steel but with a slightly less influence from the probability of occurrence. Therefore, it can be concluded that spectral density studies are not useful to determine what hydrodynamic model will lead to more or less damage. They are used to understand what is the even happening the most and why. Additionally, since both models reveal quite similar results, it is only on the 20 years fatigue life plots where the actual difference in damage for both models can be checked.

- Regrading the hybrid simulation, the obtained results revealed a good performance of the model. Here, conditions with a T_p equal or lower to 9 [s] has been simulated with the C_M factor correction whose results are shown in figures 7.14 and 7.15 and

tables 7.4 and 7.5.The hybrid values in the 20 years life plot have been obtained at the middle of Morison and MacCamy&Fuchs since load overestimation has not been accounted for in small wave periods. Specifically, the hybrid computation for steel represents the 95.88% of the Morison damage while the 91.93% has been set to MacCamy&Fuchs compared to Morison again. The difference for concrete is so inappreciable that no comments are made. Therefore, after having checked how the hybrid model behaves it must be stated the real doubt created when defining what hydrodynamic model adapts the best to the OWT. Definitely Morison is erased since wave diffraction is happening and it is not being accounted for. So, the discussion was reduced to MacCamy&Fuchs and the hybrid model where the first one was considered the most appropriate. It is estimated that MacCamy&Fuchs accounts more correctly the wave loads when going for small and large λ/D ratios. Additionally, since two different diameters are considered, the hybrid model introduces some important uncertainties when choosing the wave diffraction limit, $Tp = 9[s]$. However, keeping in mind that both models reveal similar results and that the hybrid values offer a conservative estimation, the discussion is left open.

- For the non operational conditions it is described a simulation environment where the blades are stopped and in feathered position and where the OWT is in idle status. Additionally, a hybrid model was employed where one of the most relevant results are presented in the Y bending spectrum since the wind is now not relevant at all. Here, waves have now become the largest reason why the structure is bending in the fore-aft direction where its influence is increasing while going for deeper waters. Additionally, since the wind is not considered now in the external excitation, the dynamic amplification offered in every Z bending coordinate has now been reduced.

Chapter 8

Conclusions and Future Work

8.1 Conclusions

An integrated dynamic analysis has been performed for a 5 MW OWT on top of a gravity based structure. In this scenario, the gravity based design literature as well as fatigue in concrete have been the topics to focus the most since no prior knowledge had been acquired. From the latter it was determined that after having reviewed three different references (DNV - Offshore concrete structures: [66], DNVGL - Offshore concrete structures: [64] and Spanish&Eurocode regulations: [52] [32]) the first one was finally employed for the RC fatigue assessment. Here, even though SN curves for concrete do not compute the damage correctly, they are still being used for the industry. This means that fatigue in the RC has been estimated only from the fatigue in the concrete since the stresses in the steel reinforcing bars have not been considered. This obviously has introduced some uncertainties that has been considered when treating the results.

In a second stage, the preliminary design of the GBS ended up in good results. While in the static load analysis the total vertical and horizontal forces as well as the total overturning moment were computed, the soil bearing capacity study checked that the soil was able to withstand the vertical forces coming from the OWT. While tables 3.3, 3.4 refer to the global loads analysis, table 3.7 confirmed that at any possible rotational point of the GBS, the soil had the sufficient strength to withstand the vertical force acting directly through the symmetry line of the OWT. In a final design checking step, it was reaffirmed the good behaviour of the structure. This is shown in tables 3.8 and 3.9 where it is observed how decreasing by half the soil stiffness the natural period of the OWT increased and where the maximum pitch value of the GBS caisson did not exceed a value of 0.1 [degrees]. It must never be forgotten that 35 [m] of water depth are being considered.

Thirdly, an exhaustive metocean analysis revealed how the subtropical traits of the GBS location are strongly shaped by the never ending humid trade winds. According to the data provided for 29 years, the marginal distribution study for both the U_w and H_s revealed

good fitting for the first and some disagreement for the latter in both tails, see figure 4.7, where some underestimation of the extreme values has occurred. Additionally, both the wave and wind roses, see figures 4.10 - 4.13, have shown a quite dominant north-east direction whose values will be treated as aligned, only considering one major direction component. This means that mostly the same points of the GBS will be affected by the wind and wave loads causing concentrated fatigue damage at that same locations. However, this is a widely used conservative assumption in the offshore industry leading the designs to the safe side. Finally, it was computed that 90,53% of the whole scatter was actually considered in the study where, from that percentage, 93.73% refers to an operational range, while the other 6.21% refers to an idle status.

Fourthly, a series of identification tests revealed again the good behaviour of the OWT. On the one hand, the natural frequencies from the first fore-aft and side-side bending modes resulted in 0.29 [Hz]. Additionally, while the GBS showed little interaction with the surrounding waters, as estimated from the linear damping, the quadratic drag type showed even less influence mostly characterized by the aerodynamic damping effect, see table 5.1. On the other hand, the rotor speed, thrust, power output as well as blade pitch angle were computed in order to build the so called wind turbine performance curves reflected in figures 5.5 and 5.6. From such values, the 1P and 3P rotations from the blade passing frequency showed a good distribution with the natural and external excitations for resonance problems to be avoided, see figure 5.8.

In a fifth step, the combination of the three hydrodynamic models resulted in interesting prior fatigue assessment results. On the one hand, it was determined that potential flow was rejected for the full fatigue study since similar results to MacCamy&Fuchs were obtained and much more work was needed compared to it, see figures 6.48 - 6.51. Additionally, the total integrated force as well as the potential flow hydrodynamic loads showed good answers to the wave diffraction problem. While the total integrated force revealed convergence and divergence between Morison and MacCamy&Fuchs - Potential flow for small and long wave periods respectively, see figure 6.1, the added mass for surge and heave showed a frequency dependence behaviour, while linear damping offered a much stronger dependence for every motion as seen in figure 6.11. Additionally, the first-order wave excitation and linear damping offered good responses since both the low and high frequency values tended to zero. In combination to previous studies, frequency spectrum plots and structural displacement analysis verified that the GBS was so stiff that the bending moments occurring due to large stiffness forces were not actually being transferred to the OWT's tower. This means that inertia is not considered at all when taking up the external loads affecting the GBS. In addition to the frequency spectrum plots, it is also determined how the larger the depth, the larger the wave effects on the spectrum and the larger the H_s and the shorter the T_p the more damage is induced. On the other hand, the prior fatigue assessment for the tower and shaft base, has verified that Morison accounts for the highest fatigue damage as shown in the 1 hour plot and the 20 years expected fatigue life for both steel and concrete, see figures 6.26 and 6.30. This means that results have brought forth how concrete's life has been set up to approximately 3 years and the steel one to approximately 5.5 years.

In the last chapter it could be verified how the more wave seeds are employed the higher the accuracy for fatigue damage estimation. 4 wave seeds were finally considered to balance both time and accuracy for TD simulations. Secondly, the full fatigue comparison between Morison and MacCamy&Fuchs determined how spectral density plots were not appropriate to estimate what model is leading to the highest fatigue. Specifically, table 7.3 showed how the spectral density differences did not exceed more than a 6.5% in concrete and a 1% in steel for condition 28, the one with the highest % of occurrence. So, a hybrid model was built to actually state the final difference between Morison and MacCamy&Fuchs. This meant that for T_p values lower or equal to 9 [s] the C_M factor correction was applied where the hybrid computation for steel represented the 95.88% of the Morison damage while the 91.93% was considered to MacCamyFuchs against Morison. Therefore, it must be stated that real doubts are placed on scene when finally choosing the hydrodynamic model that adapts the best to this OWT. Definitely Morison was erased since wave diffraction is happening and it is not being accounted for. So, the discussion was reduced to MacCamyFuchs and the hybrid model where the first one was considered the most appropriate since it accounts more correctly the wave loads estimation when going for small and large λ/D ratios, see figure 2.13. Additionally, since two different diameters are considered, the hybrid model introduced some important uncertainties when choosing the wave diffraction limit. However, keeping in mind that both models reveal similar results and that the hybrid values offer a conservative estimation, the discussion mostly agree that both hydrodynamic models are appropriate for the GBS. To finish this section, the non-operational status was run determining how the damage is highly influenced by the waves action since no wind is reflected in the Y bending spectrum density plots. It was also clear stated that the larger the depth the larger the waves effect.

8.2 Future Work

In order to improve the work resulted from this thesis, the following future lines must be further developed:

- Concrete is the biggest issue to look at. Firstly, in order to reduce the level of uncertainties, the approach to establish fatigue in this material must be carefully revised. Considering that SN curves do not work well, a profound research to more accurately predict fatigue loads should be considered. However, there are already PhD lines trying to replace SN curves with more accurate methods. Secondly, the loads on the reinforcements can be addressed. To perform this, FE tools can be considered like ABAQUS or ANSYS to derive the loads on the reinforcements. Alternatively, an equivalent stiffness can be built for the RC. This implies derivation of Markov matrix of stresses which can be then applied to a separate FE model to find the stresses in the reinforcement. Thirdly, the fatigue durability of the shaft and caisson would need to be revised since practically similar values are obtained for any point of the GBS. Additionally, as mentioned before, independently of the hydrodynamic model employed the prediction is mostly the same.

- To really determine how the structure would react, real soil parameters for the Gran Canaria location must be employed. Both real soil stiffness as well as real ultimate bearing stress are crucial since the static as well as dynamic loads on the GBS are highly influenced by the geotechnical characteristics. Additionally, the bearing capacity is also directly linked to the type of soil described.
- Since the RC GBS is highly stiff. Future lines can address how the concrete structure can take up the loads since large stiffness forces are now presented where zero displacement is induced. This can definitely be another reason why the concrete material is failing so soon. This means that a study could cover a more flexible GBS where inertia becomes a topic to distribute loads from the shaft to the OWT's tower.

Bibliography

[1] Agencia Estatal de Meteorologa - Gobierno de Espaa, Ministerio de Agricultura y Pesca, Alimentacin y Medio Ambiente. https://www.aemet.es/es/eltiempo. [Online; accessed 23-January-2018].

[2] Creep and Shrinkage of Concrete. https://en.wikipedia.org/wiki/Creep_and_shrinkage_of_concrete. [Online; accessed 14-February-2018].

[3] Elisa and Elican Project. https://esteyco.com/projects/elisa/index.html. [Online; accessed 25-January-2018].

[4] Environment's Aggressiveness. https://www.fdot.gov/structures/StructuresManual/2009january/DesignGuidelines/SDG1.3EnvClassifications.htm. [Online; accessed 10-April-2018].

[5] GBS Cells description. https://www.icdas.dk/viewpage.php?page_id=1. [Online; accessed 18-January-2018].

[6] International Energy Agency. https://www.iea.org/. [Online; accessed 30-May-2018].

[7] Monopile Estructure. http://www.4coffshore.com/windfarms/monopiles-support-structures-aid4.html. [Online; accessed 14-December-2017].

[8] Offshore Wind Industry review of GBSs. https://www.carbontrust.com/media/672062/ctc844-offshore-wind-industry-review-gbs-gravity-base-foundations.pdf. [Online; accessed 17-January-2018].

[9] PLOCAN Test Area. https://www.plocan.eu/index.php/es/. [Online; accessed 26-January-2018].

[10] Puertos del Estado - Gobierno de Espaa, Ministerio de Fomento. :http://www.puertos.es/es-es/oceanografia/Paginas/portus.aspx. [Online; accessed 22-January-2018].

[11] Reinforced Concrete. https://www.aboutcivil.org/reinforced-cement-concrete-design.html. [Online; accessed 17-January-2018].

[12] Strain Softening. https://www.theconcreteportal.com/intro.html. [Online; accessed 07-February-2018].

[13] Streamlines representation. https://math3402rebeccacoates.wordpress.com/2013/10/19/pathlines-streamlines/. [Online; accessed 23-March-2018].

[14] WAMIT. https://www.wamit.com. [Online; accessed 26-April-2018].

[15] Wind Europe. https://windeurope.org/about-us/new-identity/. [Online; accessed 27-September-2017].

[16] Wind Power Engineering. http://www.windpowerengineering.com/offshore-wind/foundations-that-float/. [Online; accessed 28-September-2017].

[17] Wind Shear Model. https://www.idae.es/. [Online; accessed 30-January-2018].

[18] Bhagwan D Agarwal, Lawrence J Broutman, and K Chandrashekhara. *Analysis and performance of fiber composites*. John Wiley & Sons, 2017.

[19] L Arany, S Bhattacharya, JHG Macdonald, and SJ Hogan. Simplified critical mudline bending moment spectra of offshore wind turbine support structures. wind energy, 18 (12), 2171-2197. doi: 10.1002/we. 1812.

[20] A Arntsen and HE Krogstad. Linear wave theory, part a: Regular waves. *Department of Civil and Transport Engineering, NTNU, Trondheim*, 2000.

[21] Erin Bachynski. Basic aerodynamics for wind turbines. *Lecture Notes for Course Inte*, 2015.

[22] Erin E Bachynski, Trygve Kristiansen, and Maxime Thys. Experimental and numerical investigations of monopile ringing in irregular finite-depth water waves. *Applied Ocean Research*, 68:154–170, 2017.

[23] Erin E Bachynski and Harald Ormberg. Hydrodynamic modeling of large-diameter bottom-fixed offshore wind turbines. *ASME Paper No. OMAE2015-42028*, 2015.

[24] C Bak, F Zahle, R Bitsche, T Kim, A Yde, LC Henriksen, A Natarajan, and M Hansen. Description of the dtu 10 mw reference wind turbine 2013. *DTU Wind Energy Report-I-0092*.

[25] Stig Berge. Fatigue and fracture design of marine structures, 2006.

[26] Kenneth F Bowden. *Physical oceanography of coastal waters*. E. Horwood, 1983.

[27] DJ Cerda and J van der Tempel. Aerodynamic damping in the design of support structures for offshore wind turbines. 2005.

[28] Price Code. Eurocode 2: Design of concrete structures-part 1-1: General rules and rules for buildings. 2005.

[29] Price Code. Eurocode 8: Design of structures for earthquake resistance-part 1: General rules, seismic actions and rules for buildings. *Brussels: European Committee for Standardization*, 2005.

[30] Comité Europeo de Normalización. *Eurocódigo 2: Proyecto de estructuras de hormigón*. Aenor, 1993.

[31] Robert G Dean and Robert A Dalrymple. *Water wave mechanics for engineers and scientists*, volume 2. World Scientific Publishing Company, 1991.

[32] Instrucción del Hormigón Estructural. Ehe-08. *Madrid, Ministerio de Fomento, Secretaría General Técnica*, 2008.

[33] Christof Devriendt, Pieter Jan Jordaens, Gert De Sitter, and Patrick Guillaume. Damping estimation of an offshore wind turbine on a monopile foundation. *IET Renewable Power Generation*, 7(4):401–412, 2013.

[34] DNV DNV-RP. C203 fatigue design of offshore steel structures. *Recomm Pract DNV-RPC203*, 126, 2005.

[35] BS EN. 206-1: 2000 concrete. *Specification, performance, production and conformity*, page 22, 2001.

[36] Wind Europe. The european offshore wind industry–key trends and statistics 2014, 2014.

[37] Wind Europe. The european offshore wind industry–key trends and statistics 1st half 2016, 2016.

[38] Odd Faltinsen. *Sea loads on ships and offshore structures*, volume 1. Cambridge university press, 1993.

[39] Frida Göransson and Anna Nordenmark. Fatigue assessment of concrete foundations for wind power plants. 2011.

[40] Martin OL Hansen. *Aerodynamics of wind turbines*. Routledge, 2015.

[41] Sverre Haver. *Analysis of uncertainties related to the stochastic modelling of ocean waves*. 1980.

[42] A Ho, A Mbistrova, and G Corbetta. The european offshore wind industry key trends and statistics. 2015.

[43] Kenneth Johannessen, Trond Stokka Meling, Sverre Hayer, et al. Joint distribution for wind and waves in the northern north sea. In *The Eleventh International Offshore and Polar Engineering Conference*. International Society of Offshore and Polar Engineers, 2001.

[44] Jason Jonkman, Sandy Butterfield, Walter Musial, and George Scott. Definition of a 5-mw reference wind turbine for offshore system development. Technical report, National Renewable Energy Lab.(NREL), Golden, CO (United States), 2009.

[45] RT Koekkoek. Gravity base foundations for offshore wind turbines. 2015.

[46] Marit I Kvittem and Torgeir Moan. Time domain analysis procedures for fatigue assessment of a semi-submersible wind turbine. *Marine Structures*, 40:38–59, 2015.

[47] Ivar Langen and Ragnar Sigbjörnsson. *Dynamisk analyse av konstruksjoner: Dynamic analysis of structures*. Tapir, 1979.

[48] Richard D Larrabee and C Allin Cornell. Upcrossing rate solution for load combinations. *Journal of the Structural Division*, 105(1):125–132, 1979.

[49] Lin Li, Zhen Gao, and Torgeir Moan. Joint environmental data at five european offshore sites for design of combined wind and wave energy devices. In *ASME 32nd International Conference on Ocean, Offshore and Arctic Engineering, Nantes, France, June*, pages 9–14, 2013.

[50] Enzo Marino, Alessandro Giusti, and Lance Manuel. Offshore wind turbine fatigue loads: The influence of alternative wave modeling for different turbulent and mean winds. *Renewable Energy*, 102:157–169, 2017.

[51] Torgeir Moan. Finite element modelling and analysis of marine structures. *NTNU, Institutt for Marin Teknikk*, 2003.

[52] P Jiménez Montoya, Álvaro García Meseguer, and Francisco Morán Cabré. *Hormigón armado*. Gustavo Gili, 2000.

[53] Arvid Naess and Torgeir Moan. *Stochastic dynamics of marine structures*. Cambridge University Press, 2012.

[54] John Nicholas Newman and John Grue. *Marine hydrodynamics*. MIT press, 2018.

[55] Kenneth Peire, HENDRIK Nonneman, and Eric Bosschem. Gravity base foundations for the thornton bank offshore wind farm. *Terra et Aqua*, 115:19–29, 2009.

[56] Maxime Philippe, Bruno Borgarino, Panagiotis Kotronis, and Guillaume Ducrozet. An integrated approach for the representation of concrete gravity based foundations for offshore wind turbines. In *ASME 2013 32nd International Conference on Ocean, Offshore and Arctic Engineering*, pages V008T09A033–V008T09A033. American Society of Mechanical Engineers, 2013.

[57] BRITISH STANDARD. Testing hardened concrete. 2009.

[58] Sverre Steen and Jan V Aarsnes. Experimental methods in marine hydrodynamics. *Lecture Notes, Department of Marine Technology, Norwegian University of Science and Technology, Trondheim, Norway*, 2014.

[59] Kristian Freng Svendsen. Structural design and dynamic analysis of a tension leg platform wind turbine, considering elasticity in the hull. Master's thesis, NTNU, 2016.

[60] AH Techet. Morrisons equation. *Class Notes: Spring*, 2004.

[61] AH Techet. 2.016 hydrodynamics. *Lecture Notes*, 2005.

[62] Jan Van Der Tempel. Design of support structures for offshore wind turbines. 2006.

[63] MJP van Wijngaarden. Gravity based foundations for offshore wind turbines: Cyclic loading and liquefaction. 2017.

[64] Det Norske Veritas. Offshore concrete structures. *Offshore Standard DNV-OS-C502*, 2004.

[65] DNV-Det Norske Veritas. Dnv-os-j101 offshore standard. *Design of offshore wind turbine structures*, 2010.

[66] Norske Veritas. *Guidelines for design of wind turbines*. Det Norske Veritas: Wind Energy Department, Ris National Laboratory, 2002.

[67] Ling Wan. Experimental and numerical study of a combined offshore wind and wave energy converter concept. 2016.

[68] M.(2005) Zaaijer. Design methods for offshore wind turbines at exposed sites. technical report, delft university of technology.

Appendix A

Appendix

A.1 Wave Scatter Diagrams

Percentage of ocurrence (%) - Peak Wave Period vs Significant Wave Height vs 0-1 [m/s]																									
Significant Wave Height [m]	5-6	0,000	0,000	0,000	0,000	0,000	0,000	0,000	0,000	0,000	0,000	0,000	0,000	0,000	0,000	0,000	0,000	0	0	0	0	0	0	0	0
	4-5	0,000	0,000	0,000	0,000	0,000	0,000	0,000	0,000	0,000	0,000	0,000	0,000	0,000	0,000	0,000	0,000	0	0	0	0	0	0	0	0
	3-4	0,000	0,000	0,000	0,000	0,000	0,000	0,000	0,000	0,000	0,000	0,000	0,000	0,000	0,000	0,000	0,000	0	0	0	0	0	0	0	0
	2-3	0,000	0,000	0,000	0,000	0,000	0,000	0,000	0,000	0,000	0,000	0,000	0,002	0,000	0,000	0,005	0,000	0	0,002	0	0	0	0	0	0
	1-2	0,000	0,000	0,000	0,000	0,000	0,000	0,000	0,025	0,030	0,023	0,018	0,018	0,000	0,005	0,000	0,000	0	0,002	0	0	0	0	0	0
	0-1	0,000	0,000	0,000	0,000	0,000	0,002	0,002	0,023	0,011	0,041	0,011	0,016	0,000	0,005	0,000	0,000	0	0	0	0	0	0	0	0
		1-2	2-3	3-4	4-5	5-6	6-7	7-8	8-9	9-10	10-11	11-12	12-13	13-14	14-15	15-16	16-17	17-18	18-19	19-20	20-21	21-22	22-23	23-24	24-25	25-26
		Peak Wave Period [s]																							

Figure A.1: Wave Scatter Wind Speed Range: 0-1 m/s

Percentage of ocurrence (%) - Peak Wave Period vs Significant Wave Height vs 1-2 [m/s]																									
Significant Wave Height [m]	5-6	0,000	0,000	0,000	0,000	0,000	0,000	0,000	0,000	0,000	0,000	0,000	0,000	0,000	0,000	0,000	0,000	0	0	0	0	0	0	0	0
	4-5	0,000	0,000	0,000	0,000	0,000	0,000	0,000	0,000	0,000	0,000	0,000	0,000	0,000	0,000	0,000	0,000	0	0	0	0	0	0	0	0
	3-4	0,000	0,000	0,000	0,000	0,000	0,000	0,000	0,000	0,000	0,000	0,000	0,002	0,000	0,000	0,000	0,000	0	0	0	0	0	0	0	0
	2-3	0,000	0,000	0,000	0,000	0,000	0,000	0,000	0,000	0,005	0,014	0,014	0,037	0,000	0,005	0,002	0,000	0,005	0,002	0	0	0	0	0	0
	1-2	0,000	0,000	0,000	0,000	0,000	0,007	0,002	0,107	0,132	0,226	0,169	0,196	0,002	0,091	0,034	0,000	0,016	0,002	0	0	0	0	0	0
	0-1	0,000	0,000	0,005	0,002	0,000	0,016	0,021	0,210	0,121	0,230	0,162	0,199	0,002	0,094	0,032	0,000	0,005	0,002	0	0	0	0	0	0,002
		1-2	2-3	3-4	4-5	5-6	6-7	7-8	8-9	9-10	10-11	11-12	12-13	13-14	14-15	15-16	16-17	17-18	18-19	19-20	20-21	21-22	22-23	23-24	24-25	25-26
		Peak Wave Period [s]																							

Figure A.2: Wave Scatter Wind Speed Range: 1-2 m/s

Percentage of ocurrence (%) - Peak Wave Period vs Significant Wave Height vs 2-3 [m/s]																										
Significant Wave Height [m]	5-6	0,000	0,000	0,000	0,000	0,000	0,000	0,000	0,000	0,000	0,000	0,000	0,000	0,000	0,000	0,000	0,000	0	0	0	0	0	0	0	0	0
	4-5	0,000	0,000	0,000	0,000	0,000	0,000	0,000	0,000	0,000	0,000	0,000	0,000	0,000	0,000	0,000	0,000	0	0	0	0	0	0	0	0	0
	3-4	0,000	0,000	0,000	0,000	0,000	0,000	0,000	0,000	0,000	0,000	0,000	0,005	0,000	0,000	0,000	0,000	0	0	0	0	0	0	0	0	0
	2-3	0,000	0,000	0,000	0,000	0,000	0,000	0,000	0,007	0,007	0,048	0,043	0,052	0,000	0,021	0,014	0,000	0,005	0,002	0	0	0	0	0	0	0
	1-2	0,000	0,000	0,000	0,000	0,000	0,009	0,027	0,203	0,176	0,372	0,310	0,345	0,009	0,194	0,066	0,005	0,023	0,007	0	0,002	0	0	0	0	0
	0-1	0,000	0,002	0,027	0,011	0,002	0,023	0,055	0,299	0,249	0,361	0,246	0,235	0,007	0,123	0,030	0,002	0,009	0,002	0	0	0	0	0	0	0
		1-2	2-3	3-4	4-5	5-6	6-7	7-8	8-9	9-10	10-11	11-12	12-13	13-14	14-15	15-16	16-17	17-18	18-19	19-20	20-21	21-22	22-23	23-24	24-25	25-26
		Peak Wave Period [s]																								

Figure A.3: Wave Scatter - Wind Speed Range: 2-3 m/s

Percentage of ocurrence (%) - Peak Wave Period vs Significant Wave Height vs 3-4 [m/s]																										
Significant Wave Height [m]	5-6	0,000	0,000	0,000	0,000	0,000	0,000	0,000	0,000	0,000	0,000	0,000	0,000	0,000	0,000	0,000	0,000	0	0	0	0	0	0	0	0	0
	4-5	0,000	0,000	0,000	0,000	0,000	0,000	0,000	0,000	0,000	0,000	0,000	0,000	0,000	0,000	0,000	0,000	0	0	0	0	0	0	0	0	0
	3-4	0,000	0,000	0,000	0,000	0,000	0,000	0,000	0,000	0,000	0,000	0,005	0,005	0,000	0,005	0,000	0,000	0	0	0	0	0	0	0	0	0
	2-3	0,000	0,000	0,000	0,000	0,000	0,000	0,000	0,025	0,011	0,048	0,043	0,066	0,002	0,048	0,011	0,000	0,007	0,002	0	0	0	0	0	0	0
	1-2	0,000	0,000	0,000	0,000	0,002	0,039	0,048	0,345	0,324	0,541	0,461	0,564	0,027	0,308	0,096	0,002	0,037	0,005	0	0,002	0	0	0	0	0
	0-1	0,000	0,007	0,034	0,009	0,009	0,068	0,089	0,418	0,342	0,586	0,287	0,390	0,009	0,148	0,041	0,000	0,011	0,002	0	0	0	0	0	0	0
		1-2	2-3	3-4	4-5	5-6	6-7	7-8	8-9	9-10	10-11	11-12	12-13	13-14	14-15	15-16	16-17	17-18	18-19	19-20	20-21	21-22	22-23	23-24	24-25	25-26
		Peak Wave Period [s]																								

Figure A.4: Wave Scatter - Wind Speed Range: 3-4 m/s

Percentage of ocurrence (%) - Peak Wave Period vs Significant Wave Height vs 4-5 [m/s]																										
Significant Wave Height [m]	5-6	0,000	0,000	0,000	0,000	0,000	0,000	0,000	0,000	0,000	0,000	0,000	0,000	0,000	0,000	0,000	0,000	0	0	0	0	0	0	0	0	0
	4-5	0,000	0,000	0,000	0,000	0,000	0,000	0,000	0,000	0,000	0,000	0,000	0,000	0,000	0,000	0,000	0,000	0	0	0	0	0	0	0	0	0
	3-4	0,000	0,000	0,000	0,000	0,000	0,000	0,000	0,000	0,000	0,000	0,000	0,002	0,002	0,021	0,005	0,000	0	0	0	0	0	0	0	0	0
	2-3	0,000	0,000	0,000	0,000	0,000	0,000	0,002	0,021	0,016	0,078	0,050	0,121	0,000	0,052	0,050	0,002	0,021	0,005	0	0	0	0	0	0	0
	1-2	0,000	0,000	0,000	0,005	0,005	0,062	0,091	0,596	0,548	0,758	0,648	0,947	0,030	0,413	0,167	0,005	0,066	0,005	0,002	0,002	0	0	0	0	0
	0-1	0,000	0,000	0,050	0,052	0,011	0,114	0,112	0,440	0,349	0,504	0,290	0,292	0,005	0,132	0,032	0,002	0,009	0,005	0	0	0	0	0	0	0,002
		1-2	2-3	3-4	4-5	5-6	6-7	7-8	8-9	9-10	10-11	11-12	12-13	13-14	14-15	15-16	16-17	17-18	18-19	19-20	20-21	21-22	22-23	23-24	24-25	25-26
		Peak Wave Period [s]																								

Figure A.5: Wave Scatter - Wind Speed Range: 4-5 m/s

Percentage of ocurrence (%) - Peak Wave Period vs Significant Wave Height vs 5-6 [m/s]																										
Significant Wave Height [m]	5-6	0,000	0,000	0,000	0,000	0,000	0,000	0,000	0,000	0,000	0,000	0,000	0,000	0,000	0,000	0,000	0,000	0	0	0	0	0	0	0	0	0
	4-5	0,000	0,000	0,000	0,000	0,000	0,000	0,000	0,000	0,000	0,000	0,000	0,000	0,000	0,000	0,000	0,000	0	0	0	0	0	0	0	0	0
	3-4	0,000	0,000	0,000	0,000	0,000	0,000	0,002	0,000	0,000	0,000	0,007	0,005	0,000	0,016	0,009	0,000	0,002	0	0	0	0	0	0	0	0
	2-3	0,000	0,000	0,000	0,000	0,000	0,000	0,000	0,050	0,048	0,125	0,091	0,151	0,007	0,116	0,064	0,000	0,027	0,005	0	0	0	0	0	0	0
	1-2	0,000	0,000	0,000	0,030	0,030	0,144	0,294	0,990	0,689	1,120	0,965	1,173	0,032	0,707	0,262	0,009	0,073	0,011	0	0,005	0	0	0	0	0
	0-1	0,000	0,000	0,052	0,103	0,018	0,084	0,107	0,440	0,322	0,418	0,224	0,249	0,005	0,080	0,021	0,000	0,007	0,005	0	0	0	0	0	0	0
		1-2	2-3	3-4	4-5	5-6	6-7	7-8	8-9	9-10	10-11	11-12	12-13	13-14	14-15	15-16	16-17	17-18	18-19	19-20	20-21	21-22	22-23	23-24	24-25	25-26
		Peak Wave Period [s]																								

Figure A.6: Wave Scatter - Wind Speed Range: 5-6 m/s

Percentage of ocurrence (%) - Peak Wave Period vs Significant Wave Height vs 6-7 [m/s]																										
Significant Wave Height [m]	5-6	0,000	0,000	0,000	0,000	0,000	0,000	0,000	0,000	0,000	0,000	0,000	0,000	0,000	0,000	0,000	0,000	0	0	0	0	0	0	0	0
	4-5	0,000	0,000	0,000	0,000	0,000	0,000	0,000	0,000	0,000	0,000	0,000	0,000	0,000	0,000	0,000	0,000	0	0	0	0	0	0	0	0
	3-4	0,000	0,000	0,000	0,000	0,000	0,000	0,002	0,000	0,000	0,000	0,005	0,014	0,002	0,011	0,011	0,000	0,002	0	0	0	0	0	0	0
	2-3	0,000	0,000	0,000	0,000	0,000	0,000	0,000	0,057	0,091	0,141	0,171	0,292	0,009	0,192	0,132	0,000	0,046	0,011	0	0	0	0	0	0
	1-2	0,000	0,000	0,000	0,080	0,128	0,319	0,509	1,574	0,728	1,355	1,259	1,524	0,037	0,726	0,306	0,007	0,082	0,005	0	0	0	0	0	0
	0-1	0,000	0,000	0,050	0,176	0,032	0,110	0,080	0,445	0,210	0,253	0,135	0,141	0,000	0,055	0,016	0,000	0,011	0	0	0	0	0	0	0
		1-2	2-3	3-4	4-5	5-6	6-7	7-8	8-9	9-10	10-11	11-12	12-13	13-14	14-15	15-16	16-17	17-18	18-19	19-20	20-21	21-22	22-23	23-24	24-25	25-26
		Peak Wave Period [s]																								

Figure A.7: Wave Scatter - Wind Speed Range: 6-7 m/s

Percentage of ocurrence (%) - Peak Wave Period vs Significant Wave Height vs 7-8 [m/s]																										
Significant Wave Height [m]	5-6	0,000	0,000	0,000	0,000	0,000	0,000	0,000	0,000	0,000	0,000	0,000	0,000	0,000	0,000	0,000	0,000	0	0	0	0	0	0	0	0
	4-5	0,000	0,000	0,000	0,000	0,000	0,000	0,000	0,000	0,000	0,000	0,000	0,000	0,000	0,000	0,002	0,000	0	0	0	0	0	0	0	0
	3-4	0,000	0,000	0,000	0,000	0,000	0,000	0,000	0,000	0,000	0,000	0,002	0,027	0,000	0,014	0,023	0,000	0,014	0,005	0	0	0	0	0	0
	2-3	0,000	0,000	0,000	0,000	0,000	0,014	0,005	0,176	0,107	0,219	0,228	0,461	0,018	0,345	0,167	0,000	0,052	0,018	0	0	0	0	0	0
	1-2	0,000	0,000	0,000	0,137	0,240	0,554	0,721	1,777	1,022	1,479	1,193	1,433	0,055	0,648	0,221	0,002	0,078	0,007	0	0,002	0	0	0	0
	0-1	0,000	0,000	0,037	0,167	0,037	0,055	0,059	0,178	0,116	0,141	0,041	0,068	0,000	0,023	0,002	0,000	0,002	0,002	0	0	0	0	0	0
		1-2	2-3	3-4	4-5	5-6	6-7	7-8	8-9	9-10	10-11	11-12	12-13	13-14	14-15	15-16	16-17	17-18	18-19	19-20	20-21	21-22	22-23	23-24	24-25	25-26
		Peak Wave Period [s]																								

Figure A.8: Wave Scatter - Wind Speed Range: 7-8 m/s

Percentage of ocurrence (%) - Peak Wave Period vs Significant Wave Height vs 8-9 [m/s]																										
Significant Wave Height [m]	5-6	0,000	0,000	0,000	0,000	0,000	0,000	0,000	0,000	0,000	0,000	0,000	0,000	0,000	0,000	0,000	0,000	0	0	0	0	0	0	0	0
	4-5	0,000	0,000	0,000	0,000	0,000	0,000	0,000	0,000	0,000	0,000	0,000	0,000	0,000	0,000	0,007	0,000	0,005	0	0	0	0	0	0	0
	3-4	0,000	0,000	0,000	0,000	0,000	0,000	0,000	0,000	0,002	0,009	0,011	0,014	0,000	0,032	0,027	0,002	0,014	0,002	0	0	0	0	0	0
	2-3	0,000	0,000	0,000	0,000	0,000	0,034	0,014	0,395	0,244	0,326	0,326	0,614	0,016	0,470	0,212	0,000	0,071	0,027	0	0	0	0	0	0
	1-2	0,000	0,000	0,000	0,080	0,415	0,812	0,908	1,907	0,771	1,191	0,963	1,196	0,043	0,529	0,176	0,005	0,048	0,014	0,002	0	0	0	0	0
	0-1	0,002	0,000	0,011	0,112	0,023	0,023	0,018	0,087	0,068	0,091	0,027	0,034	0,000	0,005	0,007	0,000	0	0,002	0	0	0	0	0	0
		1-2	2-3	3-4	4-5	5-6	6-7	7-8	8-9	9-10	10-11	11-12	12-13	13-14	14-15	15-16	16-17	17-18	18-19	19-20	20-21	21-22	22-23	23-24	24-25	25-26
		Peak Wave Period [s]																								

Figure A.9: Wave Scatter - Wind Speed Range: 8-9 m/s

Percentage of ocurrence (%) - Peak Wave Period vs Significant Wave Height vs 9-10 [m/s]																										
Significant Wave Height [m]	5-6	0,000	0,000	0,000	0,000	0,000	0,000	0,000	0,000	0,000	0,000	0,000	0,000	0,000	0,000	0,000	0,000	0	0	0	0	0	0	0	0
	4-5	0,000	0,000	0,000	0,000	0,000	0,000	0,000	0,000	0,000	0,000	0,000	0,000	0,000	0,000	0,000	0,000	0,002	0	0	0	0	0	0	0
	3-4	0,000	0,000	0,000	0,000	0,000	0,000	0,002	0,000	0,011	0,011	0,016	0,032	0,002	0,055	0,032	0,000	0,032	0,014	0	0	0	0	0	0
	2-3	0,000	0,000	0,000	0,000	0,005	0,100	0,084	0,687	0,262	0,402	0,472	0,737	0,027	0,525	0,210	0,002	0,062	0,016	0	0	0	0	0	0
	1-2	0,000	0,000	0,000	0,046	0,580	1,118	1,093	1,504	0,653	0,783	0,664	0,678	0,011	0,297	0,068	0,000	0,014	0,002	0	0	0	0	0	0
	0-1	0,000	0,000	0,000	0,030	0,021	0,014	0,011	0,039	0,030	0,014	0,023	0,009	0,000	0,007	0,000	0,000	0	0	0	0	0	0	0	0
		1-2	2-3	3-4	4-5	5-6	6-7	7-8	8-9	9-10	10-11	11-12	12-13	13-14	14-15	15-16	16-17	17-18	18-19	19-20	20-21	21-22	22-23	23-24	24-25	25-26
		Peak Wave Period [s]																								

Figure A.10: Wave Scatter - Wind Speed Range: 9-10 m/s

Percentage of ocurrence (%) - Peak Wave Period vs Significant Wave Height vs 10-11 [m/s]																										
Significant Wave Height [m]	5-6	0,000	0,000	0,000	0,000	0,000	0,000	0,000	0,000	0,000	0,000	0,000	0,000	0,000	0,000	0,000	0,000	0	0	0	0	0	0	0	0	0
	4-5	0,000	0,000	0,000	0,000	0,000	0,000	0,000	0,000	0,000	0,000	0,000	0,000	0,000	0,000	0,000	0,000	0,005	0,002	0	0	0	0	0	0	0
	3-4	0,000	0,000	0,000	0,000	0,000	0,000	0,002	0,002	0,025	0,034	0,048	0,080	0,000	0,066	0,050	0,000	0,025	0,009	0	0	0	0	0	0	0
	2-3	0,000	0,000	0,000	0,000	0,007	0,153	0,199	1,118	0,292	0,354	0,443	0,639	0,018	0,345	0,130	0,000	0,034	0,009	0	0	0	0	0	0	0
	1-2	0,000	0,000	0,000	0,016	0,326	1,161	1,068	0,974	0,399	0,497	0,310	0,269	0,014	0,110	0,027	0,000	0,011	0,002	0,002	0	0	0	0	0	0
	0-1	0,000	0,000	0,002	0,007	0,002	0,005	0,007	0,011	0,009	0,009	0,007	0,005	0,000	0,002	0,000	0,000	0	0	0	0	0	0	0	0	0
		1-2	2-3	3-4	4-5	5-6	6-7	7-8	8-9	9-10	10-11	11-12	12-13	13-14	14-15	15-16	16-17	17-18	18-19	19-20	20-21	21-22	22-23	23-24	24-25	25-26
		Peak Wave Period [s]																								

Figure A.11: Wave Scatter - Wind Speed Range: 10-11 m/s

Percentage of ocurrence (%) - Peak Wave Period vs Significant Wave Height vs 11-12 [m/s]																										
Significant Wave Height [m]	5-6	0,000	0,000	0,000	0,000	0,000	0,000	0,000	0,000	0,000	0,000	0,000	0,000	0,000	0,000	0,000	0,000	0	0	0	0	0	0	0	0	0
	4-5	0,000	0,000	0,000	0,000	0,000	0,000	0,000	0,000	0,000	0,000	0,000	0,000	0,000	0,002	0,000	0,000	0	0	0	0	0	0	0	0	0
	3-4	0,000	0,000	0,000	0,000	0,000	0,000	0,002	0,034	0,034	0,068	0,050	0,055	0,005	0,062	0,062	0,000	0,041	0,007	0	0	0	0	0	0	0
	2-3	0,000	0,000	0,000	0,000	0,007	0,189	0,358	1,214	0,242	0,274	0,313	0,440	0,014	0,219	0,091	0,000	0,03	0	0	0,002	0	0	0	0	0
	1-2	0,000	0,000	0,000	0,005	0,119	0,901	0,831	0,559	0,121	0,164	0,146	0,084	0,005	0,057	0,018	0,000	0,005	0	0	0,002	0	0	0	0	0
	0-1	0,000	0,002	0,005	0,000	0,007	0,000	0,002	0,009	0,002	0,002	0,002	0,005	0,000	0,002	0,000	0,000	0	0	0	0	0	0	0	0	0
		1-2	2-3	3-4	4-5	5-6	6-7	7-8	8-9	9-10	10-11	11-12	12-13	13-14	14-15	15-16	16-17	17-18	18-19	19-20	20-21	21-22	22-23	23-24	24-25	25-26
		Peak Wave Period [s]																								

Figure A.12: Wave Scatter - Wind Speed Range: 11-12 m/s

Percentage of ocurrence (%) - Peak Wave Period vs Significant Wave Height vs 12-13 [m/s]																										
Significant Wave Height [m]	5-6	0,000	0,000	0,000	0,000	0,000	0,000	0,000	0,000	0,000	0,000	0,000	0,000	0,000	0,000	0,000	0,000	0	0	0	0	0	0	0	0	0
	4-5	0,000	0,000	0,000	0,000	0,000	0,000	0,000	0,000	0,000	0,000	0,007	0,000	0,000	0,000	0,023	0,002	0,009	0	0	0	0	0	0	0	0
	3-4	0,000	0,000	0,000	0,000	0,000	0,000	0,007	0,059	0,052	0,039	0,050	0,071	0,009	0,089	0,062	0,000	0,023	0,007	0	0	0	0	0	0	0
	2-3	0,000	0,000	0,000	0,000	0,000	0,171	0,395	0,990	0,105	0,091	0,139	0,187	0,009	0,096	0,011	0,000	0,007	0,002	0,002	0	0	0	0	0	0
	1-2	0,000	0,000	0,000	0,005	0,041	0,420	0,463	0,176	0,071	0,050	0,043	0,030	0,000	0,025	0,002	0,000	0	0	0	0	0	0	0	0	0
	0-1	0,000	0,005	0,000	0,005	0,002	0,002	0,002	0,005	0,002	0,002	0,002	0,002	0,000	0,000	0,000	0,000	0	0	0	0	0	0	0	0	0
		1-2	2-3	3-4	4-5	5-6	6-7	7-8	8-9	9-10	10-11	11-12	12-13	13-14	14-15	15-16	16-17	17-18	18-19	19-20	20-21	21-22	22-23	23-24	24-25	25-26
		Peak Wave Period [s]																								

Figure A.13: Wave Scatter - Wind Speed Range: 12-13 m/s

Percentage of ocurrence (%) - Peak Wave Period vs Significant Wave Height vs 13-14 [m/s]																										
Significant Wave Height [m]	5-6	0,000	0,000	0,000	0,000	0,000	0,000	0,000	0,000	0,000	0,000	0,000	0,000	0,000	0,000	0,000	0,002	0	0	0	0	0	0	0	0	0
	4-5	0,000	0,000	0,000	0,000	0,000	0,000	0,000	0,000	0,005	0,005	0,005	0,002	0,000	0,005	0,014	0,000	0,016	0	0	0	0	0	0	0	0
	3-4	0,000	0,000	0,000	0,000	0,000	0,005	0,002	0,110	0,066	0,043	0,034	0,050	0,000	0,046	0,027	0,002	0,009	0,002	0	0	0	0	0	0	0
	2-3	0,000	0,000	0,000	0,000	0,000	0,055	0,297	0,577	0,048	0,030	0,041	0,073	0,005	0,037	0,011	0,000	0,005	0	0	0	0	0	0	0	0
	1-2	0,000	0,000	0,002	0,000	0,005	0,144	0,130	0,048	0,032	0,034	0,021	0,011	0,000	0,009	0,007	0,000	0	0	0	0,002	0	0	0	0	0
	0-1	0,000	0,000	0,000	0,000	0,005	0,000	0,000	0,002	0,000	0,000	0,000	0,000	0,000	0,000	0,000	0,000	0	0	0	0	0	0	0	0	0
		1-2	2-3	3-4	4-5	5-6	6-7	7-8	8-9	9-10	10-11	11-12	12-13	13-14	14-15	15-16	16-17	17-18	18-19	19-20	20-21	21-22	22-23	23-24	24-25	25-26
		Peak Wave Period [s]																								

Figure A.14: Wave Scatter - Wind Speed Range: 13-14 m/s

Percentage of ocurrence (%) - Peak Wave Period vs Significant Wave Height vs 14-15 [m/s]																										
Significant Wave Height [m]	5-6	0,000	0,000	0,000	0,000	0,000	0,000	0,000	0,000	0,000	0,000	0,000	0,000	0,000	0,000	0,000	0,000	0	0	0	0	0	0	0	0	0
	4-5	0,000	0,000	0,000	0,000	0,000	0,000	0,000	0,000	0,007	0,009	0,014	0,007	0,000	0,005	0,009	0,000	0,011	0	0	0	0	0	0	0	0
	3-4	0,000	0,000	0,000	0,000	0,000	0,002	0,002	0,089	0,057	0,021	0,018	0,027	0,000	0,034	0,016	0,000	0,002	0	0	0	0	0	0	0	0
	2-3	0,000	0,000	0,000	0,000	0,000	0,011	0,089	0,267	0,007	0,009	0,016	0,034	0,000	0,009	0,002	0,000	0	0	0	0	0	0	0	0	0
	1-2	0,000	0,000	0,000	0,000	0,000	0,032	0,052	0,011	0,023	0,016	0,007	0,016	0,000	0,007	0,000	0,000	0	0	0	0	0	0	0	0	0
	0-1	0,000	0,002	0,000	0,000	0,000	0,000	0,000	0,002	0,000	0,000	0,000	0,002	0,000	0,000	0,000	0,000	0	0	0	0	0	0	0	0	0
		1-2	2-3	3-4	4-5	5-6	6-7	7-8	8-9	9-10	10-11	11-12	12-13	13-14	14-15	15-16	16-17	17-18	18-19	19-20	20-21	21-22	22-23	23-24	24-25	25-26
		Peak Wave Period [s]																								

Figure A.15: Wave Scatter - Wind Speed Range: 14-15 m/s

Percentage of ocurrence (%) - Peak Wave Period vs Significant Wave Height vs 15-16 [m/s]																										
Significant Wave Height [m]	5-6	0,000	0,000	0,000	0,000	0,000	0,000	0,000	0,000	0,000	0,000	0,002	0,000	0,000	0,000	0,000	0,000	0	0	0	0	0	0	0	0	0
	4-5	0,000	0,000	0,000	0,000	0,000	0,000	0,000	0,000	0,009	0,005	0,005	0,002	0,000	0,009	0,005	0,000	0,002	0,002	0	0	0	0	0	0	0
	3-4	0,000	0,000	0,000	0,000	0,000	0,000	0,002	0,075	0,025	0,011	0,007	0,005	0,000	0,011	0,009	0,000	0,002	0	0	0	0	0	0	0	0
	2-3	0,000	0,000	0,000	0,000	0,000	0,005	0,032	0,080	0,007	0,005	0,005	0,021	0,000	0,002	0,000	0,000	0,002	0	0	0	0	0	0	0	0
	1-2	0,000	0,000	0,000	0,000	0,000	0,007	0,002	0,005	0,011	0,005	0,005	0,007	0,000	0,002	0,000	0,000	0	0	0	0	0	0	0	0	0
	0-1	0,000	0,000	0,000	0,000	0,000	0,000	0,000	0,000	0,000	0,000	0,000	0,000	0,000	0,000	0,000	0,000	0	0	0	0	0	0	0	0	0
		1-2	2-3	3-4	4-5	5-6	6-7	7-8	8-9	9-10	10-11	11-12	12-13	13-14	14-15	15-16	16-17	17-18	18-19	19-20	20-21	21-22	22-23	23-24	24-25	25-26
		Peak Wave Period [s]																								

Figure A.16: Wave Scatter - Wind Speed Range: 15-16 m/s

Percentage of ocurrence (%) - Peak Wave Period vs Significant Wave Height vs 16-17 [m/s]																										
Significant Wave Height [m]	5-6	0,000	0,000	0,000	0,000	0,000	0,000	0,000	0,000	0,000	0,000	0,000	0,000	0,000	0,000	0,000	0,000	0	0	0	0	0	0	0	0	0
	4-5	0,000	0,000	0,000	0,000	0,000	0,000	0,000	0,007	0,007	0,011	0,014	0,002	0,000	0,005	0,005	0,000	0	0	0	0	0	0	0	0	0
	3-4	0,000	0,000	0,000	0,000	0,000	0,000	0,000	0,018	0,014	0,005	0,002	0,000	0,000	0,007	0,000	0,000	0	0	0	0	0	0	0	0	0
	2-3	0,000	0,000	0,000	0,000	0,000	0,002	0,002	0,007	0,000	0,000	0,002	0,000	0,002	0,000	0,000	0,000	0	0	0	0	0	0	0	0	0
	1-2	0,000	0,000	0,000	0,000	0,000	0,000	0,000	0,014	0,002	0,000	0,002	0,007	0,000	0,002	0,000	0,000	0	0	0	0	0	0	0	0	0
	0-1	0,000	0,000	0,000	0,000	0,000	0,000	0,000	0,000	0,000	0,000	0,000	0,000	0,000	0,000	0,000	0,000	0	0	0	0	0	0	0	0	0
		1-2	2-3	3-4	4-5	5-6	6-7	7-8	8-9	9-10	10-11	11-12	12-13	13-14	14-15	15-16	16-17	17-18	18-19	19-20	20-21	21-22	22-23	23-24	24-25	25-26
		Peak Wave Period [s]																								

Figure A.17: Wave Scatter - Wind Speed Range: 16-17 m/s

Percentage of ocurrence (%) - Peak Wave Period vs Significant Wave Height vs 17-18 [m/s]																										
Significant Wave Height [m]	5-6	0,000	0,000	0,000	0,000	0,000	0,000	0,000	0,000	0,000	0,000	0,002	0,000	0,000	0,002	0,000	0,000	0	0	0	0	0	0	0	0	0
	4-5	0,000	0,000	0,000	0,000	0,000	0,000	0,000	0,002	0,014	0,007	0,000	0,000	0,000	0,000	0,000	0,000	0	0	0	0	0	0	0	0	0
	3-4	0,000	0,000	0,000	0,000	0,000	0,000	0,000	0,005	0,005	0,000	0,002	0,000	0,000	0,000	0,000	0,000	0	0	0	0	0	0	0	0	0
	2-3	0,000	0,000	0,000	0,000	0,000	0,000	0,000	0,000	0,000	0,002	0,000	0,000	0,000	0,000	0,000	0,000	0	0	0	0	0	0	0	0	0
	1-2	0,000	0,000	0,000	0,000	0,002	0,002	0,000	0,002	0,002	0,000	0,000	0,000	0,000	0,000	0,000	0,000	0	0	0	0	0	0	0	0	0
	0-1	0,000	0,000	0,000	0,000	0,000	0,000	0,000	0,000	0,000	0,000	0,000	0,000	0,000	0,000	0,000	0,000	0	0	0	0	0	0	0	0	0
		1-2	2-3	3-4	4-5	5-6	6-7	7-8	8-9	9-10	10-11	11-12	12-13	13-14	14-15	15-16	16-17	17-18	18-19	19-20	20-21	21-22	22-23	23-24	24-25	25-26
		Peak Wave Period [s]																								

Figure A.18: Wave Scatter - Wind Speed Range: 17-18 m/s

Percentage of ocurrence (%) - Peak Wave Period vs Significant Wave Height vs 18-19 [m/s]																										
Significant Wave Height [m]	5-6	0,000	0,000	0,000	0,000	0,000	0,000	0,000	0,000	0,000	0,002	0,000	0,000	0,000	0,000	0,000	0,000	0	0	0	0	0	0	0	0	0
	4-5	0,000	0,000	0,000	0,000	0,000	0,000	0,000	0,000	0,000	0,002	0,000	0,000	0,000	0,000	0,000	0,000	0	0	0	0	0	0	0	0	0
	3-4	0,000	0,000	0,000	0,000	0,000	0,000	0,000	0,002	0,000	0,000	0,002	0,000	0,000	0,000	0,000	0,000	0	0	0	0	0	0	0	0	0
	2-3	0,000	0,000	0,000	0,000	0,000	0,000	0,000	0,000	0,000	0,000	0,002	0,002	0,000	0,000	0,000	0,000	0	0	0	0	0	0	0	0	0
	1-2	0,000	0,000	0,000	0,000	0,000	0,002	0,000	0,002	0,002	0,002	0,002	0,000	0,000	0,000	0,000	0,000	0	0	0	0	0	0	0	0	0
	0-1	0,000	0,000	0,000	0,000	0,000	0,000	0,000	0,000	0,000	0,000	0,000	0,000	0,000	0,000	0,000	0,000	0	0	0	0	0	0	0	0	0
		1-2	2-3	3-4	4-5	5-6	6-7	7-8	8-9	9-10	10-11	11-12	12-13	13-14	14-15	15-16	16-17	17-18	18-19	19-20	20-21	21-22	22-23	23-24	24-25	25-26
		Peak Wave Period [s]																								

Figure A.19: Wave Scatter - Wind Speed Range: 18-19 m/s

Percentage of ocurrence (%) - Peak Wave Period vs Significant Wave Height vs 19-20 [m/s]																										
Significant Wave Height [m]	5-6	0,000	0,000	0,000	0,000	0,000	0,000	0,000	0,000	0,000	0,000	0,002	0,000	0,000	0,000	0,000	0,000	0	0	0	0	0	0	0	0	0
	4-5	0,000	0,000	0,000	0,000	0,000	0,000	0,000	0,000	0,002	0,000	0,000	0,000	0,000	0,000	0,000	0,000	0	0	0	0	0	0	0	0	0
	3-4	0,000	0,000	0,000	0,000	0,000	0,000	0,000	0,000	0,002	0,000	0,000	0,000	0,000	0,000	0,000	0,000	0	0	0	0	0	0	0	0	0
	2-3	0,000	0,000	0,000	0,000	0,000	0,000	0,000	0,000	0,000	0,000	0,000	0,000	0,000	0,000	0,000	0,000	0	0	0	0	0	0	0	0	0
	1-2	0,000	0,000	0,002	0,000	0,002	0,002	0,000	0,002	0,000	0,000	0,000	0,000	0,000	0,000	0,000	0,000	0	0	0	0	0	0	0	0	0
	0-1	0,000	0,000	0,000	0,000	0,000	0,000	0,000	0,000	0,000	0,000	0,000	0,000	0,000	0,000	0,000	0,000	0	0	0	0	0	0	0	0	0
		1-2	2-3	3-4	4-5	5-6	6-7	7-8	8-9	9-10	10-11	11-12	12-13	13-14	14-15	15-16	16-17	17-18	18-19	19-20	20-21	21-22	22-23	23-24	24-25	25-26
		Peak Wave Period [s]																								

Figure A.20: Wave Scatter - Wind Speed Range: 19-20 m/s

Percentage of ocurrence (%) - Peak Wave Period vs Significant Wave Height vs 20-21 [m/s]																										
Significant Wave Height [m]	5-6	0,000	0,000	0,000	0,000	0,000	0,000	0,000	0,000	0,000	0,000	0,000	0,000	0,000	0,000	0,000	0,000	0	0	0	0	0	0	0	0	0
	4-5	0,000	0,000	0,000	0,000	0,000	0,000	0,000	0,000	0,000	0,000	0,000	0,000	0,000	0,000	0,000	0,000	0	0	0	0	0	0	0	0	0
	3-4	0,000	0,000	0,000	0,000	0,000	0,000	0,000	0,000	0,000	0,000	0,000	0,000	0,000	0,000	0,000	0,000	0	0	0	0	0	0	0	0	0
	2-3	0,000	0,000	0,000	0,000	0,000	0,002	0,000	0,000	0,000	0,000	0,000	0,000	0,000	0,002	0,000	0,000	0	0	0	0	0	0	0	0	0
	1-2	0,000	0,000	0,000	0,000	0,000	0,002	0,002	0,000	0,000	0,000	0,000	0,000	0,000	0,000	0,000	0,000	0	0	0	0	0	0	0	0	0
	0-1	0,000	0,000	0,000	0,000	0,000	0,000	0,000	0,000	0,000	0,000	0,000	0,000	0,000	0,000	0,000	0,000	0	0	0	0	0	0	0	0	0
		1-2	2-3	3-4	4-5	5-6	6-7	7-8	8-9	9-10	10-11	11-12	12-13	13-14	14-15	15-16	16-17	17-18	18-19	19-20	20-21	21-22	22-23	23-24	24-25	25-26
		Peak Wave Period [s]																								

Figure A.21: Wave Scatter - Wind Speed Range: 20-21 m/s

Percentage of ocurrence (%) - Peak Wave Period vs Significant Wave Height vs 21-22 [m/s]																										
Significant Wave Height [m]	5-6	0,000	0,000	0,000	0,000	0,000	0,000	0,000	0,000	0,000	0,000	0,000	0,000	0,000	0,000	0,000	0,000	0	0	0	0	0	0	0	0	0
	4-5	0,000	0,000	0,000	0,000	0,000	0,000	0,000	0,000	0,000	0,000	0,000	0,000	0,000	0,000	0,000	0,000	0	0	0	0	0	0	0	0	0
	3-4	0,000	0,000	0,000	0,000	0,000	0,000	0,000	0,000	0,000	0,000	0,000	0,000	0,000	0,000	0,000	0,000	0	0	0	0	0	0	0	0	0
	2-3	0,000	0,000	0,000	0,000	0,000	0,000	0,000	0,000	0,000	0,000	0,000	0,002	0,000	0,000	0,000	0,000	0	0	0	0	0	0	0	0	0
	1-2	0,000	0,000	0,000	0,000	0,000	0,000	0,000	0,000	0,000	0,000	0,000	0,000	0,000	0,000	0,000	0,000	0	0	0	0	0	0	0	0	0
	0-1	0,000	0,000	0,000	0,000	0,000	0,000	0,000	0,000	0,000	0,000	0,000	0,000	0,000	0,000	0,000	0,000	0	0	0	0	0	0	0	0	0
		1-2	2-3	3-4	4-5	5-6	6-7	7-8	8-9	9-10	10-11	11-12	12-13	13-14	14-15	15-16	16-17	17-18	18-19	19-20	20-21	21-22	22-23	23-24	24-25	25-26
		Peak Wave Period [s]																								

Figure A.22: Wave Scatter - Wind Speed Range: 21-22 m/s

Significant Wave Height [m]	Percentage of ocurrence (%) - Peak Wave Period vs Significant Wave Height of all Data																								
5-6	0,000	0,000	0,000	0,000	0,000	0,000	0,000	0,000	0,000	0,002	0,007	0,000	0,000	0,002	0,000	0,000	0,0023	0	0	0	0	0	0	0	0
4-5	0,000	0,000	0,000	0,000	0,000	0,000	0,000	0,009	0,043	0,039	0,043	0,014	0,000	0,025	0,064	0,002	0,0502	0,005	0	0	0	0	0	0	0
3-4	0,000	0,000	0,000	0,000	0,000	0,007	0,025	0,395	0,294	0,242	0,260	0,392	0,021	0,468	0,333	0,005	0,1666	0,046	0	0	0	0	0	0	0
2-3	0,000	0,000	0,000	0,000	0,018	0,737	1,476	5,670	1,492	2,165	2,400	3,931	0,128	2,482	1,113	0,005	0,3719	0,103	0,002	0,0023	0	0	0	0	0
1-2	0,000	0,000	0,005	0,402	1,894	5,738	6,243	10,822	5,736	8,615	7,187	8,497	0,265	4,130	1,451	0,034	0,4518	0,062	0,007	0,0183	0	0	0	0	0
0-1	0,002	0,018	0,274	0,673	0,169	0,516	0,566	2,608	1,832	2,654	1,458	1,647	0,027	0,675	0,180	0,005	0,0548	0,021	0	0	0	0	0	0	0,0046
	1-2	2-3	3-4	4-5	5-6	6-7	7-8	8-9	9-10	10-11	11-12	12-13	13-14	14-15	15-16	16-17	17-18	18-19	19-20	20-21	21-22	22-23	23-24	24-25	25-26
	Peak Wave Period [s]																								

Figure A.23: Wave Scatter whole spectrum

A.2 Frequency Domain Results

A.2.1 Prior Fatigue Assessment

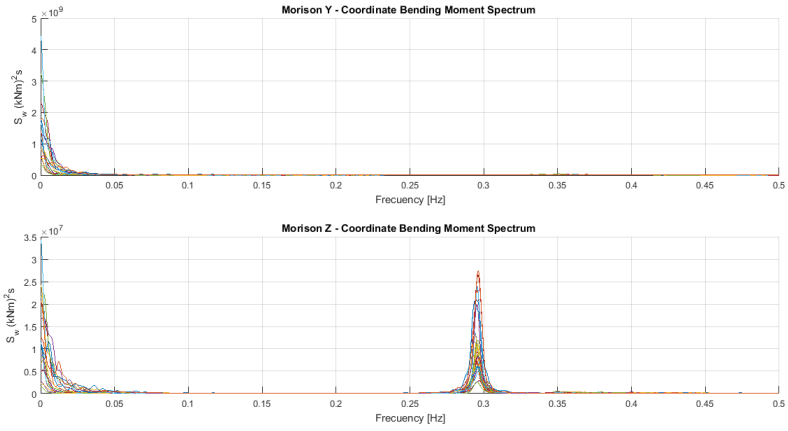

Figure A.24: Prior fatigue Morison model frequency spectrum spectrum in tower base

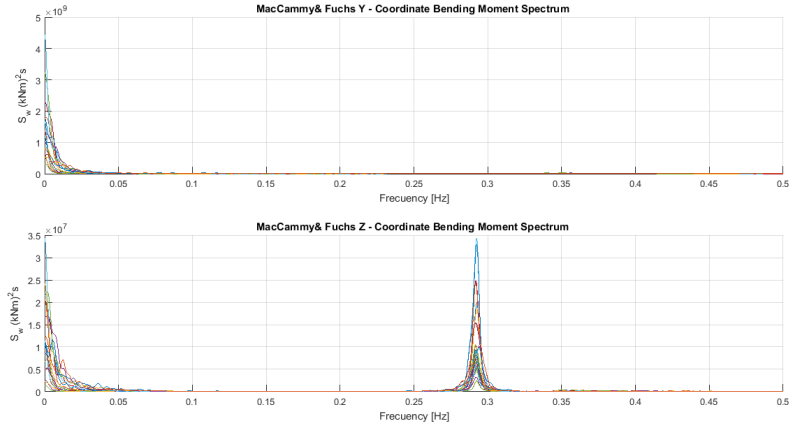

Figure A.25: Prior fatigue MacCamy&Fuchs model frequency spectrum spectrum in tower base

A.2.2 Full Fatigue Assessment Frequency Spectrums

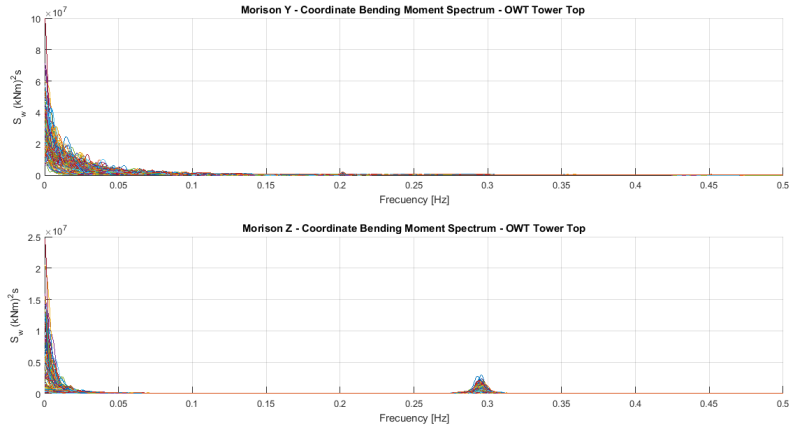

Figure A.26: Full fatigue Morison model frequency spectrum spectrum in tower top

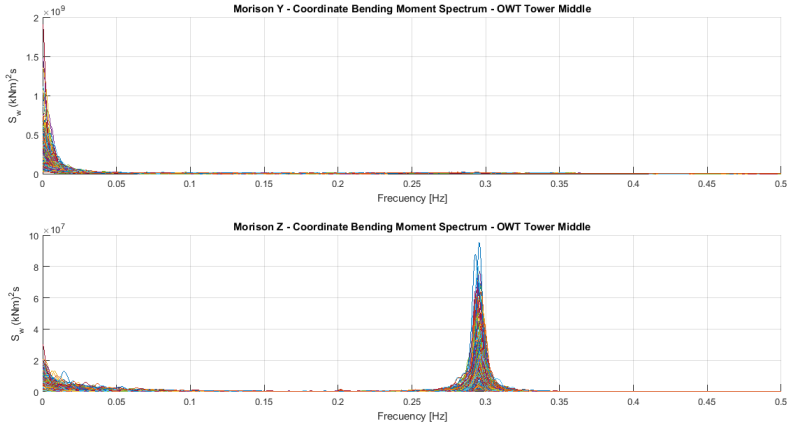

Figure A.27: Full fatigue Morison model frequency spectrum spectrum in tower middle

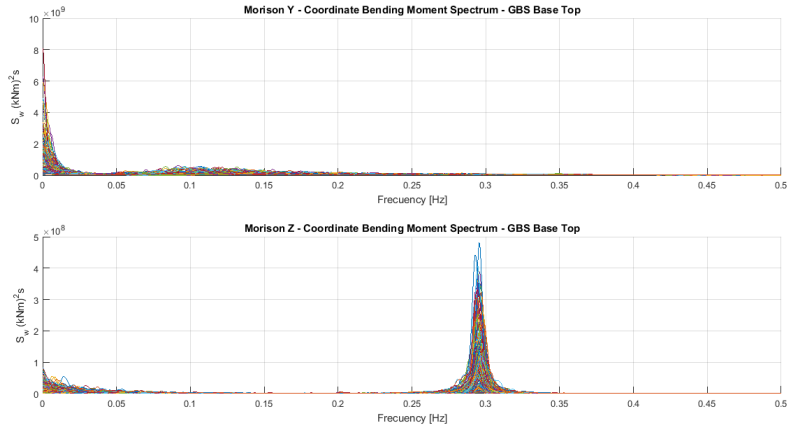

Figure A.28: Full fatigue Morison model frequency spectrum spectrum in caisson top

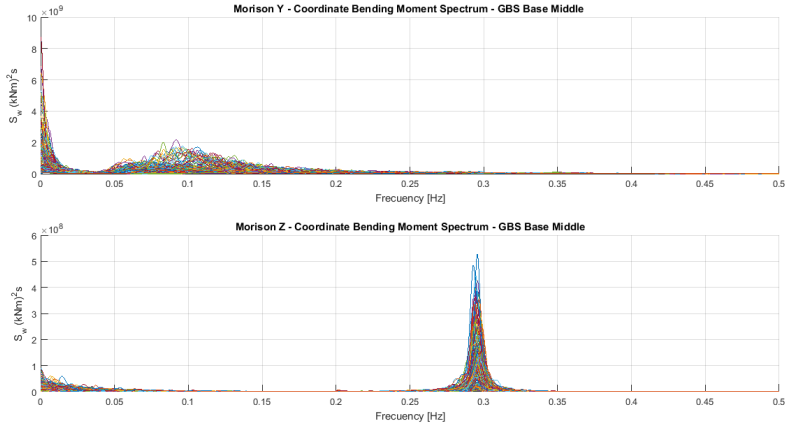

Figure A.29: Full fatigue Morison model frequency spectrum spectrum in caisson middle

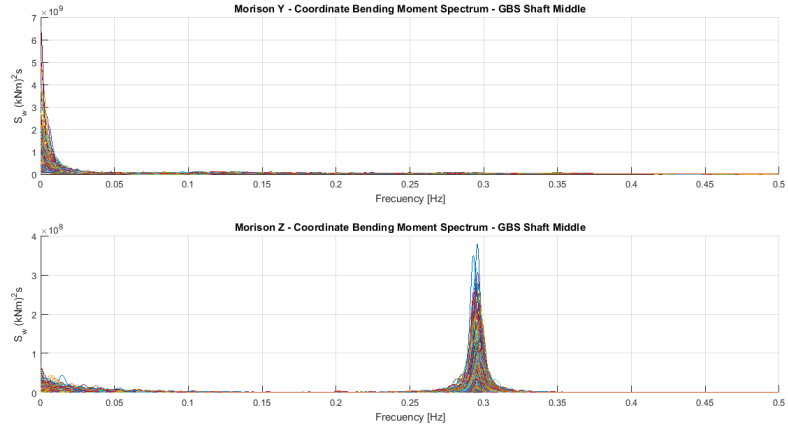

Figure A.30: Full fatigue Morison model frequency spectrum spectrum in shaft middle

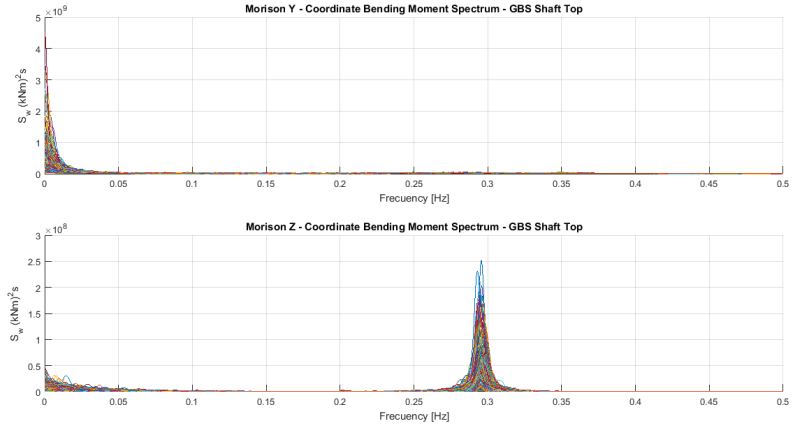

Figure A.31: Full fatigue Morison model frequency spectrum spectrum in shaft top

A.2.3 Non-Operational Frequency Spectrums

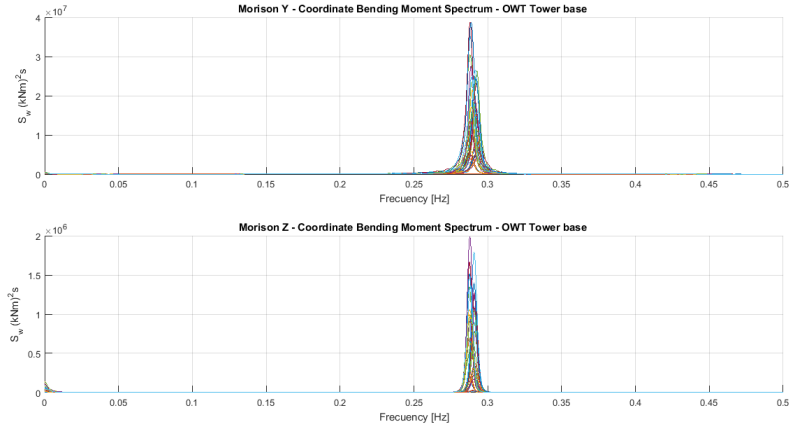

Figure A.32: Non-operational hybrid model frequency spectrum for tower top

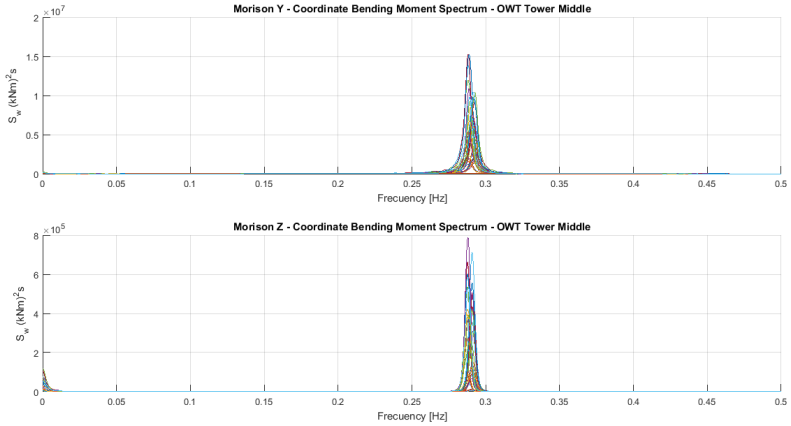

Figure A.33: Non-operational hybrid model frequency spectrum for tower middle

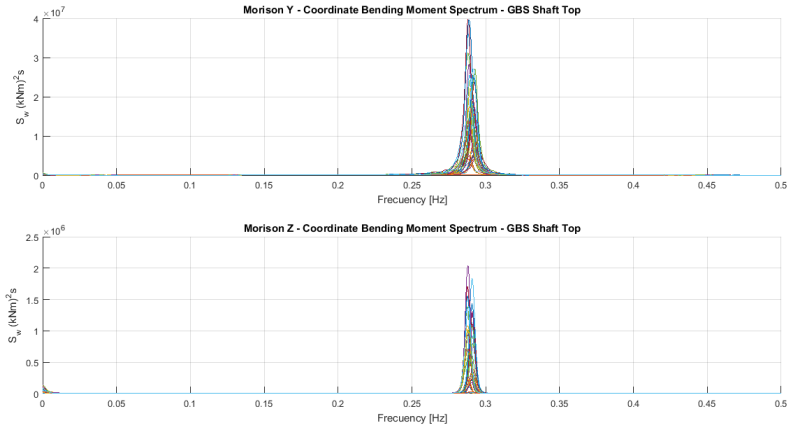

Figure A.34: Non-operational hybrid model frequency spectrum for shaft top

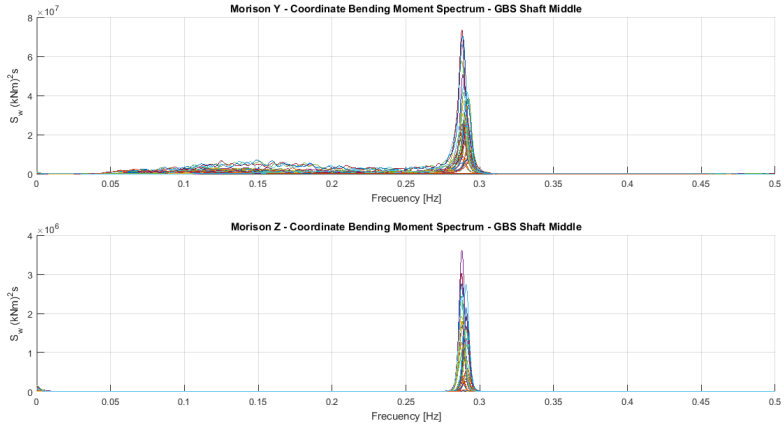

Figure A.35: Non-operational hybrid model frequency spectrum for shaft middle

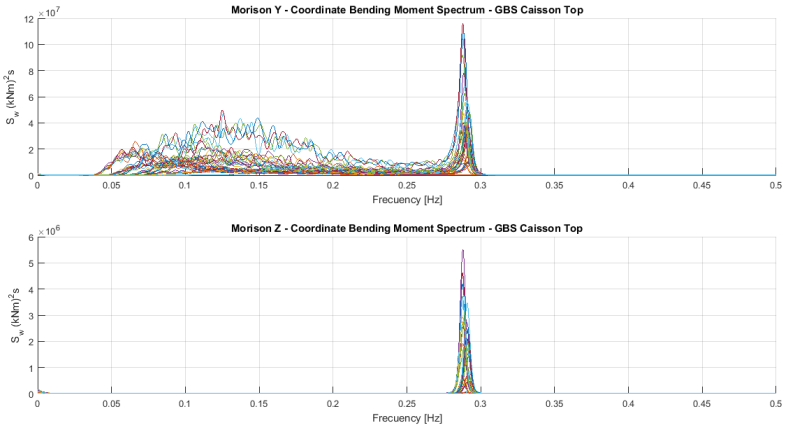

Figure A.36: Non-operational hybrid model frequency spectrum for Caisson top

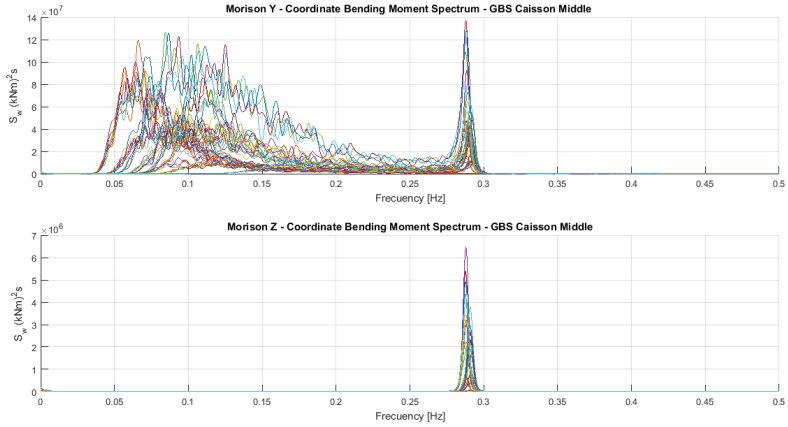

Figure A.37: Non-operational hybrid model frequency spectrum for Casisson middle

A.2.4 Time Domain Results

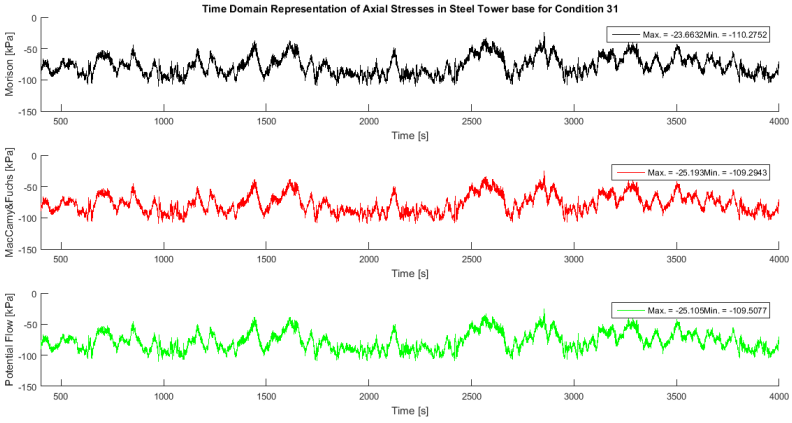

Figure A.38: TD representation of condition 31 for the three hydrodynamic models in OWT's tower base

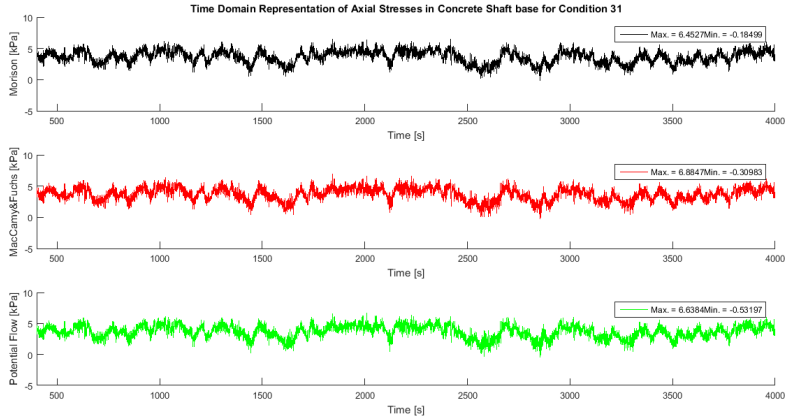

Figure A.39: TD representation of condition 31 for the three hydrodynamic models in concrete shaft

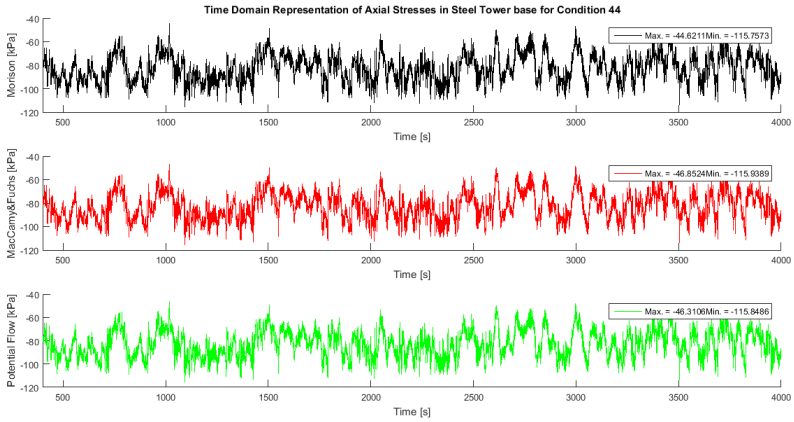

Figure A.40: TD representation of condition 44 for the three hydrodynamic models in OWT's tower base

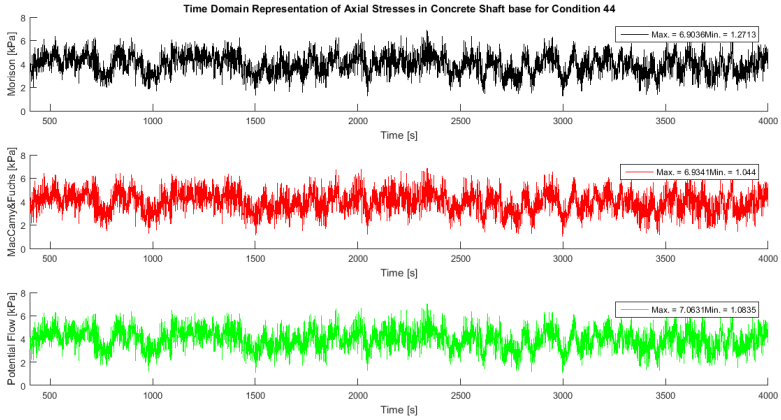

Figure A.41: TD representation of condition 44 for the three hydrodynamic models in concrete shaft

A.2.5 Constant Wind Test

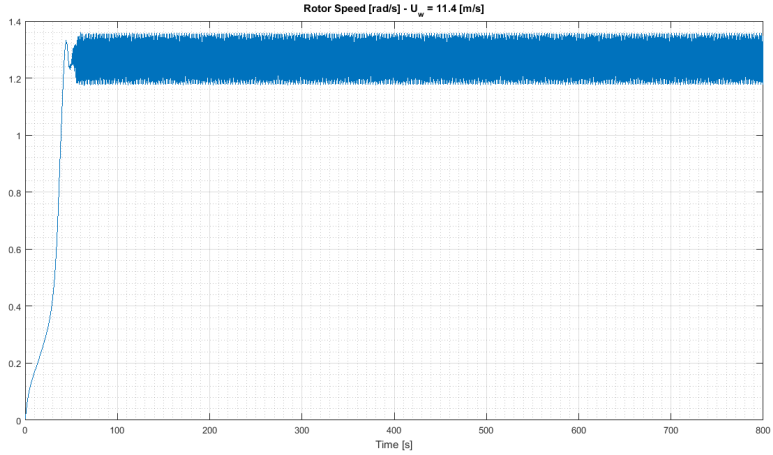

Figure A.42: Rotor speed plot for rated wind speed

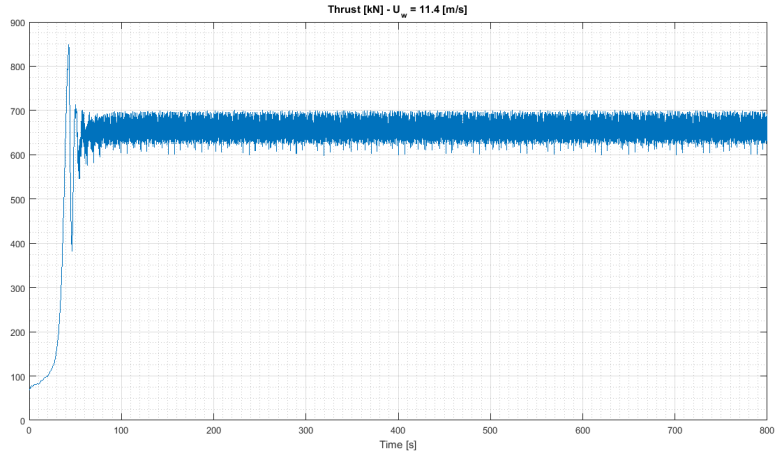

Figure A.43: Thrust plot for rated wind speed

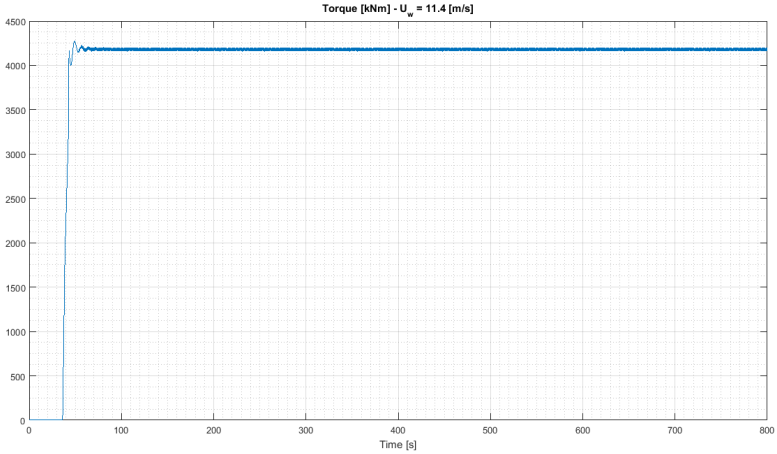

Figure A.44: Torque plot for rated wind speed

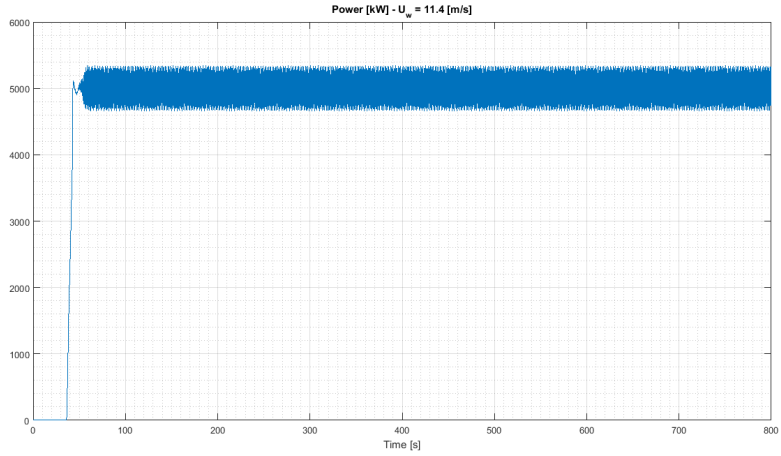

Figure A.45: Power plot for rated wind speed

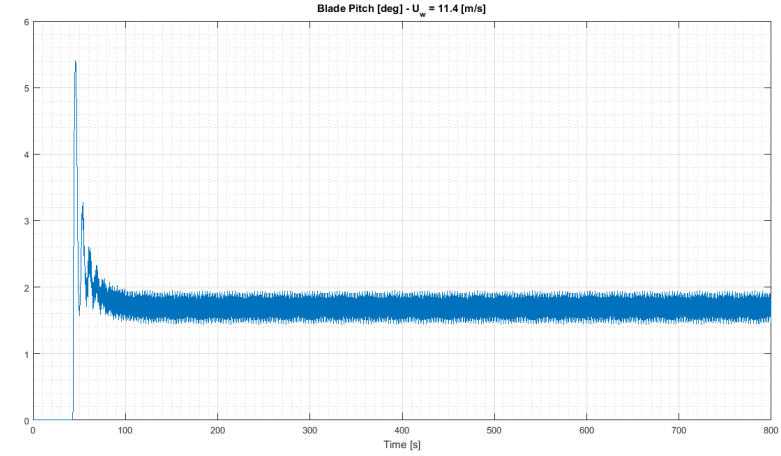

Figure A.46: Blade Pitch plot for rated wind speed